Printed & Bound by
Abbey Bookbinding
Unit 3 Clos Menter
Gabalfa Workshops
Western Avenue
Cardiff CF14 3AY
T: +44 (0) 29 2062 3290
F: +44 (0) 29 2062 5420
E: info@bookbindersuk.com
W: www.bookbindersuk.com

STOCHASTIC PROPAGATION AND PLANNING MODELS FOR BROADBAND FIXED WIRELESS ACCESS LINKS

Zaid M. H. Muhi-Eldeen

PhD 2008

STOCHASTIC PROPAGATION AND PLANNING MODELS FOR BROADBAND FIXED WIRELESS ACCESS LINKS

Zaid M. H. Muhi-Eldeen

June 2008

A thesis submitted in partial fulfilment of the requirements of the University of Glamorgan for the degree of Doctor of Philosophy

Director of Studies: Prof. Miqdad Al-Nuaimi
Second Supervisor: Dr. Jürgen Richter
Third Supervisor (External): Dr. Leo Ivrissimtzis

Declaration

I declare that the thesis has not been, nor currently being, submitted for award of any other degree or similar qualification.

Signed _____

Zaid Muhi-Eldeen
June 27th 2008.

This thesis is dedicated to my parents and fiancée Rim.

ACKNOWLEDGMENTS

My first thanks go to Almighty God who helped me in every step in bringing this piece of work to a completion.

My sincere gratitude goes to Professor Miqdad Al-Nuaimi for his supervision, support and patience during my PhD work. His help and invaluable advice led to my confidence in the choice of the project's direction and more importantly, my future life.

Very special thanks to Dr. Leonidas Ivrissimtzis. My PhD work would not have been possible without his helpfulness, patience and experienced guidance. It was under his tutelage that I developed a focus and skills through my project work. He provided me with direction, technical support and became more of a mentor and friend, than a supervisor.

I also owe thanks to Dr. Jürgen Richter who aided me during the progress of my PhD work. I am also grateful to Dr. Emad Alsusa and Dr. Hissam Tawfiq who were always there whenever I needed him.

I would like to express my gratitude to Dr. Jin Zhang for her generous support and friendship from the first day, and also to Dr. Telmo Fernandes for his technical advice. They both are sincerely thanked for their time and effort in helping me conducting my measurements.

I owe every part of this work, my education and every step forward in my life to my family. I would like to thank them for all their prayers and encouragement. Last but not the least, a deep sense of gratitude goes to my fiancée Rim Jawad for her endless love, cheerfulness and support. The smile on her face has always released my stress.

It has not been easy, but it would have been more difficult without all of you. May God bless you all.

ABSTRACT

Due to the rapid progress in wireless communication technologies and the increasing demands for new services; cutting edge techniques and research have developed wireless access delivery of broadband data. Such systems referred to as Broadband Fixed Wireless Access Systems (BFWA) or alternatively, Local Multipoint Distribution Systems (LMDS), are increasingly being regarded as a legitimate challenger to cable and digital subscriber lines (DSL), particularly in markets with poor cable or copper infrastructure. These systems have capabilities that go beyond the current WiFi and WiMAX technologies by providing users with higher bandwidths and faster data rates. The frequency of operation for such networks lies between 28 and 42 GHz according to the spectrum bands allocated for future LMDS networks.

The presented work aims at proposing a generalized stochastic model for the LMDS urban/suburban propagation channel. The model is based on a physical electromagnetic representation of the millimetre wavelength channel, with particular emphasis on fading margins in line-of-sight (LOS) links. The study focuses on the analysis, modelling and measurements of the fading effects of signal scattering caused by building surfaces and the ground on the direct field in an LMDS link at millimetre-waves. Outcomes have been validated against experimental results obtained in realistic propagation scenarios. More than 180 field measurement sets were taken at 40 GHz for model testing and validation purposes.

The main innovation of this work is the solution proposed to address the problem of signal scatter at millimetre-wave lengths. The approach uses high-frequency approximations to the analytical solution given by Kirchhoff's tangent-plane representation of rough surfaces. The electromagnetic field and signal power at the receiver are considered random and are evaluated using the Physical Optics method over different possible realizations of the surface geometry and building architectural features. This has resulted in novel derivations of the mean field, mean power density and scatter distribution of the scattered field. In comparison to deterministic models, such as ray-tracing that require intensive computations and detailed (millimetric

resolution) knowledge of topographical data that are almost impossible to obtain, the proposed model is rather efficient and yields accurate results.

The model has also been employed in analysing the effects of building scatter on the variance of the main desired link and the adjacent- or co-channel interfering link arising from neighbouring cells in cellular LMDS networks. This has enabled predictions of signal-to-interference ratio statistics and distributions for a particular underlying propagation environment.

Overall, comparisons yielded very good agreements between measurements and predictions of the main statistical parameters, thus verifying the main assumptions relating to the received signal strength, as well as the validity of a Rician distribution in describing the signal envelope variability for both the main and interference links in complex millimetre-wave propagation environments.

GLOSSARY OF TERMS

3G	Third Generation
AP	Alternative Plan
APC	Automatic Power Control
BER	Bit Error Rate
BFWA	Broadband Fixed Wireless Access Systems
BTS	Base Transceiver Station
CDF	Cumulative Distribution Function
CLT	Central-Limit-Theorem
DAB	Digital Audio Broadcasting
DEM	Digital Elevation Model
DSL	Digital Subscriber Line
EHF	Extremely High Frequency
EM	Electromagnetic
EMF	Electromagnetic Force
ETSI	European Telecommunications Standards Institute
FDD	Frequency Division Duplex
FDMA	Frequency Division Multiple Access
FM	Frequency Modulation
FSL	Free Space Loss
FWA	Fixed Wireless Access Systems
GIS	Graphical Information System
GO	Geometrical Optics
GPIB	General Purpose Interface Buss
GPS	Graphical Positioning System
GSM	Global System for Mobile
GTD	General Theory of Diffraction
GUI	Graphical User Interface
HF	High Frequency
IE	Industrial Estate

IF	Intermediate Frequency
ITU	International Telecommunication Union
LF	Low Frequency
LMDS	Local Multipoint Distribution Systems
LNA	Low Noise Amplifier
LO	Local-Oscillator
LOS	Line of Sight
MF	Medium Frequency
MMSE	Minimum Mean Square Error
NLOS	Non-Line of Sight
Ofcom	Office of Communications
PDF	Probability Density Function
PMP	Point-to-Multipoint
PO	Physical Optics
PSTN	Public Service Telephone Networks
QAM	Quadrature Amplitude Modulation
QPSK	Quadrature Phase-Shift Keying
PTP	Point-to-Point
RF	Radio Frequency
RMSE	Root-Mean-Square-Error
SHF	Super High Frequency
SIR	Signal-to-Interference-Ratio
SNR	Signal-to-Noise-Ratio
SOP	Sub Optimum Plan
SUI	Stanford University Interim
TDD	Time Division Duplex
TDMA	Time Division Multiple Access
UC	University Campus
UMTS	Universal Mobile Telecommunication Systems
UHF	Ultra High Frequency
VCO	Voltage-Controlled Oscillator
VHF	Very High Frequency
VLF	Very Low Frequency

WiFi	Wireless Fidelity
WiMAX	Worldwide Interoperability for Microwave Access
WLAN	Wireless Local Area Network
XPD	Cross Polarization Discrimination

LIST OF KEY VARIABLES

Chapter Two

λ	Wavelength
P_r	Received power
P_t	Transmitted power
G_t	Gain of transmitting antenna
G_r	Gain of receiving antenna
R_r	Rainfall rate
FSL	Free space path loss
L_P	Path loss
R_{max}	Maximum bit rate
R_r	Rain rate
K	Rician K-factor

Chapter Three

$\Delta\Phi$	Phase difference between the two rays
θ_i	Incident angle
θ_r	Reflection angle
h	surface irregularity height
ρ_s	Scattering loss factor
Γ	Modified Fresnel scatter coefficient
Z	Complex random variable
X	Real and imaginary part of Z
Y	Imaginary part of Z
R	Envelope of Z
Θ	Phase angle of Z
m_i	Mean of X (inphase component)
m_q	Mean of Y (quadrate component)
σ	Standard deviation of a random variable
s^2	Non-centrality parameter that dominates the dominant channel power component
Ω	Average amplitude

Chapter Four

$\boldsymbol{E}$	Field radiated by the transmitted antenna
$\hat{s}_T$	Unit vector emanating from the transmitter towards either, an observation point or a reflection/scatter centre.
s_T	Distance vector from the transmitter towards either, an observation point or a reflection/scatter centre.
$\hat{s}_R$	Unit vector from a surface to the receiver
s_R	Distance between the surface and the receiver

$s_{T,l}$ Distance from the transmitter to the projection of the mid-point of surface element l

$\hat{\mathbf{s}}_{T,l}$ Unit vector from the transmitter to the projection of the mid-point of element (l) on the mean plane of the building surface

$s_{R,l}$ Distance from the receiver to the projection of the mid-point of surface element l

$\hat{s}_{R,l}$ Unit vector from the projection of the mid-point of element (l) on the mean plane of the building surface to the receiver

$\hat{\mathbf{s}}_r$ Unit vector of specular reflection to the receiver

k Wave number

$\boldsymbol{e}_T$ Vector pattern function of the transmitter

$\boldsymbol{e}_R$ Vector pattern function of the receiver

$\boldsymbol{E}$ Electrical field at a point on the surface

$\boldsymbol{H}$ Magnetic field at a point on the surface

$\boldsymbol{E}_S$ Scattered field

$\boldsymbol{E}_i$ Incident electric field

$\boldsymbol{H}_i$ Incident magnetic field

E_r Electric field reflected by a plane of the flat element

H_r Magnetic field reflected by a plane of the flat element

M Total number of building surfaces

m Building surface number

z_m Unit vector perpendicular to the surface m

Δs_m Polygon area

L Number of flat elements of different material in a building

l Number of the flat element material

ζ Height above the surface mean's plane

ζ' Height above the surface mean's plane of another point similar to ζ

ζ_l z component of the l coordinate system

$\mathbf{r}_l$ Mid-point of element l

$\hat{\boldsymbol{n}}$ Unit vector perpendicular to the surface

$\hat{\boldsymbol{n}}_l$ Unit vector perpendicular to $L(M)$

$\mathbf{r}$ Point on surface element l

$\boldsymbol{\rho}_l$ Vector from the originate coordinates to the mid-point projected on the mean surface plane

$\boldsymbol{\rho}'$ A point on the projected mean surface plane

h_T Height of the transmit antenna above the ground level

h_R Height of the receive antenna above the ground level

d_0 Horizontal separation distance between the transmitter and the receiver

s_0 Direct distance between transmitter and receiver

η_0 Impedance of free space

$\hat{\boldsymbol{h}}$ Perpendicular unit vector field component

$\hat{\boldsymbol{v}}_i$ Parallel unit vector field component

R_h Fresnel reflection coefficient perpendicular to the plane of incidence

R_v Fresnel reflection coefficient parallel to the plane of incidence

θ_i Incident angle

ε_r Material complex relative dielectric constant also known as permittivity (F/m).

$\varepsilon_r^{'}$ Real part of ε_r

$\varepsilon_r^{''}$ Imaginary part of ε_r

ε_0 Vacuum permittivity

σ_e Electrical conductivity (J/E)

ω Angular frequency

$\mathfrak{I}_l$ Dyadic scattering coefficient

$\mathfrak{R}$ Constant, see Eq. (4.52)

T_l See Eq. (4.66)

U_l See Eq. (4.67)

$\boldsymbol{F}$ Perimeter of the triangle

L Triangular edge number

α_L An angle between sides of a triangle

r_s Total signal at the receiver terminals due to the field scattered by building surface (m)

r_D Total signal received from the direct field between the transmitter and receiver

r_R Total signal received due to a ground reflection between the transmitter and receiver.

F See Eq. (4.71)

J See Eq (4.72)

σ_x Standard deviation of the surface elevation in the x- directions

σ_y Standard deviation of the surface elevation in the y- directions

r Cross-correlation of the surface elevations in x- and y- directions

σ_h Standard deviation of the elevation above the rough surface mean plane

a Signal's envelope

a_D Envelope of the direct field

a_R Envelope of the reflected field

a_S Envelope of the scattered field

s^2 Direct field power.

p Total received power

σ^2 Scattered field power

f_a PDF of the received amplitude

f_p PDF of the received power

I_0 Modified Bessel function of the first-kind and zero-order

K Rician K-factor

μ_p Mean of received or measured data

σ_p^2 Standard deviation of the simulated or measured data

σ_{p4}^2 Fourth moment of the simulated or measured data

$C(x)$ Cosine Fresnel integral

$S(x)$ Sine Fresnel integral

Chapter Six

μ_{k_m}	Moment of a random variable
k_m	Order of moment
$\overline{x}$	Average value
x_i	Random variable

TABLE OF CONTENTS

ACKNOWLEDGMENTS III

ABSTRACT IV

GLOSSARY OF TERMS VI

LIST OF KEY VARIABLES IX

TABLE OF CONTENTS IXIII

LIST OF FIGURES XVIII

LIST OF TABLES XXII

CHAPTER ONE 22

INTRODUCTION 22

1.0 Overview 22

1.1 Fixed Wireless Access Systems 23

1.2 Radiowave Propagation 24

1.3 Modelling 25

1.4 Areas of Research and Aim of Investigation 27

1.5 Thesis Structure 29

1.6 References 31

CHAPTER TWO 32

LMDS NETWORKS 32

2.1 Overview 32

2.2 Local Multipoint Distribution Systems 34

2.3 Benefits 37

2.4 The Current Market 38

2.5 Millimetre-Wave Propagation 41

2.6 Impairments, Challenges and Literature Review 43

2.7 Cellular LMDS 47

2.8 Interference Considerations and LMDS Cell Plans 50

2.9 Interference Mechanisms 53
2.10 Other Frequency Cell Plans 55
2.11 Interference Literature Review 55
2.12 Interim Conclusion 57
2.13 References 59

CHAPTER THREE 64

CHANNEL & PROPAGATION MODELLING AT MILLIMETRE-WAVE LENGTH FREQUENCIES 64

3.1 Overview 64
3.1.1 Scattering of Electromagnetic Waves 64
3.1.2 Solution to Scatter by Rough Surfaces (Kirchhoff Approach) 67
3.1.3 Examples from the Literature 69
3.2 Classification of Propagation Models 70
3.2.1 Empirical Models 70
3.2.2 Deterministic Models 71
3.2.3 Statistical Models 72
3.3 Channel Models 73
3.3.1 Rician and Rayleigh Channel Fading 73
3.3.2 Rician & Rayleigh Probability Density Function (PDF) 74
3.3.3 Rician *K*-Factor 75
3.3.4 Rician *K*-Factor Extraction 75
3.3.4.1 Method of Moments 75
3.3.4.2 Graphical Moment Method 77
3.3.4.3 Second and Forth Moment Method 78
3.3.4.4 Maximum Likelihood Estimation 79
3.5 Interim Conclusion 79
3.6 References 81

CHAPTER FOUR 84

THE STOCHASTIC ELECTROMAGNETIC MODEL 84

4.1 Overview 84
4.2 Propagation Geometry 85

4.2.1 Building scatter geometry 85
4.2.2 Ground Reflection 89
4.3 Scattering Formulation 91
4.3.1 Physical Optics Scattering by Building Surfaces 91
4.3.2 Scattering by a Rough Surface 97
4.4 Statistical Formulation of the Propagation Channel 98
4.6 Antenna Modelling 100
4.5 Interim Conclusion 103
4.6 References 104

CHAPTER FIVE 105
EXPERIMENTAL SITES & MEASUREMENTS OVERVIEW 105
5.I Introduction 105
5.2 Experimental Environments 106
5.2.1 GIS Data 106
5.2.2 Trefforest Industrial Estate (IE) 107
5.2.3 University of Glamorgan Campus (UC) 116
5.3 Measurement System Overview 119
5.3.I Transmitter 120
5.3.2 Receiver 121
5.3.3 Power Link Budget 122
5.3.4 Antennas 123
5.5 Software 129
5.6 Interim Conclusion 130
5.7 References 131

CHAPTER SIX 132
MEASUREMENTS & MODEL OUTCOMES: RESULTS AND ANALYSIS 132
6.1 Introduction 132
6.2 Industrial Estate Links 133
6.2.1 PDF of the Received Signal 134
6.2.1.1 Vertical Polarization 136
6.2.1.2 Horizontal Polarization 141

6.2.1.3 Cross Polarization 145
6.2.1.4 Discussion 150
6.2.3 Signal and *K*-Factor Levels 153
6.2.3.1 Discussion 155
6.3 University of Glamorgan Campus 156
6.3.1 Received Average Power of the Azimuth Plane 156
6.3.1.1 Discussion 158
6.3.2 Building Surface Scatter Maps 159
6.3.2.1 Discussion 161
6.3.3 Average Power and *K*-Factor for Different Antenna Gains 161
6.3.3.1 Discussion 162
6.4 Cellular Interference Measurements 163
6.4.1 K-Factor vs. Antenna Gains 164
6.4.I.1. SOP Scenario I 164
6.4.1.2. AP Scenario I 166
6.4.2 Signal-to-Interference Ratio 167
6.4.3 Discussion 169

CHAPTER SEVEN 174

SUMMARY, CONCLUSIONS & FUTURE WORK 174

7.1 Summary 174
7.2 Review of the Thesis 174
7.3 Conclusions 181
7.3.1 Contributions to Modelling 181
7.3.2 Contributions to Millimetre-wave Measurements 183
7.3.3 Contributions to the Technical Literature 184
7.4 Recommendations for Future Work 185

APPENDIX 188

Appendix A: Model Flowchart 188
Appendix B: Outage Probabilities 189
Appendix C: Surface Reflectivity Constants 191
Appendix D: Results of Ofcom's Fourth Spectrum Auction 192

Appendix E: Samples of Publications.....193

LIST OF FIGURES

Figure 2.1 Radio Spectrum 35
Figure 2.3 LMDS Single cell structure 36
Figure 2.4 Block diagram of free space path loss 42
Figure 2.5 Example of a sectored LMDS cell 50
Figure 2.6 LMDS frequency-reuse schemes for: (a) a 16 cluster SOP; (b) a 36 cluster AP. 52
Figure 3.1 Rayleigh Criterion 65
Figure 3.2 Illustration of Snell's reflection concept and scatter from a rough surface 66
Figure 3.3 Kirchhoff Tangent-Plane geometry 68
Figure 3.4 Examples of a Rician distribution fitted on a measured PDF using Eq. (3.12) 77
Figure 3.5 Plot of Eq. (3.16) in a linear (left hand side) and logarithmic (right hand side) scale 78
Figure 4.1 Generic urban propagation geometry. 86
Figure 4.2 Geometry of a rectangular scattering surface. 87
Figure 4.3 Ground reflection geometry 89
Figure 4.4 Reflection geometry. 94
Figure 4.5 Pyramidal horn with the coordinate system in the *E*- and *H*-plane view. 101
Figure 5.1 Top aerial view of the IE link showing location of the transmitters and receivers. 109
Figure 5.2 3D view obtained from the GIS data for the IE measurement site 109
Figure 5.3 Photos of the Industrial link between Tx and Rx0: (a) Tx1's position facing towards inside of the photo, (b) Position of Rx0 and its route from Tx1. 110
Figure 5.4 IE link path profiles for: (a) the path route along Tx1-Rx0 (A), (b) Tx2-Rx0 link, (c) Tx3-Rx0 link 111
Figure 5.5 Examples of time series data showing the fast- and slow-fading aspects of the received power: (a) for fixed position of the receiver (b) for a receiver displaced within a couple of wavelengths along the link. 113
Figure 5.6 Index of the surfaces (including rooftops, facets, and ground patches) considered in the IE site. These indexes correspond to Table 5.1. 115
Figure 5.7 Campus site top view and measured link, with main building reflection contributions. 117
Figure 5.8 3D views of UC measurement site, showing the transmitter position facing building A and its reflected paths to the receiver. 118
Figure 5.9 Photos of the UC link showing: (a) transmitter's position and building A, (b) receiver's position and buildings B & C, (c) a zoomed in view of photo (b), (d) conical features of building C. 118
Figure 5.10 Block diagram of the 40 GHz measurement system. 120
Figure 5.11 Photo of the 40 GHz transmitter 121
Figure 5.12 Photo of the 40 GHz receiver 122
Figure 5.13 Photos of the antennas used, pyramidal-horn: (a) 10 dBi, (b) 15 dBi, (c) 20 dBi,; and lens-horn: (d) 29 dBi (e) 44 dBi. 124
Figure 5.14 A schematic diagram showing the antenna radiation pattern measurement setup. 125

Figure 5.15 Measured antenna radiation patterns of the *E*-plane. 126
Figure 5.16 Measured antenna radiation patterns of the *H*-plane. 127
Figure 5.17 Photos of the transmitter (left and top-right) and receiver (bottom-right) outdoor measurement setups 128
Figure 5.18 Snapshot of the graphical user interface developed to automate measurements. 129
Figure 6.1 PDF of the received field and comparisons with the theoretical Rician and the distribution obtained from simulations for the Tx1-Rx2 188 m vertically polarized link using antenna gains (a) 10 and (b) 20 dBi. 136
Figure 6.2 PDF of the received field and comparisons with the theoretical Rician and the distribution obtained from simulations for the Tx1-Rx1 346 m vertically polarized link using antenna gains (a) 10 and (b) 20 dBi. 137
Figure 6.3 PDF of the received field and comparisons with the theoretical Rician and the distribution obtained from simulations for the Tx1-Rx0 627 m vertically polarized link using antenna gains (a) 10, (b) 20, (c) 29 and (d) 44 dBi 139
Figure 6.4 PDF of the received field and comparisons with the theoretical Rician and the distribution obtained from simulations for the Tx2-Rx0 127 m vertically polarized link using antenna gains (a) 10 and (b) 20 dBi. 140
Figure 6.5 PDF of the received field and comparisons with the theoretical Rician and the distribution obtained from simulations for the Tx1-Rx2 188 m horizontally polarized link using antenna gains (a) 10 and (b) 20 dBi. 141
Figure 6.6 PDF of the received field and comparisons with the theoretical Rician and the distribution obtained from simulations for the Tx1-Rx1 346 m horizontally polarized link using antenna gains (a) 10 and (b) 20 dBi. 142
Figure 6.7 PDF of the received field and comparisons with the theoretical Rician and the distribution obtained from simulations for the Tx1-Rx0 627 m horizontally polarized link using antenna gains (a) 10 and (b) 20 dBi. 143
Figure 6.8 PDF of the received field and comparisons with the theoretical Rician and the distribution obtained from simulations for the Tx2-Rx0 127 m horizontally polarized link using antenna gains (a) 10, (b) 20, (c) 29 dBi 145
Figure 6.9 PDF of the received field and comparisons with the theoretical Rician and the distribution obtained from simulations for the Tx1-Rx2 188 m cross-polarized link using antenna gains (a) 10 and (b) 20 dBi. 146
Figure 6.10 PDF of the received field and comparisons with the theoretical Rician and the distribution obtained from simulations for the Tx1-Rx1 346 m cross-polarized link using antenna gains (a) 10 and (b) 20 dBi. 147
Figure 6.11 PDF of the received field and comparisons with the theoretical Rician and the distribution obtained from simulations for the Tx1-Rx0 627 m cross-polarized link using antenna gains (a) 10 and (b) 20 dBi. 148
Figure 6.12 PDF of the received field and comparisons with the theoretical Rician and the distribution obtained from simulations for the Tx2-Rx0 127 m cross-polarized link using antenna gains (a) 10, (b) 20 and (c) 29 dBi. 150
Figure 6.13 Attenuation of the received signal power with distance (logarithmic scale) for the Tx1-Rx0 route. 154
Figure 6.14 Rician *K*-factor variability with distance (logarithmic scale) for the Tx1-Rx0 route 154
Figure 6.16 Polar plot of the received radiation pattern overlaid on the receiver position 158
Figure 6.17 Pseudo-colour scatter map of the façade surface of building A. 160
Figure 6.18 Pseudo-colour scatter map of the façade surface of building C. 160

Figure 6.19 Comparison of the average received signal power and the Rician *K*-factor for different antenna gains at a fixed azimuth angle of 162° (Fig. 5.10). 162
Figure 6.20 Rician *K*-factor values obtained for a number of antenna gains for the case of SOP (I) $F2UV_1$ & $F2UV_2$ interference scenario. 165
Figure 6.21 Rician *K*-factor values obtained for a number of antenna gains for the case of AP (I) $F1UH_4$ & $F1UV_4$ interference scenario. 166
Figure 6.22 Normalised PDF of the co-channel SIR interference for a 20 dBi transmit and (a) 10, (b) 20, (c) 29, (d) 44 dBi receive antenna gains. 170
Figure 6.23 Normalised PDF of the adjacent-channel SIR interference for a 20 dBi transmit and (a) 10, (b) 20, (c) 29, (d) 44 dBi receive antenna gains. 171
Figure AB.1 Measured outage probability for different threshold values. 190

LIST OF TABLES

Table 2.1 Comparsion between wired, mobile and FWA (LMDS) networks.....33
Table 5.1 Surface descriptions and their parameters as obtained from processing the GIS data. 115
Table 5.2 UC building information 119
Table 5.3 40 GHz system power budget calculation.....123
Table 5.4 Dimensions of the horn antennas used with reference to Fig. 4.5. 124
Table 5.5 Antennas minimum far-field distance 125
Table 6.1 Statistics of the measured and simulated PDF data for the Tx1-Rx2 188 m vertical polarized link. 137
Table 6.2 Statistics of the measured and simulated PDF data for the Tx1-Rx1 346 m vertical polarized link. 138
Table 6.3 Statistics of the measured and simulated PDF data for the Tx1-Rx0 346 m vertical polarized link. 139
Table 6.4 Statistics of the measured and simulated PDF data for the Tx2-Rx0 127 m vertical polarized link. 140
Table 6.5 Statistics of the measured and simulated PDF data for the Tx1-Rx2 188 m horizontal polarized link. 142
Table 6.6 Statistics of the measured and simulated PDF data for the Tx1-Rx1 346 m horizontal polarized link. 143
Table 6.7 Statistics of the measured and simulated PDF data for the Tx1-Rx0 627 m horizontal polarized link. 144
Table 6.8 Statistics of the measured and simulated PDF data for the Tx2-Rx0 127 m horizontal polarized link. 144
Table 6.9 Statistics of the measured and simulated PDF data for the Tx1-Rx2 188 m cross-polarized link. 147
Table 6.10 Statistics of the measured and simulated PDF data for the Tx1-Rx2 346 m cross-polarized link. 148
Table 6.11 Statistics of the measured and simulated PDF data for the Tx1-Rx0 627 m cross-polarized link. 149
Table 6.12 Statistics of the measured and simulated PDF data for the Tx2-Rx0 127 m cross-polarized link. 149
Table 6.13 Full list of measured and predicted statistical parameters for the co- and adjacent-channel interference scenarios 168

CHAPTER ONE

INTRODUCTION

1.0 Overview

Over recent decades, increasing demands to provide wireless high-speed data connections for business and personal use, have been placed on the telecommunication industry. Wireless communication links have expanded rapidly over the conventional Public Service Telephone Networks (PSTN) that use fibre-optics and coaxial cables. Recently, countries and their governments have realised the importance of the wireless telecommunications both on the infrastructure and economic growth. It is not surprising to see a small town or village without water or sewer system, yet it has some form of a wireless telecommunication service. The rapid progress in wireless communication technologies and the increasing demands for bandwidth-hungry services have combined to enable societies to access data and information regardless of time and location. Recent technologies have led to the development of local and cellular wireless access networks capable of delivering broadband services with relatively high capacities. Historically, the evolution of wireless systems is based on the concept of cellular systems first invented by Bell Labs. The first generation of wireless cellular systems deployed in early 1980s was one of the most important developments of that decade [1]. The continuous growth in traffic and the emergence of new services have demanded a corresponding change in the structure of the cellular networks and air-interference techniques. These continuing demands to provide more accessible capacity requirements and economic communication services have necessitated the development and ultimately, deployment of second and third generations of cellular systems in 1992 and 2004 respectively [2]. Currently, broadband cellular networks are sought to support video and high-data communications for businesses and residential users.

While the frequency bands presently used by existing wireless technologies such as, UMTS, WiFi and WiMAX are becoming increasingly congested, there are large

portions of the radio spectrum available at the millimetre wavelength frequencies such as the 28 and 42 GHz bands. Current progress in hardware innovations combined with the ever increasing demands for more wideband communication channels offering high data rates, are compelling wireless operators to actively consider new technologies exploiting these high frequency bands. In general, the spectrum segments available at the millimetre bands range from 30 – 300 GHz, offer many advantages in broadband communication applications compared to those that operate in the lower frequency bands of the radio spectrum. Such benefits include small antenna size, reduction in transmission of source powers compensated by the much higher gain antennas, and the large number of channels potentially accommodated in the wide bandwidths assigned for future broadband wireless communication systems. These bandwidths are typically in the range of 2 – 3 GHz. Administrative practices and standardisation by official bodies are already in their final processing stages. Manufacturers have already started to produce prototype system products and consumer applications at millimetre wavelength frequencies. Nevertheless, the increasing demand for having commercial systems with higher capacity delivered at adequate signal levels with low system design and implementation costs represent the real challenges in deploying such networks.

1.1 Fixed Wireless Access Systems

The concept and design of Fixed Wireless Access Systems (FWA) are aimed at distributing information (data, voice and video) using wireless communications links between fixed terminals at relatively distant geographical areas. Networks formed from such wireless links are the obvious competitors to wired PSTN systems. Topologies of FWA networks can be either in Point-to-Point (PTP) or in Point-to-Multipoint (PMP) form. Due to their capabilities of delivering high data rates, they are referred to as Broadband-FWA (BFWA), interchangeably known also as Local Multipoint Distribution Systems (LMDS). The latter generic term will be used through the thesis. In Europe, LMDS operation frequencies are set to be in the range from 40.5 to 42.5 GHz, while in Canada and North America the range is from 27.5 to 31.225 GHz.

During the last decade, LMDS communication systems have acquired considerable importance in the communication field due to the many practicality factors such as, rapid channel assignment, capacity expansion, short installation time, and adaptation to difficult terrain and natural topographies [2] [3]. More detailed discussion of these factors is given in Chapter 2.

1.2 Radiowave Propagation

The success of a wireless communication system depends on a better understanding of the unguided nature of radiowaves in propagation channels. The behaviour of electromagnetic waves in wireless channels is an area of continuous research ever since the utilization of radiowaves in telecommunication systems was discovered.

In the mobile radio networks (such as GSM, UMTS 3G) which operate in the range 0.8 – 2.2 GHz, part of the electromagnetic radio signal radiated by a transmitter antenna reaches the receiving terminals via different propagation paths. Interactions between radio waves and various objects within the radio link occur, resulting in useful different propagation modes such as reflection, scatter and diffraction.

At the millimetre wavelengths radiowave propagation characterization differs slightly from that encountered in mobile radio networks and has recently acquired increasing importance due to the need for more broadband communication channels. Radio link design and deployment at these frequencies require a deeper understanding of the underlying propagation channel which benefit from a quantitative description of the fundamental mechanisms that affect the integrity of the link.

When an electromagnetic wave is incident on a surface, it is reflected according to well-known laws of reflection that depend on the angle of incidence, electromagnetic properties of the media, and the wavelength [4]. These laws are only applicable for plane boundaries. As the frequency of operation is increased, the wavelengths become more comparable to surface irregularities and hence, the surface boundaries are no longer plane. This effect occurs significantly in the millimetre-wave frequencies in question. Irregular surfaces consist of periodic or random variations of surface heights that can be measured from a certain mean plane. Such surfaces are usually referred to

as "rough". In this view, the same surface can be rough for some wavelengths and smooth for others depending on the frequency of the impinging wave. The main difference between a smooth and a rough surface is that the former will reflect the incident wave mostly in a specular direction, whereas the latter will scatter it incoherently into various directions [5] [6].

The received field of radio communication systems that operate on very short waves, such as LMDS systems, is likely to consist of the line-of-sight (LOS) direct ray, and a number of rays scattered from surfaces illuminated by the transmitter. In other words, the main propagation mode is primarily that due to the LOS radio link. This is related with the fact that a millimetre-wave impinging on relatively rough surfaces has two main defects. The first is connected with wave diffraction emanating from edges and building surfaces. This phenomenon only occurs when the propagating waves encounter obstacles with dimensions comparable to the impinging wavelength. Since the wavelengths in question are in millimetre scale, the effects of diffraction are minimal and their contributions to the received signal are considered negligible [5]-[7]. The second defect is due to the surface roughness being comparable with the signals' wavelength. In this case reflected or scattered rays from building and ground surfaces are not specularly reflected, but diffused incoherently with random phases. Although specular reflections can occur from superior smooth surfaces, they are most-likely to be affected by scatter arising from other surfaces existing in the radio path [5] [6]. Reflected and scattered waves are therefore expected to encounter high attenuation losses.

1.3 Modelling

Radio propagation models play an important role in providing radio engineers with predictions about the system performance which is dependent on the propagation environment in which it is deployed. As with any other communication system, the design, implementation and effective deployment of LMDS networks rely on the availability of radiowave propagation and simulation models. Moreover, the development of analytical and numerical modelling tools can enable the rationalization and optimization of system design within its main constraints. These may include, cost of deployment; cell size; frequency and polarization planning;

antenna parameters such as their positioning and radiation characteristics; link performance including coverage and outage probability levels expected at the receiving terminal. Reliable and realistic models essentially must take into consideration the interaction between radiowaves and the surrounding physical environment, including the natural man-made physical obstacles that might be present in the radio path. Such models are essential tools and are highly desired in the literature for research and commercial purposes [4].

In LMDS networks, although the wireless link is fixed, the propagation channel is generally time-varying. This is because of vegetation, motion of objects within the radio paths and the variability of the electromagnetic properties of the environment due to varying weather conditions. A full geometric description of the wireless links at these relatively high frequencies, which has to be accurate within a sub-millimetre resolution scale, is difficult to obtain and therefore highly impractical. Due to random errors in the geometrical presentation, the randomness nature of the scattered fields and the time-varying nature of the channel, analysis of the propagation mechanisms merit a statistical approach. In particular, building and ground surfaces which tend to be rough at millimetre wavelengths are usually not known in exact detail. Even if the exact structure of these surfaces were known at every point, any other approach apart from a statistical one, would be so specific that it can not be considered a general solution. Moreover, since these surfaces are neither periodic nor explicitly given and in practice, they can only be described by their statistical properties. Predictions of mean values combined with probability distributions about them, can be considered general solutions. The benefits of such statistical approaches in terms of modelling cannot be overstressed, especially when dealing with complex and large simulation algorithms, provided they are capable of attaining predictions comparable with deterministic models, such as ray-tracing. Despite the accuracy of any deterministic models, they are generally not favoured over statistical ones due to their implementation complexity and the requirement of detailed knowledge of topographical information. The application of statistical methods to a problem is not necessarily dictated by the inability to provide exact solutions. In fact if random processes are described by their mean values and distribution functions, deterministic or exact solutions are in effect special cases of statistical solutions.

1.4 Areas of Research and Aim of Investigation

Future broadband radio access systems are intended to provide variety of high-speed services such as voice, video and data communications. LMDS propose to provide such services via cost efficient high quality connections, especially in urban and suburban areas for commercial and private users.

Recent research shows that in a cluttered environment, multipaths caused by roughness of building facades and rooftops surfaces are a major source of incoherent scatter at the frequencies in question. Treatment of such rough surface scatter can be based on the Kirchhoff [5] approximation of the scatter field, also known as the Tangent Plane method. The total scatter field in a certain direction is approximated by the sum of elementary waves that emanate from each elementary rough surface. The latter can be characterized by a two-dimensional statistical distribution of its height above a certain mean level or by the statistical distribution of the surface slopes.

The literature considerably lacks of theoretical models and experimental data dealing with the radio propagation impairments and network operation constraints affecting millimetre-wave links, including the effects of interferences from co- and adjacent-cells in a fully deployed network. The presented work aims at proposing a generalized statistical model for the urban/suburban propagation channel via modelling the physical electromagnetic (EM) representation of building and ground scatter, with particular emphasis on fading margins in LOS links.

The propagation topography and, in particular, the perimeter of rooftops and facades, as well as the ground patches illuminated by both the receiving and transmitting station antenna beams, can be modelled using widely available, albeit coarse, digital Geographic Information System (GIS) data and digital images. In comparison to deterministic models, the proposed model yields rather an efficient and accurate approach. Validation of the proposed model and its predictions is implemented against experimental results conducted in realistic propagation scenarios.

Furthermore, in the foreseen LMDS cellular deployments, the LOS radio constraints affecting the link between the transmitter and receiver terminals give rise to harmful

interferences to and from neighbouring and distant cells. Interference, which tends to aggravate in smaller cells, can be amongst adjacent- and co-channel cells, or between users and Base-Transceiver-Stations (BTS). Therefore consideration of cellular interference strictly needs to be taken into account. In general, deeper millimetre-wave channel knowledge and characterisation of the propagation and interference effects that influence the performance of LMDS networks can only be acquired by field and experimental measurements.

The main aims of this research are anticipated to contribute to the development of knowledge in the current and future millimetre-wavelength broadband communication systems. A summary of the aims is given below:

- Research in LMDS networks and technology, including past and present planning models and their relative performance.
- Insight on the propagation phenomena at 40 GHz, which is the frequency band earmarked for UK LMDS networks, via a campaign of field measurement conducted in outdoor urban and suburban environments.
- Establishment of the effects of building and other structures on millimetre wavelength radio links including factors affecting signal strength on both wanted and interference sources.
- Development of an analytical stochastic electromagnetic propagation model based on realistic antenna characteristics and GIS data at millimetre wavelengths, applicable for predictions of LMDS signal power and cellular interference statistics.
- Investigating, modelling and experimental measurements of the interference mechanisms associated with frequency-reuse strategies for cellular LMDS networks [8].
- Modelling, examining and evaluation of non-LOS (NLOS) paths in a microcell environment via field measurements and simulations.
- Validation of the stochastic EM model proposed with the conducted measurements.

1.5 Thesis Structure

The thesis deals with four major topics, namely, EM modelling of millimetre wavelength propagation including scattering and ground reflections; field propagation measurements of PTP radio paths at 40 GHz in urban and suburban cells; measurements and assessment of the frequency-reuse strategies for cellular LMDS networks; and finally validation of the proposed model predictions with the results obtained from the experimental measurement data. In this view, the thesis is organized in as follows:

Following this introduction, *Chapter 2* lists the key aspects of LMDS networks and outlines the motivation of research into this new technology. The architecture structure, benefits, and current market position of LMDS networks are reported. Furthermore, since LMDS is established to operate in a cellular architecture, this chapter extends to explore the associated frequency-reuse strategies and reports on the potential interference scenarios addressed as part of this research. This chapter also summarises the relevant literature review conducted on LMDS networks, millimetre-wave radio propagation and cellular radio interference.

The first section of *Chapter 3* describes the scattering phenomena and its effects at millimetre-wavelength propagation. Classification of channel and propagation modelling are given in the second section of this chapter. The third section presents methods of useful parameter extractions for measured and simulated data.

Chapter 4 presents derivations of the proposed stochastic EM model aimed at predicting the radiowave propagation characteristics for millimetre-wavelength channels operating in urban and suburban cells, in which building surfaces and rooftops give rise to multipath effects due to reflection and scattering of EM waves.

The first section of *Chapter 5* covers site surveys of the experimental sites selected in terms of their link geometries, distinctive surfaces and path profiles. The second section presents the 40 GHz measurement hardware system and the associated software methods used to record data and to control both the equipments and instruments used.

Chapter 6 presents in details the outcomes of the field measured data along with comparisons with those obtained from the proposed EM model predictions. The outcomes are presented in terms of the Rician K-factor and its associated parameters,

and the probability distribution functions of the received normalized power and signal-to-interference-ratios.

Chapter 7 reviews the outcomes and assess the objectives of this thesis and the extent to which they have been fulfilled. Discussions and conclusions based on results from both measurements and the proposed EM model predictions are presented. Finally, some of the potential avenues for future work are proposed.

1.6 References

[1] MacDonald, V. H, "The Cellular Concept", *The Bell Systems Technical Journal*, vol. 58, no. 1, pp33-37, July 1978.

[2] Smith C., *LMDS*, McGraw Hill Book Co, 2000, ISBN 0-07-136254-1.

[3] Vacca J. R., *Wireless Broadband Networks Handbook, 3G, LMDS & Wireless Internet*, McGraw Hill Book Co, 2001, ISBN 0-07-213031-8.

[4] Cost 231, Digital Mobile Radio Towards Future Generation Systems, COST 231 Final Report, 1999.

[5] Beckmann P. and Spizzichino A., *The Scattering of Electromagnetic Waves from Rough Surfaces*, Artech House, ISBN 0-89006-238-2, 1987.

[6] Stratton J.A., *Electromagnetic Theory*, McGraw Hill Book Co., 1941, ISBN 0070621500.

[7] Thomas H. J., R. S. Cole, and G. L. Siqueira, "An Experimental Study of the Propagation of 55 GHz Millimeter Waves in an Urban Mobile Radio Environment", *IEEE Transactions On Vehicular Technology*, Vol. 43, No. I, February 1994

[8] ACTS Project 215, *Cellular Radio Access for Broadband Services (CRABS), Specification of Next Generation of LMDS Architecture,* D2P1B, 1999.

CHAPTER TWO

LMDS NETWORKS

2.1 Overview

Historically, the invention of the telegraph over wireless channels was first introduced by Samuel Morse in 1884. The development from wired to wireless data communication is owed to Marconi who used Morse's Code for radio communications in1901. Thirty years later, the first television transmission took place in the UK, France and Germany. This was followed by the start of mobile phone services and microwave PTP networks in 1946 and 1953 respectively. In recent times, one of the most vital developments was the revolution of communication systems represented by the introduction and utilization of the cellular concept introduced in 1983.

Wireless communications and computer technology have experienced rapid growths during the last decade. The telecommunication industry is witnessing a surge in delivering broadband services, evident by daily proclamations referencing the internet and IP based telecommunication systems. Wired connections, such as the ISDN, ADSL and VDSL technologies, are only capable of delivering data rates up to 25 megabits per second (in certain conditions). Video interactive services envisaged in broadband networks require simultaneously multi-user, high capacity return channels that are not offered in any known wired technology. A comparison of wired and wireless mobile/fixed networks is presented in Table 2.1. The possibility of fully upgrading the current deployed PSTN to two-way fibre-optical connections in order to achieve higher bandwidth connections and broadband requirements was found to be difficult to accomplish or prohibitively expensive [1], especially in remote areas and in new developed infrastructures. As a result, no further research has been proposed for wired connections in any technical literature. Broadband wireless networks are not only perceived to be a viable alternative, they also represent an improved solution in

terms of the following: suitability for multiple access and backbone infrastructures; rapid network deployments; low installation costs; simple network upgrading procedures; high data rate speeds; and variable bandwidth on demand [1].

	Wired Lines	**Wireless Mobiles**	**FWA Wireless**
Propagation Component	-	Diffuse components	LOS or a NLOS dominant component
Fading	Attenuation	Rayleigh	Rician
Transmission & Antennas	Expensive wires	Omni-directional antennas	Narrow beamwidth antennas
Channel Re-usage & Range	Limited by wires	Large re-use distances	Smaller re-use distances & more channels
Mobility	Fixed	High	Fixed
Design	Simple but expensive to build and maintain	Complex - require power control	Simple
Deployment	Lengthy and time-consuming – full installation is required to the infrastructure	Rapid but more complex – requires handoffs and extensive management	Rapid – connection on demand
Bandwidth	Limited	Very limited	Substantial but limited
Scalability	Limited and expensive	Limited	Better scalability
Data Rate	Up to 30Mbps	Up to 2 Mbps (3G)	Up to 1.8Gbps
Access Scheme	Varies	W-CDMA	TDMA/FDMA
Modulation Scheme Supported	Varies	QPSK or higher	QPSK or higher
Main Channel Impairments	Noise	Noise	Interference, scatter & attenuation

Table 2.1 Comparsion between wired, mobile and FWA (LMDS) networks

The need for high rates of data transmission and the increased race in delivering broadband services have culminated in the convergence of a number of technologies and platforms that are targeted to facilitate wireless broadband applications. LMDS is considered to be the ultimate wireless broadband solution and the key enabler for accommodating the broadband revolution, driven by the allocation of wide bandwidth segments in the radio spectrum.

2.2 Local Multipoint Distribution Systems

The term "Local" indicates the limits on the signal range, "Multipoint" indicates a broadcast signal from the subscribers, and the term "Distribution" defines the wide range of data that can be transmitted. As with the other wireless technologies, the implementation time scale is significantly reduced in LMDS networks. Expansions are possible without the need to dig roads in order to install underground ducts and cables. LMDS is a promising technology that not only aims in providing users with services that are equal or more reliable than PSTN, but also in offering more functions and features at relatively low cost.

LMDS is a two-way communication system that provides a wide range of high-quality broadband services to homes and business premises at potently low cost. These services may include:

- High-speed Internet access, email, hosting and virtual ISP.
- Real-time multi-media file transfer.
- Voice Telephony and VoIP
- Interactive video, video-on-demand, video conferencing.
- E-commerce
- ISDN
- ATM support
- GSM backhaul

LMDS structures employ PTP and PMP topologies at the uplink and the downlink [2]-[5], respectively, and utilize narrow beam directional antennas at the subscriber's premises, forming a classical cellular network structure. LMDS, as mentioned in Chapter 1, operate at the high-frequency range of the radio spectrum known as the millimetre wave band. Typically, the frequency of operation ranges between 26 - 42 GHz depending on the country of deployment. Figure 2.1 shows how the radio spectrum is managed and the names some of the applications utilized at different segments of the spectrum. The choice for using the abovementioned LMDS band is governed by the spectrum available to support the increased demands for broadband

applications. In the UK, LMDS networks are licensed to operate between 40.5 - 42.5 GHz, with possibilities of extensions to 43.5 GHz.

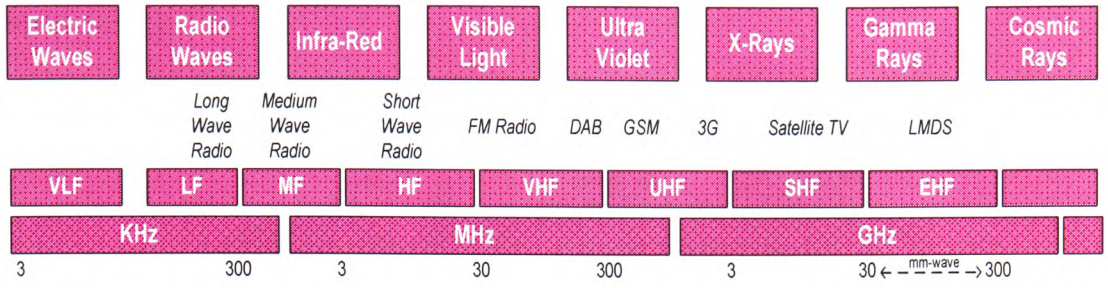

Figure 2.1 Radio Spectrum

Due to the propagation constraints of millimetre-wave signals, service areas in LMDS networks are normally designed for short operational distances, with a maximum cell radius of the order of a few kilometres only [2]-[5]. In fact, millimetric radiowave propagation is mainly restricted to LOS links or in some cases, to dominant signals that might exist in NLOS paths. Such paths can be established from reflections of smooth building surfaces or special reflectors. In general, an urban or suburban environment, millimetre-wave propagation is particularly affected by diffuse scatter emanating from buildings surfaces and facades. Due to the size of the wavelength, contributions of diffuse scatter and diffraction paths at the receiver side are of minimal significance since they are accompanied by high propagation losses.

LMDS network architecture consists primarily of antennas and transceivers on both, the subscriber receiving equipment and the central hub BTS. The latter is connected to the PSTN through either fibre-optics or wireless PTP connections. In a typical LMDS network, the BTS is likely to be placed on building rooftops as shown in Fig 2.2. The receiving antennas at the subscriber premises are very small in size, proportional to the size of the wavelength. For example, in a 10 dBi and 44 dBi antennas, the largest dimensions lie approximately within a range of 2 - 30 cm, respectively. Transmission generally consists of a digital modulated carrier baseband signal in the millimetre-wave band range. Reception can be easily established by a low-noise down converter and a decoder. The integrated transmitting and receiving radio-frequency (RF) circuitry and components are placed as close as possible to the antennas in order to avoid significant line attenuation losses. For receivers to achieve a LOS path, they are

typically fixed at lamp-post heights and placed on roof-tops or buildings side walls [6] depending on the topographical conditions. In places where it is difficult to achieve an unobstructed LOS path, repeaters maybe be installed to cover the shadowed areas as shown in Fig. 2.2.

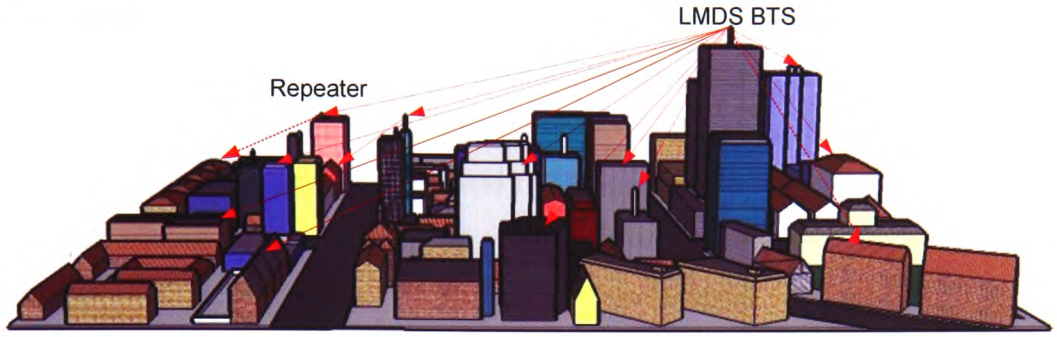

Figure 2.2 Example of an urban LMDS profile

Figure 2.3 shows a simplified plan of a LMDS structure for a single cell. The 360° area surrounding BTS contains multiple subscribers and is typically configured using four sectors, each deploying a specific set of radio frequencies and polarisations in order to reduce the likelihood of interferences between adjacent- and co-channel cells. Cells are limited in size, and it terms of capacity, they can serve hundreds or thousands of subscribers simultaneously.

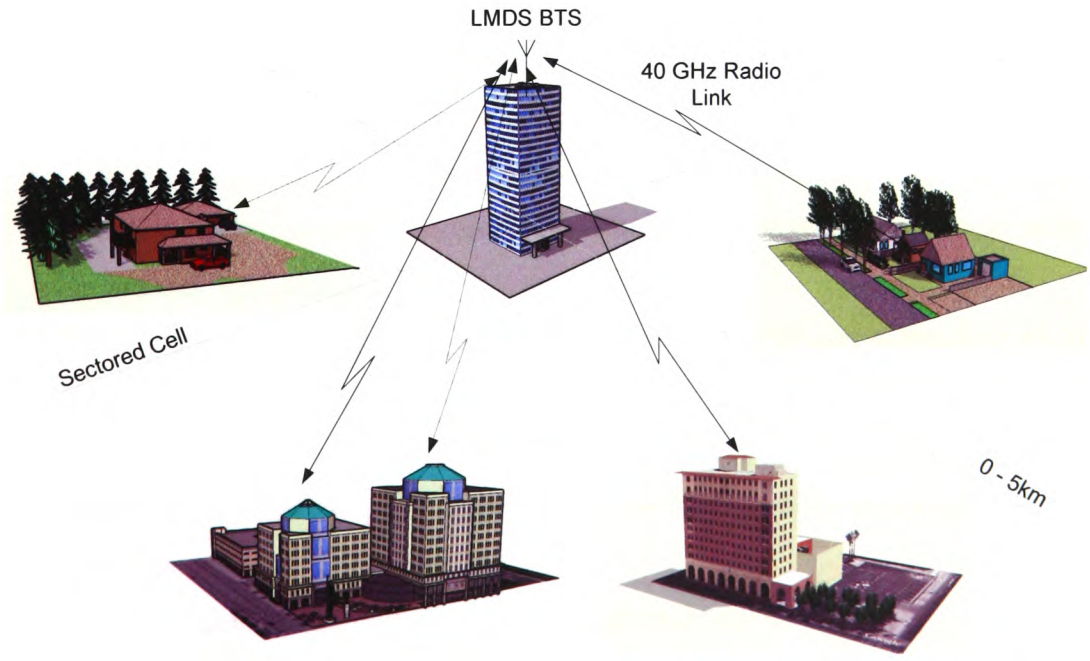

Figure 2.3 LMDS Single cell structure

In terms of system architecture, LMDS is very much similar to that employed in a cellular mobile system apart from the fact that subscribers receiving stations are fixed, and the comprehensive requirement of a LOS path to most of the subscribers. In terms of operations, LMDS differs in the fact that ubiquitous coverage is not always required since LMDS can provide services on demand and only to places where subscribers are located. Additionally, in cases where subscribers exist in the same block or building, for example in a household or even in a large business enterprise, a single radio equipment can be efficiently utilized for all customers. This aids in reducing operating expenses and maximising the benefits of the infrastructure investment.

2.3 Benefits

LMDS has proven to be a cost-effective last-mile solution for broadband services better than any other current technology may offer [7]. Some of its main advantages have already been mentioned in Table 2.1. More details of these benefits are listed below:

- Availability of a wide radio spectrum which is in the range of 2 - 3 GHz.
- Large system capacity, for example it is expected that a single LMDS cell can support up to 3800 telephone lines.
- Large uplink and downlink bandwidths making LMDS the most suitable candidate for video interactive services.
- Multi gigabit capacity networks with 28 MHz channels sufficient for serving business and residential wireless communications networks in urban, semi-urban and rural areas.
- Capability of delivering broadband services swiftly to any subscriber within the coverage area.
- Delivery of broadband services in areas not covered by wired connections.
- The accommodation of a wide variety of high quality telecommunication services.
- Scalable architecture and on-demand bandwidth and capacity.
- Fast and simple installation procedures with minimal disruption to local communities and environments.

- Low entry and setup costs including network maintenance, management and operational costs.
- The ability to integrate with other wireless technologies, including satellite systems, and cabled connections.
- New technologies and mass productions of components and systems are now being available for LMDS systems with competitive prices.
- Short range cells with higher frequency-reuse utilization.
- Small size subscriber antennas that can be easily mounted on or below the rooftop levels.
- Due to the small wavelengths, any arrangements for spatial diversity techniques will only require very small separation distances to implement.
- A new market that contributes to economic growth.

2.4 The Current Market

Operators and governments are forever seeking the development of better communication systems. The twenty-first century demands the establishment of broadband networks due to the tremendous increasing trends in data and internet traffic. The current large capacity networks are based on fibre-optics; however surveys and statistics show that less than five percent of commercial structures worldwide are being served by fibre-optics, this mainly due to the high establishment costs involved [8].

The widely recognized advantages of LMDS are now pushing the telecommunication industry to take a step forward in broadband innovations. LMDS networks are suitable for many segments of the current market, ranging from large and small businesses to residential individual users. The technology is readily available and costs are being further reduced as suggested by many manufactures. Trials have been taking places and commercial systems and services are increasingly becoming available. Below are some key examples from countries worldwide [9].

Belgium

MAC Telecom has established an LMDS system, which operates in the 28 GHz band using ETSI standard Alcatel equipment. The backhaul is also provided by PTP radio

links with transmissions in the 18, 26 or 38 GHz bands. This system has five base stations, which cover about one million people in Brussels and the surrounding areas. The traffic levels generated currently are accommodated in the 56 MHz license allocation with QPSK modulation.

Czech Republic

LMDS systems at 26 GHz, using Alcatel equipment, were installed in Prague in 2000. The Prague system comprises about 14 BTS and has proved to be very successful. In fact LMDS did provide back-up services for Prague when most of the other telecommunication systems collapsed during the extensive flooding in the summer of 2002. Bratislava, in Slovakia, has 5 BTS using 56 MHz band licenses. It is believed that a second phase of 26 GHz equipment installation in Prague is now being considered by Telenor to cope with increasing demands. At current growth rates in Czech Republic, saturation capacity of 26 GHz services is expected in the next few years.

Denmark

Butler Networks32 is a major provider of wireless broadband connections in Denmark at 26 GHz and has been operational since 2001. By the end of 2003 an extensive network of about 25 BTS in metropolitan areas (about 10 in Copenhagen) had been deployed, providing over 600 connections and more than 450 terminals. The system operates in TDD mode and uses an advanced adaptive modulation and coding scheme, which can function with QPSK, 16QAM and 64QAM modulation schemes, depending on link characteristics. A range of approximately 2, 4 and 8 km has been achieved with 64QAM, 16QAM and QPSK modulations, respectively. Coverage which has been in excess of 80%, seems to be much higher than what normally experienced by LMDS operators.

Portugal

Portugal is one of the leading countries in employing LMDS networks and systems. LMDS is the only technology to threaten the dominance of Portugal Telecom, and has potentially emerged as a broadband platform. The 24.5 - 26.5 GHz and the 27.5 - 29.5 GHz bands have been specified for these LMDS networks which include TV

broadcast. Portugal has also plans to license the 40.5 - 43.5 GHz frequency band in the near future.

United Kingdom

In the UK market surveys have shown that the UK penetration to broadband is slow compared to other countries, however this indicates significant growth opportunities for broadband services. The Office of Radio Communications (Ofcom) has very recently published a consultation document setting out proposals to hold an auction for the award of wireless telegraphy licences in the higher frequency bands at 10 GHz to 40 GHz. Consultation responses on spectrum packaging and auction design from the industry showed interest in acquiring spectrum in the 40 GHz band. As a result Ofcom has considered its position and has proposed to split the band into six UK-wide portions of six 2x250 MHz, each lot being sufficiently large to allow wideband data usage. Results of Ofcom's spectrum auction held in February 2008, whereby licenses have been awarded to ten organizations, are given in the Appendix D.

Your Communications are one of the leading organisations currently operating a commercial LMDS services in the UK. Their system operates in the Manchester, Lancashire, Yorkshire, Cumbria and Birmingham areas. The Birmingham system is largest, having three BTS with several more planned. Some customers are receiving shared broadband services through a combination of 28 GHz LMDS radio terminal with 2.4 GHz WiFi access point for the final connection to the customer, i.e. a two-layered network. Surveys show that between 3 and 6 customers have received a better broadband service, when compared with ADSL. More services to residential customers were also being planned near Manchester. Two more base stations are planned to be fed through a combination of a 3 km LOS link at 28 GHz from central Manchester and a 1.5 km link at 2.4 GHz. These base stations are expected to feed between 20 and 100 customers.

Another leading organization in the UK is MAC Telecom. The company is in a commercial venture with Broadnet, which holds one of the 28 GHz BFWA licenses for Greater London. The firm has started deploying similar services to Your Communications in the London area since 2004.

Japan

The market for LMDS in Japan has focused on large businesses, typically multinational companies who do not want to wait for the installation of fibre-optic, since LMDS deployment time is within days. The 25 - 27 GHz band has been assigned for LMDS networks to be used in communal spaces, such as roadsides, parks, libraries, and conference halls.

United States & Canada

Both countries are at the forefront of this technology. LMDS applicants have invested over $5 billion in Canada alone, and licenses have already been sold. Field experiments have been successfully carried out and the US government has recently introduced LMDS networks on a wide scale. Revenues are expected to be approximately $11 million per year. A detailed report on the Canadian experience can be found in [10].

2.5 Millimetre-Wave Propagation

At millimetre wavelength and corresponding high frequency bands, the wireless channel in a communication system differs with that in GSM/UMTS mobile, WiFi or WiMAX technologies which operate at lower frequencies (less than 10 GHz) mainly because of the smaller nature of the wavelength. For example at 40 GHz the wavelength is about 7.15 mm only, while at UMTS and WiFi operational frequencies, it is 16.7 cm and 12.5 cm respectively and, hence, these differences are likely to be significant in radiowave propagation terms.

Transmitted signals in radio channels at millimetre wavelengths do not easily penetrate through building surfaces and material, and therefore can only reach the receiver, mainly, through unobstructed LOS paths. Accordingly, the radio channel is often described as being either a LOS link from a direct and unobstructed path between the BTS and the receiver's antenna, or a NLOS in which the attenuated signal in this case, reaches the receiver through reflections, scattering and diffractions of electromagnetic waves from and around building surfaces and edges. However at these high frequencies (i.e. as the wavelength decreases) diffraction path contributions decrease significantly and building surfaces tend to generate many incoherent

reflections accompanied by high propagation losses. Building scatter becomes a significant issue in determining dominant and interfering signal levels. These levels, in conjunction with the radiation characteristics of the hub and subscriber antennas, can influence system planning and deployment of interference limited networks.

In the literature, free-space path loss, also known as the propagation loss, is basically the simplest model of characterising the large scale effects in microcellular propagation environment [7]-[11]. Many common models are based on the path loss formula given in Eq. (2.1) which assumes that the propagating wave is present in a vacuum with no obstacles, such as the Hata-Okumura model [12] [13]. They are also only valid for frequency range from 500 - 1500 MHz and for receiver distances that are greater than 1 km from the base stations. The path loss model is based on the Friis transmission formula which is a function of the operating frequency and on the transmitter-receiver (Tx-Rx) separation distances as shown in Eq. (2.1):

$$P_r = P_t G_t G_r \left(\frac{\lambda}{4\pi d}\right)^2 \tag{2.1}$$

where P_r is the received power, P_t is the transmitted power, G_t and G_r are the gains of the transmitting and receiving antennas respectively, λ is the wavelength of the operating frequency and d is the Tx-Rx separation distance as shown in Fig 2.4.

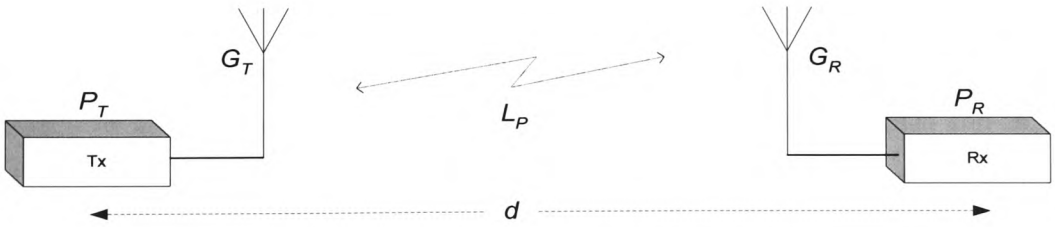

Figure 2.4 Block diagram of free space path loss

The losses expected in the propagation path are usually written in a logarithmic scale (dB) as follows:

$$L_P = \log_{10}\left(\frac{P_R}{P_T}\right) = 20\log_{10}(FSL) + 10\log_{10}(G_T) + 10\log_{10}(G_R) \tag{2.2}$$

where FSL is the free-space-loss and is given by $\lambda/4\pi d$. Because the multipaths are not considered in the above formula, the path loss model alone is not adequate for

accurate field strengths predictions. Therefore additive propagation factors need to be considered in order to more accurately characterise the millimetre-wave channel.

2.6 Impairments, Challenges and Literature Review

The use of extremely high frequencies, such as those in the millimetre-wave band immediately raises challenges in mitigating propagation issues. These propagation impairments radically differ with those arising at the lower bands. This section endeavours to identify those impairments and challenges presented by radiowave propagation at millimetre wavelength frequencies, along with the results found in the published literature on field measurements conducted at these frequencies.

From the literature, reflection and scatter signal levels from buildings obtained by measurements at 38 GHz are presented in [14]. These were found to be in the range of -10 to -24 dB compared to mean power level of the received signals. The corresponding cross polarization discrimination (XPD) measured was -13 dB. These results show the importance of building scatter considerations in the millimetre-wave band. The extensive measurements results given in this article are presented in terms of cumulative distribution functions (CDF) of signal strength, autocorrelation functions, power spectral density functions and fade statistics.

In terms of coverage and signal range, the radio channel is extremely sensitive to the presence of any obstacles in the transmission link radio path. Obstacles can in fact lead to complete blockages in coverage. Measured propagation results at 9.6, 28.8 and 57.6 GHz bands conducted at a street level are reported in [15]. Paths considered were obstructed by buildings constructed of several materials. Their results indicated that clear glass attenuated signals by 25 dB, and in glass coated by metal structures, signals attenuation increased significantly up to 50 dB. Multipaths and scatter from building surfaces, signs, cars and trucks, in general, were found to produce fades in excess of 30 dB with time delays in the order of 1 ns. Antennas with wider beamwidths caused the multipath time delay to increase to 10 ns. Improvements on system gain and coherence bandwidth increased with higher gain antennas. Furthermore, impulse responses from vertical and horizontal signal polarizations were found to exhibit similar behaviours.

Papazian *et al.* [4] reported also on radio coverage and identified fundamental impairments relative to the attenuation and its variability, as well as the delay spread, due to obstruction by buildings and vegetation for LMDS. Both narrow- and broad-band measurements in the frequency band 27.5 - 29.5 GHz were conducted at small suburban cells.

Analyses of mobile radio propagation measurements at 62 GHz in a suburban cell are presented in [16]. It has been shown that the received signal mean level drops rapidly by a significant value when the LOS component is blocked by buildings. Another similar experimental study of mobile radio wave propagation at 55 GHz is presented in [17]. Ranges up to 400 m were used and measurements of the received signal's fast fading envelope, local mean, signal versus distance power law, and coherence bandwidth were obtained in the presence of traffic.

Seidel and Arnold reported propagation experiments at 28 GHz addressing coverage limitations imposed by path loss in the presence of specular reflections as a function of antenna heights [18]. Their outcomes indicated that more than 71% of the receiver locations that fell within 1 km distance from the transmitter received sufficient signal strengths. Less than 10 % of those were reflected paths. Despite the long Tx-Rx separation distances, it has been shown that specular reflections may potentially be used to fill in coverage nulls in service areas.

According to [19], in a typical urban cell it was estimated that only 30% of dispersed receivers had experienced a LOS link provided they were actually mounted on building rooftops. Such a limitation places large constraints on the systems' reliability and therefore, it is important that system planners are able to understand the effects of such obstacles on design and system performance.

Narrow- and wideband measurements in suburban environments at 28.5 and 29.5 GHz were reported in [20]. Parameters discussed are, propagation losses, probability CDF, XPD and multipath temporal dispersion statistics. Path losses in a LOS and NLOS links were found to fade by a propagation exponent of 2 and 5 respectively. The XPD values obtained were between 20 and 30 dB.

The authors in [21] have covered propagation measurements in urban, suburban and rural environments, focusing studies on, K-factor, mean delay, delay-spread characteristics and excess loss. The latter was found to be the most serious

propagation impairment. A linear relationship was established between delay spread and environmental loss. In the same paper, a tap-delay impulse response model was also introduced.

Results reported in the literature outlined above have confirmed the necessity of providing adequately unobstructed radio paths in the coverage areas. Weather conditions on the other hand can also influence the millimetre-wave wireless channel performance. For example radio wave signals at these frequencies can be heavily attenuated by high intensity rain with drop sizes that are relatively large compared to the wavelength. Accordingly attenuation occurs due to absorption and scattering by rain drops. Rain attenuation has received a great deal of interest in the literature where a significant amount of research has been conducted in developing models to quantify the impact of rain attenuation on LMDS communications and link performance [22]-[27].

Rain attenuation is measured as a function of the rainfall rate, defined by the average millimetres of rain that falls over an hour. Rainfall rate data are available from the International Telecommunication Union (ITU) on worldwide maps and are classified into rain zone profiles [28].

Two models are primarily used in predicting the rain fade impact; namely, the Crane fade model and the ITU-R rain fade and depolarization model. Crane [29] in the early 1970's was one of the first pioneers in studying the effects of rain attenuation. Few years later Crane presented models for rain attenuation predictions for earth-to-space and terrestrial paths. Two versions of the Crane fade model were further developed between 1980 and 1989; these are the Global 2-component Crane model, and the Revised 2-component model [29]. Apart from the rain rates, the models take into account the paths lengths and the regression frequency dependent coefficients. The ITU recommendation for modelling rain in terrestrial systems [28] is very similar to the Crane's model; however the rainfall rate values and the zone maps differ slightly.

Yet these models are only applicable for paths longer than 5 km and therefore they are not directly applicable to short range LMDS systems. A number of other researchers have published measurements and models for such short links. Most important

amongst these is the work presented by Xu *et al.* [30]. Xu has investigated the broadband and dispersive channel behaviour due to multipath for LOS links at 38 GHz under different weather conditions and proposed a Rician based model, along with a rain-rate dependent *K*-factor, for the short term variability of the signal attenuation. The measurements were conducted at 38 GHz utilizing a transmitter horn antenna of 19 dBi and a receiver parabolic antenna of 39 dBi gain. The transmitter-receiver separation distance is 265 m and the path is a partly obstructed (mostly by trees) LOS link. An additional attenuation of 5.2 dB more than the Crane's model was reported. The authors have also applied a Minimum Mean Square Error (MMSE) fit to their measured data, suggesting the following relationship between the rain rate (mm/hr) and the Rician *K*-factor (dB):

$$K = 16.88 - 0.04R_r \tag{2.3}$$

where K is the Rician *K*-factor and R_r is the rainfall rate (in mm/hr).

Distortion losses of signal phases due to the effects of multipath via scattering from rain drops on ground-based links at 30 - 50 GHz are presented in [23]. Depolarization effects due to scattering from rain drops are given in [24]. The same authors have also provided mathematical expressions derived for the depolarization of microwave signals in orthogonal channels.

The dynamic effects of temporal variations on signal levels due to moving vehicles or foliage induced by wind at 29.5 GHz is presented in [25]. The effects of a moving rain cell over a LMDS system is analysed in [26]. It has been shown that these dynamic effects not only cause attenuation on the radio links, but also vary the SIR values. Moreover, more measurements on dynamic effects in the Oxford area on a 2.5 km link at 28 GHz and 42 GHz using 15 dBi horn antennas are presented in [2]. Outcomes were displayed in terms of fade durations and distributions. Results of similar measurements conducted in wet snow and sleet were presented in the same report.

Moreover, in a recent paper presented by Hendrantoro [31], a cell-site diversity scheme has been used to combat the effects of rain attenuation. The latter can vary from location to location giving rise to a variable horizontal rain structure where the

most frequently high intensity rain can be localized in a very small area. The cell-site diversity scheme can be a promising method for improving the link availability and coverage in such circumstances. Nevertheless, this method requires the subscribers' receiving antennas to be capable of rotating either electronically or physically for hub handovers, which will require further installation complexity at the customer's premises. Alternatively, in another approach rain fades can be counteracted with automatic power control (APC), whereby the transmitted power can be increased when necessary to maintain the required bit-error-rate (BER) [32].

Another effect of precipitation is incurred in the form of water, snow or ice being on antenna surfaces, which can cause severe losses. Depending on the frequency range, air pressure and humidity; attenuation not only increases at high frequencies but also becomes more dependent upon the peculiar absorption characteristics of oxygen and water vapour molecules.

Furthermore, effects from vegetation obstructing the LOS path, may lead to serious signal attenuation and depolarization. These effects have been measured and useful models are reported extensively in the literature. It can be concluded that the effects of radio waves propagating through vegetation arise because of three principal propagation mechanisms, namely, diffraction around the vegetation edges; reflection by the ground underneath the vegetation canopy; and finally scattering due to multiple reflections inside the canopy or from tree trunks [33]-[39].

Measurements of dielectric parameters of wall materials at 60 GHz are reported in [40]. Similar measurements of reflection transmissions of buildings at 60 GHz are presented in [41] and [42].

2.7 Cellular LMDS

The cellular concept, invented first in 1983, is a form of wireless communication coverage architecture which is capable of delivering higher system and user capacities. The cellular structure of LMDS is very similar to that employed in GSM/UMTS networks apart from the fact that the receiving terminals are stationary. The number of users and the amount of spectrum available to each user is primarily

associated with the allocated RF bandwidth. As with any cellular plan, the objective is to maximise the utilization of the spectrum and to efficiently use the available RF finite resource. This is achieved through reusing the frequencies in other cells; hence user capacities can be increased in a geographical area. The radio channel can be used simultaneously in multiple cells as long they are sufficiently isolated and transmitted with low power levels in order to avoid interferences from adjacent- and co-channels. Handoff is another aspect of the cellular concept; however it is applicable only for mobile applications and hence is not portrayed in the context of LMDS networks.

As mentioned earlier, LMDS structures employ PTP and PMP topology at the uplink and the downlink, respectively, and utilize narrow beam directional antennas at the subscriber's premises, forming a typical cellular network structure. Narrow beam antennas optimise the employment of frequency-reuse by minimizing the effects of unwanted scattered multipaths and cross polarized signals. The benefits of using such directional antennas in small cells are evident and well supported in the technical literature [2] [43] [44].

Radiowave propagation at millimetre wavelengths is restricted to LOS paths and heavily depends on the topography of the channel. Cell sizes and signal levels are strongly reliant on the propagation environments; these include building layouts, terrain details, rain statistics and vegetation. Depending on the cell structure and the layout of buildings, NLOS coverage can be possible via strong reflected signals, however is limited to very short ranges and depends on the surface roughness of ground patches and building facades.

In addition to the cell's topography, there are other system factors used in determining cell sizes. These include the following; type of antennas used at the BTS and subscriber premises and their elevation heights above the ground; the required SIR to achieve a predefined quality of service; traffic capacity; system availability and the selected modulation scheme.

Short frequency-reuse distances are beneficial; however LMDS operators will require more cells to achieve ubiquitous coverage of the service areas [45] in a fully deployed network. Cells can be assumed to be rectangular or square in shape. Each cell is

divided into a number of sectors for more effective frequency-reuse utilization. Sectorisation is considered to be a capacity expansion tool since it effectively reduces the bandwidth requirements, for example in a dual-frequency reuse scheme, sectorisation reduces the bandwidth by a factor of two.

Cellular LMDS, as in any communication system, utilizes two separate channels; one is for the downlink between the BTS and the subscriber, and another for the uplink between the subscriber and its BTS. This channel assignment configuration is known as Frequency Division Duplex (FDD) and is illustrated in Fig. 2.5, where *F1* and *F2* are channel divisions of the full bandwidth (*F*) and refer to the frequency channel used at either, the uplink or downlink, whereas *V* and *H* refer to the applied vertical or horizontal wave polarization, respectively.

In a typical LMDS configuration, the 360° service area covered by the BTS is typically divided into 90° sectors, each covering the full bandwidth of the allocated spectrum. Sectors are distinguished by dual-frequency and dual-polarization as shown in Fig. 2.6. The (orthogonal) polarisation discrimination reused throughout the network is intended to provide the necessary isolation between the adjacent cells.

Depending on the selected LMDS applications and services, the spectrum assignment of channels *F1* and *F2* are not necessarily half the full bandwidth (*F*). For example in TV broadcasting applications, large uplink bandwidths are not required, while in video interactive applications considerable bandwidths are crucial for both links. With large bandwidths available at high frequencies, LMDS potentially is able to support the next generation of interactive and video applications. According to the information capacity theorem, the maximum bit rate (R_{max}) at which symbols can be transmitted through a channel is *2F*. This clearly means that larger channel bandwidths can offer higher data transmission rates. In the work presented in [2], an estimation of data transmission rate was calculated for a few hundred active users per cell. Even with the employment of the less efficient QPSK modulation scheme, the total uplink capacity for LMDS was found to be 386 Mbit/s.

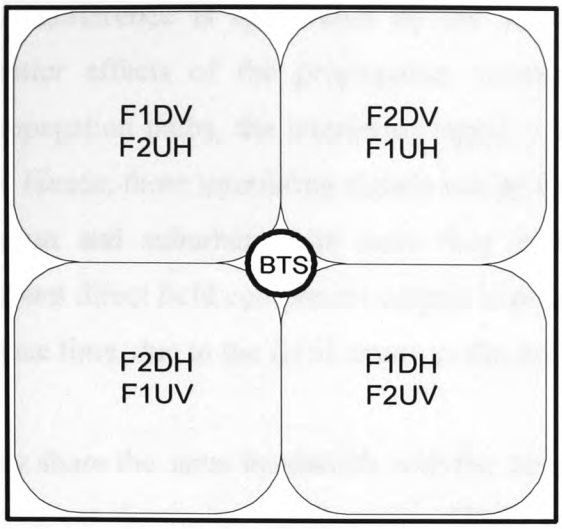

Figure 2.5 Example of a sectored LMDS cell

Many of the LMDS networks are foreseen to exploit the FDD transmission scheme. In some countries of south East Asia, the alternative Time Division Duplex (TDD) has been under consideration. Simulations of a TDD LMDS cellular network deployed at 26 GHz are presented in [46]. TDD transmission only benefits from the fact that co-channel interference only occurs when two cells use the same timeslot division. However, in a network where traffic tends to be symmetrical, TDD is not as spectrally efficient as FDD. Other factors, such as flexibility and spectrum efficiency tradeoffs, synchronization problems, limited operating range and coverage issues, make FDD a more favourite option than TDD for LMDS applications [47] [48].

As with other wireless systems, in order to share the same channel with multiple users, FDD is used with either a frequency or time division multiple access method (FDMA and TDMA respectively). The possibility of employing the more efficient CDMA, as an alternative to TDMA or FDMA, faces the crucial problem of unavailability of useful multipath signals and is still in its early stages for any practical considerations [48].

2.8 Interference Considerations and LMDS Cell Plans

Frequency and polarization reuse plans for optimum spectral efficiency in LMDS networks are subject to severe interference levels on the uplink and downlink signal streams arising either from nearby cells or from the intra-sectorised cells. In actual

fact, cellular LMDS interference is aggravated by the use of highly directional antennas and the scatter effects of the propagation environment. Assuming no obstructions in the propagation paths, the interfering signal is discriminated only by free space attenuation. Hence, these interfering signals can be relatively close to those wanted signals in urban and suburban cells since they each are most likely to comprise form a dominant direct field component subject to propagation fading with a relatively long coherence time, due to the fixed nature of the link.

Interfering signals may share the same bandwidth with the desired signal and, hence, their levels in a network can determine signal quality (BER) and, ultimately, system capacity. The level of interference can be directly related to a number of factors, such as the frequency and polarization reuse plans, the propagation environment, depolarization effects from building surfaces, vegetation and rain droplets, antenna radiation patterns, as well as the underlying medium access scheme. Depending on its source, interference can be characterized as adjacent- or co-channel interference. In the former case, interference is caused by an adjacent cell operating with a cross-polarized signal at the same frequency, whereas in the latter case, the interference is caused by a distant cell operating at the same frequency and polarization, and can be from either, an inter-cell or an intra-cell. Overall, interference in LMDS networks is considered an operational constraint since it tends to limit the system capacity and influences the link performance.

The most common underlying technology and architectures approved locally and internationally for cellular LMDS, are based on FDD with TDMA and TDM access schemes at the uplink and downlink, respectively. Two dual-frequency and dual-polarization (double capacity) cellular plans for LMDS networks are envisaged by [2], a report considered by Ofcom, and are proposed as starting points in the UK MPT 1560 [5]. These plans are also widely accepted in the technical literature and are referred to here as the conventional Sub-Optimal Plan (SOP) and the Alternative Plan (AP) as illustrated in Fig. 2.6. For both plans, the 360° service area covered by the BTS is typically divided into 90° sectors. Dual signal polarization and frequency discrimination are used to provide the necessary isolation between cells. The main interference scenarios for the two dual-frequency and -polarization plans shown in Fig. 2.6 are mostly, proposed originally by the authors.

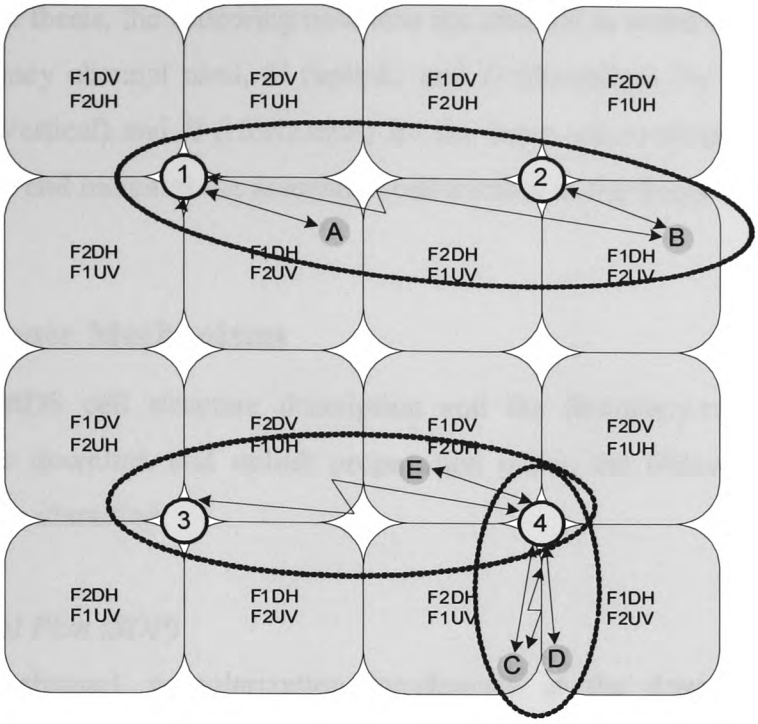

(a)

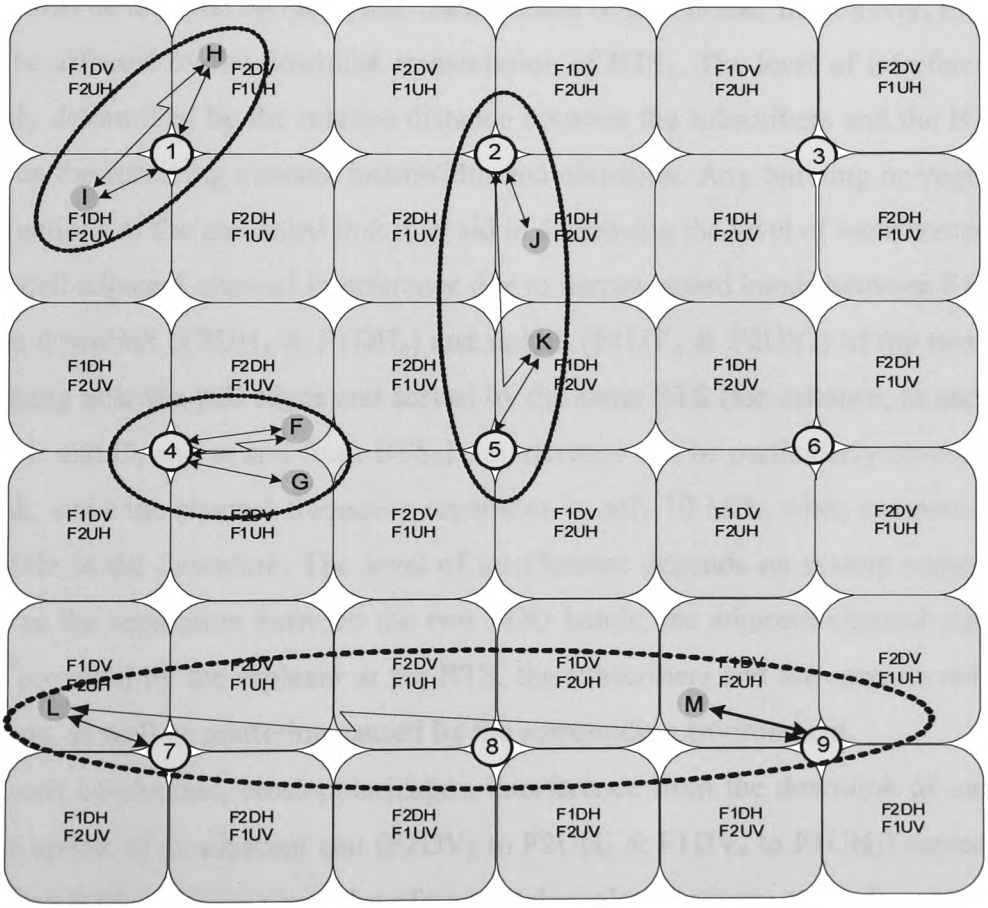

(b)

Figure 2.6 LMDS frequency-reuse schemes for: (a) a 16 cluster SOP; (b) a 36 cluster AP.

Throughout the thesis, the following notations are adopted as noted earlier: *F1* and *F2* for the frequency channel used, *U* (uplink) and *D* (downlink) for the transmission direction, *V* (Vertical) and *H* (Horizontal) for the wave polarizations, and finally the subscript at the end indicates the associated cell number in the frequency plan.

2.9 Interference Mechanisms

Given the LMDS cell structure description and the frequency-reuse plans; with relation to the downlink and uplink propagation paths, the following interference mechanisms are identified:

A. Sub-Optimal Plan (SOP)

I. Inter-cell co-channel, co-polarization interference at the downlink ($F1DH_1$ & $F1DH_2$) and uplink ($F2UV_1$ & $F2UV_2$) from and to subscribers A and B. User A and BTS_1 will be affected by the uplink transmission of user B and, most likely, the latter will be affected by the downlink transmission of BTS_1. The level of interference is mainly determined by the relative distance between the subscribers and the BTS, as well as the receiving antenna beamwidth and elevation. Any building or vegetation obstructions of the unwanted link may aid in decreasing the level of interference.

II. Intra-cell adjacent-channel interference due to narrow guard bands between F1 & F2 in the downlink ($F2DH_4$ & $F1DH_4$) and uplink ($F1UV_4$ & $F2UV_4$) of the two users operating near the cell edges and served by the same BTS (for instance, to and from users C and D, and to and from BTS_4). Interference can be particularly severe in the uplink, since the channel frequency separation is only 10 MHz when compared with 39 MHz in the downlink. The level of interference depends on system parameters, such as the separation between the two FDD bands, the adjacent-channel rejection ratio provided by the diplexer at the BTS, the subscribers and the antenna radiation patterns, as well as scattering caused by the surrounding environment.

III. Inter-cell co-channel, cross-polarization interference from the downlink of one cell to the uplink of an adjacent cell ($F2DV_3$ to $F2UH_4$ & $F1DV_4$ to $F1UH_3$) served by a different BTS and vice versa. Interference takes place between two adjacent sectors operating at the same frequency and different wave polarization. For example, leakage from the downlink of BTS_3 interferes with the uplink of user E served by BTS_4. Such interference can be particularly significant in the case of a 90° sectored

BTS antenna beam. Reductions in interference would be expected if a narrower multi-beam sectored BTS antenna is deployed. The level of interference is mainly determined by depolarization effects due to rainfall and environmental (building and vegetation) scatter, as well as the radiation characteristics of the antennas used at the BTS.

B. Alternative Plan (AP)

I. Intra-cell co-channel, cross-polarization interference at the downlink ($F2DV_4$ & $F2DH_4$) and uplink ($F1UH_4$ & $F1UV_4$), experienced by users F & G near the edges of the adjacent cells, to and from BTS_4, due to the depolarization effects mentioned earlier.

II. User intra-cell, co-channel interference in the uplink and downlink of users H and I. The transverse sectors $F2UV_1$ and $F2DV_1$, served by the same BTS share the same frequency (F2) between the uplink of one sector and the downlink of the other. The same case applies to the other transverse pair (F1). However, a BTS is normally placed on a building roof-top, and together with the utilization of narrow beamwidth receiving antennas, the LOS interfering paths between any two transverse intra-cell users are quite likely to be shielded.

III. Inter-cell co-channel interference at the downlink ($F1DH_2$ & $F1DH_5$) and uplink ($F2UV_5$ & $F2UV_2$), potentially due to specular reflections from a nearby building surface. For instance, on the downlink of user K served by BTS_5, the received signal can interfere with a signal transmitted by BTS_2 reflected by structures in the vicinity of the terminal. Similarly, the uplink of user K may interfere with the uplink of user J. The level of the interfering signal is determined by the presence of potential specular reflections.

IV. Inter-cell co-channel, co-polarization interference at the downlink ($F1DV_7$ & $F1DV_9$) and uplink ($F2UH_9$ & $F2UH_7$). A similar situation occurs in the SOP (I). However, the fact that use of co-channels is repeated at every fifth sub-cell, such as the case of users L and M, combined with the low probabilities of an existing LOS for paths in excess of 1 km, results here in low interference levels.

2.10 Other Frequency Cell Plans

Two other possibilities for frequency re-use plans are presented in a white paper by Hughes Network systems [50]. The first method is a capacity doubling strategy which involves using four frequencies per cell instead of two as in the SOP and AP. The second method is set by increasing the number of sectors to 8 instead of 4 using 45° sectors. The authors of [50] claim benefits of the latter approach combined with expectations of attaining lower interference levels. Depending on the propagation geometry, it is anticipated that very sharp narrow beamwidth antennas (1-3°) at the receiver terminal will be essential. Undesirably, such antennas, in addition to their large physical size, involve more complex installation procedures. Nevertheless, the possibility of deploying these alternative cell plans will need to be tested through dedicated simulation predictions tools and experimental field measurements. The architectural complexity of deployment, costs and system management is another aspect that needs to be taken into consideration in such alternative plans.

2.11 Interference Literature Review

Addressing interference issues is in fact the most significant challenge in system deployment [51] and frequency-reuse planning schemes [50]. Significant amount of research has been carried out in determining the effects of cellular interference in mobile radio frequencies and systems. LMDS, being a new technology, interference concerns have received minimal consideration. Part of the work presented here is therefore aimed towards examining and understanding the propagation effects of interference in LMDS cells. This is provided not only through modelling and simulations but also through field experimental measurements that are essential in validating the theoretical hypothesis and assumptions considered here and in the published literature.

It is worth stating that deterministic EM-wave solutions used at lower frequencies (less than 10 GHz), such as ray-tracing or classical propagation models are not considered suitable for millimetre-wave frequencies, mainly because of fundamental differences in the underlying propagation modes, the relatively imprecise description of the geometry, and directive antenna properties [50]. On the other hand, radio

channel numerical and analytical modelling approaches developed for microcellular networks [52]-[55] can be extended to provide meaningful treatment of interference in LMDS networks.

From the available literature, there are only a few relevant publications on LMDS cellular interference and propagation models, but hardly any on field measurements. A general analysis of cellular LMDS networks has been presented by Panagopoulos *et al.* [56]. The authors have focused their studies on the effects of rain on inter-cell interference by taking into consideration the statistical properties of the SIR levels. Their derivations of SIR are analytical, and only take into account the azimuthal dependence of the intercell interference on the antenna patterns.

Bose *et al.* [57] carried out two-dimensional simulations for co- and adjacent channel interferences. Their analysis is based on half-power beamwidth of the antennas, the time percentage of short term enhancement due to atmospheric multipath and the cell radius on the SIR distribution, irrespective of the propagation geometry. Their simulation results indicated that 12.5 % to 25.5 % of a LMDS cell area would suffer from interference for a cell radius of 2 km. These percentages have been significantly reduced by decreasing the user's receiving antenna beamwidth to a 2^0. Presented also is a simple technique for reducing downlink co-channel interference by reorienting those receivers which experience severe interference levels, to and alternative BTS. Another similar cell diversity method to mitigate co-channel interferences for LMDS is given in [61].

More recently [44], the same authors as in [57], incorporated terrain data from an urban topology to focus on obstructions by tall buildings, based on half-power antenna beamwidths in the azimuth and elevation planes. Reduction in co-channel interference levels was obtained by keeping the user's receiving antennas as low as possible, yet with sufficient heights used to establish a LOS link with the desired BTS. Hence some kind of a trade-off applies for the receiver antenna heights, which primarily depends on the topography of the channel, propagation environments and the LMDS system parameters. Propagation data and field measurements were strongly recommended by the authors to authenticate any general conclusions.

LMDS links are designed to be available essentially at all times with adequate signal reception levels. Outage probability provides an effective statistical measure of the radio link performance in an interference limited environment, where frequencies are reused over relatively short distances. It can be defined as the probability of the ratio of the desired signal to interference power that falls below a predefined threshold. The latter primarily depends on the modulation type and other system design requirements. An example from the measurements conducted is provided in Appendix B. System and co-channel interference characteristics of representative LMDS links were studied analytically and numerically by Gong and Falconer [59]. Their analysis accounted for the subscriber and hub antenna parameters, site diversity, and power control in LOS and NLOS scenarios. Outage probability was the main parameter selected for the comparisons presented. The LOS links were found to have three times better outage probabilities than those in the NLOS links. From their simulations, subscribers in the overlapping areas between the cells were expected to experience severe interference and high outage levels. Similar analytical approaches of the outage probability of Rician/Rician channels applicable for LMDS networks can be found in many other articles [60] - [63].

2.12 Interim Conclusion

In the published literature and considering the advantages of LMDS networks as compared to other available broadband communication systems available today, cellular LMDS systems are perceived to be the next generation of wireless broadband networks. LMDS systems are envisaged to either operate as pure networks or integrated with current available technologies.

From a cell planning point of view, in urban areas, where buildings and obstacles not only produce scatter but also play a significant role in radio terminal shielding, frequency-reuse assignment plans can be utilized for better coverage and capacity maximization. Two dual-frequency and polarization reuse plans have been assigned for the deployment of LMDS networks. However, the deployment of these plans causes harmful interference signals that may exist from co- and adjacent-channels due to the short reuse cell distances and the utilization of narrow beamwidth antennas at the transmits and receive terminals. Description of a number of possible interference

mechanisms in a FDD LMDS with TDMA access have been presented exclusively in this chapter.

Before presenting the details of the proposed electromagnetic model in Chapter 4, the next chapter focuses on demonstrating the scattering phenomena at the millimetre wave frequency bands. The next chapter also provides classifications of the radio channel and propagation models.

2.13 References

[1] Vacca J. R., *Wireless Broadband Networks Handbook, 3G, LMDS & Wireless Internet*, McGraw Hill Book Co, 2001, ISBN 0-07-213031-8.

[2] ACTS Project 215, *Cellular Radio Access for Broadband Services (CRABS), Specification of Next Generation of LMDS Architecture D2P1B*, 1999.

[3] Nordbotten A., "LMDS systems and their application", *IEEE Commun. Mag.*, vol. 38, no. 6, pp. 150–154, June 2000.

[4] Papazian P.B, Hufford G.A, Achatz, R.J. and Hoffman, R., "Study of the local multipoint distribution service radio channel", *IEEE Trans. Broadcast.*, vol. 43, no. 2, pp.175–184, June 1997.

[5] MPT 1560, "Performance specification for digital multi point video distribution systems (MVDS) transmitters and transmit antennas operating 40.5–42.5 GHz", *Radio Communications Agency*, UK, 1995.

[6] Muammar H.R., "Co-channel interference in microcellular mobile radio systems" *IEEE Proc. VTC '91*, pp. 198–203, May 1991.

[7] Smith C., *LMDS*, McGraw Hill Book Co, 2000, ISBN 0-07-136254-1.

[8] Eklund C., Marks R. B and Stanwood K. L, "*IEEE Standard 802.16: A Technical Overview of the WirelessMAN™ Air Interface for Broadband Wireless Access", IEEE Communications Magazine*, June 2002

[9] Federal Office of Communications UK, www.ofcom.org.uk, (Feb 2008).

[10] Falconer D.D. and DeCruyenaere, J.-P. "Coverage enhancement methods for LMDS", *IEEE Communications Magazine*, vol. 41, issue 7, July 2003.

[11] Neskovic A., Neskovic N., and Paunovic G., "Modern Approaches in Modelling of Mobile Radio Systems Propagation Environment", *IEEE Communications Surveys, The Electronic Magazine of Original Peer-Reviewed Survey Articles*, Third Quarter 2000.

[12] Okumura Y., Ohmori E., Kawano T., and Fukua K, "Field strength and its variability in UHF and VHF land-mobile radio service," *Rev. Elec. Communication Lab.*, vol. 16, no. 9, 1968.

[13] Hata M., "Empirical formula for propagation loss in land mobile radio services," *IEEE Trans. Veh. Technol.*, vol. 29, pp. 317-325, Aug. 1980.

[14] Dilworth I.J and Ebraly B. L, "Propagation effects due to foliage and building scatter at millimetre wave lengths", *Ninth International Conference on Antenna and Propagation*, Netherlands 4 -7 April 1995.

[15] Violette, E.J., Espeland R.H., DeBolt, R.O., and Schwering, F.K., "Millimeter-wave propagation at street level in an urban environment", *IEEE Transactions on Geoscience and Remote Sensing*, vol 26, issue 3, May 1988 Page(s):368 – 380

[16] Hammoudeh, A.M and Sanchez, M.G. Grindrod, E., "Analysis of millimetric wave propagation in a sub-urban microcell", *IET Electronic Letters*, Mar, 1997, vol 33, issue 6.

[17] Thomas H. J., Cole R. S., and Siqueira G. L., "An Experimental Study of the Propagation of 55 GHz Millimeter Waves in an Urban Mobile Radio Environment, *IEEE Transactions On Vehicular Technology*, vol. 43, no. I, February 1994

[18] Seidel S.Y. and Arnold H.W., "Propagation measurements at 28 GHz to investigate the performance of Local Multipoint Distribution Service (LMDS)," *Proc. IEEE Global Telecommunications Conference*, GLOBECOM '95, vol.1, pp 754- 757, 1995.

[19] D. Gesbert, Haumont L., B¨Olcskei H., Krishnamoorthy R., and Paulraj A. J., "Technologies and Performance for Non-Line-Of-Sight Fixed Broadband Wireless Access Networks", *IEEE Communications Magazine* (Broadband Access Series), March 2002.

[20] Bultitude R., Hou P., Hahn R., Hendrantoro G., Falconer D. and Bérubé R., "Radio Propagation Data Pertinent to the Design of LMCS Systems at 28 GHz", *Proc. ANTEM '98*, Ottawa, Aug., 1998

[21] Soma P., Ong L.C., Sun S., and Chia M.Y.H, "Propagation Measurements and Modeling of LMDS Radio Channel in Singapore", *IEEE Transactions On Vehicular Technology*, vol. 52, no. 3, May 2003

[22] ITU-R P.530 Propagation data and prediction methods required for the design of terrestrial line-of-sight systems. *Tech. Rep., International Telecommunication Union.*

[23] Wolf D. A. and Ligthart L. P., " Multipath Effects Due to Rain at 30-50-GHz Frequency Communication Links", *IEEE Transactions on Antennas and Propagation*, vol. 41, no. 8, august 1993.

[24] KAYA P., "A Model for Calculating the Depolarization of Microwave Signals Propagating Through Rain", *IEEE Transactions on Antennas and Propagation*, vol. Ap-28, no. 2, March 1980

[25] Naz N. and Falconer D.D., "Temporal Variations Characterization for Fixed Wireless at 29.5GHz", *Vehicular Technology Conference Proceedings*, VTC 2000-Spring Tokyo. 2000 IEEE 51st

[26] Sinka C. and Bito J., "Rain Attenuation Countermeasure Technique for Broadband Fixed Wireless Access Networks", *IEE Electronic Journals* 2003.

[27] Myers W., IEEE 802.16.2 Topical Outline for "Recommended Coexistence Practices for Broadband Wireless Access Systems", *IEEE 802.16cc*, July 99.

[28] ITU R. 838, Specific Attenuation Model for Rain for Use in Prediction Methods, *Tech. Rep., International Telecommunication Union.*

[29] Crane R. K., *Electromagnetic Wave Propagation Through Rain*, New York: Wiley, ISBN 0-471-61376-2, 1996.

[30] Xu H., Rappaport T.S, Boyle R.J, and Schaffner J.H, "Measurements and Models for 38-GHz Point-to-Multipoint Radiowave Propagation", *IEEE Journal on Selected Areas in Communications*, March 2000.

[31] Hendrantoro G., Bultitude R. J. C, and Falconer D. D., "Use of Cell-Site Diversity in Millimeter-Wave Fixed Cellular Systems to Combat the Effects of Rain Attenuation", *IEEE Journal on Selected Areas in Communications*, vol. 20, No. 3, April 2002.

[32] Anderson H. R., *Fixed Broadband Wireless System Design*, John Wiley, 2003, ISBN 0-470-84438-8.

[33] Rogers N. C., Seville A., Richter J., Ndzi D., Caldeirinha R., Shukla A., Al-Nuaimi M., Craig K., and Austin J., "A generic model of 1-60GHz radio propagation trough vegetation - Final report", *Tech. Rep., Radiocommunications Agency*, May 2002.

[34] Caldeirinha R. F. S., *Radio characterisation of single trees at micro- and millimetre wave frequencies*, PhD thesis, University of Glamorgan, 2001.

[35] Al-Nuaimi M. O. and Stephens R.B.L, "Measurements and prediction model optimisation for signal attenuation in vegetation media at centimetre wave frequencies", *IEE Proc. Micro. Antennas Propag.*, vol. 145, no. 3, pp. 201-206.

[36] Seville A., "Vegetation attenuation: modeling and measurements at millimetric frequencies", *Proceedings of the 10th International Conference on Antennas and Propagation*, April 1997, vol. 1, pp. 2.5-2.8

[37] Papazian P. B., Lo Y., "Seasonal variability of a local multipoint distribution service radio channel," *Proc. IEEE RAWCON'99* , 1999, pp. 211–214.

[38] Chavero M., *et al*, "Impact of vegetation on the performance of 28 GHz LMDS transmission," *Microwave Symp. Dig., IEEE MTT-S International*, 1999, pp. 1063–1066.

[39] Paulsen A. and Seville A., "Attenuation and distortion of millimetre radio waves propagation through vegetation," *Millennium Conf. Antennas Propagat.*, vol. AP2000, 2000.

[40] Lähteenmäki J. and Karttaavi T., "Measurement of dielectric parameters of wall materials at 60GHz band", *IET Electronic Letters*, August 1996, vol. 32, no. 16.

[41] Sato, K, Manabe T., Ihara T., Saito H., Ito S., Tailaka T., Sugai K., Ohmi N., Murakami Y., Shibayama M., Konishi Y., Kimura T, "Measurements of reflection and transmission characteristics of interior structures of office building in the 60 GHz band", *Personal, Indoor and Mobile Radio Communications*, 1996, vol. 1, Oct 1996 Page(s):14 – 18.

[42] Hayn A., Bose R. and Jakoby R., "Mulitpath Propagation and LOS Interference Studies for LMDS Architecture", *11th International Conference on Antennas and Propagation*, April 2001.

[43] Seidel S.Y. and Arnold H.W., "Propagation measurements at 28 GHz to investigate the performance of Local Multipoint Distribution Service (LMDS)," *Proc. IEEE Global Telecommunications Conference*, GLOBECOM '95, vol.1, pp 754-757, 1995.

[44] Bauer G., Bose R., and Jakoby R., "Three-Dimensional Interference Investigations for LMDS Networks Using an Urban Database", *IEEE Transactions on Antennas and Propagation*, Vol. 53, No. 8, August 2005

[45] Clark M.V., Erceg V. and Greenstein L.J., "Reuse efficiency in urban microcellular networks", *IEEE Trans. Veh. Tech. '97*, vol. 46, no. 2, pp. 279–288, May 1997.

[46] Matsuda M. and Watanabe K,, "26-GHz Band FWA Systems Employing Co-channel Interference Avoidance Method Using TDMA/TDD Frame Timing Control", *IEEE Communication Society*, Globecom 2004

[47] Hughes Network Systems, "Airlink Management in Point-to-Multipoint Systems: an Examination of FDMA, FDD, and TDD", *White Paper for Telecommunications Service Providers Using the AIReach® 9000 System*, 2002.

[48] Tardy I., Grondalen O. and Vezzani G., "Interference in TDD based LMDS System", *IST Mobile and Wireless Communications Summit*, Thessaloniki, 17-19 June 2002

[49] Arapoglou P.-D.M., *et al*, "Intercell Radio Interference Studies in CDMA-Based LMDS Networks", *IEEE Transactions on Antennas and Propagation*, ISSN: 0018-926X, 2005

[50] Hughes Network Systems, "System analysis for point-to-multipoint networks Part 1: frequency reuse planning", *White Paper for Telecommunications Service Providers Using the AIReach® 9000 System*, 2003.

[51] Roman V.I., "Frequency reuse and system deployment in local multipoint distribution service", *IEEE Personal Communications*, pp. 20–27, Dec. 1999.

[52] Muammar H.R., "Co-channel interference in microcellular mobile radio systems" *IEEE Proc. VTC '91*, pp. 198–203, May 1991.

[53] Yu-Dong Y. and Sheikh U.H., "Investigations into cochannel interference in microcellular mobile radio systems", *IEEE Trans. Veh. Tech.*, vol. 41, no. 2, pp. 114–123, May 1992.

[54] Wijk V.D., Kegel F., and Prasad A., "Assessment of a pico-cellular system using propagation measurements at 1.9 GHz for indoor wireless communications", *IEEE Trans. Veh. Tech.*, vol. 44, no. 1, pp. 155–162, 1995.

[55] Zhang Q.T., "Co-channel interference analysis for mobile radio suffering lognormal shadowed Nakagami fading", *IEE Proc. Commun.*, vol. 146, no. 1, pp. 49–54, Feb. 1999.

[56] Panagopoulos A.D. *et al.* "Intercell radio interference studies in broadband wireless access networks", *IEEE Trans. Veh. Tech.*, vol. 56, no. 1, Jan. 2007.

[57] Bose R., Bauer G., and Jakoby R., "Two-dimensional line of sight interference analysis for LMDS networks for the downlink and uplink", *IEEE Trans. Antennas Prop.*, vol. 52, no. 9, pp. 2464–2470, Sept. 2004.

[58] Liolis K.P., Panagopoulos A.D., and Cottis P.G., "Use of cell-site diversity to mitigate co-channel interference in 10-66 GHz broadband fixed wireless access networks", *Radio and Wireless Symposium*, IEEE 2006.

[59] Gong S.Q. and Falconer D., "Cochannel interference in cellular fixed broadband access systems with directional antennas", *Wireless Pers. Commun.*, vol. 10, pp. 103–117, Oct. 1998.

[60] Karagiannidis G.K., Kotsopoulos S.A., and Mathiopoulos P.T., "A Generalised approach for evaluation of outage performance in micro- and pico-cellular networks", *IEE Proceedings on Communications*, April 2002, Volume 149, Issue 2, p. 123-128.

[61] Annamalai A., Tellambura, C. and Bhargava, V.K., "Simple and accurate methods for outage analysis in cellular mobile radio systems-a unified approach", *IEEE Transactions on Communications*, vol 49, no. 2, Feb. 2001.

[62] Tjhung, T.T., Chai, C.C., and Dong, X.: "Outage probability for a Rician signal in L Rician interferers", *IEE Electron. Letter*, 1995, 31, (7), pp. 532–533.

[63] Wong A.H., Neve M.J., and Sowerby K.W. "Performance analysis for indoor wireless systems employing directional antennas", *IEE Proceedings Communications*, vol 152, issue 6, p. 890-896, Dec2005.

CHAPTER THREE

CHANNEL & PROPAGATION MODELLING AT MILLIMETRE-WAVE LENGTH FREQUENCIES

3.1 Overview

The behaviour of electromagnetic waves is an area of continuous research. It is widely acknowledged that LOS links are the main modes of propagation at millimetre-wave lengths as reported in Chapter 2. Channel behaviour at millimetre wavelengths can be straightforwardly represented by either a Rician or a Rayleigh fading distribution for LOS and severe NLOS links, respectively. The usefulness of other propagation modes such as reflection or diffraction at the receiving terminals is considered insufficient, and at most times destructive due to miniature nature of the wavelength. The occurrence of specular reflection is very limited as it requires superior smooth surfaces with very small height irregularities. On the other hand, diffracted signals over and around buildings edges and other obstacles experience high path losses at these frequencies. Seemingly, scatter and the complexity associated with modelling this propagation mode is considered one of the main complex problems encountered by the propagation channel at millimetre wavelengths.

This chapter is organized as follows: the first section is dedicated to the scatter phenomena. A brief description is given on scatter emanating from rough surfaces and its analytical solutions. The second section of this chapter illustrates the fading distribution models and parameters considered, along with their classifications and derivations.

3.1.1 Scattering of Electromagnetic Waves

Scatter arises significantly at millimetre-waves wireless links since the propagation path between the transmitter and the receiver is likely to contain obstacles with surface irregularities that are comparable with the signal wavelength. In such cases the

incident surface plane is considered rough, consisting of arbitrary height distributions of surface irregularities. Statistically, a geometrical measure of the surface roughness is characterised by its standard derivation, i.e. the second order moment of surface height distribution (σ_h). Depending on the incident angle (θ_i), and how comparable the signal wavelength is with the surface height irregularities (h); surfaces can be categorised as either rough or smooth according to [1]:

$$\Delta\Phi = \frac{4\pi h}{\lambda}\sin\theta_i \tag{3.1}$$

where $\Delta\Phi$ is the phase difference between the two rays shown in Fig. 3.1.

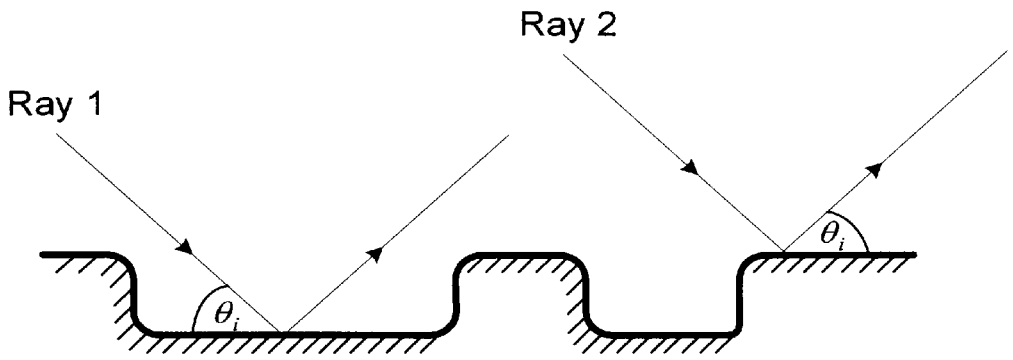

Figure 3.1 Rayleigh Criterion

If the two rays are reflected with very small $\Delta\Phi$ values, i.e. they are almost in parallel; the reflected surface is considered to be smooth. For a perfect smooth surface, $\Delta\Phi$ equals (or is very close to) zero, whereas in a rough surface, $\Delta\Phi$ will be close to π. The separation principle between smooth and rough surfaces is known as the Rayleigh criterion for rough surfaces for which $\Delta\Phi = \pi/2$. This is achieved by satisfying the following formulation for the surface irregularity height (h):

$$h < \frac{\lambda}{8\sin\theta_i} \tag{3.2}$$

In [1]-[3] it has been suggested that a more realistic criteria is given by setting $\Delta\Phi = \pi/8$. Clearly and as stated in [1], for an effective measure of surface roughness; a surface is considered smooth if it satisfies one of the following conditions:

$$\frac{h}{\lambda} \to 0 \quad or \quad \theta_i = 0 \tag{3.3}$$

The well known Snell's law of reflection [1] states; in a two homogenous isotropic media, the ray impinging onto an infinite perfectly smooth surface is reflected in the specular direction, in which the angle of incidence (θ_i) is equal to that of reflection (θ_r) as shown in Fig. 3.2.

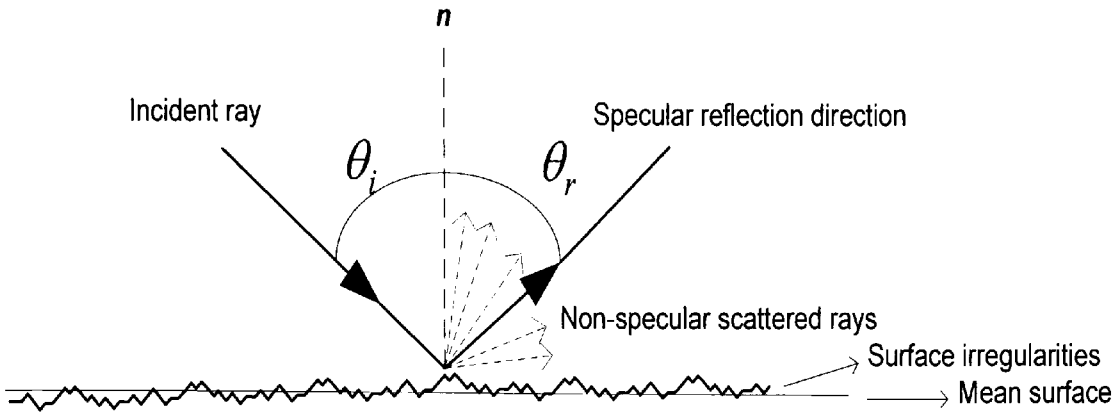

Figure 3.2 Illustration of Snell's reflection concept and scatter from a rough surface

The prominent difference between reflection and scatter is that in the latter case, the rough surface will coherently and incoherently reflect waves in different phases. Therefore the signal will be diffused in various directions, (although some directions might be more privileged than others). Snell's law, which accounts only for specular reflection from smooth surfaces, is no longer applicable for millimetre wavelength signals. The mean value of the scattered field in the specular direction is referred to as coherent, whereas the diffuse part which is scattered in all directions is referred to as incoherent. At low frequencies (less than 10 GHz), it is usually acceptable to ignore the incoherent part of the scatter field provided that a scattering loss factor (ρ_s) is introduced as in [4]. Assuming that the surface heights are Gaussian distributed, ρ_s is given by

$$\rho_s = \exp\left[-8\left(\frac{\pi\sigma_h \cos\theta_i}{\lambda}\right)^2\right] I_0\left[8\left(\frac{\pi\sigma_h \cos\theta_i}{\lambda}\right)^2\right] \tag{3.4}$$

where σ_h is the standard deviation of the surface height irregularities about the mean surface plane and I_o is the modified Bessel function of zero order. Eq. (3.4) is known as the Gaussian rough surface scatter model. In conjunction with the well-known Fresnel reflection coefficients (defined below in Eq. (3.6)), the low-frequency rough scattering model can be written as [3]-[5]

$$\Gamma_{rh} = \rho_s R_h$$
$$\Gamma_{rv} = \rho_s R_v \tag{3.5}$$

In the above Γ_{rh} and Γ_{rv} represent the modified Fresnel scatter coefficients whereas R_h and R_v represent the modified Fresnel reflection coefficients for perpendicular and parallel polarizations respectively. Fresnel reflection coefficients are determined by the surface reflection material properties, angle of incidence (θ_i) and frequency, as follows

$$R_v = \frac{\cos\theta_i - \sqrt{\varepsilon_r - \sin^2\theta_i}}{\cos\theta_i + \sqrt{\varepsilon_r - \sin^2\theta_i}} \tag{3.6a}$$

and

$$R_h = \frac{\varepsilon_r \cos\theta_i - \sqrt{\varepsilon_r - \sin^2\theta_i}}{\varepsilon_r \cos\theta_i + \sqrt{\varepsilon_r - \sin^2\theta_i}}. \tag{3.6b}$$

where the complex relative dielectric constant of the material (permittivity)

$$\varepsilon_r = \varepsilon_r^{'} - j\varepsilon_r^{''} = \varepsilon_r^{'} - \frac{j\sigma_e}{\omega\varepsilon_0}. \tag{3.7}$$

In the above equation, $\varepsilon_r^{'}$ and $\varepsilon_r^{''}$ are the real and complex parts of ε_r respectively, ε_0 is the vacuum permittivity, σ_e is the electrical conductivity of the material, and ω is the angular frequency of the incident wave.

As the surface irregularities become comparable with the incident wavelength, the incoherent diffuse component of scatter becomes more significant and can not be simply neglected. Hence Eqs 3.4 and 3.5 are only applicable at relatively low frequencies. For higher frequencies such as those corresponding to millimetre wavelengths, consideration of the incoherent diffuse scatter becomes highly necessary.

3.1.2 Solution to Scatter by Rough Surfaces (Kirchhoff Approach)

Solution characterising the scatter effects by numerical methods are available in the literature (see references given by [9]). However these numerical methods require large computational processing times and extensive storage memories. The most common and widely accepted stochastic analytical treatment of scattering by rough

infinite surfaces of incidence plane wave is the Kirchhoff approach. This method, illustrared in Fig 3.3, is also known as the Tangent-Plane approach since it is based on the assumption that each point on the random surface is replaced by its tangent plane. The reflected wave field is represented by the summation of the incident field (E_i , the field of assigned sources in an infinite empty space) and the field reflected from a point ***r*** on the plane tangent to the incident surface, provided that the local radius of curvature is much larger than the wavelength of the incident field [1]-[9].

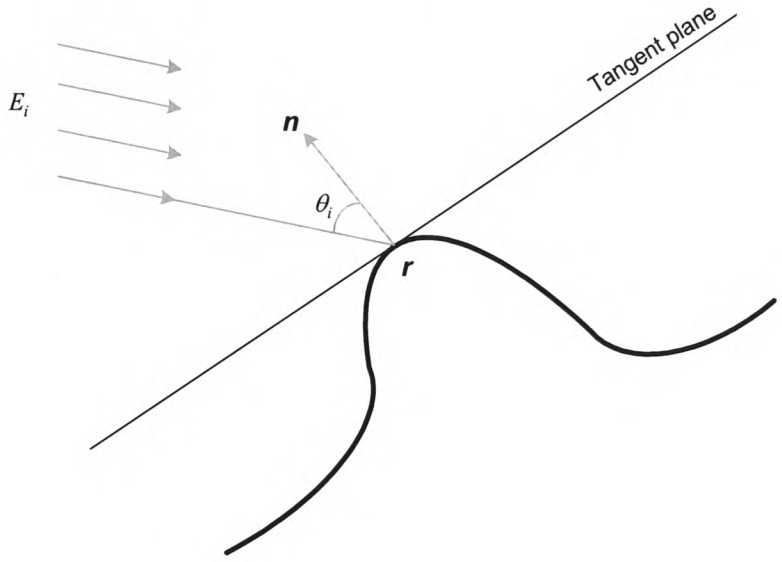

Figure 3.3 Kirchhoff Tangent-Plane geometry

The Kirchhoff approach is a well known method in Physical Optics (PO) since the 1970s, and has been extensively employed in scattering studies from rough surfaces. In this context, Kirchhoff and PO methods are used interchangeably as they both refer to the integrations of currents flowing on a surface. These theories are applicable for surfaces with gentle undulations, and whose horizontal surface dimensions are similar or larger compared to the incident wavelength [1] [10]-[12]. The employment of Kirchhoff solution for scattering from rough surfaces is detailed in Chapter 4.

Its worth noting that by taking a high-frequency limit of the PO method, the latter is known as the Geometrical Optics (GO) model which is only valid when the wave-number (k) is very large. The GO method is widely used due its simplicity and

adaptability. The total field is obtained by summing up the individual field values of each ray [13]. Therefore GO is in fact a ray-tracing technique, with postulates based on the following:

- Wave-fronts are locally plane.
- The wave direction is specified by a unit vector perpendicular to the ray.
- Rays travel in straight lines in an homogenous medium.
- In a non-homogenous medium the unit vector perpendicular to the ray, rotates around the ray in a specific way as it slides through the medium [13].
- Reflection and refraction obey Snell's law.

The GO model is widely used in the determination of wave intensities, polarizations and phases through space. One of its main applications is the interpretation of the reflected signals from ocean surfaces [14]. The main drawback of GO however is that it doesn't take into account the fields in the shadowed areas. This issue has been eliminated by the innovation of the Geometrical Theory of Diffraction (GTD). GO and GTD are usually jointly utilized in a number of wireless applications such as wireless local area networks (WLAN), fixed, mobile and cellular communication systems and GPS navigation.

3.1.3 Examples from the Literature

Classical random rough surface scattering techniques established on an asymptotic reduction of the PO integral can be useful around the specular region of surfaces with random deviations of their height above a mean plane presenting a continuous distribution (e.g. corrugated rooftops or ground patches). However there are very low numbers of publications in the literature that include radiowave scatter from rough surfaces in complete radio communication system models. Below are some examples.

The authors of [10] have included a rough surface scatter in their ray-tracing model, whereby the coherent and incoherent scatter fields are accounted for in their model derivations based on the Kirchhoff's approach. In a very recent work [15], Pongsilamanee and Bertoni investigated the scattering from building facades with nearly periodic placement of their features employing PO and random realizations of

their periodicity. In [16], the authors have presented a site specific, statistical EM propagation model based on Kirchhoff's approach for large scale surface irregularities. Al-Nuaimi and Ming [17] studied the near-field scatter effects based on measurements from flat building surfaces. Their results highlighted high scattering signal levels within the specular region at around 10 GHz. Similar findings are reported in [18]. In [19] the reflection coefficient is modified by a factor that takes into account the surface roughness determined by the standard deviation of the surface distribution as an alternative approach to using dielectric parameters of building surfaces as in [20]. An example of employing the Kirchhoff approach for calculating the reflection coefficient from rough surfaces applicable for low-angle propagation is presented in [21].

In terms of measurements, analysis of rough surface scatter properties of limestone and brick walls at 28 GHz are presented in [22]. Similarly, reflection and transmission coefficients for various rough (and smooth) building surfaces at 62.4 GHz are given in [19].

3.2 Classification of Propagation Models

The first section of this chapter has outlined the scattering problem in millimetre-wave propagation which is addressed in details in Chapter 4 as part of the EM propagation model derivations. The proposed model is classified as a statistical model suitable for LMDS and PMP millimetre-wave wireless links. The reason for choosing such a statistical solution, which is probably the only solution since ray-tracing methods are impractical (see Section 3.2.3), is primarily based on the stochastic nature of the scattering field and the randomness of surface irregularities. In an effort to outline the benefits of statistical approaches, the sections below provide a general classification of propagation models. These are namely, empirical, deterministic and statistical models.

3.2.1 Empirical Models

Empirical models are those based on observations and statistical analysis of signal performances found in large number of measurements. These models consist of diagrams or equations used to predict path loss due to multipaths and rain-fades [23].

Overall, empirical models can be divided into two sub-categories namely, time dispersive and non-time dispersive [24]. Time dispersive models are designed to provide information relating to the multipath delay spread of the channel [25] such as the Stanford University Interim (SUI) channel models, while non-time dispersive empirical models are more concerned with path loss and local clutter parameters such as the COST-231 Hata model [26]. These empirical models require relatively less site specific information when compared to the statistical and deterministic models. However prediction results from the empirical models tend to be less accurate and provide little insight into the underlying propagation modes.

3.2.2 Deterministic Models

Deterministic models are based on fixed geometries and make use of the laws governing electromagnetic wave propagation to determine the received signal power, attenuation and channel response at a particular location. In order to characterize the propagation environment, deterministic models require highly detailed databases of buildings and topographical maps which are sometimes expensive or even impossible to obtain particularly in the scale of millimetres. Higher prediction accuracy can be expected from these models when compared to empirical models. Nonetheless, the algorithms used in the deterministic models are usually very complex. Therefore the implementation of deterministic models is only suitable for small cell areas or indoor environments operating at low frequencies (less than 10 GHz) whereby surface irregularities of any obstacles in the radio path are negligible.

One notable example of deterministic modelling is the ray-tracing technique. This is one of the most popular techniques used for modelling propagation in wireless channels. It assumes that the location and reflection properties of objects propagation are accurately known. Ray-tracing approximates the radio propagation by a finite number of rays originating from the transmitter. Each ray encounters reflection and transmission upon intersection with an obstacle (such as walls, doors, windows, etc.). The propagation pattern of the ray is dictated by the geometry of the floor layout and the materials from which these obstacles are made [27]. Ray-tracing methods offer highly accurate predictions, however they are computationally demanding and inefficient. This inefficiently in fact increases at higher frequencies. The first model,

proposed by McKown [28], was able to trace paths from the receiver locations by taking into consideration site specific geometric databases. Ever since, intensive research has been carried out on numerous aspects of ray-tracing algorithms concerning indoor and outdoor propagations, most of which are based on GO in determining the relative contributions from transmission path losses and multiple reflections from plane surfaces.

3.2.3 Statistical Models

In deterministic models, all environmental influences are implicitly taken into account regardless of whether they can be separately recognized. This reveals the only advantage of these models as they are capable of yielding accurate predictions. However, this comes at the price of implementation complexity which is considerably aggravated at millimetre-wave frequencies in which each scattered ray needs to be traced. In fact the geometrical representation of an outdoor environment in an accurate millimetric scale required by deterministic models is almost impossible.

Statistical models, on the other hand, represent a trade-off between empirical models and the accuracy of numerical solutions obtained by ray-tracing. Stochastic models treat the physical attributes of the medium as a random process with few parameters and distributions generally derived from empirical measurements data, theoretical deductions or both. When compared with deterministic models, the accuracy of statistical predictions maybe slightly less accurate, nonetheless they demand less information about the propagation environment. This favourably aids in reducing the implementation complexities and speeds up the computational processing time of statistical models, particularly for those models designed for built-up urban environments. Conditions of propagation in such areas are the most difficult of all types of terrestrial communication due to the formation of miltiray reflected and scattered fields which lead to significant amplitude and phase variations [29] – [33]. Therefore the process of radiowave propagation in such environments is observed to be best described by statistical models. Examples of these models are widely available in the literature. Most of these however are designed for relatively low (mobile) frequencies. For instance, the authors of [34] have presented a multislit waveguide statistical model that applies for LOS paths of UHF (L-band) propagation along a street with randomly distributed walls and gaps between them. Parameters taken into

account are; street widths, mean distribution of buildings, electrical properties (surface permittivity and conductivity) of the walls, heights and positions of the antennas. More examples can be found in [35] – [39].

3.3 Channel Models

Fading in a general multipath environment may follow different distributions and depends precisely on the area covered by measurements and the presence or absence of a dominant strong component. In the case of LMDS networks, presence of a strong component in the received signal is essential. In such cases, the propagation channel can be characterized using a Rician fading distribution, whereas in the case of non-dominant signals, the channel is most likely to follow a Rayleigh fading distribution. Knowledge of the channel distributions and parameters is crucial for implementation of the propagation models for LMDS systems. These fading models along with the methods used to extract their parameters from measured (or simulated) data are presented in the following sections.

3.3.1 Rician and Rayleigh Channel Fading

The model behind Rician fading is similar to that for Rayleigh fading except that Rician fading includes a strong dominant component, which, for instance, can be either a LOS ray or a cumulative sum of scatter rays reflected in the specular direction. Rayleigh fading used for paths with no dominant signal is derived from the studies provided by Clarke [40]. On the other hand, the Rician distribution proposed by Rice [41] in 1944 is a fading model suitable for representing the small scale fluctuations of the signal envelope in a narrowband channel. In other words, the effect of a dominant signal arriving with many weaker scatter signals that are Rayleigh faded, together give rise to the Rician distribution. As the dominant signal becomes weaker, the composite signal resembles more of a noise signal, which has an envelope that is described by Rayleigh distribution. Thus, the Rician distribution degenerates into a Rayleigh one when the dominant component fades away.

The hidden assumption behind the Rician model is that the numerous individual constituent propagation paths of both the in-phase and quadrature-phase components

of the received signal are correlated by joint Gaussian random variables. The distribution of the sum of a large number of random variables is a normal distribution that can completely be described by its mean and variance. This is known as the Central-Limit-Theorem (CLT) which justifies the use of random variables in many engineering applications [1].

In the case of a Rayleigh fading channel, the in-phase and quadrature-phase components will both have zero-means, whereas in the case of a Rician fading, the mean value of (at least) one component is non-zero due to existence of a strong constant component in the received signal.

3.3.2 Rician & Rayleigh Probability Density Function (PDF)

Let $Z = X + jY$ be a complex random variable with real and imaginary components that are independent. In a polar coordinate representation, the random variables $X = R\cos\theta$ and $Y = R\sin\theta$ have an envelope and phase defined by $R = \sqrt{X^2 + Y^2}$ and $\Theta = \tan^{-1}\left(\frac{Y}{X}\right)$, respectively. While the imaginary component Y has a zero mean (m_q), the real component X, which represents the dominant signal, will have a positive non-zero mean (m_i). It can be shown that for the joint distribution of R and Θ, the Rician PDF can be given by [42]:

$$P_{RICE}(a) = \frac{a}{\sigma^2} e^{-\frac{a^2+s^2}{2\sigma^2}} I_0\left(\frac{as}{\sigma^2}\right) \tag{3.8}$$

where a is the amplitude of the received envelope, σ is the standard deviation of the random variable, and the parameter s^2 is the so called non-centrality parameter computed from the first moment and is given by:

$$s^2 = \sum_{i=1}^{N} (m_i)^2 \tag{3.9}$$

In Eq. (3.8) I_0 is the zeroth order modified Bessel function of first kind. As $s \to 0$, $I_0(0) = \mathrm{I}$ and Eq. (3.8) yields the Rayleigh distribution given by:

$$P_{RAYLEIGH}(a) = \frac{a}{\sigma^2} e^{-\frac{a^2}{2\sigma^2}} \tag{3.10}$$

3.3.3 Rician *K*-Factor

According to [39] [42] [43] and elsewhere in the literature, $s^2/2$ dominates the coherent (LOS path) power whereas σ^2 dominates the incoherent power (indirect paths) of the total received signal. The Rician *K*-factor is physically defined as the signal power ratio of the dominant component over the (local-mean) scattered power, and is simply given in dB by:

$$K = 10\log 10\left(\frac{s^2}{2\sigma^2}\right) \tag{3.11}$$

For short radio paths, knowledge of the Rician *K*-factor can be, among many other useful metrics, useful in determining and analysing the signal strengths, channel capacity and outage probabilities (See Appendix B for an example). It is also important in describing the distribution of the density functions in multipath environments. Therefore the *K*-factor will be considered one of the assessment parameters in analysing results of the measurements conducted and subsequently will be compared to those obtained from predictions using the proposed model given in Chapter 4. Given Eq. (3.8) we can now write a PDF of the Rician distribution as a function of *K*-factor as follows:

$$P_{RICE}(r) = \frac{a}{\sigma^2} e^{-\frac{a^2}{2\sigma^2}} e^{-K} I_0\left(\frac{a}{\sigma}\sqrt{2K}\right) \tag{3.12}$$

3.3.4 Rician *K*-Factor Extraction

As mentioned earlier, the *K*-factor represents the ratio of the received dominant component to the scattered ones. This concept of *K*-factor, first put forth in [44], is very difficult to measure in a physically meaningful manner, i.e. by isolating the direct signal from the scattered components. Extraction from measured or simulated data is not straightforward either. Below is a brief outline taken from the literature of approaches available for extracting the Rician *K*-factor from the measured power time-series data.

3.3.4.1 Method of Moments

Traditional methods of estimating the Rician *K*-factor from the measured received power versus time, such as the Maximum Likelihood method (described below in

Section 3.3.4.4) involve an exhaustive search, and hence are relatively impractical and time consuming. Alternatively, it is possible to obtain the Rician moments from the measured data, and as a result it can then be possible to estimate a locally constant signal s from the given data.

The authors in [45] have presented a significant moment method for estimating the Rician K-factor. The method is simple and rapid, whereby the K-factor is given as an exact function of moments of the time-series data. The method simply applies the definition of K-factor given in Eq. (3.4) which requires the estimation of the Rician parameters s (mean) and σ (variance). These can be calculated from the mean and standard deviation of the measured data by extracting the first two moments of the measured data.

Using the same notation in [43], the first moment is the time averaged amplitude of the measured data, i.e. its theoretical mean value μ_p. The second moment of interest is σ_p, which is the local root-mean-square (RMS) fluctuation of the received signal about μ_p.

The formulations of the first and second moments are given by:

$$\mu_p = \sigma^2 + s^2/2 \tag{3.13}$$

$$\sigma_p^2 = \sigma^4 + s^2\sigma^2 \tag{3.14}$$

By using the above definitions and subsequently by solving for the Rician parameters s and σ, the Rician K-factor (in dB) can be written as:

$$K = 10\log 10\left(\frac{s^2}{2\sigma^2}\right) = 10\log 10\left(\frac{\sqrt{\mu_p^2 - \sigma_p^2}}{\mu_p - \sqrt{\mu_p^2 - \sigma_p^2}}\right) \tag{3.15}$$

This leads to the same derivation given in [47], which also contains the validation of the proposed moment method. A simple example is given in Fig. 3.4 whereby the theoretical Rician distribution given in Eq. (3.12) is plotted using a K-factor value that is extracted from the method of moments, along with the empirical PDF obtained

from measurements. Clearly, the theoretical distribution fits well with the measured data.

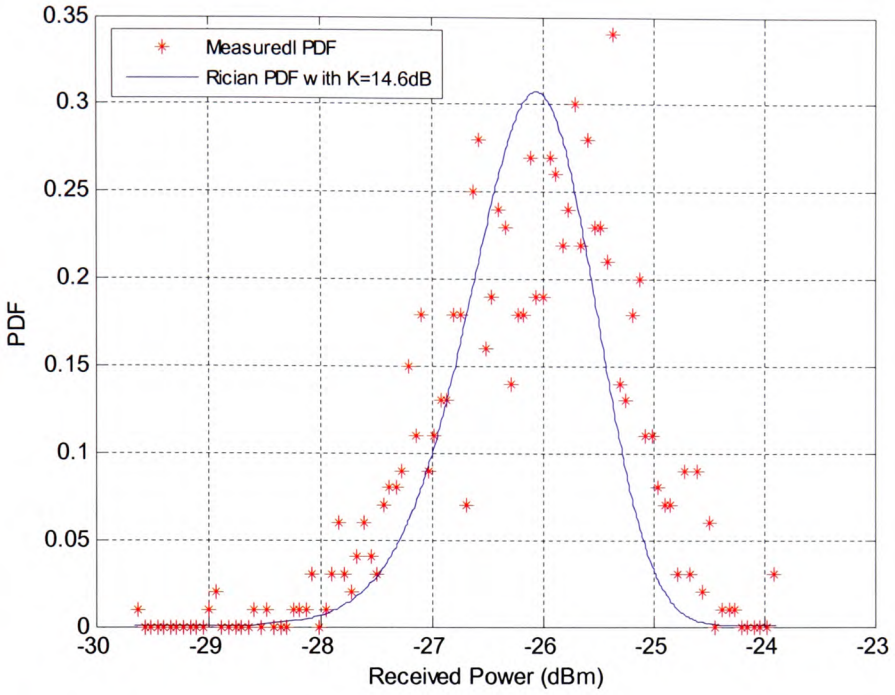

Figure 3.4 Examples of a Rician distribution fitted on a measured PDF using Eq. (3.12)

3.3.4.2 Graphical Moment Method

Another method for extracting the K-factor is given in [46]. This method is very much similar to the moment method described formerly, and is based on the following expression:

$$\frac{\mu_p}{\sigma_p^2} = \sqrt{\frac{\pi}{4K+1}} \exp\left(-\frac{K}{2}\right)\left[(K+1)I_0\left(\frac{K}{2}\right) + KI_1\left(\frac{K}{2}\right)\right] \tag{3.16}$$

which is plotted in Fig. 3.5. Graphically, from the ratio of the 1st moment to the 2nd, the K-factor can then be estimated.

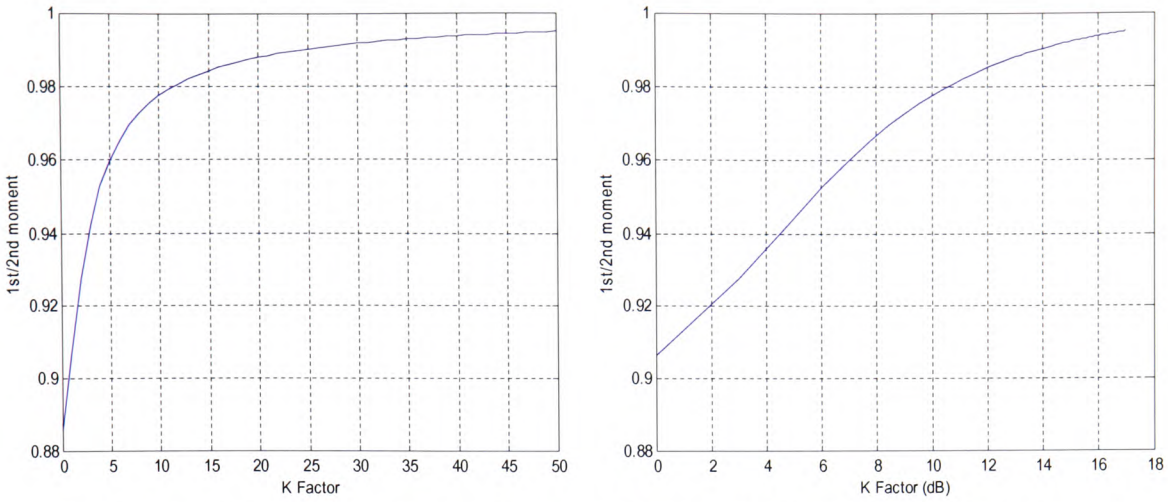

Figure 3.5 Plot of Eq. (3.16) in a linear (left hand side) and logarithmic (right hand side) scale

3.3.4.3 Second and Forth Moment Method

Another moment-based method very similar to the graphical method is proposed by [47]. This attempt aims at providing a closed form expression for extracting the *K*-factor values. The method is developed from the graphical method by the use of the 4th moment of the measured data. The motivation behind this method is finding the exact value for the *K*-factor to solve equation (3.16) as opposed to the estimation of the Graphical method. This solution involves a complex inverse numerical procedure applied to the following formula:

$$f_{2,4}(K) = \frac{(K+1)^2}{K^2 + 4K + 2} \tag{3.17}$$

where $f_{2,4}$ is a function of *K*-factor and is the ratio of the 2nd moment to the 4th moment of the measured data. Clearly, calculating the inverse of the above equation involves finding the roots of a second-order polynomial which can be done in a closed form. The solution is given by:

$$K_{2,4} = \frac{-2\sigma_{p2}^2 + \sigma_{p4} + \sigma_{p2}\sqrt{2\sigma_{p2}^2 - \sigma_{p4}}}{\sigma_{p2}^2 - \sigma_{p4}} \tag{3.18}$$

where σ_{p2} and σ_{p4} are the 2nd moment to the 4th moment of the measured data.

3.3.4.4 Maximum Likelihood Estimation

The authors in [48] have composed an optimum maximum likelihood estimator for the Rician distributed data. The maximum estimator of s is defined as the estimator maximizing L_M or $\log L_{ML}$ as a function of s, where L_{ML} is the joint PDF of a sample of N independent observations. This is called the likelihood function of the measured sample and is given by:

$$L_{ML} = \prod_{i=1}^{N} P_{RICE}(s,a). \tag{3.19}$$

Using Eq. (3.8), the above becomes:

$$\log L_{ML} \approx \sum_{i=1}^{N} \log I_o\left(\frac{as_i}{\sigma^2}\right) - \sum_{i=1}^{N} \frac{s^2}{2\sigma^2} \tag{3.20}$$

The maximum likelihood is the global maximum of $\log L_{ML}$ and is given by:

$$\hat{a}_{ML} = \arg\{\max_s (\log L_{ML})\} \tag{3.21}$$

From the above, finding the optimum value for a is not direct and requires finding the maximum of $\log L_{ML}$ which will be an exhaustive iterative numerical process.

The authors of [47] studied the statistical characteristics of moment-based derivation of the K-factor as a less complex alternative to the maximum likelihood method. Their analysis reveals that both methods are equally efficient, however the maximum likelihood is unsuitable for practical applications due to its complexity. Utilisation of this method is only necessary in certain instances [48] that are outside scope of this thesis.

3.5 Interim Conclusion

One of the main propagation impairments that face propagation of millimetre-wave frequencies is scatter from rough surfaces. The latter dominates the incoherent component of millimetre-wave signals. The use of detailed propagation models that account for the scattering at millimetre-wave signals is vital for realistic field predictions. Most of the millimetre-wave propagation models currently available are extrapolated from measurements and, hence, are empirical and lack applicability in more general and complex propagation scenarios. On the other hand, many elaborate ray-tracing solutions have been around for some time, these incorporate edge and

vertex diffractions, as well as higher order effects, however they are of limited use due to the unavailability and impracticality of obtaining detailed building information. Ray-tracing carried out at millimetre scale resolution is computationally highly complex and demands large memory resources and processing times.

Treating the rough surface scatter as a stochastic process is thus highly preferred on deterministic prediction approaches. This has motivated the research effort in this thesis to pursue a more tractable theoretical treatment of propagation at millimetre wavelengths based on a statistical EM propagation approach, offering higher accuracies and affordable computational complexities.

The received signal at millimetre wavelength frequencies consists of both a dominant and incoherent signals that are best described by Rician and Rayleigh channel fading distributions, respectively. Extraction of Rician parameters, namely the first and second order moments and ultimately, the K-factor can be obtained by numerous methods. Most efficient of these is the method of moments which is widely used in the technical literature. Knowledge of the Rician K-factor is a useful measure in determining performance and signal strengths in Rician fading channels provided there is a sufficient dominant component. Hence it will be used as one of the main assessment parameters in analysing the outcomes of the model predictions and the experimental measurements in Chapter 6.

The next chapter presents the derivations of the proposed stochastic EM model based on the PO approach for the treatment of rough surface scatter. The model also utilizes GIS data for identifying building locations and processing surface details. It is envisaged that such GIS-based prediction models combined with EM field predictions, can play a significant role in the study of LMDS links including system characterization and network planning.

3.6 References

[1] Beckmann P and Spizzichino A., *The Scattering of Electromagnetic Waves from Rough Surfaces*, Artech House, ISBN 0-89006-238-2, 1987.

[2] Ruck G. T., Barrick E. D. and Stuart W. D., *Radar Cross Section Handbook*, Plenum, New York, 1970.

[3] Ulaby F. T., Moore R. K., and Fung A. K., *Microwave Remote Sensing: Active and Passive*, London, U.K.: Addison-Wesley, 1981–83, vol. I–III.

[4] Ament W. S. "Toward a theory of reflection by a rough surface," *Proc. IRE*, vol. 41, no. 1, pp. 142-146, Jan. 1953.

[5] Landron O., Feuerstein M. J., and Rappaport T. S., "A comparison of theoretical and empirical reflection coefficients for typical exterior wall surfaces in a mobile radio environment," *IEEE Trans. Antennas Propagation,* vol. 44, pp. 341–351, Mar. 1996.

[9] Ripoll J, Ntziachristos V, Carminati R, and Nieto-Vesperinas M., "Kirchhoff Approximation for Diffusive Waves", *The American Physical Society*, vol. 64, 2001.

[10] Didascalou D, Dottling, M., Geng, N., and Wiesbeck, W., "An Approach to Include Stochastic Rough Surface Scattering Into Deterministic Ray-Optical Wave Propagation Modeling", *IEEE Transactions On Antennas and Propagation*, Vol. 51, No. 7, July 2003

[11] Sultan-Salem A. K and Tyler G. L, "Validity of the Kirchhoff approximation for electromagnetic wave scattering from fractal surfaces", *IEEE transactions on Geoscience and Remote Sensing,* vol. 42, pp. 1860-1870, 2004. .

[12] Robert J and. Lennon J. F., "Conditions for the Validity of Physical Optics in Rough Surface Scattering", *IEEE Transactions on Antennas and Propagation*, vol. 36, no. 5, May 1988

[13] Keller J. B., "Geometrical Theory of Diffraction", *Journal of Tile Optical Society of America*, vol. 5, num. 2 February, 1962

[14] Thompson D. R., Elfouhaily T. M., and Garrison J. L, "An Improved Geometrical Optics Model for Bistatic GPS Scattering from the Ocean Surface", *IEEE Transactions on Geoscience and Remote Sensing*, vol. 43, no. 12, Dec. 2005

[15] Pongsilamanee P. and Bertoni H. L., "Specular and nonspecular scattering from building facades", *IEEE Trans. Antennas Propag.*, vol. 52, no. 7, pp. 1879-1889, July 2004.

[16] Zhang J., Richter J., Ivrissimtzis L. P., and Al-Nuaimi M. O., "Statistical modeling at 20GHz for fixed wireless access systems in urban multipath environments", IEE Proc.-Microw. Antennas Propag., vol. 152, no. 4, pp. 278-283, Aug. 2002.

[17] Al-Nuaimi M. O. and Ding M. S., "Prediction models and measurements of microwave signals scattered from buildings", *IEEE Trans. Antennas Propag.*, vol. 42, no. 8, pp. 1126-1137, Aug. 1994.

[18] Budiarto H., Horihata K., Haneda K., And Takada J., "Experimental Study of Non-specular Wave Scattering from Building Surface Roughness for the Mobile Propagation Modeling", *IEICE Trans. Commin.*, Vol. E87-B, No.4, April 2004.

[19] Hammoudeh A., Pugliese J.-P., Sanchez M.G., and Grindrod E., "Comparison of reflection mechanisms from smooth and rough surfaces at 62 GHz", *IEE National Conference on Antennas and Propagation*, p. 144 -147, April 1999.

[20] Hammoudeh, A., Garcia Sanchez M., and Grindrod E., "Experimental Analysis of Propagation at 62 GHz in Suburban Mobile Radio Microcells", *IEEE Transactions on Vehicular Technology*, vol. 48, no. 2, March 1999.

[21] Rana D, Webster A. R, and Sylvain M., "Surface Reflection at Low-Angle Propagation", *IEEE Transactions on Antennas and Propagation*, Vol. 43, No. 7, M Y 1995.

[22] Dillard C.L., Gallagher T.M., Bostian C.W., and Sweeney D.G. "Rough Surface Scattering from Exterior Walls at 28 GHz", *IEEE Transactions on Antennas and Propagation*, vol. 52, no. 12, December 2004 3173

[23] Abhayawardhana V. S., Wassell I.J., Crosby, D., Sellars M.P., and Brown M.G. "Comparison of empirical propagation path loss models for fixed wireless access systems", *IEEE 61st Vehicular Technology Conference,* Stockholm, Spring 2005.

[24] Anderson H. R., "Fixed Broadband Wireless System Design", John Wiley, 2003, ISBN 0-470-84438-8

[25] Erceg V., Hari K.V.S., Smith M.S., and Baum D.S, "Channel models for fixed wireless applications," *Tech. Rep., IEEE 802.16 Broadband Wireless Access Working Group*, January 2001.

[26] ITU-R P.1546, "Method for point-to-area predictions for terrestrial services in the frequency range 30 MHz to 3000 MHz," *Tech. Rep., International Telecommunication Union.*

[27] Hassan-Ali M., and Pahlavan K., "A New Statistical Model for Site-Specific Indoor Radio Propagation Prediction Based on Geometric Optics and Geometric Probability", *IEEE Transactions on Wireless Communications*, Vol. 1, No. 1, January 2002

[28] McKown J.W. and Hamilton R.L., "Ray tracing as a design tool for radio networks", *IEEE Network Magazine*, Nov. 1991, pp. 27-30.

[29] Kegami F. I., Yoshida S., and M. Takahar, "Analysis of multipath propagation structure in urban mobile radio environments," *IEEE Trans. Antennas Propagat.*, vol. 20, pp. 531–537, May 1980.

[30] Chan G. K., "Propagation and coverage prediction for cellular radio systems," *IEEE Trans. Veh. Technol.*, vol. 40, pp. 665–670, July 1977.

[31] Rustako A. J., Owens M.J., and Roman R.S., "Radio propagation at microwave frequencies for line-of-sight microcellular mobile and personal communications," *IEEE Trans. Veh. Technol.*, vol. 40, pp. 203–210, Feb. 1991.

[32] Chia S. T. S., "Radiowave propagation and handover criteria for microcells," *British Telecom Tech. J.*, vol. 8, pp. 50–61, Oct. 1990.

[33] Fumio J. and Susumi, J., "Analysis of multipath propagation structure in urban mobile radio environments," *IEEE Trans. Antennas Propagat.*, vol. 28, pp. 531–538, May 1980.

[34] Blaunstein N., "Average field attenuation in the nonregular impedance streed waveguide," *IEEE Trans. Antennas Propagat.*, vol. 64, pp. 1782–1788, Dec. 1998.

[35] Franceschett M., Bruck J., and Schulman L.J., "A Random Walk Model of Wave Propagation", *IEEE Trans. Antennas Propagation*, vol. 52, no. 5, May 2004.

[36] Blaunstein N., Giladi R., and Levin M., "Characteristics' prediction in urban and suburban environments," *IEEE Trans. Veh. Technol.*, vol. 47, pp. 225–234, Jan. 1998.

[37] Mazar R., Bronschtein A., and Lu I. T. , "Theoretical analysis of UHF propagation in a city street modelet as a random multislit waveguide," *IEEE Trans. Antennas Propagat.*, vol. 46, pp. 864–871, June 1998.

[38] Blaunstein N. and Andersen J. B., *Multipath Phenomena in Cellular Networks*. Norwood, MA: Artech house, 2002, ch. 4.

[39] Blaunstein N., Katz D., Censor D., Freedman A., Matityahu I., and Gur-Arie I., "Prediction of loss characteristics in built-up areas with various buildings' overlay profiles," *IEEE Antennas Propagat. Mag.*, vol. 43, pp. 181–191, 2001.

[40] Clarke R. H., "A statistical theory of mobile-radio reception," *Bell System Tech. Journal.*, vol. 47, pp. 957–1000, 1968.

[41] Rice, S. O., "Mathematical Analysis of Random Noise," *Bell System Tech. Journal*, 1944.

[42] Steel R., *Mobile Radio Communications*, Pentech Press, New York, 1992.

[43] Xu, H., Rappaport T.S., Boyle R.J., and Schaffner J.H., "Measurements and Models for 38-GHz Point-to-Multipoint Radiowave Propagation", *IEEE Journal on Selected Areas in Communications*, March 2000.

[44] Norton K.A., Vogler L.E., Mansfield W.V., and Short P.J., "The probability distribution of the amplitude of a constant vector plus a Rayleigh-distributed vector", *Proc. of the IRE*, Oct. 1955, pp. 1354-1361.

[45] Greenstein L. J., Michelson D. G., and Erceg V., "Moment-Method Estimation of the Ricean K-Factor", *IEEE Communications Letters*, vol. 3, no. 6, June 1999.

[46] Purwaha J., Mank A, Matic D, Witrisal K, and Prasad R, "Wide-Band Channel Measurements at 60GHz in Indoor Environments", *Center for Wireless Personal Communications (CEWPC), IRCTR* , The Netherlands.

[47] Abdi, A., Tepedelenlioglu C., Kaveh M., Giannakis G., "On the Estimation of the K Parameter for the Rice Fading Distribution", *IEEE Communications Letters*, vol. 5, no. 3, March 2001

[48] Sijbers J., Dekker A.J., Scheunders P., and Van Dyck, D. "Maximum Likelihood estimation of Rician distribution parameters", *IEEE Transactions on Medical Imaging*, vol. 17, iss. 3, Jun 1998.

CHAPTER FOUR

THE STOCHASTIC ELECTROMAGNETIC MODEL

4.1 Overview

LMDS link design and deployment requires the understanding of the underlying propagation channel and the quantitative description of the fundamental mechanisms that affect the integrity of the link due to attenuation, noise, and interference. Development of analytical and numerical modelling tools enables the rationalization and optimization of system design and its main constraints, by accounting for the impairments introduced by the wireless channel.

Presented in this chapter is a physical statistical model for the electromagnetic propagation channel in fixed wireless links at millimetre-wavelengths. The model, which is suitable for LMDS networks operating within urban or suburban channels, has potential applications in the characterization, design and deployment of the pertinent networks. A specific goal of this model and the thesis in general is the parameterization of the physical attributes of the channel and the associated electromagnetic propagation modes and, ultimately, the representation of the channel in terms of universal probabilistic distribution functions for the LOS received field power and the channel interference. An extensive experimental campaign supported the main postulates of the stochastic representation and provided means to assess the accuracy of the propagation channel parameters obtained by simulations from the statistical model. These validations are presented in the next chapter.

The propagation topography and, in particular, the perimeter of building rooftops and facades, as well as the ground patches illuminated by both the receive and transmit station antenna beams, are modelled using widely available, relatively coarse, digital GIS data and digital images of building facades. The electromagnetic (EM) field and signal power at the receiving station are considered random and calculated employing irregular surface scattering methods, augmented by GO techniques. This is done over different possible realizations of the surface geometry and its architectural features,

namely, the height above or below a mean plane and their inclination with respect to the unit vector perpendicular to the mean surface plane. The scattering from surfaces with random height deviations and, especially, irregular ground sections and corrugated rooftops, is approximated using classic random rough surface scattering methods, with surface statistics obtained from sampling GIS elevation data. The calculations assume realistic transmitting and receiving antenna systems and directive gain patterns. The random nature of the EM fields suggests a presentation in terms of the PDF and their associated first and higher order moments. Of particular interest is the parameterization of the random simulations and their association with universal statistical models, such as the Rayleigh and Rician distributions, i.e., the description of the received field strength and the characterization of the channel in terms of simple parameters. Such parameterization is useful in the classification of the environment and can readily be utilized in network design deployment, since it quantifies in a relatively simple manner the effects of the environmental scatter.

The notation introduced in this section will be used throughout the thesis. Bold-faced characters are used to denote vectors, while the hat above a character signifies a unit vector or one of its Cartesian components; script bold characters correspond to dyadic (double-vector) operator; subscripts R and T refer to the receiver and transmitter, respectively.

4.2 Propagation Geometry

4.2.1 Building scatter geometry

The generic propagation geometry under consideration is illustrated in Fig. 4.1, where the receiving and transmitting antennas, although not necessarily elevated above the highest rooftop, establish a LOS link, i.e. there is always an unobstructed direct field from the transmitter to the receiver. The direct link does not have to coincide with the boresight axes of the two directional antennas. In case of a vegetation obstruction, its effect is accounted for by using the signal attenuation model in [1].

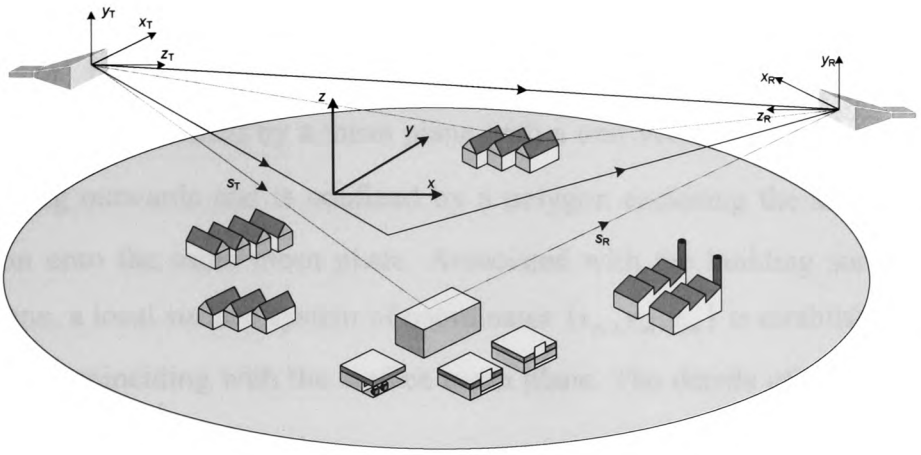

Figure 4.1: Generic urban propagation geometry.

The field radiated by the transmitter antenna in free space and in the direction of the unit vector $\hat{s}_T$ and at a distance s_T from the transmitter is written as

$$\boldsymbol{E}(\hat{\boldsymbol{s}}_T; s_T) = \boldsymbol{e}_T(\hat{\boldsymbol{s}}_T)\frac{e^{-jks_T}}{s_T}, \tag{4.1}$$

where $k = 2\pi/\lambda$ is the wave-number, λ is the wavelength of the operational frequency, and $\boldsymbol{e}_T(\hat{\boldsymbol{s}}_T)$ is a vector pattern function that depends only on the direction of the observation point in the antenna-associated coordinate system. Similarly, the scattered field can be written as

$$\boldsymbol{E}_S(\hat{\boldsymbol{s}}_R; s_R) = \boldsymbol{e}_S(\hat{\boldsymbol{s}}_R)\frac{e^{-jks_R}}{s_R}. \tag{4.2}$$

The scattered field $\boldsymbol{E}_S$ emanating from a scattering source at a distance s_R and direction $\hat{\boldsymbol{s}}_R$ with respect to the receiving antenna position, induces an electromagnetic force (emf) at the receiver terminals proportional to

$$r_S \approx \boldsymbol{e}_S(\hat{\boldsymbol{s}}_R)\cdot\boldsymbol{e}_R(\hat{\boldsymbol{s}}_R)\frac{e^{-jks_R}}{s_R}, \tag{4.3}$$

where $e_R(\hat{s}_R)$ and $e_S(\hat{s}_R)$ correspond to the receiving antenna and scattering vector pattern functions, respectively.

The link area and raw GIS data, augmented by digital images of site specific geometry, are translated and processed to provide polygonal plates, corresponding to building surfaces and ultimately building structures. The propagation environment,

thus, comprises a ground plane and a set of M building surfaces, which can be either rooftops or building facets. In the most general case, a building surface $m, (m = 1,2,...M)$ is defined by a mean plane with a unit vector $\hat{z}_m$ perpendicular to it and pointing outwards and is confined by a polygon enclosing the area Δs_m of the projection onto the same mean plane. Associated with the building surface and its mean plane, a local surface system of coordinates (x_m, y_m, z_m) is established, with the $x_m y_m$-plane coinciding with the surface mean plane. The details of the geometry are highlighted in Fig. 4.2.

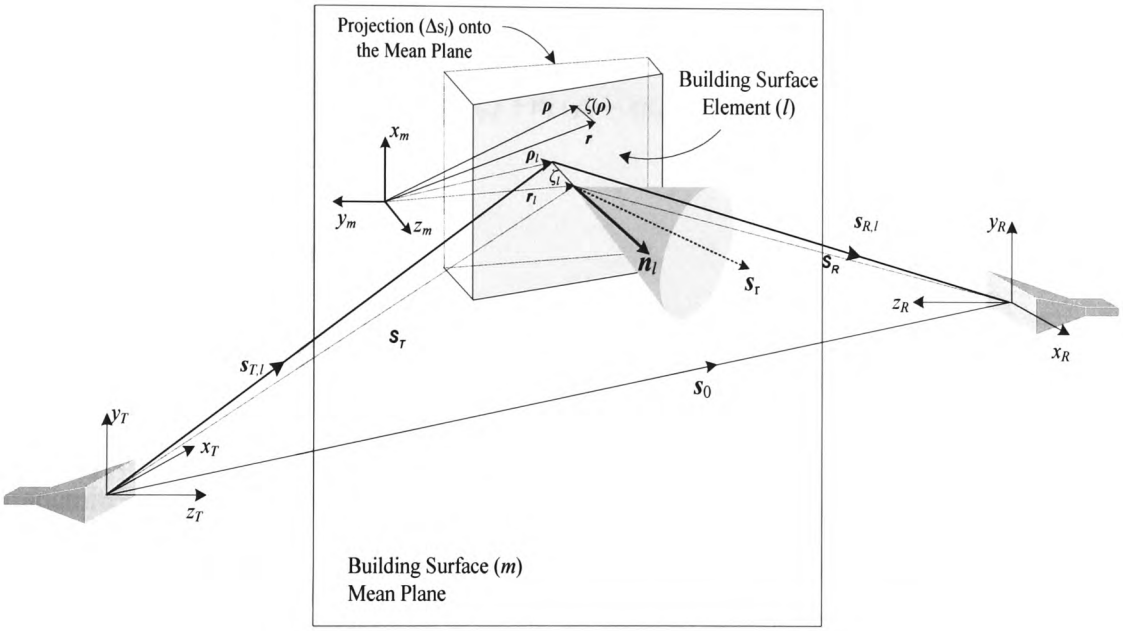

Figure 4.2: Geometry of a rectangular scattering surface.

Each building surface can further be divided into $L(m)$ flat elements of different building materials, such as glass, steel, bricks, etc., with irregularities small or comparable with the wavelength of radiation. The reflectivity properties for a wide range of building materials are available in the technical literature [2]-[7]. Each flat element (l) of a building surface (m) is geometrically characterized by the coordinates (x_l, y_l, ζ_l) of its mid-point

$$\boldsymbol{r}_l = x_l \hat{\boldsymbol{x}}_m + y_l \hat{\boldsymbol{y}}_m + \zeta_l \hat{\boldsymbol{z}}_m = \boldsymbol{\rho}_l + \zeta_l \hat{\boldsymbol{z}}_m \tag{4.4}$$

and a unit vector $\hat{\boldsymbol{n}}_l$ perpendicular to its plane as shown in Fig. 4.2, where $l = 1,2,...L(m)$ and

$$\boldsymbol{\rho}_l = x_l \hat{\boldsymbol{x}}_m + y_l \hat{\boldsymbol{y}}_m . \tag{4.5}$$

Clearly, the plane of the flat surface element is defined by the equation

$$\hat{\boldsymbol{n}}_l \cdot (\boldsymbol{r} - \boldsymbol{r}_l) = 0 \tag{4.6}$$

where $\boldsymbol{r}$ is a point on the surface given by

$$\boldsymbol{r} = x\hat{\boldsymbol{x}}_m + y\hat{\boldsymbol{y}}_m + \zeta(x,y)\hat{\boldsymbol{z}}_m , \tag{4.7}$$

or alternatively from Eq. (4.5)

$$\boldsymbol{r} = \boldsymbol{\rho} + \zeta(x,y)\hat{\boldsymbol{z}}_m \tag{4.8}$$

Hence, by making use of Eq. (4.4), (4.5), (4.7) and (4.8) in Eq. (4.6)

$$x\hat{n}_{x,l} + y\hat{n}_{y,l} + \zeta(x,y)\hat{n}_{z,l} = \hat{\boldsymbol{n}}_l \cdot \boldsymbol{\rho}_l + \hat{n}_{z,l}\zeta_l , \tag{4.9}$$

and

$$\zeta(x,y) = \frac{\hat{\boldsymbol{n}}_l \cdot \boldsymbol{\rho}_l}{\hat{n}_{z,l}} + \zeta_l - x\frac{\hat{n}_{x,l}}{\hat{n}_{z,l}} - y\frac{\hat{n}_{y,l}}{\hat{n}_{z,l}} = \zeta_l + \boldsymbol{n}_l \cdot \boldsymbol{\rho}_l - xn_{x,l} - yn_{y,l} . \tag{4.10}$$

Therefore,

$$\zeta(x,y) = \zeta_l - \boldsymbol{n}_l \cdot (\boldsymbol{\rho} - \boldsymbol{\rho}_l) \tag{4.11}$$

where we substituted

$$\boldsymbol{n}_l = \hat{\boldsymbol{n}}_l / \hat{n}_{z,l} . \tag{4.12}$$

Considering the point $\boldsymbol{r}$ on the surface, with distances at s_T and s_R from the transmitting and receiving antenna, respectively, if $s_{T,l}$ and $s_{R,l}$ are the corresponding distances from the projection of the mid-point on the mean building surface plane and provided that the surface element is in the far field of both antennas, we have

$$s_T + s_R \approx s_{T,l} + s_{R,l} - (\hat{\boldsymbol{s}}_{R,l} - \hat{\boldsymbol{s}}_{T,l}) \cdot (\boldsymbol{r} - \boldsymbol{\rho}_l) . \tag{4.13}$$

By introducing the vector

$$\boldsymbol{u}_l = \hat{\boldsymbol{s}}_{R,l} - \hat{\boldsymbol{s}}_{T,l} , \tag{4.14}$$

Eq. (4.13) becomes

$$s_T + s_R \approx s_{T,l} + s_{R,l} - \boldsymbol{u}_l \cdot (\boldsymbol{r} - \boldsymbol{\rho}_l) , \tag{4.15}$$

whereby, from Eqs. (4.8) and (4.11), it can be shown that

$$\boldsymbol{u}_l \cdot (\boldsymbol{r} - \boldsymbol{\rho}_l) = \boldsymbol{u}_l \cdot (\boldsymbol{\rho} - \boldsymbol{\rho}_l) + u_{z,l}\zeta(x,y) = \boldsymbol{u}_l \cdot (\boldsymbol{\rho} - \boldsymbol{\rho}_l) + u_{z,l}[\zeta_l - \boldsymbol{n}_l \cdot (\boldsymbol{\rho} - \boldsymbol{\rho}_l)]$$

and, therefore,

$$\boldsymbol{u}_l \cdot (\boldsymbol{r} - \boldsymbol{\rho}_l) = (\boldsymbol{u}_l - u_{z,l}\boldsymbol{n}_l) \cdot (\boldsymbol{\rho} - \boldsymbol{\rho}_l) + u_{z,l}\zeta_l . \tag{4.16}$$

Thus, by substituting Eq. (4.16) in (4.15)

$$\boldsymbol{s}_T + \boldsymbol{s}_R \approx \boldsymbol{s}_{T,l} + \boldsymbol{s}_{R,l} - (\boldsymbol{u}_l - \boldsymbol{u}_{z,l}\boldsymbol{n}_l)\cdot(\boldsymbol{\rho} - \boldsymbol{\rho}_l) - \boldsymbol{u}_{z,l}\zeta_l \tag{4.17}$$

With the translation of coordinates $\boldsymbol{\rho} = \boldsymbol{\rho}_l + \boldsymbol{\rho}'$, Eq (4.16) becomes

$$\boldsymbol{u}_l \cdot (\boldsymbol{r} - \boldsymbol{\rho}_l) = (\boldsymbol{u}_l - u_{z,l}\boldsymbol{n}_l)\cdot \boldsymbol{\rho}' + u_{z,l}\zeta_l \tag{4.18}$$

that leads to

$$jk\boldsymbol{u}_l \cdot (\boldsymbol{r} - \boldsymbol{\rho}_l) = j\beta_l[(\boldsymbol{q}_l - \boldsymbol{n}_l)\cdot \boldsymbol{\rho}' + \zeta_l] \tag{4.20}$$

with

$$\beta_l = ku_{z,l} \tag{4.21}$$

and

$$\boldsymbol{q}_l = \boldsymbol{u}_l / u_{z,l}\,. \tag{4.22}$$

Eq. (4. 20) represents the relative phase of the field scattered from surface element (m,l) with respect to the origin of the Cartesian system (x_m, y_m, z_m).

4.2.2 Ground Reflection

The receiving and transmitting antennas are assumed to be elevated by h_T and h_R above the mean ground and are separated by a horizontal distance d_0, as shown in Fig. 4.3.

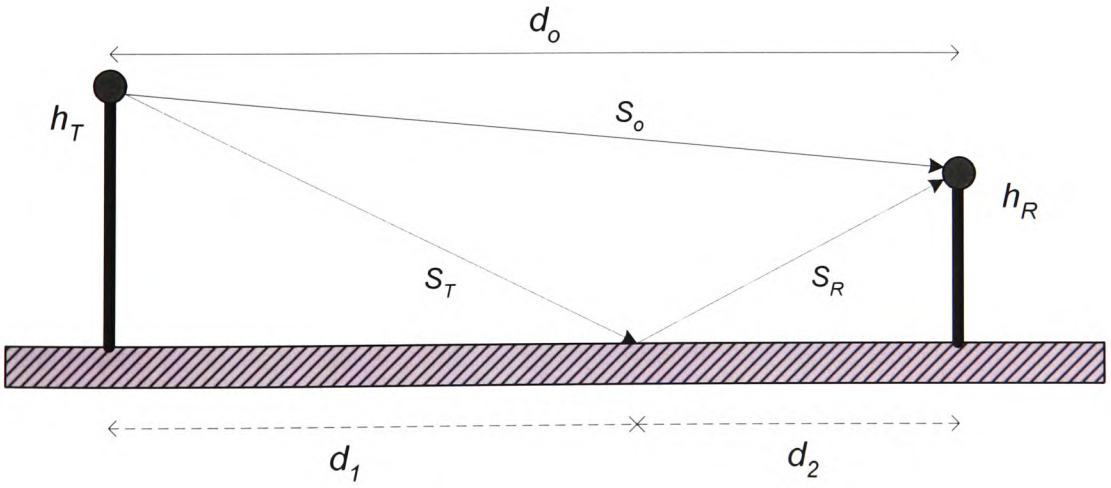

Figure 4.3: Ground reflection geometry.

The objective here is to determine the relative delay and attenuation of the reflected field from the ground with respect to the direct field. The distances of the transmitter and receiver from the reflection point are s_T and s_R respectively. Referring to Fig.

4.3, the following equations can be adopted from the theory of GO from a large ground plane:

$$\frac{d_1}{d_2} = \frac{h_T}{h_R}, \tag{4.23}$$

$$d_1 + d_2 = d_0, \tag{4.24}$$

$$(s_T)^2 = (d_1)^2 + (h_T)^2, \tag{4.25}$$

and

$$(s_R)^2 = (d_2)^2 + (h_R)^2 \tag{4.26}$$

Hence, from the above

$$d_1 = \frac{d_0 h_T}{h_R + h_T}, \tag{4.27}$$

$$d_2 = \frac{d_0 h_R}{h_R + h_T}, \tag{4.28}$$

$$s_T = h_T \sqrt{1 + \left(\frac{d_0}{h_R + h_T}\right)^2} \tag{4.29}$$

and

$$s_R = h_R \sqrt{1 + \left(\frac{d_0}{h_R + h_T}\right)^2}. \tag{4.30}$$

For $d_0 >> h_T + h_R$, the following approximations can be made using Taylor series:

$$s_T \approx d_1 + \frac{d_1}{2}\left(\frac{h_R + h_T}{d_0}\right)^2 \tag{4.31}$$

and

$$s_R \approx d_2 + \frac{d_2}{2}\left(\frac{h_R + h_T}{d_0}\right)^2 \tag{4.32}$$

and hence

$$s_T + s_R \approx d_0 + \frac{d_0}{2}\left(\frac{h_R + h_T}{d_0}\right)^2. \tag{4.33}$$

The distance s_0 between the transmitter and receiver becomes

$$s_0 = d_0 \sqrt{1 + \left(\frac{h_R - h_T}{d_0}\right)^2} \approx d_0 + \frac{d_0}{2}\left(\frac{h_R - h_T}{d_0}\right)^2, \tag{4.34}$$

and therefore

$$s_T + s_R - s_0 \approx \frac{2h_R h_T}{d_0}. \tag{4.35}$$

4.3 Scattering Formulation

4.3.1 Physical Optics Scattering by Building Surfaces

Classical rough surface scattering approaches, such as the one presented in Section 4.3.2, are more suitable for irregular surfaces where the random height of each surface point above the mean plane follows a continuous probabilistic distribution. However, this is not the usual case with building surfaces, since their facets are most likely to have canonical features. This section deals with such surfaces. Although the concept is still based PO and Kirchhoff tangent plane method, the surface irregularities are dealt with in a different manner.

Let us consider the scattering from flat surface element (panel) l of a building surface m. It is worth noting here that the dimensions of each elementary panel (l) are sufficiently small to approximate the size of the most prominent building features, yet much larger than the wavelength of operation. Although the building surface is non-uniformly illuminated by the incident transmitted spherical waveform and the receiver can be within the near-field region of the building, each elementary surface is sufficiently small so that incident wave can be considered locally plane and a far-field scattering approximation can be applied.

For convenience, at the initial stages of the formulation, the building surface index subscript m is omitted. The total field on the surface of this element is approximated by the vector sum of the incident and reflected waves, assuming a semi-infinite interface and locally plane-wave incidence. In particular, assuming plane wave incidence across the length and breadth of each building surface element, the electric and magnetic field incident on the surface can be written in transmitting antenna spherical coordinates as

$$\boldsymbol{E}_i = \boldsymbol{e}_T(\hat{\boldsymbol{s}}_T)\frac{\exp(-jks_T - jk\hat{\boldsymbol{s}}_T \cdot \boldsymbol{r})}{s_T} \tag{4.36}$$

and

$$\boldsymbol{H}_i = \frac{\hat{\boldsymbol{s}}_T \times \boldsymbol{E}_i}{\eta_0}. \tag{4.37}$$

respectively, where η_0 is the impedance of free space.

The incident field is analyzed into components that are perpendicular (h-subscript) and parallel (v-subscript) to the plane of incidence, which is defined by the normal vector $\hat{\boldsymbol{n}}$ to the surface and the direction $\hat{\boldsymbol{s}}_T$ of incidence as in Eqs. (4.38) and (4.39)

$$\boldsymbol{E}_i = E_{i,h}\hat{\boldsymbol{h}} + E_{i,v}\hat{\boldsymbol{v}}_i \tag{4.38}$$

and

$$\boldsymbol{H}_i = H_{i,h}\hat{\boldsymbol{h}} + H_{i,v}\hat{\boldsymbol{v}}_i = \left(E_{i,v}/\eta_0\right)\hat{\boldsymbol{h}} + \left(-E_{i,h}/\eta_0\right)\hat{\boldsymbol{v}}_i. \tag{4.39}$$

In the above equations, the perpendicular and parallel unit vectors are given by

$$\hat{\boldsymbol{h}} = \frac{\hat{\boldsymbol{s}}_T \times \hat{\boldsymbol{n}}}{\left\|\hat{\boldsymbol{s}}_T \times \hat{\boldsymbol{n}}\right\|} \tag{4.40}$$

and

$$\hat{\boldsymbol{v}}_i = \hat{\boldsymbol{h}} \times \hat{\boldsymbol{s}}_T. \tag{4.41}$$

The incident wave is reflected by the surface in the specular direction of observation as shown in Fig. 4.2, i.e. in the direction of the unit vector

$$\hat{\boldsymbol{s}}_r = -\left(\hat{\boldsymbol{s}}_T \cdot \hat{\boldsymbol{n}}\right)\hat{\boldsymbol{n}} + \left(\hat{\boldsymbol{s}}_T \cdot \hat{\boldsymbol{n}} \times \hat{\boldsymbol{h}}\right)\left(\hat{\boldsymbol{n}} \times \hat{\boldsymbol{h}}\right). \tag{4.42}$$

Further, the components of the reflected wave in the $\hat{\boldsymbol{h}}$ (perpendicular to the plane of incidence) and

$$\hat{\boldsymbol{v}}_r = \hat{\boldsymbol{h}} \times \hat{\boldsymbol{s}}_r \tag{4.43}$$

(parallel to the plane of incidence), assuming an infinite plane interface, will be given by

$$E_{r,h} = R_h E_{i,h},\ E_{r,v} = R_v E_{i,v}, \tag{4.44}$$

and

$$H_{r,h} = R_v H_{i,h},\ H_{r,v} = R_h H_{i,v} \tag{4.45}$$

In the above, R_h and R_v are the standard reflection (Fresnel) coefficients from a plane interface of a medium with a complex dielectric permittivity and correspond to polarizations perpendicular and parallel to the plane of incidence. These coefficients (as given previously in Section 3.1.1) are defined as

$$R_h = \frac{\cos\theta_i - \sqrt{\varepsilon_r - \sin^2\theta_i}}{\cos\theta_i + \sqrt{\varepsilon_r - \sin^2\theta_i}}, \tag{4.46}$$

$$R_v = \frac{\varepsilon_r \cos\theta_i - \sqrt{\varepsilon_r - \sin^2\theta_i}}{\varepsilon_r \cos\theta_i + \sqrt{\varepsilon_r - \sin^2\theta_i}}. \tag{4.47}$$

with the incident angle

$$\cos\theta_i = -(\hat{s}_T \cdot \hat{n}), \tag{4.48}$$

and the complex relative dielectric constant of the material (permittivity)

$$\varepsilon_r = \varepsilon_r' - j\varepsilon_r'' = \varepsilon_r' - \frac{j\sigma_e}{\omega\varepsilon_0}. \tag{4.49}$$

In the above equation, ε_r' and ε_r'' are the real and complex parts of ε_r, ε_0 is the vacuum permittivity, σ_e is the electrical conductivity of the material, and ω is the angular frequency of the incident wave. It is noted that for a perfectly conducting surface $\varepsilon_r \to \infty$, $R_h \approx -1$ and $R_v \approx 1$. It should also be noted that although the relative complex permittivity ε_r is defined as a constant, its value depends on the frequency of the incident wave.

If the total electric and magnetic fields at each point $\boldsymbol{r}$ of the surface are $\boldsymbol{E}$ and $\boldsymbol{H}$, respectively, the scattered field $\boldsymbol{E}_S$ from the surface in its far-field region can be described in terms of a Stratton-Chu integral [8]. Accordingly, a double (or surface) integral representation of the scattered field from the surface element (an example can be found in [9]) for an $\exp(j\omega t)$ time-dependence reads

$$\boldsymbol{E}_{S,l} \approx \frac{-jk}{4\pi}\frac{\exp(-jks_{R,l})}{s_{R,l}} \iint_{(\Delta s)_l} \left[\eta_0 \boldsymbol{n}_l \times \boldsymbol{H}_r + \hat{\boldsymbol{s}}_{R,l} \times (\boldsymbol{n} \times \boldsymbol{E}_r) - (\boldsymbol{n}_l \cdot \boldsymbol{E}_r)\hat{\boldsymbol{s}}_{R,l}\right] \cdot \exp(jk\hat{\boldsymbol{s}}_{R,l} \cdot \boldsymbol{r}) \cdot dxdy \tag{4.50}$$

where $\hat{\boldsymbol{s}}_{R,l}$ is the unit vector from the projection of the mid-point of element (l) on the mean plane of the building surface to the receiver, $\boldsymbol{n}_l$ is related to the unit vector $\hat{\boldsymbol{n}}_l$ perpendicular to surface element via $\boldsymbol{n}_l = \hat{\boldsymbol{n}}_l / n_{z,l}$ and $(\boldsymbol{E}_r, \boldsymbol{H}_r)$ are the electric and magnetic field reflected by the plane of the flat element due to a locally plane wave incident from the direction $\hat{\boldsymbol{s}}_{T,l}$, as shown in Fig. 4.2. The double integration in Eq. (4.50) takes place over the projection $(\Delta s)_l$ of the surface element onto the mean building surface plane (x_m, y_m).

In the following, we derive a compact form of the vector integrand in Eq. (4.50). In particular, referring also to Fig. 4.4,

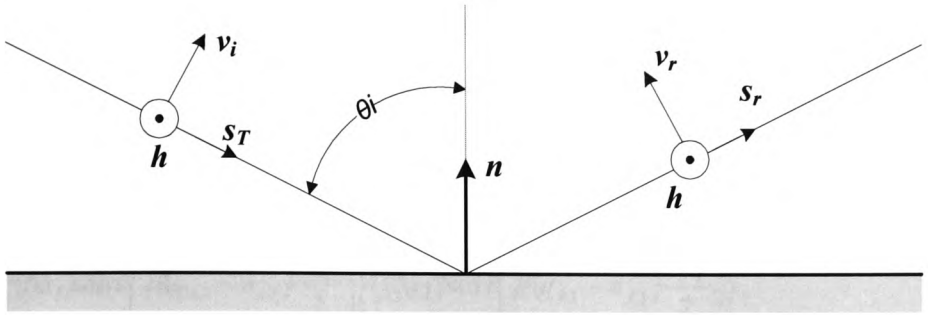

Figure 4.4: Reflection geometry.

$$\eta_0 \boldsymbol{n}\times\boldsymbol{H}_r = \eta_0 \boldsymbol{n}\times\left(H_{r,h}\hat{\boldsymbol{h}} + H_{r,v}\hat{\boldsymbol{v}}_r\right) = \eta_0\left[H_{i,h}R_v \boldsymbol{n}\times\hat{\boldsymbol{h}} + R_h H_{i,v}\cos\theta_i \cdot \hat{\boldsymbol{h}}\right]$$
$$= -E_{i,h}R_h\left(\hat{\boldsymbol{s}}_T\cdot\boldsymbol{n}\right)\hat{\boldsymbol{h}} + E_{i,v}R_v \boldsymbol{n}\times\hat{\boldsymbol{h}}$$

$$\hat{\boldsymbol{s}}_R\times\left(\boldsymbol{n}\times\boldsymbol{E}_r\right) = \hat{\boldsymbol{s}}_R\times\left(\boldsymbol{n}\times\left(E_{r,h}\hat{\boldsymbol{h}} + E_{r,v}\hat{\boldsymbol{v}}_r\right)\right) = \hat{\boldsymbol{s}}_R\times\left(E_{i,h}R_h \boldsymbol{n}\times\hat{\boldsymbol{h}} + R_v E_{i,v}\cos\theta_i\cdot\hat{\boldsymbol{h}}\right)$$
$$= E_{i,h}R_h\hat{\boldsymbol{s}}_R\times\left(\boldsymbol{n}\times\hat{\boldsymbol{h}}\right) + E_{i,v}R_v\left(\hat{\boldsymbol{s}}_T\cdot\boldsymbol{n}\right)\left(\hat{\boldsymbol{s}}_R\times\hat{\boldsymbol{h}}\right)$$

Hence, for building surface element (l), the integrand in Eq. (4.50) becomes

$$\eta_0 \boldsymbol{n}\times\boldsymbol{H}_r + \hat{\boldsymbol{s}}_R\times\left(\boldsymbol{n}\times\boldsymbol{E}_r\right) = -E_{i,h}R_h\left(\hat{\boldsymbol{s}}_T\cdot\boldsymbol{n}\right)\hat{\boldsymbol{h}} + E_{i,v}R_v \boldsymbol{n}\times\hat{\boldsymbol{h}} + E_{i,h}R_h\hat{\boldsymbol{s}}_R\times\left(\boldsymbol{n}\times\hat{\boldsymbol{h}}\right) + E_{i,v}R_v\left(\hat{\boldsymbol{s}}_T\cdot\boldsymbol{n}\right)\left(\hat{\boldsymbol{s}}_R\times\hat{\boldsymbol{h}}\right)$$
$$\eta_0 \boldsymbol{n}\times\boldsymbol{H}_r + \hat{\boldsymbol{s}}_R\times\left(\boldsymbol{n}\times\boldsymbol{E}_r\right) = R_h\left[-\left(\hat{\boldsymbol{s}}_T\cdot\boldsymbol{n}\right)\hat{\boldsymbol{h}} + \hat{\boldsymbol{s}}_R\times\left(\boldsymbol{n}\times\hat{\boldsymbol{h}}\right)\right]E_{i,h} + R_v\left[\boldsymbol{n}\times\hat{\boldsymbol{h}} + \left(\hat{\boldsymbol{s}}_T\cdot\boldsymbol{n}\right)\left(\hat{\boldsymbol{s}}_R\times\hat{\boldsymbol{h}}\right)\right]E_{i,v}$$

and, finally,

$$\eta_0 \boldsymbol{n}\times\boldsymbol{H} + \hat{\boldsymbol{s}}_R\times\left(\boldsymbol{n}\times\boldsymbol{E}\right) = \mathcal{R}_l\cdot\boldsymbol{e}_T\frac{\exp\left(-jks_T - jk\hat{\boldsymbol{s}}_T\cdot\boldsymbol{r}\right)}{s_T} \tag{4.51}$$

with

$$\mathcal{R}_l = \boldsymbol{R}_{h,l}\left[\hat{\boldsymbol{s}}_{R,l}\times\left(\boldsymbol{n}_l\times\hat{\boldsymbol{h}}_l\right) - \left(\hat{\boldsymbol{s}}_T\cdot\boldsymbol{n}_l\right)\hat{\boldsymbol{h}}_l\right]\hat{\boldsymbol{h}}_l + \boldsymbol{R}_{v,l}\left[\boldsymbol{n}_l\times\hat{\boldsymbol{h}}_l + \left(\hat{\boldsymbol{s}}_{T,l}\cdot\boldsymbol{n}_l\right)\left(\hat{\boldsymbol{h}}_l\times\hat{\boldsymbol{s}}_R\right)\right]\hat{\boldsymbol{v}}_{i,l}. \tag{4.52}$$

Hence, from Eqs (4.20) - (4.22) and (4.50) - (4.52), for plane wave incidence and far-field observation, the field scattered by surface element (l) becomes

$$\boldsymbol{E}_{S,l} \approx \frac{-jk}{4\pi}\frac{\exp\left[-jk\left(s_{R,l} + s_{T,l}\right)\right]}{s_{R,l}s_{T,l}}\exp\left(j\beta_l\zeta_l\right)\mathcal{T}_l\cdot\boldsymbol{e}_T\left(\hat{\boldsymbol{s}}_{T,l}\right), \tag{4.53}$$

where the dyadic scattering coefficient $\mathcal{T}_l$ can be written as

$$\mathcal{T}_l = \mathcal{R}_l \iint_{\Delta s_l} \exp\{j\beta_1(\boldsymbol{q}_1 - \boldsymbol{n}_1)\cdot\boldsymbol{\rho}'\}dxdy \tag{4.54}$$

where $\boldsymbol{q}_l$ and $\boldsymbol{n}_l$ are given by Eqs. (4.22) and (4.12) respectively, and $\boldsymbol{\rho}' = \boldsymbol{\rho} - \boldsymbol{\rho}_l$. It is noted that the double integral above can obtain closed form expressions for polygonal plates in terms of the coordinates of their corners.

In particular, for a rectangular projection $(\Delta s)_l = \Delta x_l \Delta y_l$, the above yields the closed form expression

$$\mathcal{T}_l = \mathcal{R}_l \left\{ (\Delta x_l) \sin c\left[\beta(q_{x,l} - n_{x,l}) \frac{\Delta x_l}{2} \right] \right\} \left\{ (\Delta y_l) \sin c\left[\beta(q_{y,l} - n_{y,l}) \frac{\Delta y_l}{2} \right] \right\}, \tag{4.56}$$

where $\sin c(x) = \sin x / x$.

For a triangular projection, we can use Stoke's theorem [11] to reduce the surface integral in Eq. (4.54) to a line integral along the perimeter of the triangle. We define the vector function

$$F = \sum_{L} \exp\{j\beta(q_1 - n_1)\cdot\rho'\} l_{L,1} \tag{4.57}$$

where $\boldsymbol{l}_L$ is a unit vector along triangle edge L, i.e.

$$\boldsymbol{l}_{L,l} = \cos\alpha_{L,1}\,\hat{\boldsymbol{x}} + \sin\alpha_{L,1}\,\hat{\boldsymbol{y}}, \tag{4.58}$$

where $L = 1,2,3$,

and α_L are the angle between the sides of the triangle and $\hat{x}$ -axis in a anti-clockwise direction. The rotation of vector function $\boldsymbol{F}$ is given by

$$\begin{aligned} \nabla \times F &= \begin{vmatrix} \hat{x} & \hat{y} & \hat{z} \\ \frac{\partial}{\partial x} & \frac{\partial}{\partial y} & \frac{\partial}{\partial z} \\ F_x & F_y & 0 \end{vmatrix} = -\hat{x}\frac{\partial F_y}{\partial z} - \hat{y}\frac{\partial F_x}{\partial z} + \hat{z}\left(\frac{\partial F_y}{\partial x} - \frac{\partial F_x}{\partial y} \right) = \\ &= \hat{z}\sum_{L} \left\{ j\beta\left[\sin\alpha_{L,l}(q_{x,l} - n_{l,x}) - \cos\alpha_{L,l}(q_{y,l} - n_{l,y}) \right] \right\} \exp\{j\beta(\boldsymbol{q}_l - \boldsymbol{n}_l)\cdot\boldsymbol{\rho}'\} = \\ &= j\beta \cdot \sum_{L} (\boldsymbol{l}_{L,l} \times \hat{z})\cdot(\boldsymbol{q}_l - \boldsymbol{n}_l) \exp\{j\beta(\boldsymbol{q}_l - \boldsymbol{n}_l)\cdot\boldsymbol{\rho}'\}\hat{z} \end{aligned} \tag{4.59}$$

Application of Stoke's theorem gives

$$\iint_{\Delta s_l} \exp\{j\beta(\boldsymbol{q}-\boldsymbol{n}_l)\cdot\boldsymbol{\rho}'\}\cdot dx'dy' = \sum_L \frac{1}{j\beta\cdot(\boldsymbol{l}_{L,l}\times\hat{\boldsymbol{z}})\cdot(\boldsymbol{q}-\boldsymbol{n}_l)} \int_{l_k} \exp\{j\beta(\boldsymbol{q}-\boldsymbol{n}_l)\cdot\boldsymbol{\rho}'\}\cdot dl' \tag{4.60}$$

By writing

$$\boldsymbol{\rho}' = \boldsymbol{\rho}_L + l\boldsymbol{l}_L, \tag{4.61}$$

in which $\boldsymbol{\rho}_L$ is the vector from the mid-point of the triangle to the mid-point of edge L we obtain

$$\iint_{\Delta s_l} \exp\{j\beta(\boldsymbol{q}-\boldsymbol{n}_l)\cdot\boldsymbol{\rho}'\}\cdot dx'dy' = \sum_L \frac{2\exp\{j\beta(\boldsymbol{q}-\boldsymbol{n}_l)\cdot\boldsymbol{\rho}_L\}}{\beta^2(\boldsymbol{l}_{L,l}\times\hat{\boldsymbol{z}})\cdot(\boldsymbol{q}-\boldsymbol{n}_l)} \frac{\sin\left[\beta\frac{\Delta l_{L,l}}{2}(\boldsymbol{q}-\boldsymbol{n}_l)\cdot\hat{\boldsymbol{l}}_{k,l}\right]}{(\boldsymbol{q}-\boldsymbol{n}_l)\cdot\hat{\boldsymbol{l}}_{L,l}} \tag{4.62}$$

By incorporating Eqs. (4.53) in (4.3), the signal captured from the receiver antenna due to the scattering field $\boldsymbol{E}_{S,l}$, is therefore proportional to

$$r_{S,l} \approx \frac{jk}{4\pi}\frac{\exp[-jk(s_{R,l}+s_{T,l})]}{s_{R,l}s_{T,l}} e_R(\hat{\boldsymbol{s}}_{R,l})\cdot\mathfrak{T}_l\exp(j\beta_l\zeta_l)\cdot e_T(\hat{\boldsymbol{s}}_{R,l}) \tag{4.63}$$

and the total signal at the receiver terminals due to the field scattered by building surface (m) is approximated by

$$r_S(m) \approx \frac{jk}{4\pi}\sum_l \frac{\exp[-jk(s_{R,l}+s_{T,l})]\exp(j\beta_l\zeta_l)}{s_{R,l}s_{T,l}} e_R(\hat{s}_{R,l})\cdot\mathfrak{T}_l\cdot e_T(\hat{s}_{T,l}) \tag{4.64}$$

or

$$r_S(m) \approx \frac{jk}{4\pi}\sum_l \frac{\exp[-jk(s_{R,l}+s_{T,l})]exp(j\beta_l\zeta_l)}{s_{R,l}s_{T,l}} T_l, \tag{4.65}$$

where from Eq. (4.56)

$$T_l = \left\{(\Delta x_l)\sin c\left[\beta(q_{x,l}-n_{x,l})\frac{\Delta x_l}{2}\right]\right\}\left\{(\Delta y_l)\sin c\left[\beta(q_{y,l}-n_{y,l})\frac{\Delta y_l}{2}\right]\right\}U_l \tag{4.66}$$

with

$$U_l = \boldsymbol{e}_R\cdot\boldsymbol{\mathfrak{R}}_l\cdot\boldsymbol{e}_T. \tag{4.67}$$

Assuming $\Delta x_l = \Delta x$ and $\Delta y_l = \Delta y$, the power of the scattered field becomes

$$r_S(r_S)^* \approx \left(\frac{k}{2\pi}\right)^2(\Delta x)(\Delta y)\sum_{l,l'} \frac{\left\{(\Delta x)\mathrm{sinc}^2\left[\beta(q_{x,l}-n_{x,l})\frac{\Delta x}{2}\right]\right\}\left\{(\Delta y)\mathrm{sinc}^2\left[\beta(q_{y,l}-n_{y,l})\frac{\Delta y}{2}\right]\right\}}{\cdot U_l(U_{l'})^*\exp[j\beta(z_l-z_{l'})]\frac{\exp[-jk\cdot(s_{T,l}+s_{R,l}-s_{T,l'}-s_{R,l'})]}{s_{R,l}s_{T,l}s_{T,l'}s_{R,l'}}} \tag{4.68}$$

4.3.2 Scattering by a Rough Surface

For an irregular surface Δs, for which the random height of each surface point above the mean plane follows a continuous distribution, the Kirchhoff approximation [10] to the Stratton-Chu integral can be estimated asymptotically in terms of the large parameter β of Eq. (4.21). At the stationary points, i.e. the points of specular reflection from the surface for which $\hat{\boldsymbol{q}} = \hat{\boldsymbol{n}}$ where $\hat{\boldsymbol{q}} = \hat{\boldsymbol{s}}_R - \hat{\boldsymbol{s}}_T$. Here, a plane wave incidence and far-field observation is assumed. By taking the slowly varying factor outside of the integrand of Eq. (4.50), the random signal at the receiver reads

$$r_S \approx \frac{jk}{4\pi} \frac{\exp[-jk(s_R + s_T)]}{s_R s_T} \boldsymbol{e}_R(\hat{\boldsymbol{s}}_R) \cdot \mathcal{T} \cdot \boldsymbol{e}_T(\hat{\boldsymbol{s}}_T) \tag{4.69}$$

where, as above,

$$\mathcal{T} = \mathcal{R} \iint_{\Delta s} \exp\{j\beta[\zeta(x,y) + \boldsymbol{q} \cdot \boldsymbol{\rho}]\} dxdy$$

and $\mathcal{R}$ is given by Eq. (4.52) by setting $\hat{\boldsymbol{n}}_I = \hat{\boldsymbol{q}}$. We are primarily interested in the second order moment of the received signal, which can be written as

$$E\{r_S r_S^*\} \approx \left(\frac{k}{4\pi s_R s_T}\right)^2 F(\hat{\boldsymbol{s}}_R, \hat{\boldsymbol{s}}_T) E\{J(\hat{\boldsymbol{q}})\} \tag{4.70}$$

with $F(\hat{\boldsymbol{s}}_R, \hat{\boldsymbol{s}}_T) = |\boldsymbol{e}_R \cdot \mathcal{T} \cdot \boldsymbol{e}_T|^2$ (4.71)

and

$$J(\hat{\boldsymbol{q}}) = \iint_{\Delta s} \iint_{\Delta s} \exp\{j\beta[\boldsymbol{q} \cdot (\boldsymbol{\rho} - \boldsymbol{\rho}') + \zeta(\boldsymbol{\rho}) - \zeta(\boldsymbol{\rho}')]\} \cdot dxdydx'dy'. \tag{4.72}$$

Bass and Fuks [8] provide an asymptotic approximation of a double integral of the form of Eq. (4.72) for a homogeneous Gaussian surface with $\beta\sigma_h >> 1$, with σ_h being the standard deviation of the elevation above the rough surface mean plane. Assuming a Gaussian correlation function for the random heights $\zeta(\boldsymbol{\rho}), \zeta(\boldsymbol{\rho}')$ and angles of incidence and observation not close to grazing incidence, it turns out that

$$E\{J(\hat{\boldsymbol{q}})\} \approx \frac{2\pi(\Delta s)}{\beta^2 \chi_x \chi_y} \exp\left\{-\frac{1}{2}\left(\frac{q_x^2}{\chi_x^2} + \frac{q_y^2}{\chi_y^2}\right)\right\}, \tag{4.73}$$

where χ_x and χ_y are standard deviations of the (random) slope angles $\partial\zeta/\partial x$ and $\partial\zeta/\partial y$. Sampling of GIS elevation data yields approximations for the standard deviations of χ_x and χ_y.

4.4 Statistical Formulation of the Propagation Channel

The scattering contribution from the urban propagation environment at the receiver is written as the superposition of randomly distributed scattered components from building surfaces, i.e.

$$r_S = a_S e^{j\phi_S} = \sum_{m=1}^{N} r_{S,(m)} \tag{4.74}$$

where $a_S = |r_S|$, $\phi_S = \arg r_S$ and $r_{S,(m)}$ is given by Eqs. (4.52) - (4.65) or (4.69) - (4.73). The random scattered field power intercepted by the receiving antenna is incoherently superimposed on a deterministic direct field in the direction $\hat{s}_0$ from the transmitter to the receiver location, namely,

$$r_D = \frac{\boldsymbol{e}_T(\hat{s}_0)\cdot\boldsymbol{e}_R(-\hat{s}_0)}{s_0}, \tag{4.75}$$

and that of the field reflected from the ground (in a GO sense), depending on the propagation geometry. The ground reflection component can be determined from

$$\boldsymbol{r}_R = \boldsymbol{e}_T(\hat{s}_T)\cdot\boldsymbol{\mathcal{R}}\cdot\boldsymbol{e}_T(\hat{s}_r)\frac{\exp[-jk(s_T+s_r)]}{s_T+s_r}. \tag{4.76}$$

In summary, in terms of the envelopes of the constituents of the received signal, the total emf at the receiver terminals can be represented by the complex random variable

$$r_T = a\exp(j\varphi) = a_D\exp(j\varphi_D) + a_R\exp(j\varphi_R) + a_S\exp(j\varphi_S), \tag{4.77}$$

in which a_D, a_R, and a_S are the envelope amplitudes of the direct, reflected and scattering components respectively. The envelope of $a_R\exp(j\varphi_R)+a_S\exp(j\varphi_S)$ is Rayleigh distributed, whilst the relative phases are independent random variables uniformly distributed in $(0,2\pi)$.

Given this stochastic nature of the reflected and scattering contributions, the envelope of the total received signal in the presence of a deterministic direct field will have a Rician distribution, i.e.

$$f_a(a)=\frac{a}{\sigma^2}\exp\left(-\frac{a^2+s^2}{2\sigma^2}\right)I_0\left(\frac{as}{\sigma^2}\right), \tag{4.78}$$

where I_0 is the modified Bessel function of the first-kind and zero-order, $a = | r_T |$,

$$2\sigma^2=(a_R)^2+(a_S)^2 \tag{4.79}$$

and the direct field power given by

$$s^2=\left(a^d\right)^2. \tag{4.80}$$

Correspondingly, the distribution of the total received power $p=a^2/2$ is given by

$$f_p(p)=\frac{1}{\sigma^2}\exp\left(-\frac{2p+s^2}{2\sigma^2}\right)\cdot I_0\left(\frac{s\sqrt{2p}}{\sigma^2}\right). \tag{4.81}$$

Introducing the ratio between the direct and indirect (via reflection and scatter) known by the Rician *K*-factor

$$K=s^2/(2\sigma^2), \tag{4.82}$$

where σ^2 corresponds to the scattered field power, the distribution of the total received power for a normalized direct field ($s^2=1$), becomes

$$f_p(p)=2K\exp[-K(2p+1)]\cdot I_0\left(2K\sqrt{2p}\right). \tag{4.83}$$

It readily follows that, given a set of random simulated or measured data; the *K*-factor can be derived from the mean

$$\mu_p=\sigma^2+s^2/2 \tag{4.84}$$

and standard deviation

$$\sigma_p^2=\sigma^4+s^2\sigma^2 \tag{4.85}$$

of received power samples via

$$K=\frac{\sqrt{\mu_p^2-\sigma_p^2}}{\mu_p-\sqrt{\mu_p^2-\sigma_p^2}}. \tag{4.86}$$

The determination of the *K*-factor allows a simple, albeit complete, narrow-band characterization of the flat-fading effects of the wireless propagation channel, including the effects of building and ground scatter on the received signal. Hence, the

characterization of the wireless channel with fixed LOS links reduces to an approximate derivation of average power and the Rician K-factor. The latter is expected to attain high values for short LOS links or high directivity antennas, where the direct boresight field from the transmitter dominates the received signal, nevertheless, it can reduce to small values for longer links or antenna polarization and beam misalignments. It degenerates to a Rayleigh distribution ($K \rightarrow 0$) for severe NLOS reception paths.

Interference studies of the same type of channel assume LOS for both the interfering and desired useful link between the BTS and hub receiver. The envelope in either type of link follow a Rician distribution with differing K-factors, nominally a much higher value for the direct link. It has been shown from [12] that the SIR is distributed according to the following PDF

$$f_z(z) = \frac{2zb}{\left(b+z^2\right)^2} \exp\left(-\frac{K_I z^2 + Kb}{b+z^2}\right) \cdot \left[\left(1+\frac{Kz^2+K_I b}{b+z^2}\right) I_0(c(z)) + c(z) I_1(c(z))\right], \tag{4.87}$$

with

$$c(z) = \frac{\sqrt{4KK_I bz^2}}{b+z^2}, \tag{4.88}$$

where $b = \sigma_0^{\,2} / \sigma_I^2$ is the ratio of the scattered field power of the wanted to that of the interfering link, z is the ratio of the direct field power of the wanted to that of the interfering link, K_0 and K_I denote the K-factor of desired and interfering link respectively. The above equation is referred to as the Oetting's distribution.

4.6 Antenna Modelling

Employment of directive antennas is foreseen in LMDS networks, as pointed out in the previous chapters. One of the most widely used directive antennas is the horn antenna due to its simplicity in construction, ease of excitation, large gain and superior performance over other antenna types [13]. A horn antenna can take many different shapes and forms. Here we consider the pyramidal- and lens-horn antennas which are ones that are flared in both directions as shown in Fig. 4.5. The latter

consists of a circular waveguide horn antenna and a special designed lens that aids in obtaining higher gains, precise beam patterns and inherently low side-lobes.

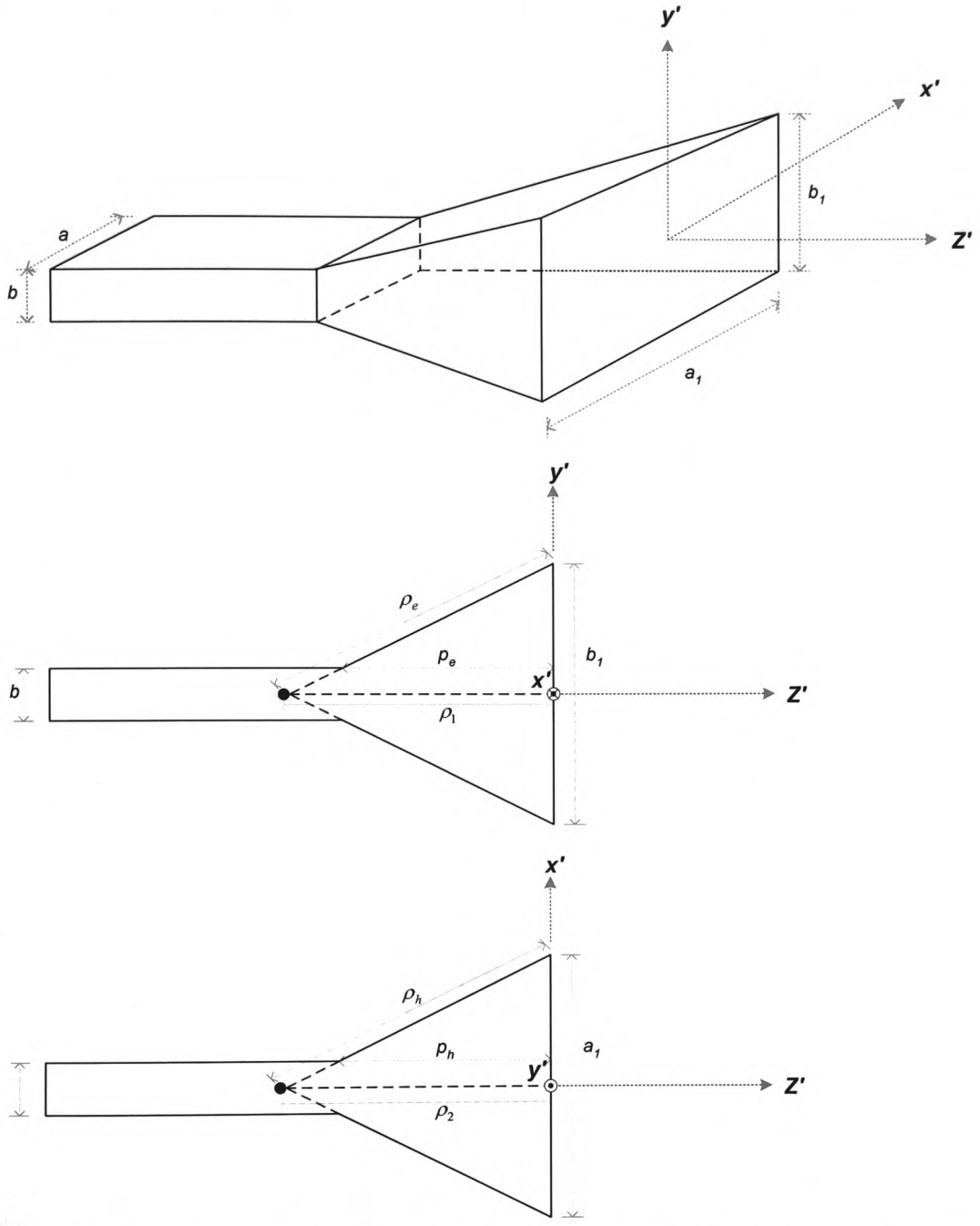

Figure 4.5: Pyramidal horn with the coordinate system in the *E*- and *H*-plane view.

In the model simulations, the horn antenna radiation patterns are described in terms of the following analytical expressions from Balanis' derivations [13],

$$E_{r_a} = 0$$

$$E_{\theta_a} = j\frac{kE_0 e^{-jkr_a}}{4\pi r}\left[\sin\phi(1+\cos\theta)I_1 I_2\right] \tag{4.89}$$

$$E_{\phi_a} = j\frac{kE_0 e^{-jkr_a}}{4\pi r}\left[\cos\phi(1+\cos\theta)I_1 I_2\right]$$

where E_{r_a}, E_{θ_a} and E_{ϕ_a} are the spherical components of the antenna E- field in the far-zone,

$$t_1' = \sqrt{\frac{1}{\pi k\rho_2}}\left(-\frac{ka_1}{2} - k_x'\rho_2\right), \tag{4.90}$$

$$t_2' = \sqrt{\frac{1}{\pi k\rho_2}}\left(\frac{ka_1}{2} - k_x'\rho_2\right), \tag{4.91}$$

$$t_1'' = \sqrt{\frac{1}{\pi k\rho_2}}\left(-\frac{ka_1}{2} - k_x''\rho_2\right), \tag{4.92}$$

$$t_2'' = \sqrt{\frac{1}{\pi k\rho_2}}\left(\frac{ka_1}{2} - k_x''\rho_2\right), \tag{4.93}$$

$$k_x' = k\sin\theta\cos\phi + \frac{\pi}{a_1}, \tag{4.94}$$

$$k_x'' = k\sin\theta\cos\phi - \frac{\pi}{a_1}, \tag{4.95}$$

$$I_1 = \frac{1}{2}\sqrt{\frac{\pi\rho_2}{k}}\left(\begin{array}{l} e^{j\left(k_x'^2\rho_2/2k\right)}\left\{\left[C(t_2') - C(t_1')\right] - j\left[S(t_2') - S(t_1')\right]\right\} \\ + e^{j\left(k_x''^2\rho_2/2k\right)}\left\{\left[C(t_2'') - C(t_1'')\right] - j\left[S(t_2'') - S(t_1'')\right]\right\} \end{array}\right), \tag{4.96}$$

$$I_2 = \sqrt{\frac{\pi\rho_1}{k}}\left(e^{j\left(k_y^2\rho_1/2k\right)}\left\{\left[C(t_2) - C(t_1)\right] - j\left[S(t_2) - S(t_1)\right]\right\}\right), \tag{4.97}$$

and finally $C(x)$ and $S(x)$ are the cosine and sine Fresnel integrals. In the case of lens-horn, the antennas are represented by equivalent circular apertures with field distributions that yield the same gain, beamwidth and first-side-lobe level taken from anechoic chamber measurements.

It's clear from the above that in the far field, only the θ and ϕ components of the E-field dominate, although the radial component is not necessarily zero but negligible [13].

4.5 Interim Conclusion

A stochastic model for the characterization of fixed wireless links operating in millimetre-wave frequencies in urban propagation environments is presented. The model is based on a physical representation of the electromagnetic scatter by irregular surfaces comprising the propagation environment, with large-scale irregularities, augmented with realistic assumptions on the statistical description of the cumulative scattered, ground reflected and direct fields.

The representation of the millimetre-wave channel is based on the PO approach to approximate the building scatter, along with the GO approach with an effective reflection coefficient accounting for the surface roughness at the points of ground reflection. The utilization of PO and GO in the model derivations has succesfully resulted in yielding a stochastic representation of the propagation channel. The model is also based on a GIS representation of the wireless channel topographies and, hence, it is believed to have potential applications in the characterization, design and deployment of point-to-point and point-to-multi-point fixed wireless networks.

Random simulations over different realization of the building surfaces comprising the propagation environment have been carried out and compared with measurements in Chapter 6. The next chapter presents site surveys of the experimental sites selected to validate the outcomes of the proposed model, and the 40 GHz hardware system used during the measurements.

4.6 References

[1] Al-Nuaimi M. O. and Stephens R. B. L., "Measurements and prediction model optimization for signal attenuation in vegetation media at centimeter wave frequencies", *IEE Proc.-Microw. Antennas Propag.*, vol. 145, no. 3, pp. 201-206, June 1998.

[2] Cuiñas I, Pugliese J-P, Hammoudeh A, and Sánchez M.G., "Frequency dependence of dielectric constant of construction materials in the microwave and millimeter wave bands", *Microw. & Opt. Tech. Lett.*, vol. 30, no. 2, pp. 123-124, July 2000.

[3] L. J. Li, Y. Wang, and Gong Ke., "Measurements of building construction materials at Ka band", *Int. J. Infr. & mm-waves*, vol. 19, no. 9, pp. 1293-1298, 1998.

[4] Lahteenmaki J. and Karttaavi, T. "Measurements of dielectric parameters of wall materials at 60 GHz", *Electron. Lett.*, vol. 32, no. 16, Aug. 1996.

[5] Dillard C. L., Gallagher T.M., Bostian C.W., and Sweeney D.G., "Rough surface scattering from exterior walls at 28GHz", *IEEE Trans. Antennas Propag.*, vol. 52, no. 12, pp. 3173-3179, Dec. 2004.

[6] Sato, K, Manabe T., Ihara T., Saito H., Ito S., Tailaka T., Sugai K., Ohmi N., Murakami Y., Shibayama M., Konishi Y., Kimura T, "Measurements of reflection and transmission characteristics of interior structures of office building in the 60 GHz band", *Personal, Indoor and Mobile Radio Communications*, 1996, vol. 1, Oct 1996, Page(s):14 – 18.

[7] Hayn A., Bose R. and Jakoby R., "Mulitpath Propagation and LOS Interference Studies for LMDS Architecture", *11th International Conference on Antennas and Propagation*, April 2001.

[8] Bass F. G. and Fuks I. M., *Wave Scattering From Statistically Rough Surfaces*, Pergamon Press, 1979.

[9] Kong J. A., *Electromagnetic Wave Theory*, EMW Pub., 2000.

[10] Beckmann P. and Spizzichino A., *Scattering of Electromagnetic Waves from Rough Surfaces*, Artech House Publishers, 1987.

[11] Franklin K, Hobson M. P. and Bence S. J, *Mathematical Methods for Physics and Engineering*, Cambridge University Press, 2006.

[12] Oetting J. D., "The effects of fading on antijam performance requirements", *IEEE J. Sel. Areas Comm.*, vol. 5, pp. 155-161, Feb. 1987.

[13] Balanis C. A., *Antenna Theory and Design*, Harper & Row, 1981.

CHAPTER FIVE

EXPERIMENTAL SITES & MEASUREMENTS OVERVIEW

5.1 Introduction

In order to study the effects of building and rooftop scatter on the radio channel of LMDS systems, over 180 sets of measurements were conducted. These measurements took place within the University of Glamorgan Campus (UC) and at a neighbouring Industrial Estate site (IE) for the propose of: (i) acquiring insight into the behaviour of the urban/suburban wireless channel at the frequency of interest, and (ii) to provide validation of the field predications obtained from the stochastic EM model proposed in Chapter 4. It is worth noting that the experimental campaign involved narrow-band measurements only, since it primarily targeted the validation of the principal model assumptions relating to urban scatter and the statistical descriptions of the channel fading effects.

As presented in the previous chapters, scattering is considered to be the most frequently occurring propagation mode influencing LMDS links at the millimetre-wave frequency bands. Scattering is particularly important when the propagation path contains obstacles with surface irregularities that are larger or comparable with the wavelength of the incident radiowave. To provide useful experimental studies of scatter, appropriate measurement sites were selected in urban/suburban propagation environments.

Before going into the details of the measurements setup, it is useful to outline the characteristics of an LMDS cell. The radio channel is typically, a microcell that operates in urban/suburban environment, consisting of a number of buildings. The radio paths are relatively short, with receiving antennas placed either on rooftops or

on side-walls. Signals are transmitted at a relatively low power in order to reduce the undesired effects of scatter and cellular interference. With BTS placed at roof-level heights, street paths tend to act as waveguides and the coverage area is usually governed by the shape of the surrounding buildings.

5.2 Experimental Environments

This section presents a description of the topographical data used, followed by surveys of the experimental sites. All measurement sites were carefully selected to ensure that an obstructed LOS path was achieved for each link with a considerable amount of multipath propagation contributions from the surrounding environment. Measurements were conducted in good dry weather. The sun index was no less than 2 and the wind speed was always less than 10 mph (4.4 m/s) based on weather reports obtained for all measurements.

5.2.1 GIS Data

The increased interest over the last ten years in incorporating GIS data in the design of communication systems reflects the importance of space, spatial concepts and spatial modelling. The GIS data of the environment used is provided by a Digital Elevation Model (DEM) which is essentially a digital terrain model that describes elevations of grounds, trees and buildings [1]. The data are acquired by a Laserscan method. Generally, this method consists of a number of multi-sensors integrated into an airborne platform of a flight surveying at 1600 m above the ground. The measurement frequency reaches 80000 samples per seconds and provides an accuracy of +/- 15 cm vertically and +/- 43 cm horizontally [2]. Currently, this is the best accuracy known to be available commercially in the public domain.

GIS data were purchased and integrated into the EM model proposed, whereby geometries of the environment and the locations of buildings and transceivers are simply defined. Features of the ground and building surfaces, including rooftops and facades, such as surface irregularities and orientations, were obtained by processing the GIS data.

5.2.2 Trefforest Industrial Estate (IE)

A measurement campaign was carried out within an industrial area near to the University of Glamorgan. The purpose for selecting this suburban site was to establish measurements of both, the received signal trend against distances, and some of the interference scenarios from those presented in Section 2.9. The IE site consists of a number of buildings and a long busy road, in which three receiving positions were selected. These positions were almost in a straight line as shown in Fig. 5.1, and were therefore considered ideal for conducting signal trend measurements. The site also consisted of three transmitter positions, one placed on an elevated football field (Tx1) and other two (Tx2 & Tx3) on the sides of the main road as shown in Fig. 5.1.

GIS representation of the site, showing a better (3-D) view of the building structures, their relative heights and the visibility between the hubs, is provided by Fig. 5.2. It is apparent that the GIS Laserscan data is an updated version of the aerial photo of Fig. 5.2, as a number of buildings are missing from the latter. It is worth mentioning that the layers of information provided by the GIS data do differentiate between buildings and trees, which are reasonably represented within the given data accuracy.

For the signal trend measurements, radio links were established between Tx1 and all the other receiving positions, namely, Rx2, Rx1 and Rx0 shown in Fig. 5.1. Due to cars parked on the sides of the road along the Tx1-Rx0 path, it was not possible to attain exactly equal separation distances between the receivers during the measurements at anytime of the day. Instead, the received signal power was measured at the following distances from Tx1: 188 m (Rx2), 346 m (Rx1) and 627 m (Rx0). Along the Tx1-Rx0 path, there are a number of industrial buildings that are widely diverse both in their shapes and footprints. At the time of the measurements, considerable amount of vegetation existed in the vicinity of the Tx1 position and along its route to Rx0 as shown in the photos of Fig 5.3. In part (a) of the latter figure, the transmitter was placed on elevated grounds with its antenna facing into the direction of the photo such that it overlooked the route to Rx0, as shown in part (b).

The two other transmitter positions considered, namely, Tx2 & Tx3 were considered for the purpose of evaluating channel interferences from different transmitters

associated with the LMDS cellular frequency-reuse plans. These transmitters, as shown in Fig. 5.2, established short radio routes that were linked with the receiver position of Rx0 only. In both of these links, apart from a few nearby parked vehicles found during the measurements, these paths were almost clear of any obstacles. In the context of the interference scenarios, Tx1 and Tx3 were always referred to as the interference sources, whilst Tx2 was referred as the desired source. Moreover, combinations of the three transmitter positions and their individual radio links with Rx0 were used to establish the co- and adjacent-channel interference scenarios of the SOP and AP frequency-reuse plans, respectively.

Furthermore, path profiles, which are essential elements in site surveys, were obtained prior to any measurements, since they provide plots of elevations vs. distance along the path between the transmitter and the receiver. Accordingly, the direct field could be maximised by ensuring that the selected measurement path between the transmitter and receiver is as clear as possible of any obstacles. Such plots, in addition to the LOS visibility, show several other important characteristics about the link in question such as, obstacles and antenna heights, antenna clearances and earth curvature.

In all measurements conducted on this site, the transmitters and receivers, as shown in the path profile of Fig. 5.4, were elevated by 6.3 m and 4 m from the ground level respectively, apart from Tx1 which was on high grounds giving a total elevation of 14 m. Clearly, its link with all the receivers was almost clear of any obstacles. For the path profiles of Tx2-Rx0 and Tx3-Rx0, the transmitting and receiver hubs are not shown in the figure simply because their heights were outside the height range of obstacles between the hubs, which is less than 2 m. These obstacles are believed to be either trees, lamp- or sign-posts. It is worth noting here that all the elevation heights given in the link profiles are with respect to the sea-level.

Figure 5.1* Top aerial view of the IE link showing location of the transmitters and receivers.
* Photo taken from Google Earth™

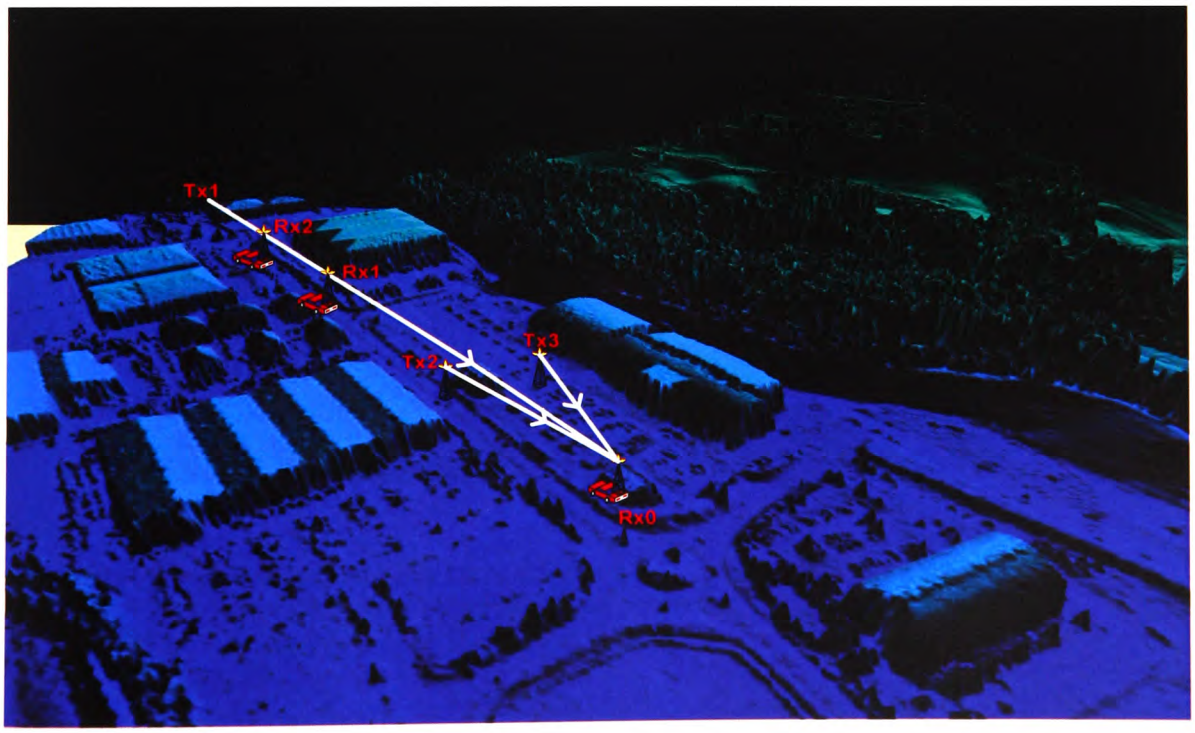

Figure 5.2 3D view obtained from the GIS data for the IE measurement site.

(a)

(b)

Figure 5.3 Photos of the Industrial link between Tx and Rx0: (a) Tx1's position facing towards inside of the photo, (b) Position of Rx0 and its route from Tx1.

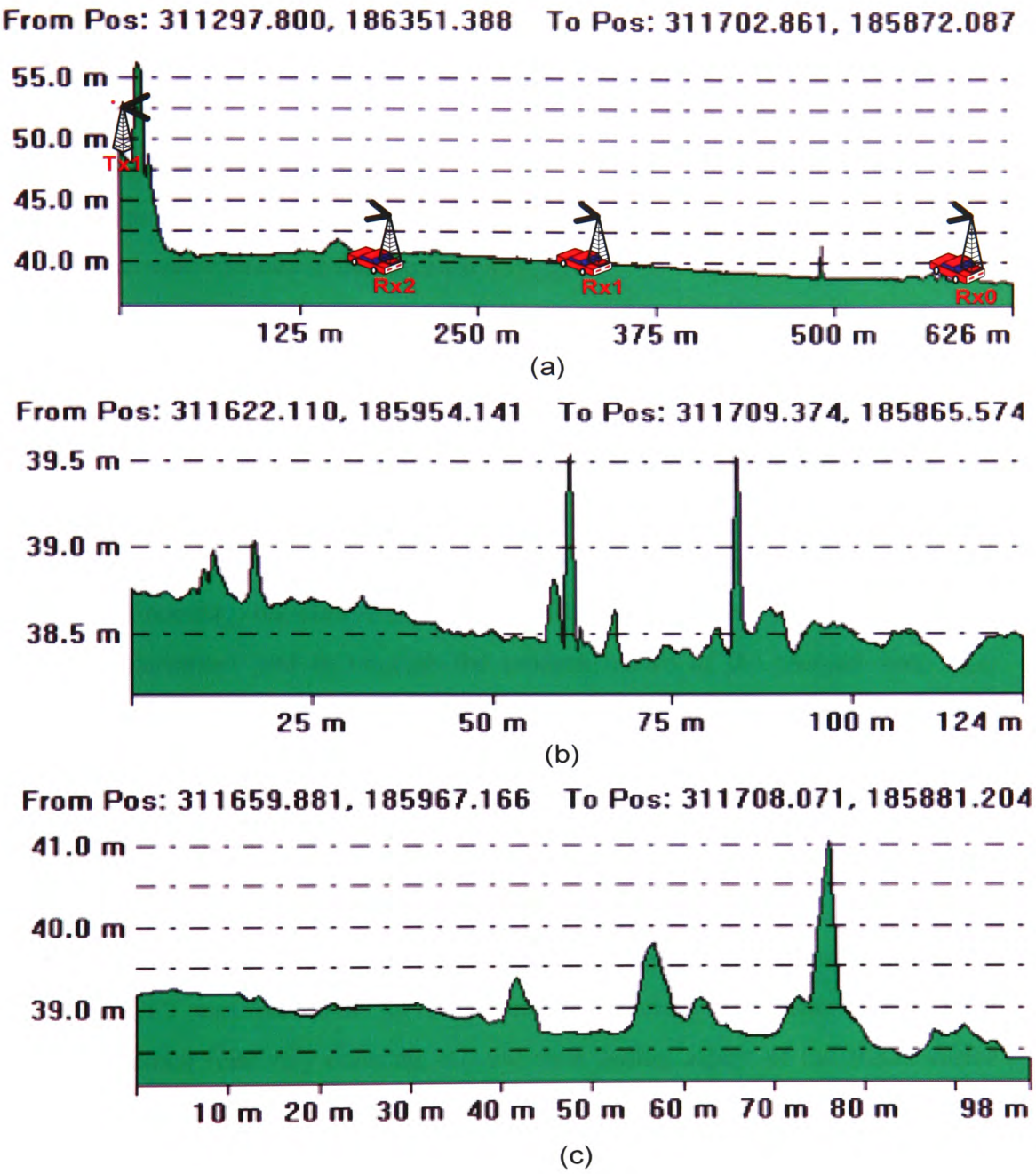

Figure 5.4 IE link path profiles for: (a) the path route along Tx1-Rx0 (A), (b) Tx2-Rx0 link, and (c) Tx3-Rx0 link.

In most cases and wherever possible, measurements (and the corresponding simulations) conducted at each position on this site consisted of the following:

- Employment of five different gain pyramidal-horn or lens-horn antennas (10, 15, 20, 29, & 44 dBi) at the receiving terminal, whilst at the transmitter side a 20 dBi horn antenna was always used due to its moderate beamwidth. These antennas and their specific gains, which are described in Section 5.3.3, are in fact recommended in the literature [3]-[5].

- Measurements of co- and cross-polar links, i.e. vertical to vertical, vertical to horizontal, horizontal to horizontal, and horizontal to vertical radio links.

- Two procedures to capture the received signal power: in the first, the receiver position was totally fixed, whilst in the second, the receiver was displaced continuously, but slowly and only by a few wavelengths. The purpose of this displacement was to emulate the random nature of the channel and, most importantly, towards establishing a spatial mean of different receiving positions. A stepper-motor, as shown in Fig. 5.10, was used to establish the receiver movement. The motor speed and rotation direction were controlled by a computer.

- In most cases, the received power for each measurement run at both sites (IE & UC) was recorded for 800 samples, whereby the mean power level remained relatively constant and the slow fading aspect of the signal varied gradually around its mean level. Examples of plots for the normalised received power versus the samples taken, referred to as the *time series data* plots, are shown in Fig. 5.5. These data were processed, according to the derivations in Section 4.4, to extract the probabilistic distributions and their associated parameters.

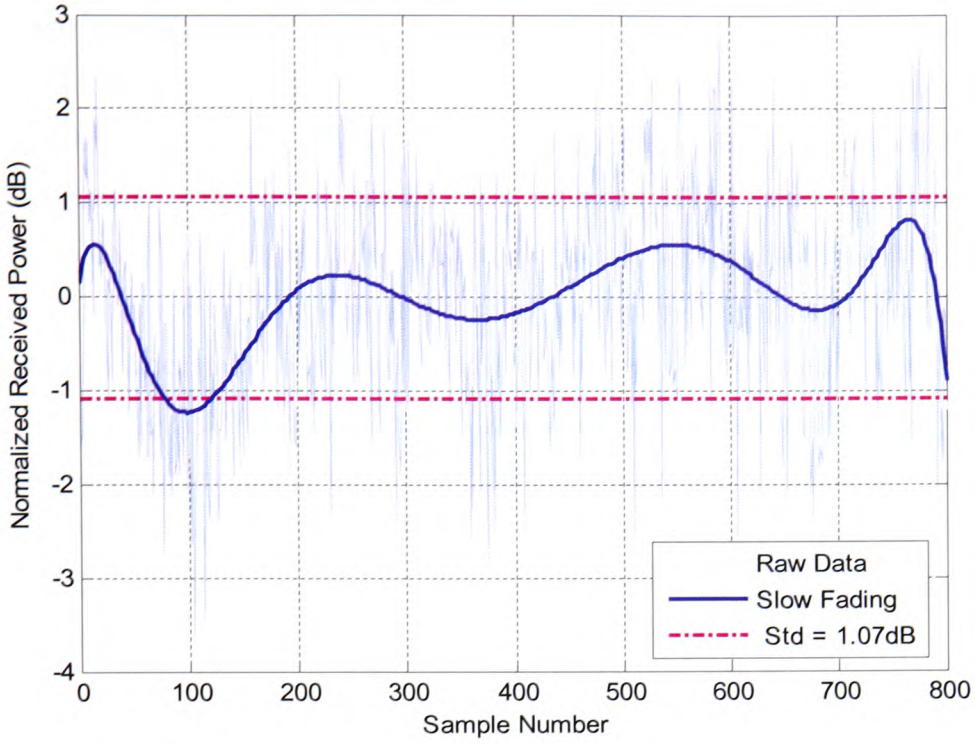

(a)

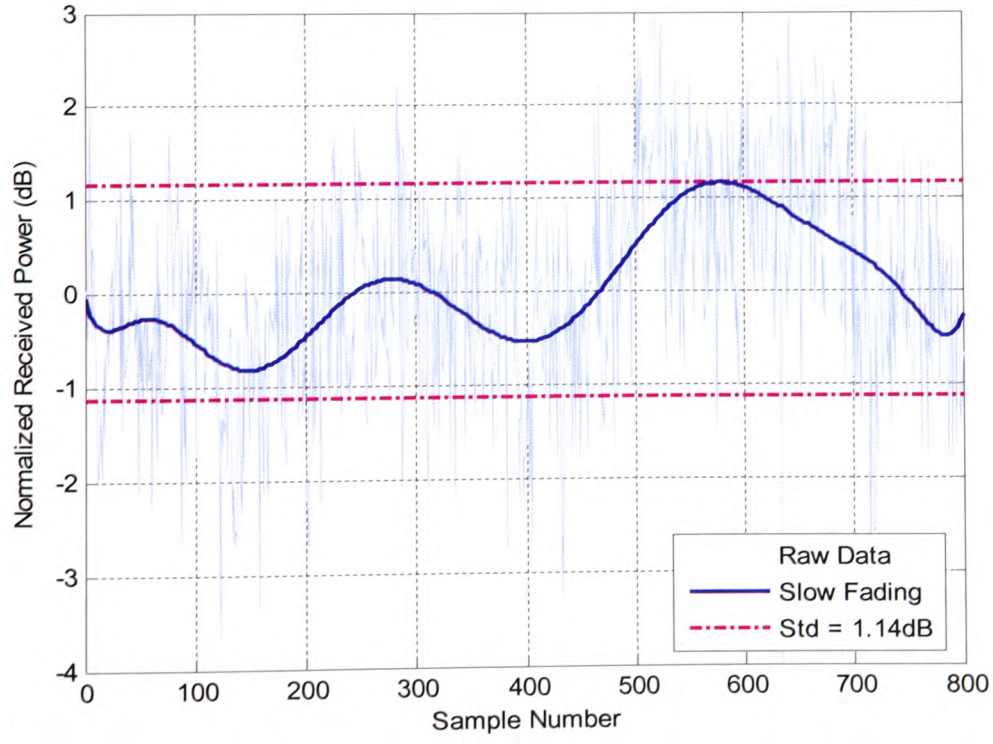

(b)

Figure 5.5 Examples of time series data showing the fast- and slow-fading aspects of the received power: (a) for fixed position of the receiver (b) for a receiver displaced within a couple of wavelengths along the link.

Given the fact that transmitter Tx1 was elevated well above the buildings in the radio link to Rx0, one of the main reasons for selecting the IE site was to include the effects of slant and horizontal surfaces that are expected to contribute towards the received signal levels. The inclusion of these surfaces in the model depended on whether they were illuminated by the transmit and receive antennas. While vertical surfaces are not expected to have a significant role here, their effects have been taken exclusively into consideration in the UC site described in the next section. The considered slant and horizontal surfaces here included building rooftops, facades and ground patches totalling up to 42 different surfaces. These surfaces are indexed in Fig. 5.6 and described correspondingly in Table 5.1. The latter tabulates the statistical parameters that characterize these surfaces, which are obtained from processing the GIS data information for each surface and its subsequent elements according to the derivations of the proposed EM model requirements described in Chapter 4.

The statistical parameters in Table 5.1 are defined as follows:

(i) number of triangular or rectangular elements in which each surface was divided into during the EM simulations;

(ii) standard deviations of the elevations and slopes in the x- and y-directions for each surface element denoted by σ_x, σ_y and χ_x, χ_y respectively;

(iii) surface material type which determines the value of the complex reflection coefficient. A list of these reflection coefficients collected from the published literature is provided in Appendix C.

The surface parameters, together with the antenna locations and their parameters, namely, the radiation patterns and gains that are determined by the antenna physical dimensions (see Table 5.4); are the main input parameters required by the EM propagation model. A flowchart of the model describing the process involved can be found in Appendix A.

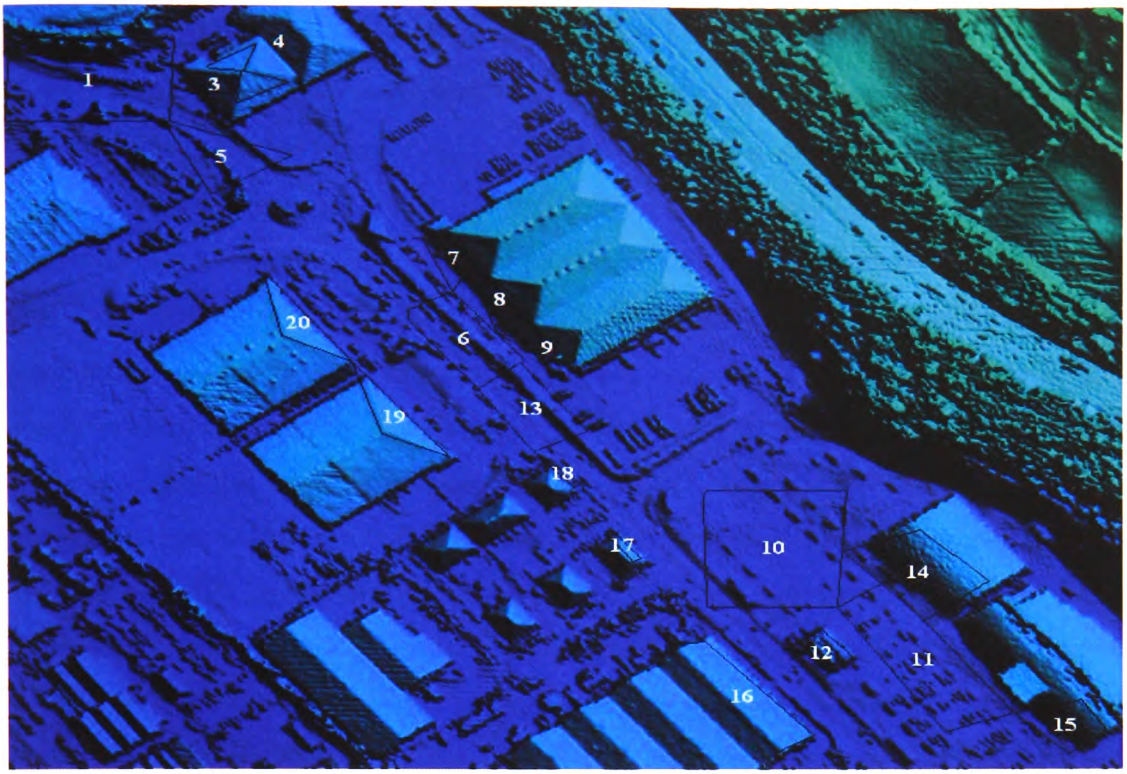

Figure 5.6 Index of the surfaces (including rooftops, facets, and ground patches) considered in the IE site. These indexes correspond to Table 5.1.

Index	Description	Num. of Elements	σ_x (m)	σ_y (m)	χ_x	χ_y	Material
1	Ground Patch 1	2	3.3	3.2	4.1	1.3	Asphalt
2	Building Rooftop 1	2	0.9	0.9	0.7	0.6	Slate
3	Building Rooftop 2	1	0.9	0.9	0.7	0.6	Slate
4	Building Rooftop 3	2	0.9	0.9	0.7	0.6	Slate
5	Ground Patch 2	2	0.7	0.5	0.7	0.3	Asphalt
6	Ground Patch 3	2	0.7	0.5	0.7	0.3	Asphalt
7	Building Face 1	2	2.6	1.4	0.7	0.5	Concrete
8	Building Face 2	2	2.6	1.4	0.7	0.5	Concrete
9	Building Face 3	2	2.6	1.4	0.7	0.5	Concrete
10	Ground Patch 4	2	0.3	0.4	0.4	0.2	Asphalt
11	Ground Patch 5	2	1.4	0.6	1.2	0.4	Asphalt
12	Restaurant Rooftop	2	0.9	0.9	0.7	0.6	Slate
13	Ground Patch 6	6	0.3	0.4	0.4	0.2	Asphalt
14	Building Face 4	2	0.4	0.3	0.3	0.2	Plaster Board
15	Building Face 5	2	0.4	0.3	0.3	0.2	Plaster Board
16	Building Rooftop 4	4	0.4	0.3	0.3	0.2	Slate
17	Building Rooftop 5	2	0.9	0.9	0.7	0.6	Clay
18	Building Rooftop 6	2	0.9	0.9	0.7	0.6	Clay
19	Building Rooftop 7	1	0.4	0.3	0.3	0.2	Slate
20	Building Rooftop 8	1	0.4	0.3	0.3	0.2	Slate

Table 5.1 Surface descriptions and their parameters as obtained from processing the GIS data.

5.2.3 University of Glamorgan Campus (UC)

Further measurements were conducted on a number of sites at the UC. Most of these, however, were carried out during the preliminary stages of exploration of both the proposed propagation model and the millimetre-wave channel behaviour. One of the sites was eventually considered for its numerous reflection and scatter paths deemed ideal for examining the EM model prediction capability in such rich multipath environments. This selected site is shown in Fig. 5.7. The transmitting and receiving antennas were deliberately placed below building rooftop heights, since the aim here is focused on the study of scatter from canonical features of buildings facades. Moreover, one of the criteria for selecting this particular site was connected with acquiring a better knowledge on the behaviour of NLOS path links, particularly those that benefit from strong reflections. The investigation of such links at millimetre wavelengths is considered useful for evaluation purposes and link establishment using reflections. Quantifying the effects of NLOS links is also useful in deployment considerations, where reflected cells may act as interference sources to the adjacent cells.

The radio links established here are rather short when compared to those considered in the IE site. The dimensions of these links are shown in the site's aerial photo of Fig. 5.7. The environment can be characterized as an urban centre consisting of a number of semi-aligned buildings. A NLOS radio path was realized by illuminating building A, a five storey building, producing the reflected rays shown in the same figure. These rays were captured by rotating the receiver in the azimuth plane ($\phi = 0 \rightarrow 360^0$). Discussion and analysis of these are given in Chapter 6, where it will also be shown that even though the main-lobe of the transmitter was not facing the receiver, a direct link did exist between the two hubs due to the side-lobe peaks of the transmit antenna.

3-D GIS representations of the site along with the photos taken during the measurements are given in Figs. 5.8 & 5.9 respectively. These figures show the building structures and their relative heights, as well as the descending ground levels of the environment. In particular, Fig 5.9 (a) shows the transmitter position and also building A which was utilized for the main reflection path; Fig. 5.9 (b) shows buildings B & C and the receiver's position; Fig. 5.9 (c) shows a clearer view of the

receiver and building C; finally part (d) shows building B from the receiver's position where its canonical features are clearly noticeable.

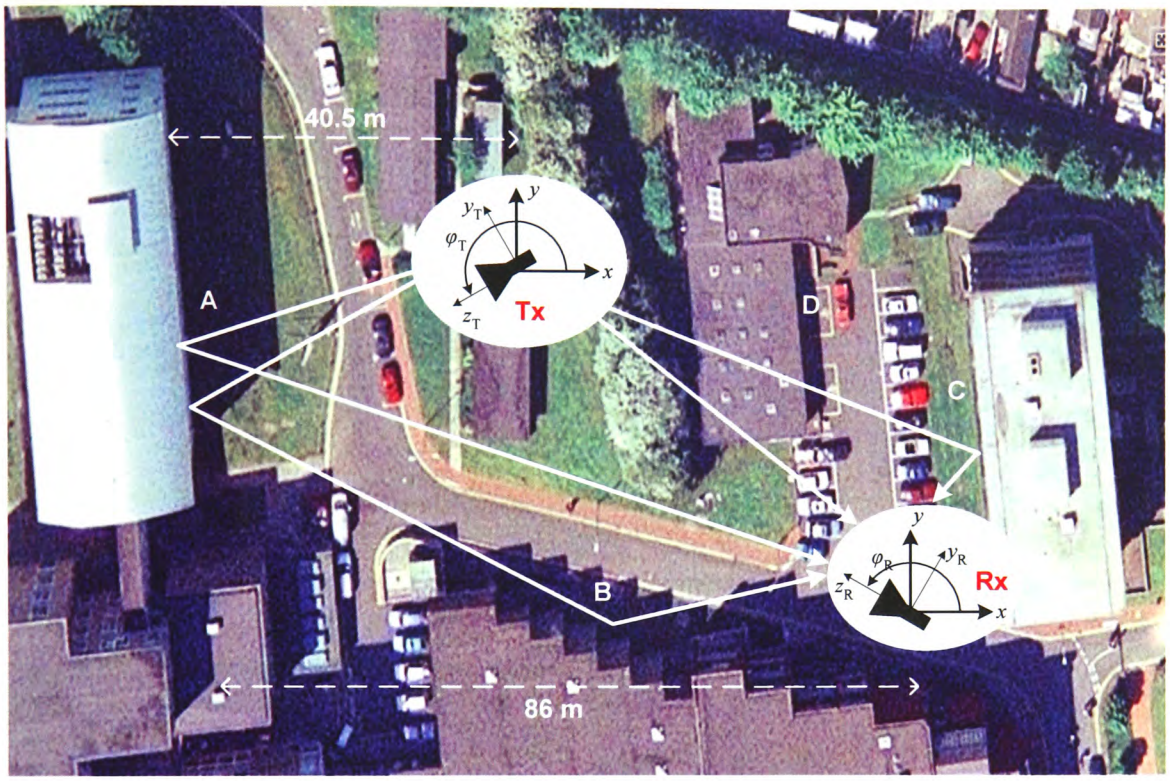

Figure 5.7* Campus site top view and measured link, with main building reflection contributions.
* Photo taken from Google Earth™

The differences in the measurement setup and procedures compared to those considered at the IE site include the following:

- Heights of the transmitter and receiver antennas were below buildings rooftops and approximately set to 10.5 m and 6.5 m respectively.

- Employment of four different horn gain antennas (10, 15, 20 and 29 dBi) at the receiving terminal, whilst at the transmitter side, a 10 dBi gain antenna with a relatively broad beamwidth was selected in order to illuminate as much as possible of the urban cell.

- Measurements were for co-polarized vertical radio links only.

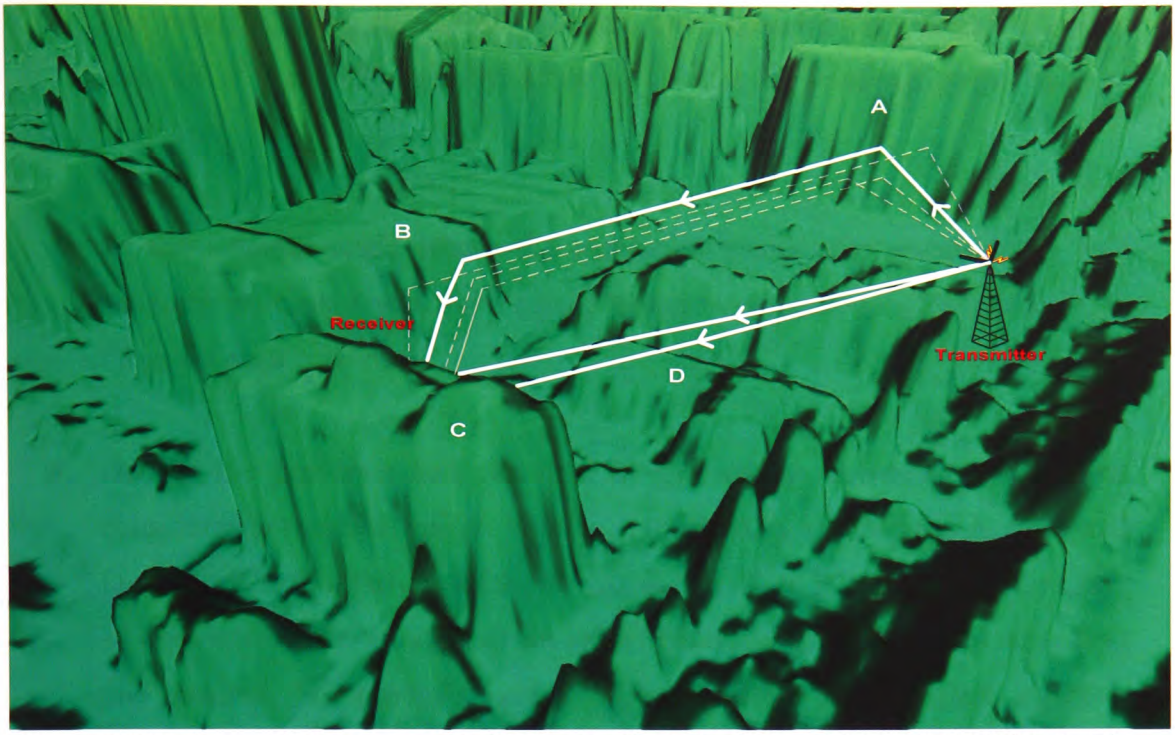

Figure 5.8 3D views of UC measurement site, showing the transmitter position facing building A and its reflected paths to the receiver.

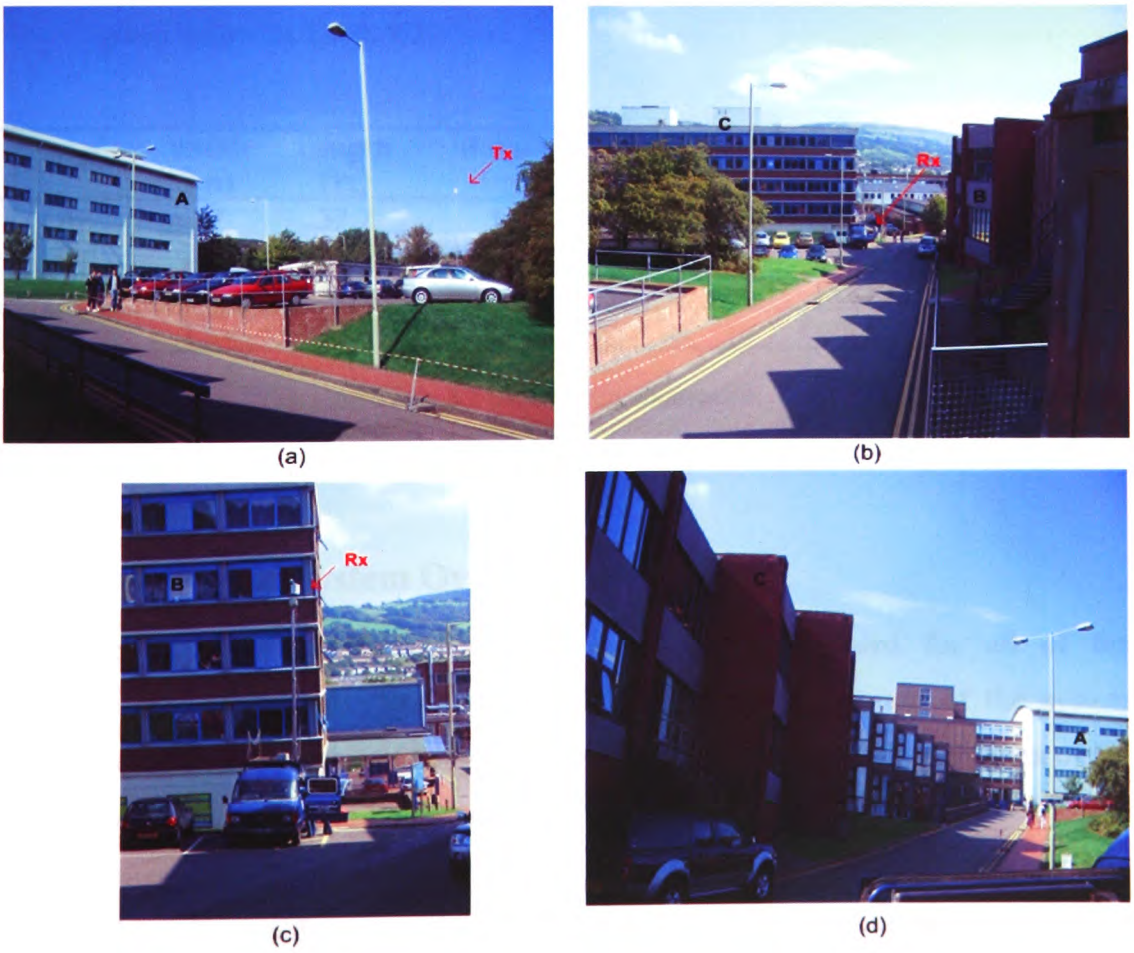

Figure 5.9 Photos of the UC link showing: (a) transmitter's position and building A, (b) receiver's position and buildings B & C, (c) a zoomed in view of photo (b), and (d) conical features of building C.

- The receiver, using the 29 dBi antenna only, scanned the azimuth plane in steps of 2^0 with 100 samples taken to capture the received power at each position.

- At the azimuth angle where the maximum power was received, all four antennas were used and the received power was recorded with 800 samples taken for each antenna.

- Due to the positions and elevation heights of the antennas, the surfaces considered are vertical surfaces only, i.e. the facades of buildings A, B, C, and D of Fig. 5.7. Similarly as in the IE site, each surface is divided into a number of elements. However, surface elements here were categorized into more than one material. For example, surface elements which contain glass windows might cover a significant percentage of the façade surface and hence are taken statistically into consideration. A description of the buildings considered is given below in Table 5.2.

Building	Width (m)	Length (m)	Height (m)	Num. of Elements	Material 1	Material 2
A	17	37.7	16	120	Plasterboard	Glass
B	25.1	74.6	7.4	96	Bricks	Glass
C	15.3	35.4	9.2	84	Bricks	Glass
D	13.2	34.8	2.9	14	Concrete	Glass

Table 5.2 UC building information.

5.3 Measurement System Overview

This section describes the narrowband 40 GHz system used for all of the measurements conducted. Fig. 5.10 below shows a block diagram of the system developed at the University of Glamorgan by previous researchers. Major parts of the transmitter circuitry had to be rebuilt due to a breakdown incident, during one of the outdoor measurement sessions. Additionally, some of the unnecessary waveguide sections have been either removed or restructured in a more efficient manner in an attempt to minimize any signal losses in the system.

The transmitter and receiver each have a power-up sequence procedure driven by a built-in precision supply circuitry, whereby the main 12 V_{DC} power supply is regulated to different levels according to the requirements of components and recommendations provided by the manufacturer. In all measurements, a lead-acid battery was used to power-up the transmitter. The receiver on the other side, together with all its accompanied equipment, namely, laptop, spectrum analyser, DC power supplies, function generator, mast elevator and stepper motor displacer mechanism, all were powered up using a suitable power generator.

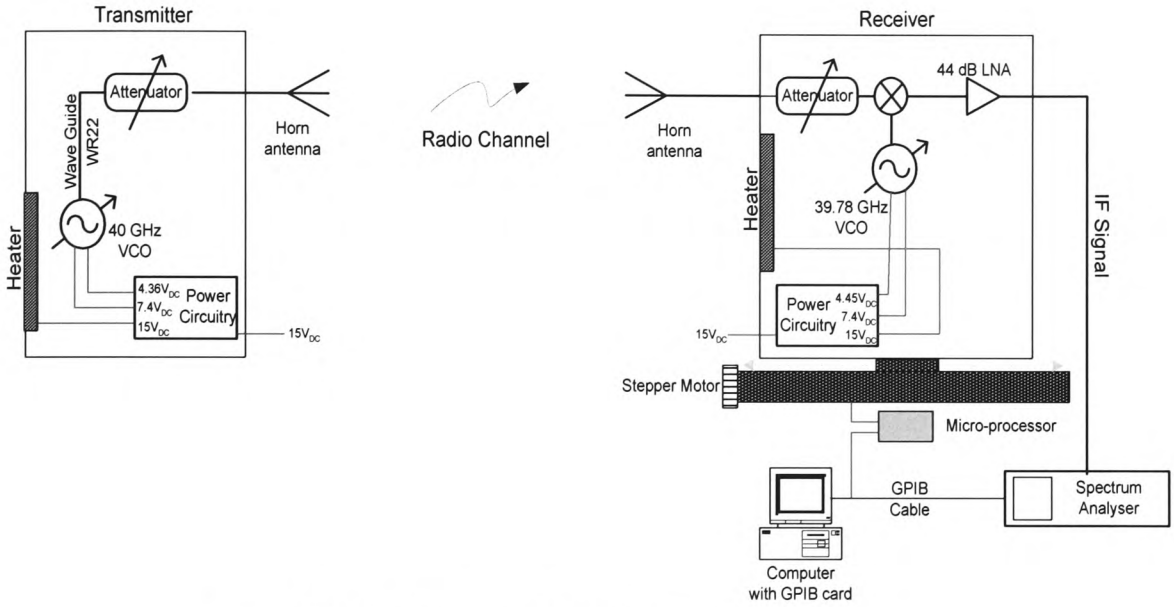

Figure 5.10 Block diagram of the 40 GHz measurement system.

5.3.1 Transmitter

The transmitter comprises a GV-22H varactor tuned Gunn diode oscillator that provides a stable reference between 39.75 and 40.25 GHz. According to the manufacturer (Farran) specifications, the output power is 150 mW, i.e. approximately 22 dBm. The Gunn diode ensures frequency stability and is supplied with 4.43 V_{DC}. The varactor, attached to the Gunn Diode, tunes the oscillating frequency to 40 GHz via a reference voltage of 7 V_{DC} set by the manufacturer. The thermal stability of the voltage-controlled oscillator (VCO) is provided via an integrated heater connected to a 15 V_{DC} supply; this effectively aids in minimizing the effects of frequency drifts.

Attached to the VCO is a 0-30 dB attenuator fitted with a stable precession attenuating element driven across the waveguide section by a micrometer. The attenuator was set to zero in most cases, and other settings were used only when conducting antenna radiation pattern measurements in the anechoic chamber. A photo of the transmitter is shown below in Fig. 5.11.

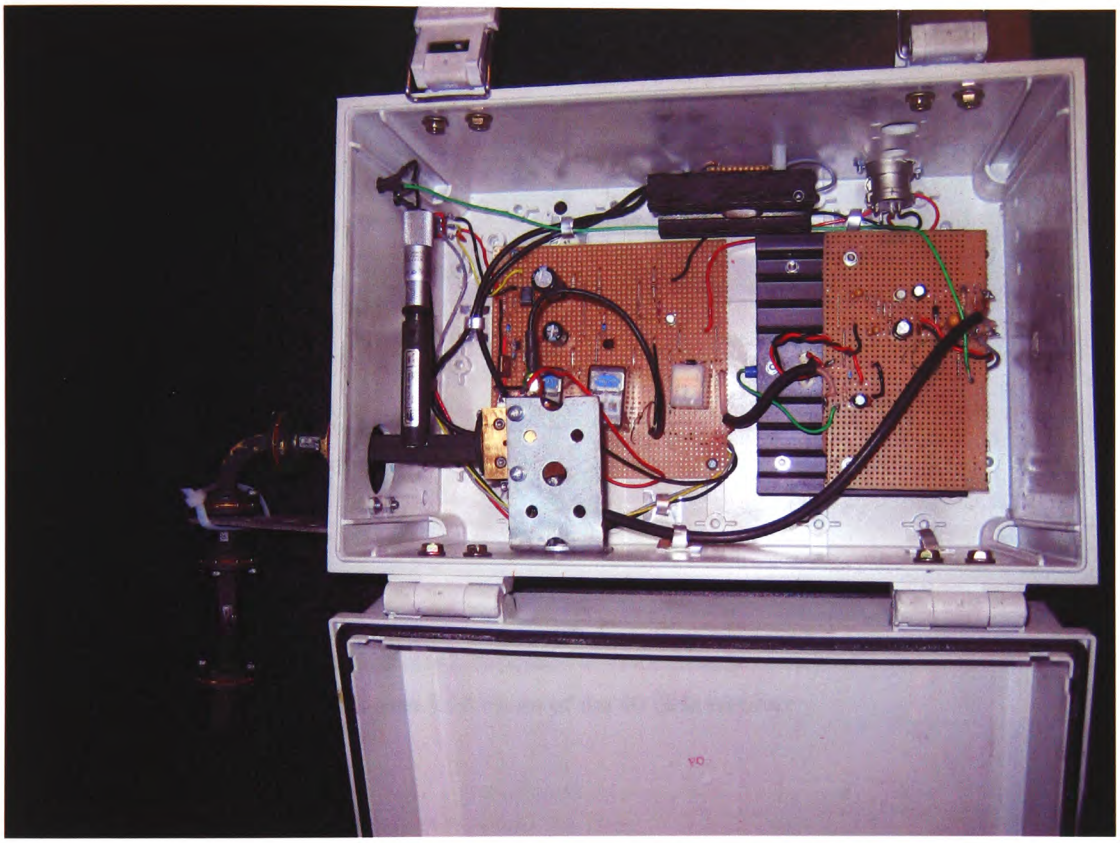

Figure 5.11 Photo of the 40 GHz transmitter.

5.3.2 Receiver

The received signal on the other side is down-converted to an intermediate-frequency (IF) via a biased mixer (Farren BMF-22) and a local-oscillator (LO). The latter is provided by a mechanically tuned GO-22 varactor in the frequency range 38.96 and 41.4 GHz. This varactor developed from the one used in the transmitter by a larger frequency output tuning range, which is very useful when selecting an appropriate frequency for the IF signal. During the measurements the IF signal was set to 220 MHz. The output from the mixer is amplified using a low-noise-amplifier (LNA) with a gain of 44 dB and a noise figure of 1.6 dB. Finally a spectrum analyser (HP8590A)

is used to capture the data, whereby the received signal is peak-held, and sampled with a resolution bandwidth of 1 MHz.

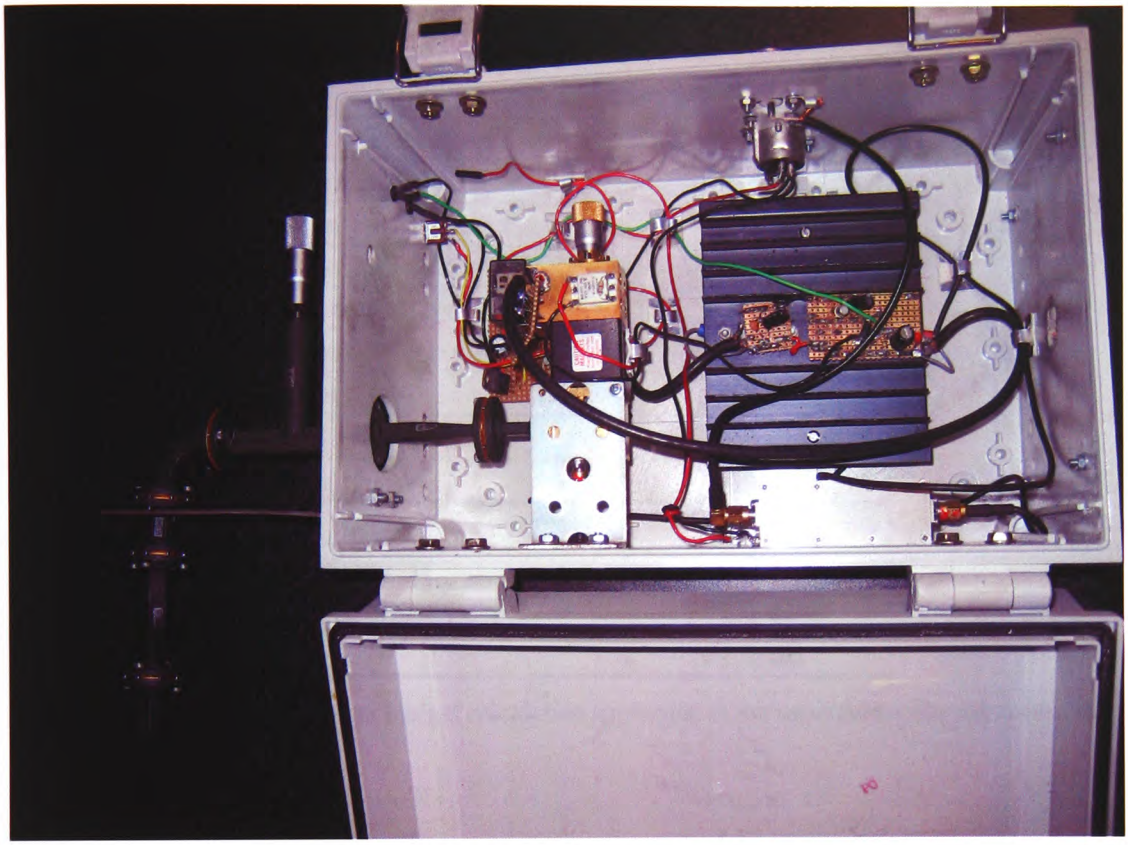

Figure 5.12 Photo of the 40 GHz receiver

5.3.3 Power Link Budget

Accounting for the propagation losses through the waveguide and system devices, a power link budget was established and shown in Table 5.3. The total noise power in the system is calculated as follows:

$$N = N_0 + 10\log_{10}(BW) + F. \tag{5.1}$$

In the above, N_0 is the thermal noise power spectral density in dBm/Hz, defined by

$$N_0 = KT \tag{5.2}$$

where $K = 1.38 \times 10^{-23}$ J/K is the Boltzmann's constant and $T = 290^0$ K is the nominal ambient temperature, BW is the resolution bandwidth of the spectrum analyser, and F is the noise figure of the receiver which was found to be approximately 10 dB via

$$F = F_{mixer} + \frac{F_{amp} - 1}{G_{mixer}}. \tag{5.3}$$

The link budget calculation was done for the worst case measurement setup, where an antenna gain of 10 dBi was used for the maximum radio link length measured, which was approximately 700 m. The signal-to-noise ratio (SNR) at the spectrum analyzer for this distance calculated was found to be approximately 31.6 dB.

Parameter	Gain	Units
Transmit Power	22.0	dBm
Transmitter Antenna Gain	20.0	dBi
FSL (at 700m) see Eq. 2.2	-121.4	dB
Receiver Antenna Gain	10.0	dBi
Receiver Attenuation	0.0	dB
Receiver Amplifier	44.0	dB
Receiver Power	-25.4	dBm
Thermal Noise	173.9	dBm/Hz
Noise Figure	10.0	dB
Resolution BW	1.0	MHz
Receiver Noise Power	-57.0	dBm
SNR	31.6	dB

Table 5.3 40 GHz system power budget calculation applicable to the maximum radio link measured.

5.3.4 Antennas

In all of the measured links a 20 dBi pyramidal-horn antenna was used for transmission, unless otherwise specified. At the receiver side, different antenna gains and types were employed, including three pyramidal-horns with nominal gains of 10, 15, and 20 dBi (beamwidths 39 – 20°), and two lens-horns with gains of 29 and 44 dBi (beamwidths 5 – 1.8°). The reason for utilizing two different antenna types was to enable performance investigations and comparisons over a wider range of 3 dB beamwidths. Photos of these antennas are shown in Fig. 5.13 and their corresponding dimensions are given in Table 5.4 with reference to Fig. 4.5

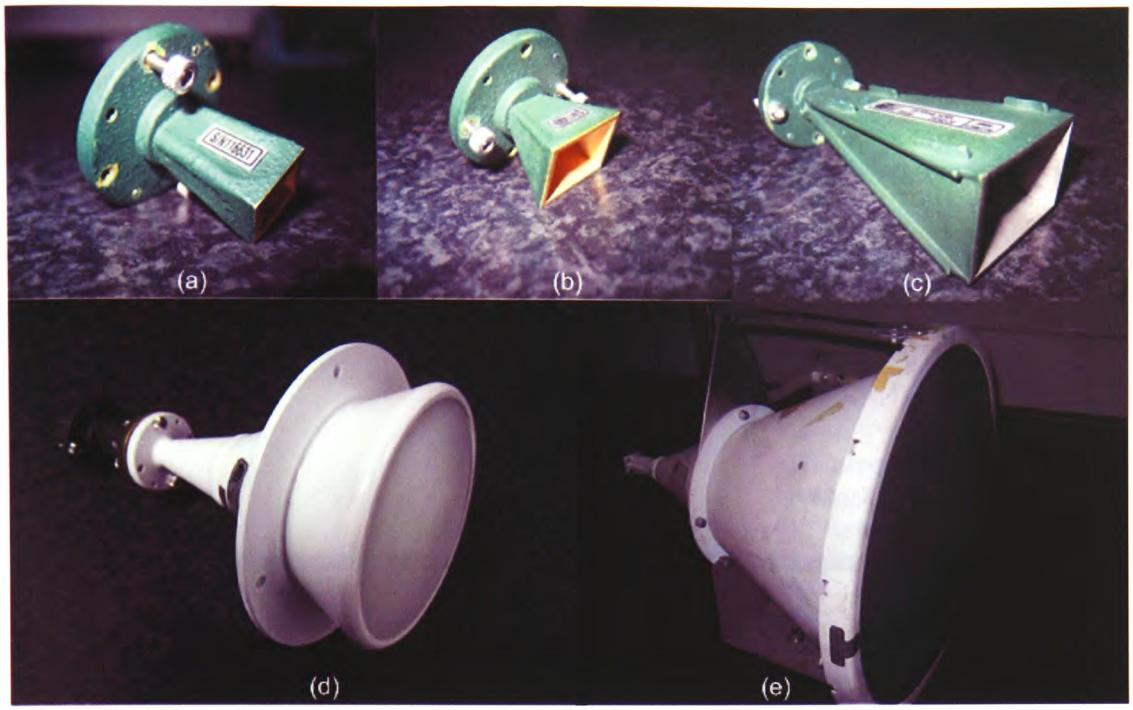

Figure 5.13 Photos of the antennas used, pyramidal-horn: (a) 10 dBi, (b) 15 dBi, (c) 20 dBi,; and lens-horn: (d) 29 dBi (e) 44 dBi.

Antenna (dBi)	a1 (mm)	b1 (mm)	P_e (mm)
10	9.5	6	20
15	17.5	14	15
20	28	21	60
29	69	69	91
44	415	415	910

Table 5.4 Dimensions of the horn antennas used with reference to Fig. 4.5.

Knowledge of the actual characteristics of the antennas employed is essential for both the selection of the right antenna for a specific measurement setup, and for processing and analysing the measured and simulated data. The radiation pattern of each antenna was measured in an anechoic chamber. The setup of such measurements is shown schematically in Fig. 5.14. The antenna under test was placed on a motorized turn-table. Rotation of the turn-table was accurately controlled in a Matlab™ environment. The realization of 2-plane radiation patterns was possible simply by rotating the antennas around their two main planes. The narrowest beamwidth transmit antenna was always used in order to reduce the effects of side-lobes and unwanted subsequent reflections that might still occur inside the chamber. The measured radiation patterns on the *E*- and *H*-planes are plotted in Fig. 5.15 & 5.16 respectively, and compared

with their theoretical representation (used in the proposed model) given analytically by Balanis in Eq. 4.98.

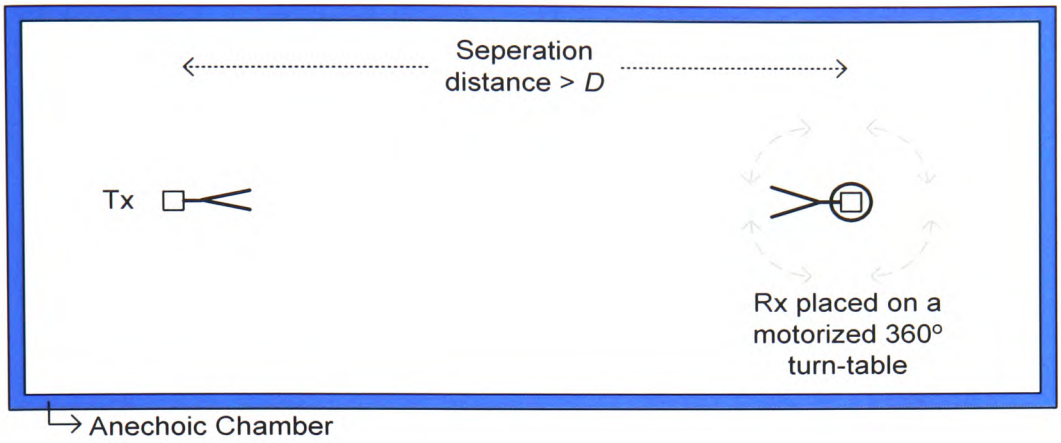

Figure 5.14 A schematic diagram showing the antenna radiation pattern measurement setup.

The space surrounding the antenna is known to have three distinct regions: the reactive near-field region, the radiating near-field (Fresnel) region and the far-field (Fraunhofer) region. Our main concern here is the distance criterion for far-field radiation, for which the angular field distribution is essentially independent of the radial distance from the antenna. The far-field region criterion was always met during the radiation pattern measurements. It typically exists at distances greater than $2D^2/\lambda$, where D is defined as the maximum overall dimension of the antenna aperture and must be greater than the wavelength (λ). The far-field distances of the antennas used at 40 GHz are given below in Table 5.1.

.

Antenna Gain (dBi)	*D* (cm)	Far-field distance (cm)
10	0.8	1.8
15	1.5	5.9
20	2.8	21.3
29	6.8	120
44	33.5	300

Table 5.5 Minimum far-field distance for the antennas used.

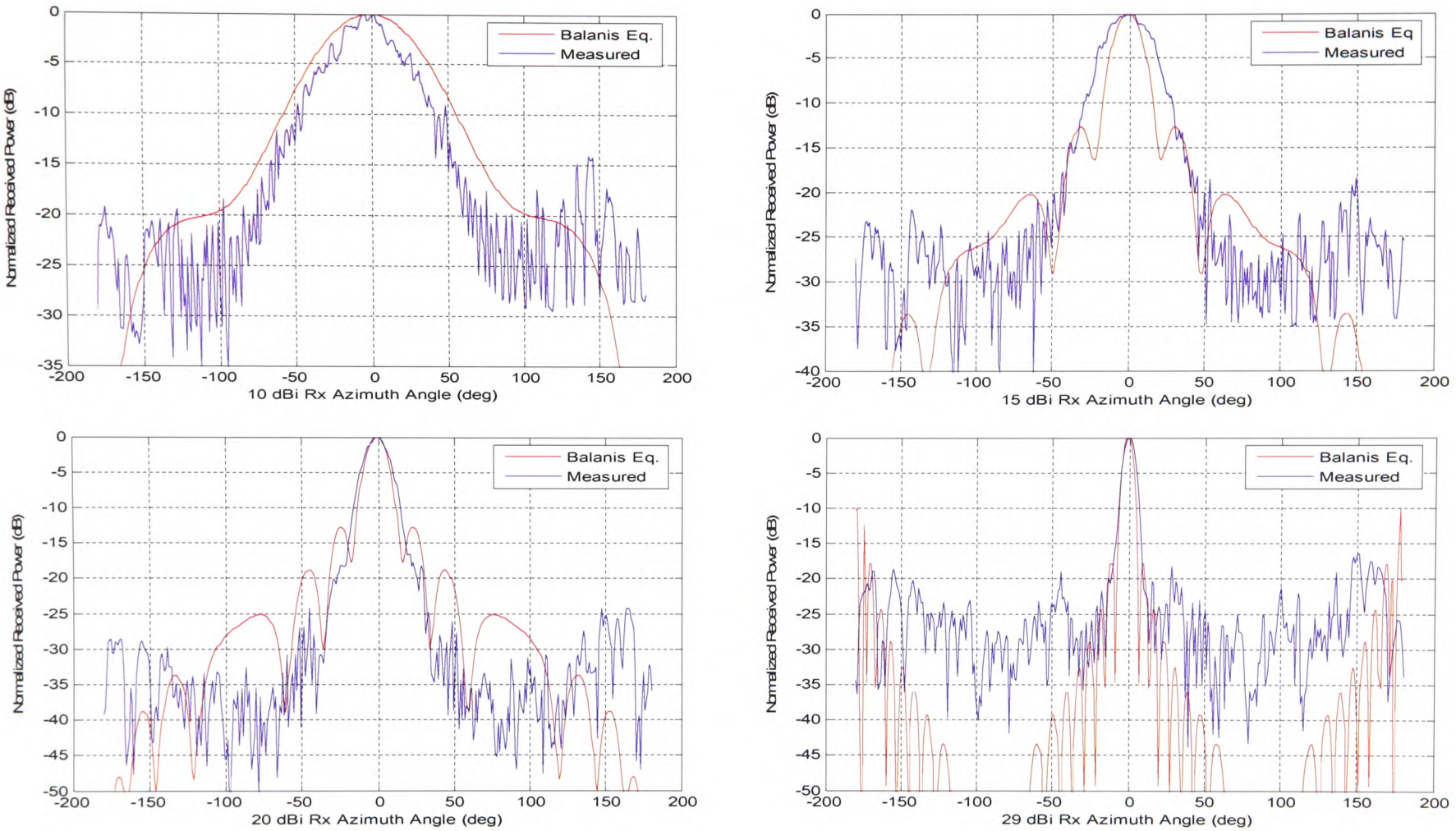

Figure 5.15 Measured antenna radiation patterns of the *E*-plane.

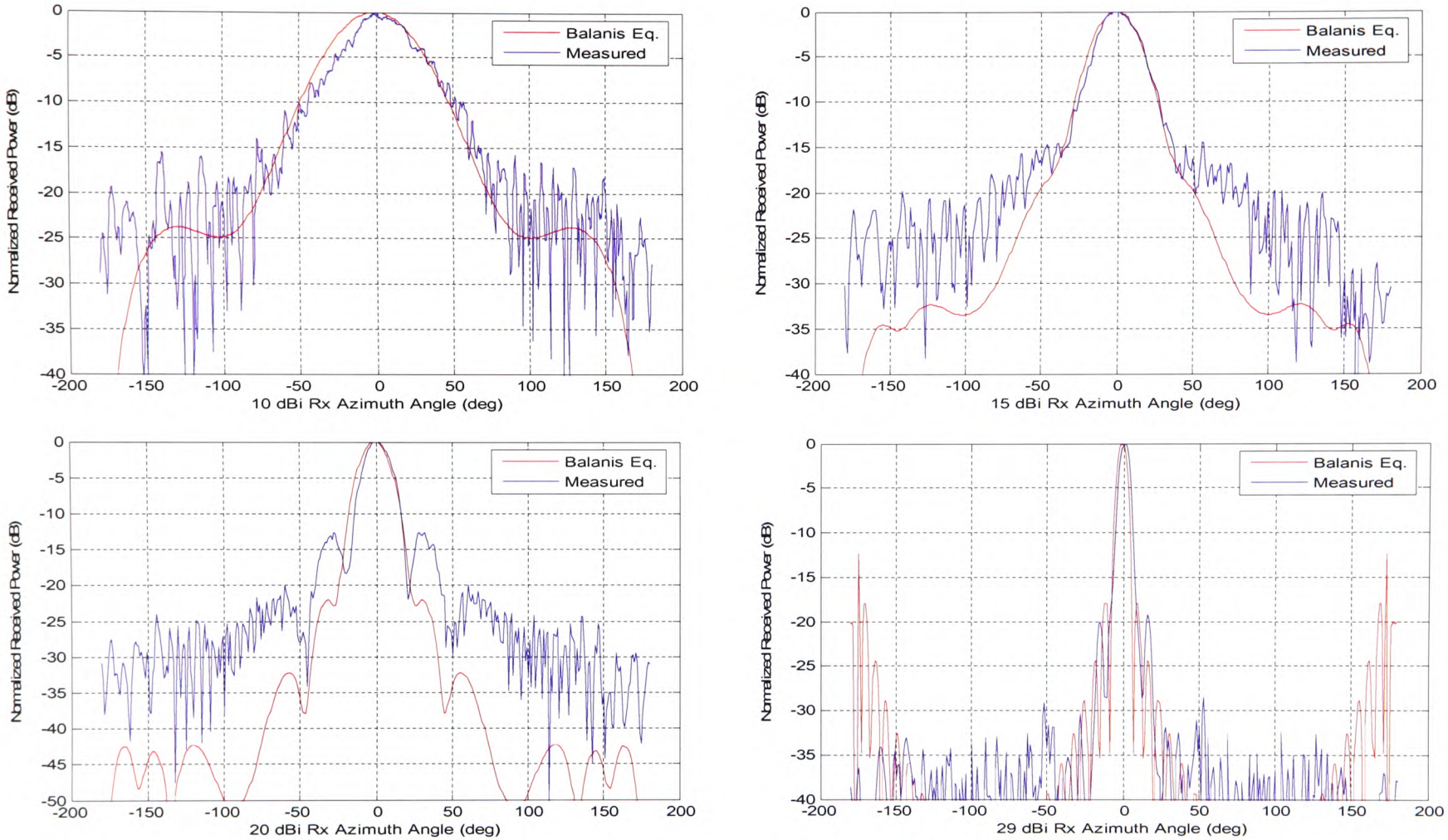

Figure 5.16: Measured antenna radiation patterns of the *H*-plane.

From Table 5.5, the far-field region of the 44 dBi antenna is observed at a minimum distance of 3 m. Since the anechoic chamber available at the University of Glamorgan has only 3 m of useful length, it was considered unsuitable for measuring the radiation pattern of the 44 dBi lens-horn antenna. For this antenna the 3 dB beamwidth of 1.8° was taken from the specifications supplied by the manufacturer.

In all of the outdoor measurements, the transmitter was placed on an adjustable, elevated mast. The height of the transmitter varied at different sites. The mast itself has height-adjustable legs for unlevelled grounds which enabled the transmitter to be placed parallel to the horizontal plane. The receiver on the other hand was always placed on top of a motorized mobile platform at approximately 3.5 m above the ground level. An example of a transmitter and a receiver outdoor setup is shown in Fig. 5.17.

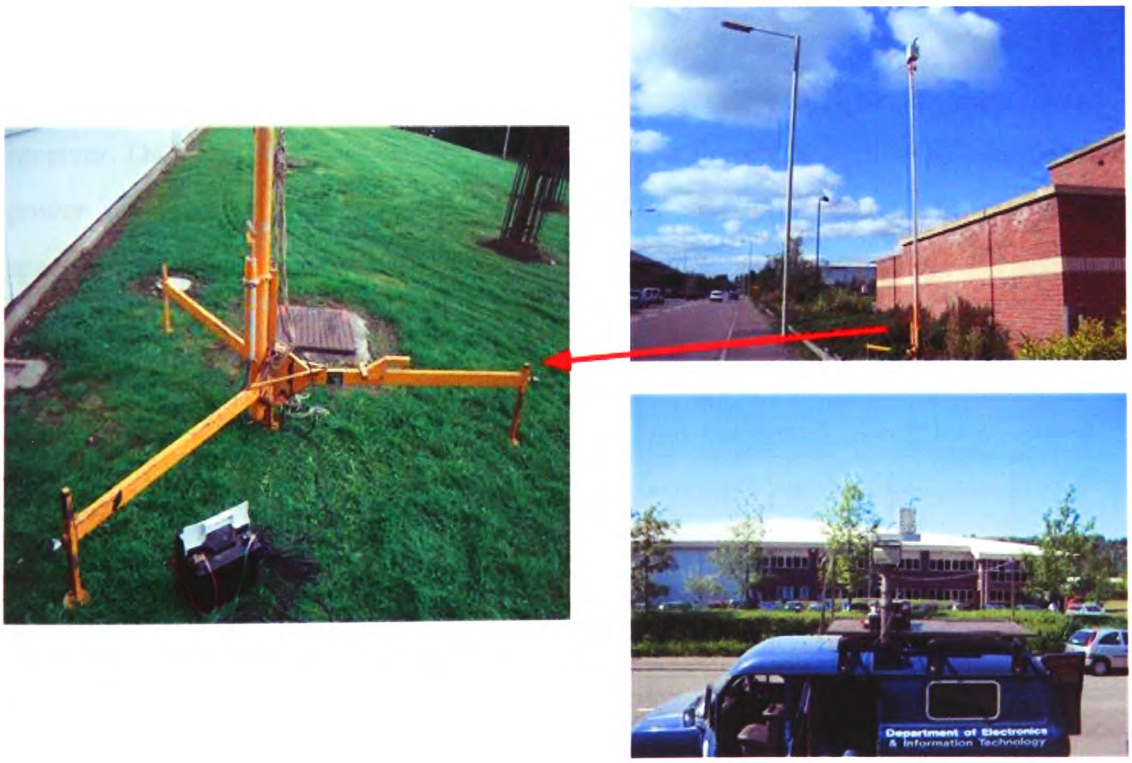

Figure 5.17 Photos of the transmitter (left and top-right) and receiver (bottom-right) outdoor measurement setups.

5.5 Software

In order to record the captured data and automate the measurement process, a software code was written in MATLAB®, which facilitated communication with the instruments, namely the spectrum analyser and the function generator. Both of the instruments were connected to a computer via a GPIB (General Purpose Interface Buss) card, which enabled control commands and data strings to be sent and received between the PC and instruments. The function generator only required a simple frequency configuration which controls the speed of the stepper motor used to move the receiver. Its direction, however, was controlled manually via a switch. The spectrum analyser on the other hand required the following parameter configuration settings: centre frequency, span frequency, sweep time and the number of samples taken per measurement. The measured received signal amplitudes were captured by commanding the spectrum analyser to record the maximum peak signal at each sweep. The period of the sweep was always set at its minimum of 20 ms. Fig. 5.18 shows a snapshot of the graphical user interface (GUI) developed which enabled full control of the measurement and the configuration of the receiver. Data recorded were stored in a matrix containing the number of samples and the power received at each sample. The GUI was also programmed for an alternative spectrum analyser, namely, the Advantest R3263.

Figure 5.18 The graphical user interface developed to automate and record measurements.

5.6 Interim Conclusion

The first section of this chapter presented site surveys of the measurement environments. Two sites were chosen as typical representations of LMDS cells for urban and suburban environments. The first was within the campus of University of Glamorgan, and the other was in a nearby industrial estate. All surveys were based on digital maps and GIS data. The topographical information was used in the EM model, as described in Chapter 4, for determining the transmitter, receiver and building surface coordinates, and also for obtaining statistical parameters related to the surface irregularities.

The second section is concerned with presenting the software interface and the hardware components, including the five horn antennas used along with their radiation characteristics. A power link budget calculation was also presented, showing sufficient dynamic range for all measurements. The next chapter presents the outcome of the measurements conducted on these sites and how they compare with predictions obtained from the proposed EM model.

5.7 References

[1] Tomlinson R., *Thinking about GIS: Geographic Information System Planning for Managers*, ISBN:1589480708, ESRI 2003.

[2] Fritsch D., Englich M. and Sester M., "Laserscan DEM for various applications", *ISPRS Commission IV Symposium on GIS – Between Visions and Applications*, Vol. 32/4, Stuttgart, Germany.

[3] ACTS Project 215, *Cellular Radio Access for Broadband Services (CRABS), Specification of Next Generation of LMDS Architecture D2P1B*, 1999.

[4] Nordbotten, A., "LMDS systems and their application", *IEEE Commun. Mag.*, vol. 38, no. 6, pp. 150–154, June 2000.

[5] Papazian P.B, Hufford G.A, Achatz, R.J. and Hoffman, R., "Study of the local multipoint distribution service radio channel", *IEEE Trans. Broadcast.*, vol. 43, no. 2, pp.175–184, June 1997.

CHAPTER SIX

MEASUREMENTS & MODEL OUTCOMES: RESULTS AND ANALYSIS

6.1 Introduction

This chapter presents the results obtained from the proposed model predictions and the radiowave propagation measurements, described in Chapters 4 & 5, respectively. These measurements were aimed at exploring the propagation aspects at millimetre-wavelengths and examining the cellular interference scenarios of LMDS networks described in Section 2.9. The outcomes of the measurements are compared with those obtained from simulations for evaluation and validation purposes.

From Chapters 3 & 4, it is reported that the statistical behaviour of the building and ground scatter was observed at the receiver station due to random variations of the phase and amplitude of the scattered waves intercepted by the receiver antenna. This random nature of the EM fields suggests a useful representation in terms of the PDF and the associated first and second order moments. Of particular interest is the parameterization of the simulations and measurements, and their association with the Rician distribution, i.e., the description of the received field strength and the characterization of the channel in terms of the parameters that define this particular distribution. Consequently, from such parameterization, the Rician K-factor can be extracted as shown in the derivations of Chapter 4.

Due to the nature of the measurements conducted at the IE link, in which the receiver was always pointing towards a desired transmitter, i.e. in the presence of a LOS dominant component, the probabilistic distributions and Rician K-factor are considered both useful and sufficient parameters for general channel assessments and comparison purposes. The

associated theoretical distribution functions, namely, the Rician (given in Eq. (4.92)) and Otteing's SIR (given in Eq. (4.96)) distributions, are obtained from the sampling of the received signal, while translating the receiver antenna in directions longitudinal or transversal to the direct link axis, with a maximum displacement of 50 wavelengths from its central position. Within this displacement window, the orientation of the two beams, as well as the moving average of the signal power samples remained relatively constant (see Fig. 5.5). Measurements in the UC site were conducted in a slightly different manner. The receiver position was fixed and benefited from a 360° rotation in the azimuth plane and, therefore, comparisons with the proposed model were given as a function of the received angle and represented by a polar plot.

In terms of simulations, up to 42 surfaces were identified in the IE link between the transmitter and receiver that could cause a measurable effect on the scatter. Such surfaces represented building rooftop and facades, as well as ground patches. On the other hand, simulations of the UC link mainly involved scatter from façade surfaces only. These were those of buildings A, B, and C of Fig. 5.7.

This chapter is organized as follows. The first section deals with the signal and K-factor measured and simulated trends versus distance for the different links selected in the IE site. Results of the NLOS link in the UC site are given in Section 6.3 in terms of power levels received in the azimuth plane and the trends of the Rician K-factor with different antenna gains. Finally, the last section describes outcomes of the interference measurements of the two selected scenarios connected with the LMDS frequency-reuse plans. The results are presented in terms of Rician K-factor trends with the different antenna gains used. Interim remarks and discussions are presented at the end of each section.

6.2 Industrial Estate Links

The IE measurement site and its link were shown in Fig. 5.1. At each position along the Tx1-Rx0 route, different antennas gains were utilized for horizontal and vertical, co- and

cross-polarized radio links. Separation distances of the three receiver positions from Tx1 are 188, 346, and 627 m. Again from the aerial photo in Fig. 5.1, it is clear that the environment consists of few buildings and includes some vegetation in the form of trees and bushes. In addition to Tx1, two other links were deliberately established from transmitters Tx2 and Tx3, which were almost clear of any obstructions. The main reason for adopting these additional links was to permit interference measurements for cellular LMDS networks.

During the measurement campaigns and with the aid of GIS-derived path profiles, extra precaution was taken to ensure that each position attained a clear unobstructed LOS path. At the worst case scenario, both the transmitter and receiver antenna axes remained within the 10 dB beamwidth of each other. The orientation of the receiver antenna on the horizontal plane was adjusted so that maximum power was attained at each location along the measured routes.

6.2.1 PDF of the Received Signal

The PDF of the normalized received signal power, as obtained from measurements and model predictions, is shown and compared individually with the theoretical Rician distribution. The K-factor values extracted from the measured data are used in the theoretical distribution (plotted with a solid line) from the formula given by Eq. (4.92). In other words, in the case of measurements, the PDF data obtained from each link is compared with a Rician distribution that is fitted by the actual K-factor value extracted from the measured data (bearing in mind that the Rician distribution is a function of the K-factor as per Eq. (4.92)). While in the case of the simulated data, in order to see how the distribution of the measured data compare with those of simulations, the value of the K-factor used in the theoretical distribution, in this case, is the one obtained from measurements and not from the simulated data.

Furthermore in addition to the K-factor, for each measured link the second, third, fourth and fifth order moments are tabulated after each figure and are compared, via a root-

mean-square error (RMSE), with simulations. The formula of the RMSE for any measured ($x_{mes,i}$) and predicted ($x_{sim,i}$) parameter is given as:

$$RMSE = \sqrt{\left(\frac{1}{n} \sum_{i=1}^{n} \left(x_{mes,i} - x_{sim,i} \right)^2 \right)} . \tag{6.1}$$

In probability theory and statistics, moments are considered an efficient method for comparisons since they provide valuable information on the form of a probabilistic distribution. In the case of normalized data, the first moment, which is the mean value of the power, is zero. The second moment is the variance about the mean known as the standard deviation and is given by:

$$\sigma = \sqrt{\mu_{k_m}} \tag{6.2}$$

where

$$\mu_k = \frac{1}{n} \sum_{i=1}^{n} \left(x_i - \bar{x} \right)^{k_m} , \tag{6.3}$$

k_m is order number of the moment and

$$\bar{x} = \frac{1}{n} \sum_{i=1}^{n} x_i \tag{6.4}$$

which is the first order moment of a random variable x_i. The third moment about the mean is used to define skewness which is a measure of the asymmetry of the probability distribution. The fourth order moment about the mean is used to define the kurtosis of the distribution, which essentially is a measure of peakedness of the probability distribution. Although higher order moments above the fourth do not have any physical interpretation, they are often employed in statistical analysis for further comparisons. In all the comparisons presented, the fifth moment was the highest moment considered.

Due to the large number of measured data obtained from the utilization of different antenna gains and receiver positions, only representative samples are presented in the figures of the following sections.

6.2.1.1 Vertical Polarization

Figs 6.1 - 6.3 show the PDF of the measured and simulated raw data each compared individually with the theoretical Rician PDF's obtained from the three receiver positions, namely, the Tx1-Rx3, Tx1-Rx2 and Tx1-Rx0 links. The transmit and receive antennas are both vertically polarized. The data displayed in this section are for receiving antennas gains of 10 and 20 dBi for Rx1, Rx2 and Rx0. In some these positions, a 29 and a 44 dBi antenna gains have been employed and their pertinent results are shown.

Similarly, Fig. 6.4 shows the measured, simulated and theoretical PDF's obtained this time from the second transmitter, i.e. the Tx2-Rx0 link, with the transmit and receive antennas both vertically polarized. Results displayed are from antenna gains 10 and 20 dBi.

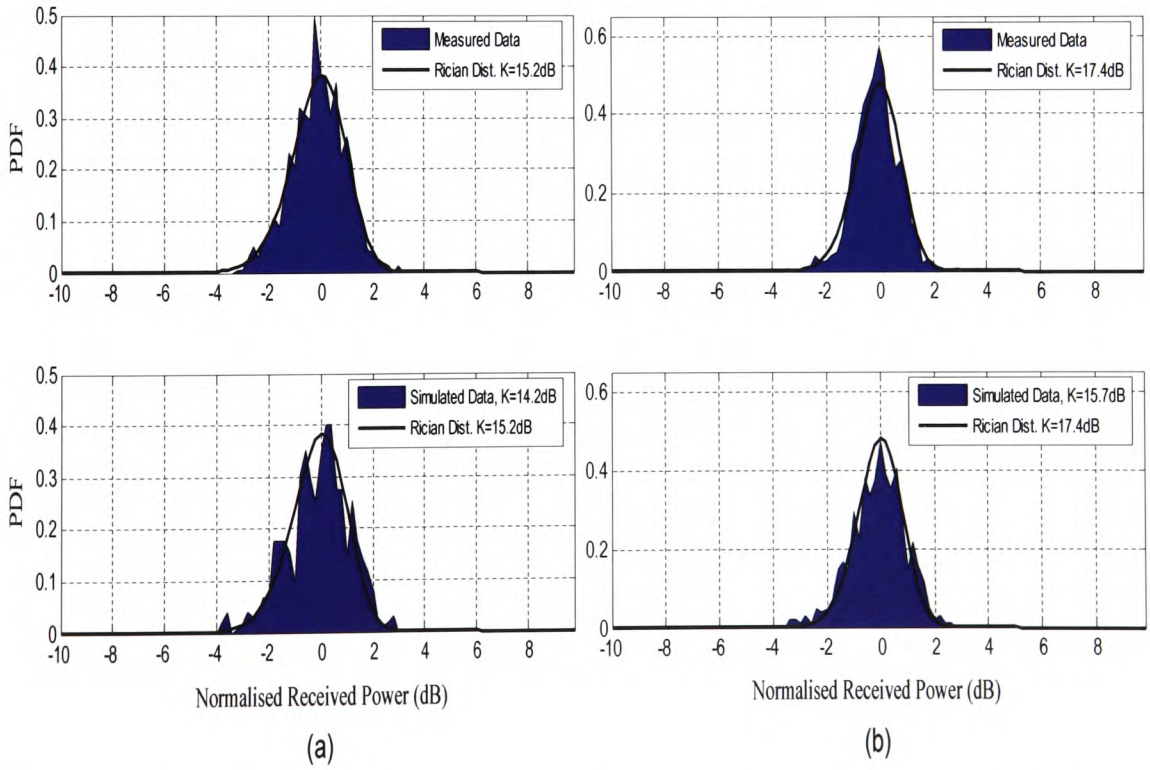

Figure 6.1 PDF of the received field and comparisons with the theoretical Rician and the distribution obtained from simulations for the Tx1-Rx2 188 m vertically polarized link using antenna gains (a) 10 and (b) 20 dBi.

Link	Pol.	Ant, Gain (dBi)	Rician *K*-Factor (dB)	2nd moment (dB)	3rd moment (dB)	4th moment (dB)	5th moment (dB)
188m measured	VV	10	15.20	1.05	0.27	1.40	1.31
188m simulated	VV	10	14.20	1.18	0.30	1.63	1.48
Error %			6.6%	12.6%	10.2%	16.3%	12.8%
RMSE (dB)					0.5		
188m measured	VV	20	17.40	0.70	0.30	0.92	0.94
188m simulated	VV	20	15.70	0.95	0.21	1.27	1.21
Error %			9.8%	35.9%	30.8%	37.2%	28.8%
RMSE (dB)					0.9		

Table 6.1 Statistics of the measured and simulated PDF data for the Tx1-Rx2 188 m vertically polarized link.

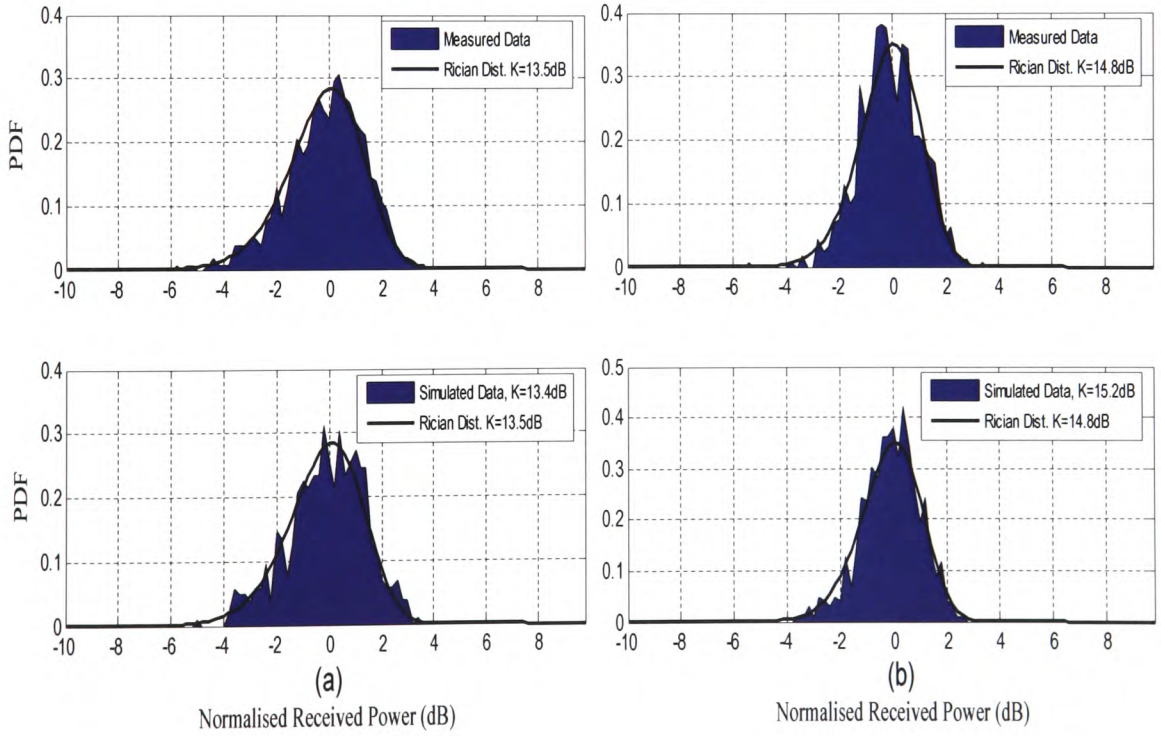

Figure 6.2: PDF of the received field and comparisons with the theoretical Rician and the distribution obtained from simulations for the Tx1-Rx1 346 m vertically polarized link using antenna gains (a) 10 and (b) 20 dBi.

Link	Pol.	Ant, Gain (dBi)	Rician *K*-Factor (dB)	2nd moment (dB)	3rd moment (dB)	4th moment (dB)	5th moment (dB)
346m measured	VV	10	13.50	1.47	0.41	1.99	1.73
346m simulated	VV	10	13.40	1.39	0.57	1.91	1.28
Error %			0.7%	5.6%	39.4%	4.0%	26.3%
RMSE (dB)					0.3		
346m measured	VV	20	14.80	1.14	0.79	1.54	1.42
346m simulated	VV	20	15.20	1.32	0.46	1.79	1.59
Error %			2.7%	15.8%	42.2%	16.0%	12.6%
RMSE (dB)					0.3		

Table 6.2 Statistics of the measured and simulated PDF data for the Tx1-Rx1 346 m vertically polarized link.

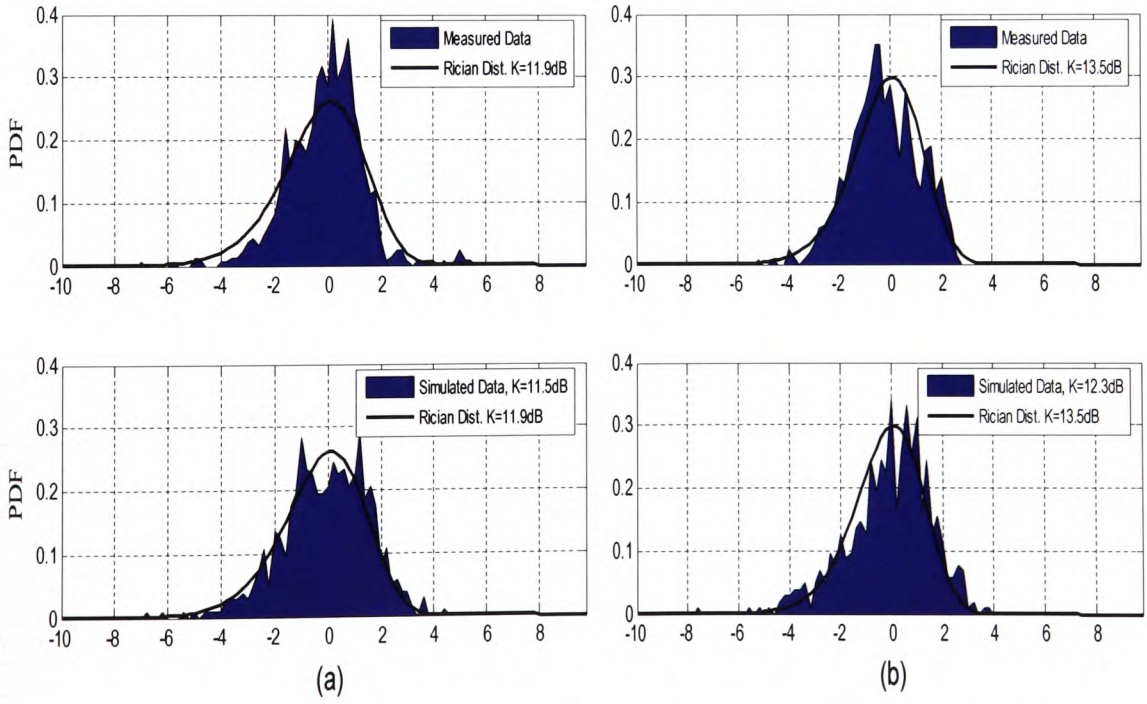

Figure 6.3: PDF of the received field and comparisons with the theoretical Rician and the distribution obtained from simulations for the Tx1-Rx0 627 m vertically polarized link using antenna gains (a) 10 and (b) 20 dBi.

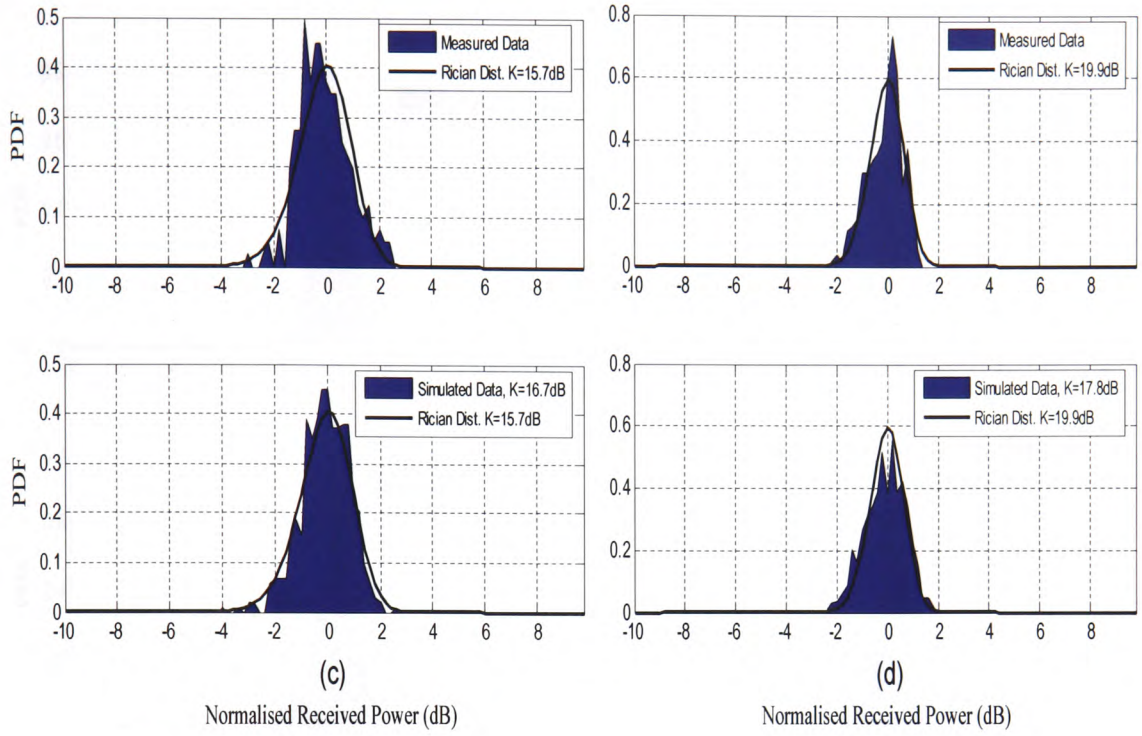

Figure 6.3: PDF of the received field and comparisons with the theoretical Rician and the distribution obtained from simulations for the Tx1-Rx0 627 m vertically polarized link using antenna gains (c) 29 and (d) 44 dBi.

Link	Pol.	Ant, Gain (dBi)	Rician *K*-Factor (dB)	2nd moment (dB)	3rd moment (dB)	4th moment (dB)	5th moment (dB)
627m measured	VV	10	11.90	1.36	0.90	2.28	1.70
627m simulated	VV	10	11.50	1.55	0.73	2.02	1.83
Error %			3.4%	14.3%	19.1%	11.5%	7.6%
RMSE (dB)					0.3		
627m measured	VV	20	13.50	1.34	1.10	1.72	1.55
627m simulated	VV	20	12.50	1.59	0.61	2.14	1.84
Error %			7.4%	18.9%	44.1%	24.3%	19.0%
RMSE (dB)					0.6		
627m measured	VV	29	15.70	0.52	0.38	0.68	0.74
627m simulated	VV	44	16.70	0.69	0.23	0.74	0.99
Error %			6.4%	32.3%	39.0%	8.9%	34.2%
RMSE (dB)					0.5		

Table 6.3 Statistics of the measured and simulated PDF data for the Tx1-Rx0 346 m vertically polarized link.

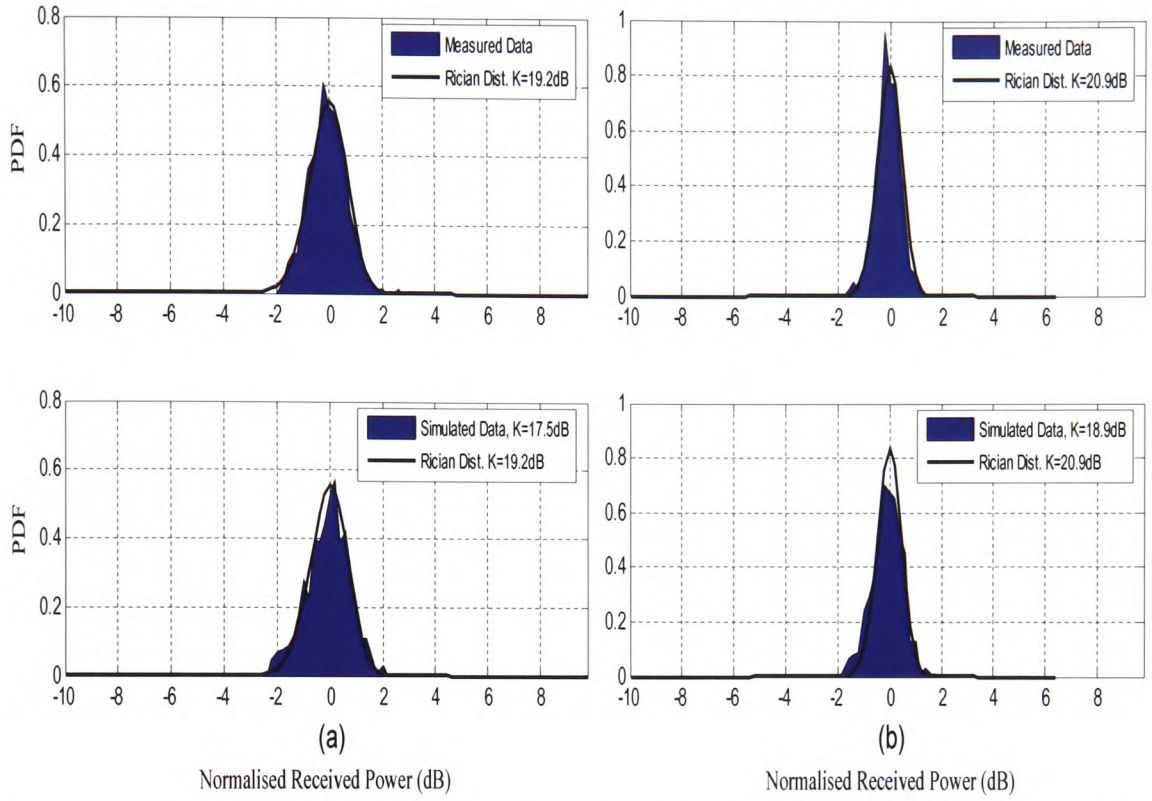

Figure 6.4: PDF of the received field and comparisons with the theoretical Rician and the distribution obtained from simulations for the Tx2-Rx0 127 m vertically polarized link using antenna gains (a) 10 and (b) 20 dBi.

Link	Pol.	Ant, Gain (dBi)	Rician *K*-Factor (dB)	2nd moment (dB)	3rd moment (dB)	4th moment (dB)	5th moment (dB)
127m measured	VV	10	19.20	0.68	0.37	1.06	1.04
127m simulated	VV	10	17.50	0.61	0.20	0.83	0.86
Error %			8.9%	9.0%	44.6%	21.7%	17.8%
RMSE (dB)					0.8		
127m measured	VV	20	20.90	0.59	0.43	1.06	1.15
127m simulated	VV	20	18.90	0.46	0.23	0.61	0.67
Error %			9.6%	21.0%	47.2%	42.5%	41.7%
RMSE (dB)					1.1		

Table 6.4 Statistics of the measured and simulated PDF data for the Tx2-Rx0 127 m vertically polarized link.

6.2.1.2 Horizontal Polarization

In the same manner, Figs 6.5 – 6.7 show the PDF of the measured and simulated raw data each compared individually with the theoretical Rician PDF's for the three links along the Tx1-Rx0 route. This time both, the transmit and receive antennas are horizontally polarized. The figures displayed in this section are for data obtained from the 10 and 20 dBi antennas. Likewise, measured, simulated and theoretical PDF's of those obtained from the second transmitter in the Tx2-Tx0 link, are shown subsequently in Fig. 6.8 for antenna gains of 10, 20, 29 and 44 dBi.

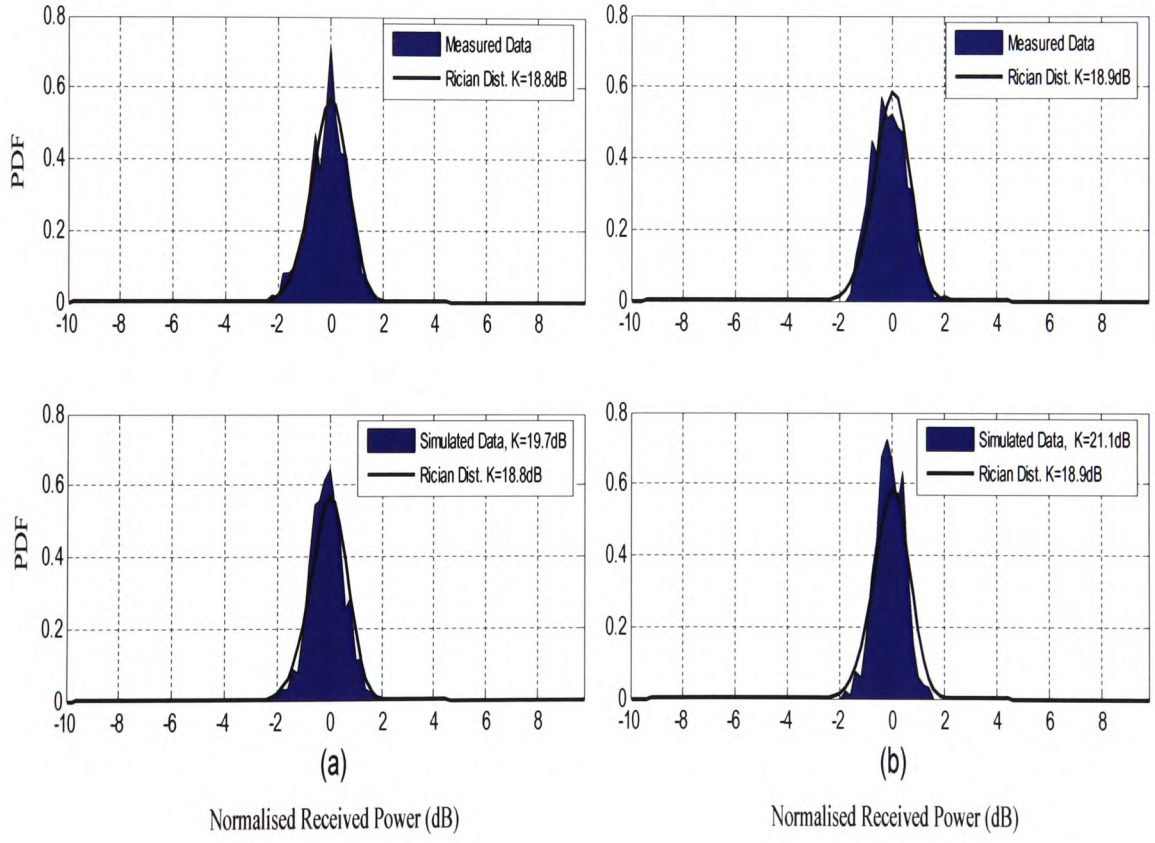

Figure 6.5: PDF of the received field and comparisons with the theoretical Rician and the distribution obtained from simulations for the Tx1-Rx2 188 m horizontally polarized link using antenna gains (a) 10 and (b) 20 dBi.

Link	Pol.	Ant, Gain (dBi)	Rician *K*-Factor (dB)	2nd moment (dB)	3rd moment (dB)	4th moment (dB)	5th moment (dB)
188m measured	HH	10	18.80	0.71	0.09	0.94	0.95
188m simulated	HH	10	19.70	0.63	0.12	0.86	0.89
Error %			4.8%	11.6%	34.7%	8.0%	6.4%
RMSE (dB)					0.5		
188m measured	HH	20	18.90	0.67	0.63	0.85	0.88
188m simulated	HH	20	21.20	0.66	0.31	0.85	0.88
Error %			12.2%	1.8%	50.6%	0.2%	0.2%
RMSE (dB)					1.2		

Table 6.5 Statistics of the measured and simulated PDF data for the Tx1-Rx2 188 m horizontally polarized link.

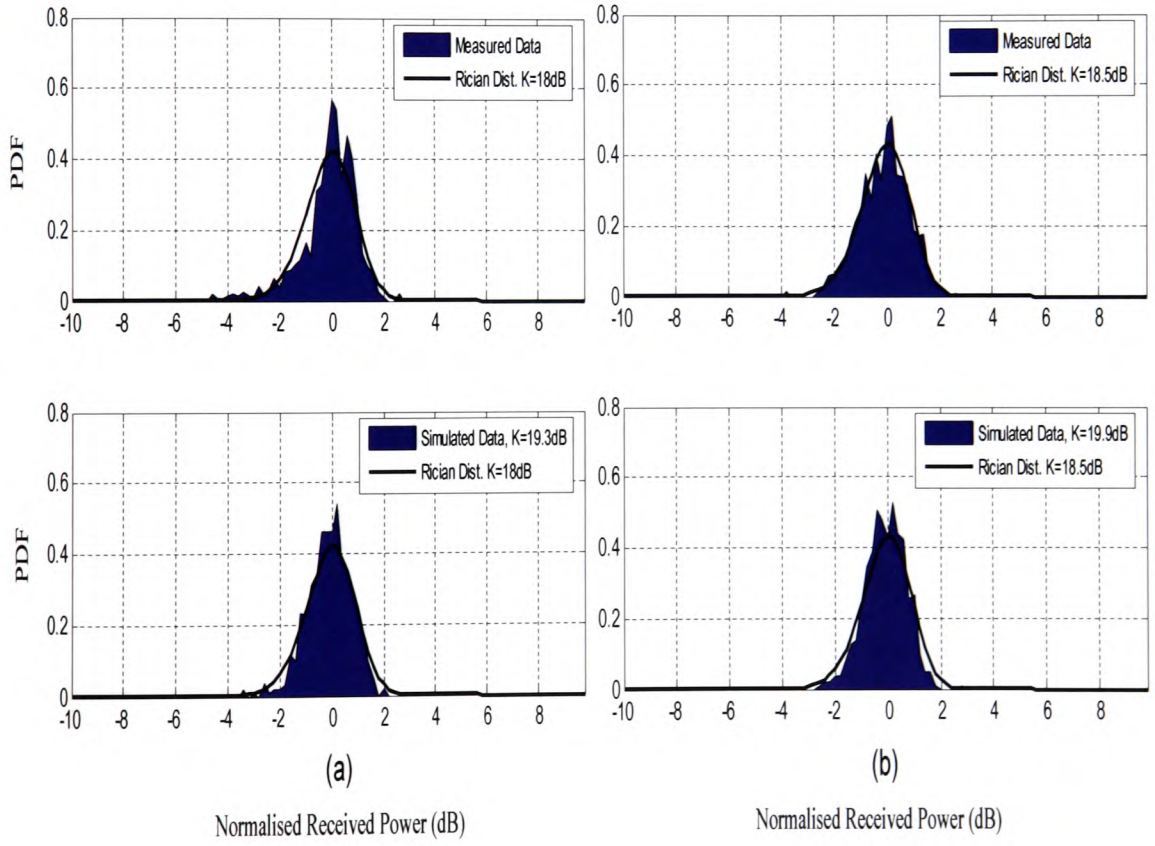

Figure 6.6: PDF of the received field and comparisons with the theoretical Rician and the distribution obtained from simulations for the Tx1-Rx1 346 m horizontally polarized link using antenna gains (a) 10 and (b) 20 dBi.

Link	Pol.	Ant, Gain (dBi)	Rician *K*-Factor (dB)	2nd moment (dB)	3rd moment (dB)	4th moment (dB)	5th moment (dB)
346m measured	HH	10	18.00	1.27	0.66	1.64	1.89
346m simulated	HH	10	19.30	0.94	0.41	1.33	1.26
Error %			7.2%	25.6%	38.6%	18.7%	33.3%
RMSE (dB)					0.8		
346m measured	HH	20	18.50	0.93	0.70	1.25	1.19
346m simulated	HH	20	19.90	0.86	0.43	1.14	1.11
Error %			7.6%	8.3%	38.7%	8.9%	7.3%
RMSE (dB)					0.7		

Table 6.6 Statistics of the measured and simulated PDF data for the Tx1-Rx1 346 m horizontally polarized link.

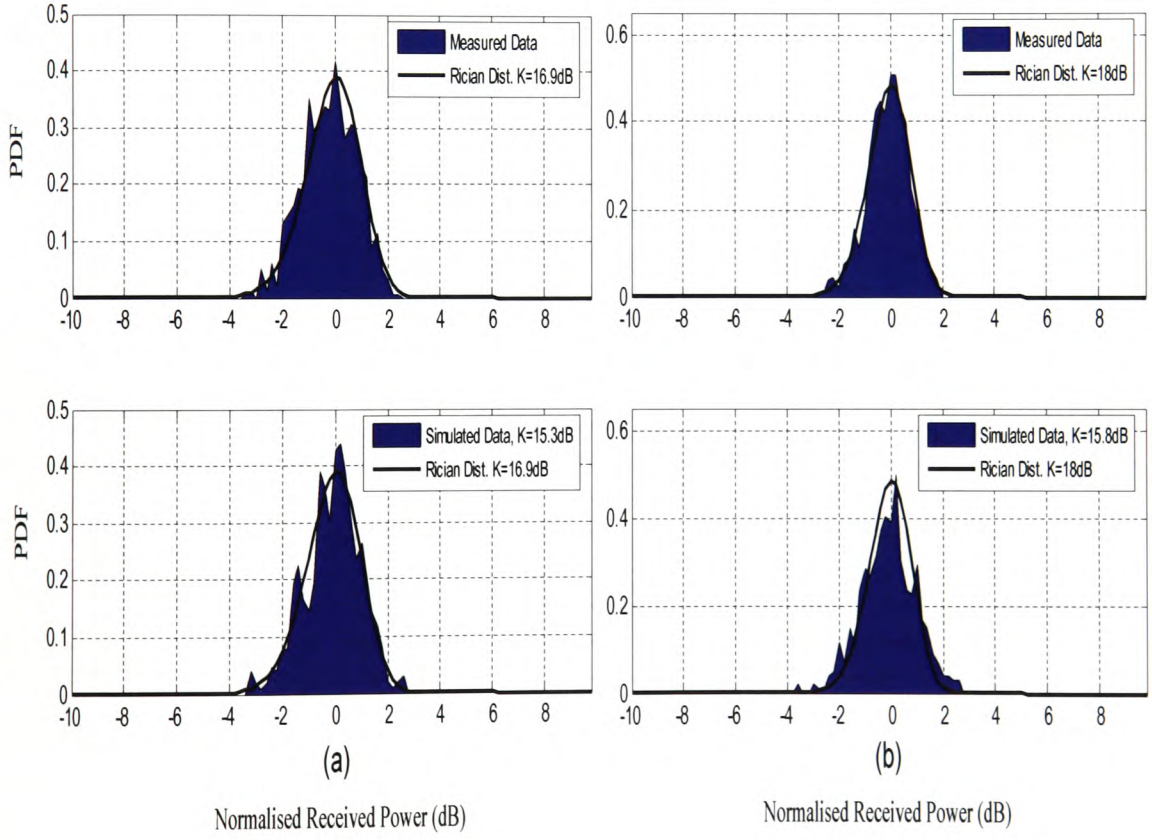

Figure 6.7: PDF of the received field and comparisons with the theoretical Rician and the distribution obtained from simulations for the Tx1-Rx0 627 m horizontally polarized link using antenna gains (a) 10 and (b) 20 dBi.

Link	Pol.	Ant, Gain (dBi)	Rician *K*-Factor (dB)	2nd moment (dB)	3rd moment (dB)	4th moment (dB)	5th moment (dB)
627m measured	HH	10	16.90	1.08	0.90	1.37	1.29
627m simulated	HH	10	15.30	1.16	0.51	1.55	1.42
Error %			9.5%	8.0%	42.8%	12.8%	10.1%
RMSE (dB)					0.8		
627m measured	HH	20	18.00	0.84	0.59	1.12	1.10
627m simulated	HH	20	15.80	0.99	0.33	1.30	1.23
Error %			12.2%	18.7%	43.5%	15.5%	12.2%
RMSE (dB)					1.1		

Table 6.7 Statistics of the measured and simulated PDF data for the Tx1-Rx0 627 m horizontally polarized link.

Link	Pol.	Ant, Gain (dBi)	Rician *K*-Factor (dB)	2nd moment (dB)	3rd moment (dB)	4th moment (dB)	5th moment (dB)
127m measured	HH	10	18.20	0.37	0.06	0.39	0.49
127m simulated	HH	10	19.40	0.54	0.11	0.54	0.87
Error %			6.6%	31.5%	44.3%	28.0%	43.7%
RMSE (dB)					0.6		
127m measured	HH	20	23.40	0.41	0.37	0.53	0.55
127m simulated	HH	20	23.80	0.49	0.23	0.71	0.77
Error %			1.7%	19.4%	36.7%	33.4%	39.6%
RMSE (dB)					0.3		
127m measured	HH	29	24.40	0.51	0.08	0.67	0.92
127m simulated	HH	29	24.10	0.37	0.11	0.39	0.46
Error %			1.2%	27.6%	37.7%	41.9%	49.9%
RMSE (dB)					0.3		

Table 6.8 Statistics of the measured and simulated PDF data for the Tx2-Rx0 127 m horizontally polarized link.

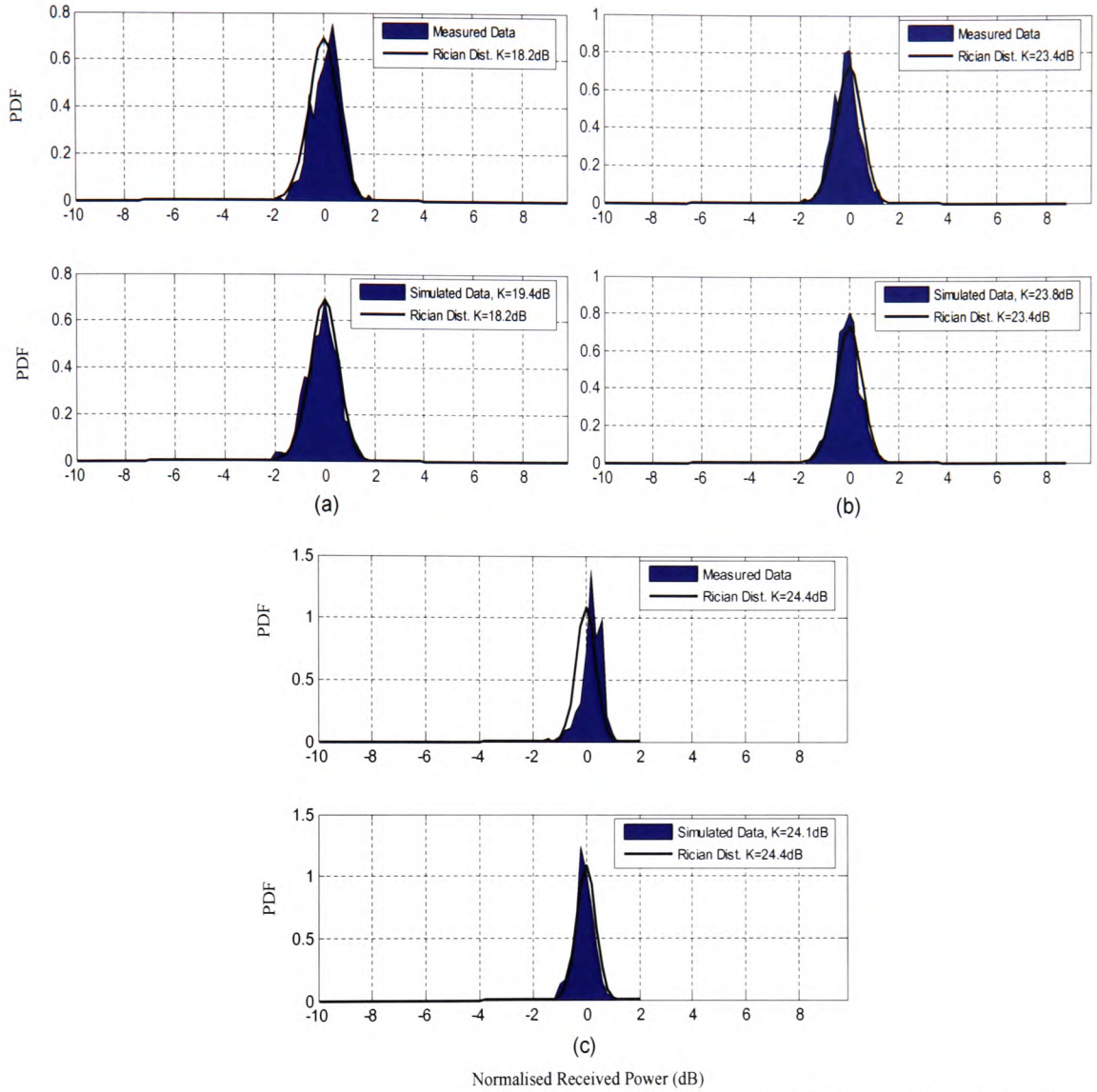

Figure 6.8: PDF of the received field and comparisons with the theoretical Rician and the distribution obtained from simulations for the Tx2-Rx0 127 m horizontally polarized link using antenna gains (a) 10, (b) 20 and (c) 29 dBi.

6.2.1.3 Cross Polarization

The received signal distributions of cross-polarized signals that occurred from either, a horizontal to vertical or a vertical to horizontal polarized link for the three receiver positions along the Tx1-Rx0 route are compared with simulations and the Rician

theoretical distribution as shown in Figs 6.9 – 6.11. These figures are for data obtained from for the 10 and 20 dBi antenna gains.

Since a dominant signal was still obtained (despite the cross-polarization discrimination of the antennas) in these measured links, i.e. the power of the direct field was higher than that of the scattered field; the theoretical fitting was still successfully achieved with the Rician distribution.

Subsequently, the measured, simulated and theoretical PDF's of the cross-polarizations obtained this time from the second transmitter in the Tx2-Rx0 link is shown in Fig. 6.12. These included an additional plot of a 29 dBi antenna gain.

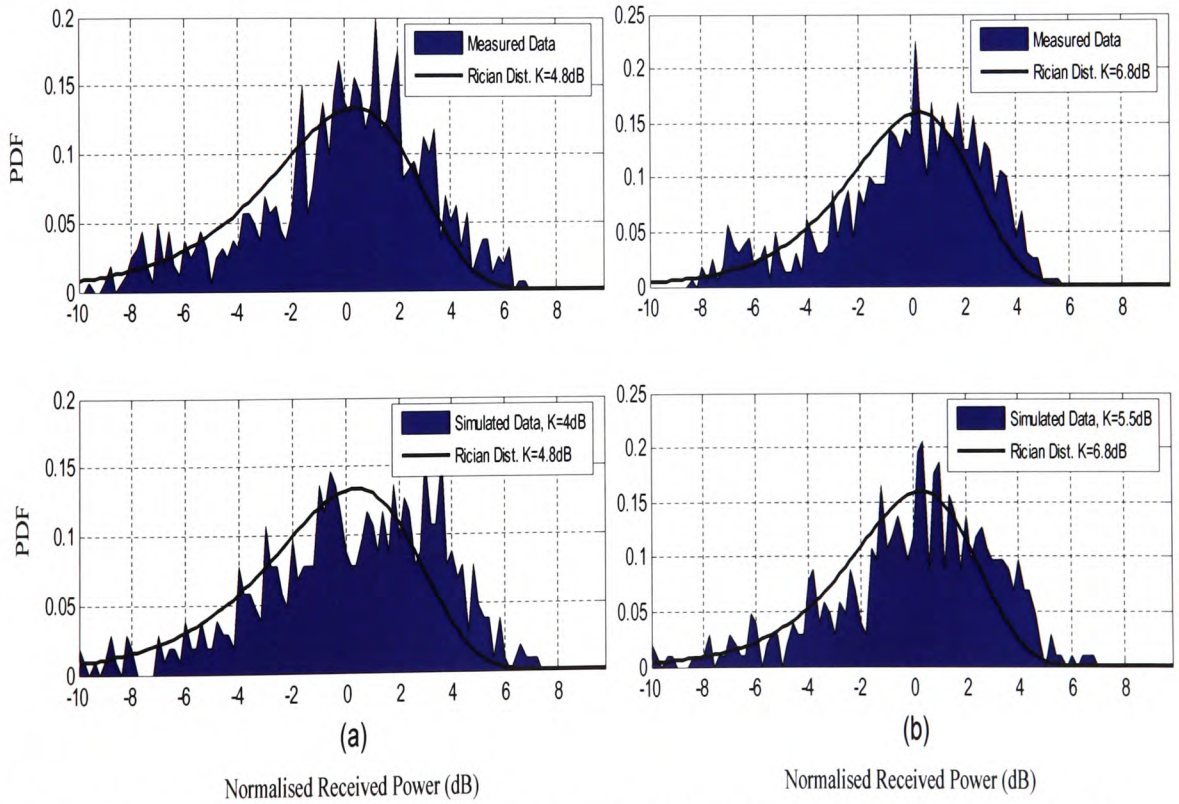

Figure 6.9: PDF of the received field and comparisons with the theoretical Rician and the distribution obtained from simulations for the Tx1-Rx2 188 m cross- polarized link using antenna gains (a) 10 and (b) 20 dBi.

Link	Pol.	Ant, Gain (dBi)	Rician *K*-Factor (dB)	2nd moment (dB)	3rd moment (dB)	4th moment (dB)	5th moment (dB)
188m measured	HV	10	4.80	3.21	0.80	4.24	3.18
188m simulated	HV	10	4.00	3.45	1.07	4.82	3.52
Error %			16.7%	7.4%	33.7%	13.6%	10.7%
RMSE (dB)					0.6		
188m measured	HV	20	6.80	2.90	0.42	3.83	2.93
188m simulated	HV	20	5.50	3.30	0.53	5.09	3.67
Error %			19.1%	13.8%	25.9%	33.1%	25.6%
RMSE (dB)					1.0		

Table 6.9 Statistics of the measured and simulated PDF data for the Tx1-Rx2 188 m cross-polarized link.

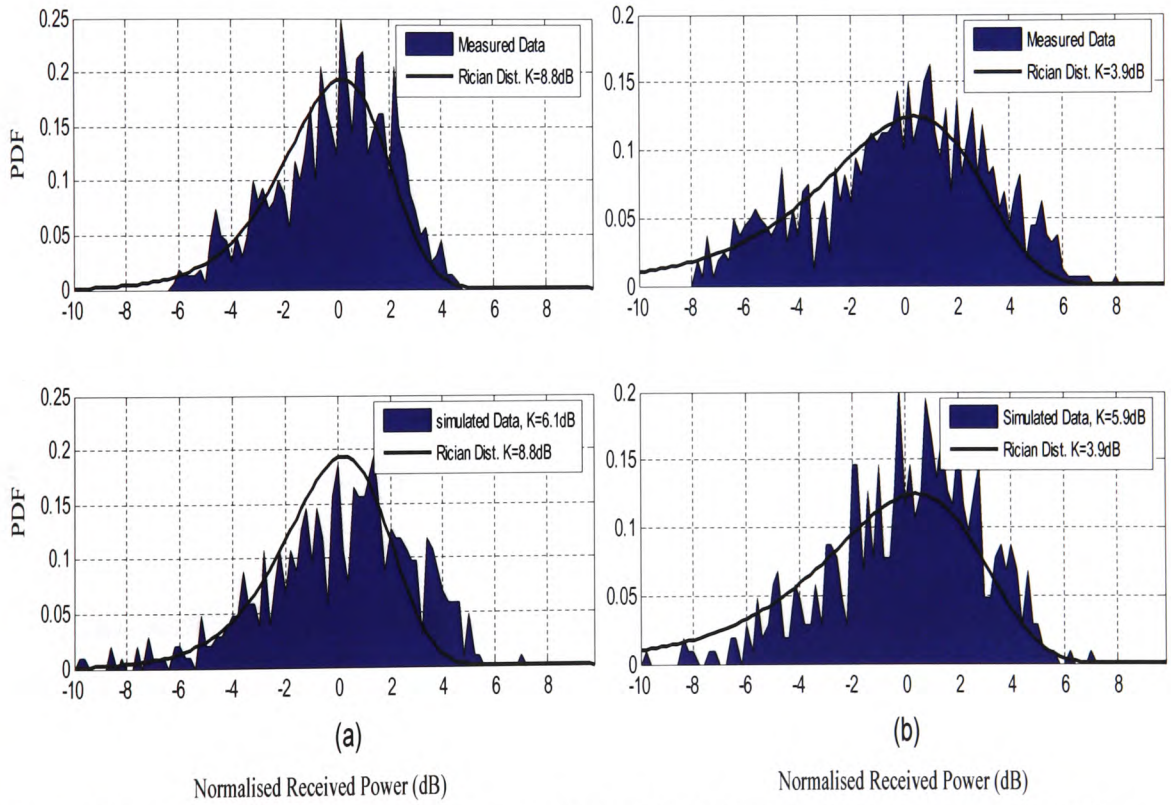

Figure 6.10: PDF of the received field and comparisons with the theoretical Rician and the distribution obtained from simulations for the Tx1-Rx1 346 m cross-polarized link using antenna gains (a) 10 and (b) 20 dBi.

Link	Pol.	Ant, Gain (dBi)	Rician *K*-Factor (dB)	2nd moment (dB)	3rd moment (dB)	4th moment (dB)	5th moment (dB)
346m measured	HV	10.00	8.80	2.20	0.52	2.80	2.28
346m simulated	HV	10.00	6.10	2.61	0.86	3.79	2.90
Error %			30.7%	18.6%	39.1%	35.2%	27.3%
RMSE (dB)					1.5		
346m measured	HV	20.00	3.90	3.23	0.79	4.05	3.06
346m simulated	HV	20.00	5.90	4.15	1.47	6.59	4.52
Error %			51.3%	28.4%	46.1%	38.6%	32.3%
RMSE (dB)					1.9		

Table 6.10 Statistics of the measured and simulated PDF data for the Tx1-Rx2 346 m cross-polarized link.

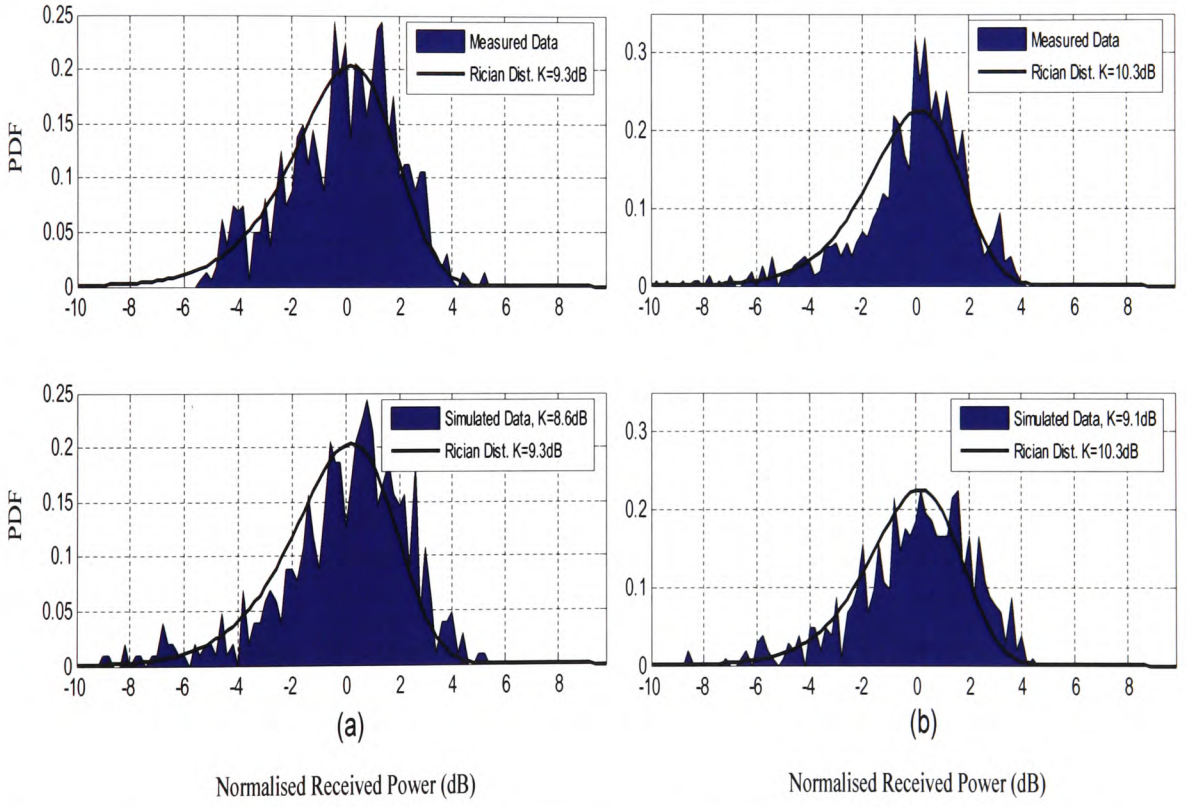

Figure 6.11: PDF of the received field and comparisons with the theoretical Rician and the distribution obtained from simulations for the Tx1-Rx0 627 m cross- polarized link using antenna gains (a) 10 and (b) 20 dBi.

Link	Pol.	Ant, Gain (dBi)	Rician *K*-Factor (dB)	2nd moment (dB)	3rd moment (dB)	4th moment (dB)	5th moment (dB)
627m measured	HV	10	9.30	2.04	1.34	2.59	2.14
627m simulated	HV	10	8.60	2.40	0.85	3.48	2.71
Error %			7.5%	17.9%	36.5%	34.4%	26.8%
RMSE (dB)					0.7		
627m measured	HV	20	10.30	2.10	1.02	3.89	2.23
627m simulated	HV	20	9.10	2.20	0.92	3.10	3.00
Error %			11.7%	5.1%	9.9%	20.5%	34.3%
RMSE (dB)					0.8		

Table 6.11 Statistics of the measured and simulated PDF data for the Tx1-Rx0 627 m cross-polarized link.

Link	Pol.	Ant, Gain (dBi)	Rician *K*-Factor (dB)	2nd moment (dB)	3rd moment (dB)	4th moment (dB)	5th moment (dB)
127m measured	HV	10	6.90	2.04	1.34	2.79	2.14
127m simulated	HV	10	7.30	2.47	1.27	4.06	3.07
Error %			5.8%	21.2%	4.6%	45.6%	43.6%
RMSE (dB)					0.8		
127m measured	HV	20	11.40	1.47	1.26	2.07	1.81
127m simulated	HV	20	6.90	1.93	0.79	2.67	2.19
Error %			39.5%	30.9%	37.1%	28.8%	21.0%
RMSE (dB)					2.3		
127m measured	HV	29	13.60	3.22	2.07	4.55	3.36
127m simulated	HV	29	11.70	2.98	1.75	4.20	2.99
Error %			14.0%	7.3%	15.1%	7.8%	10.9%
RMSE (dB)					1.0		

Table 6.12 Statistics of the measured and simulated PDF data for the Tx2-Rx0 127 m cross-polarized link.

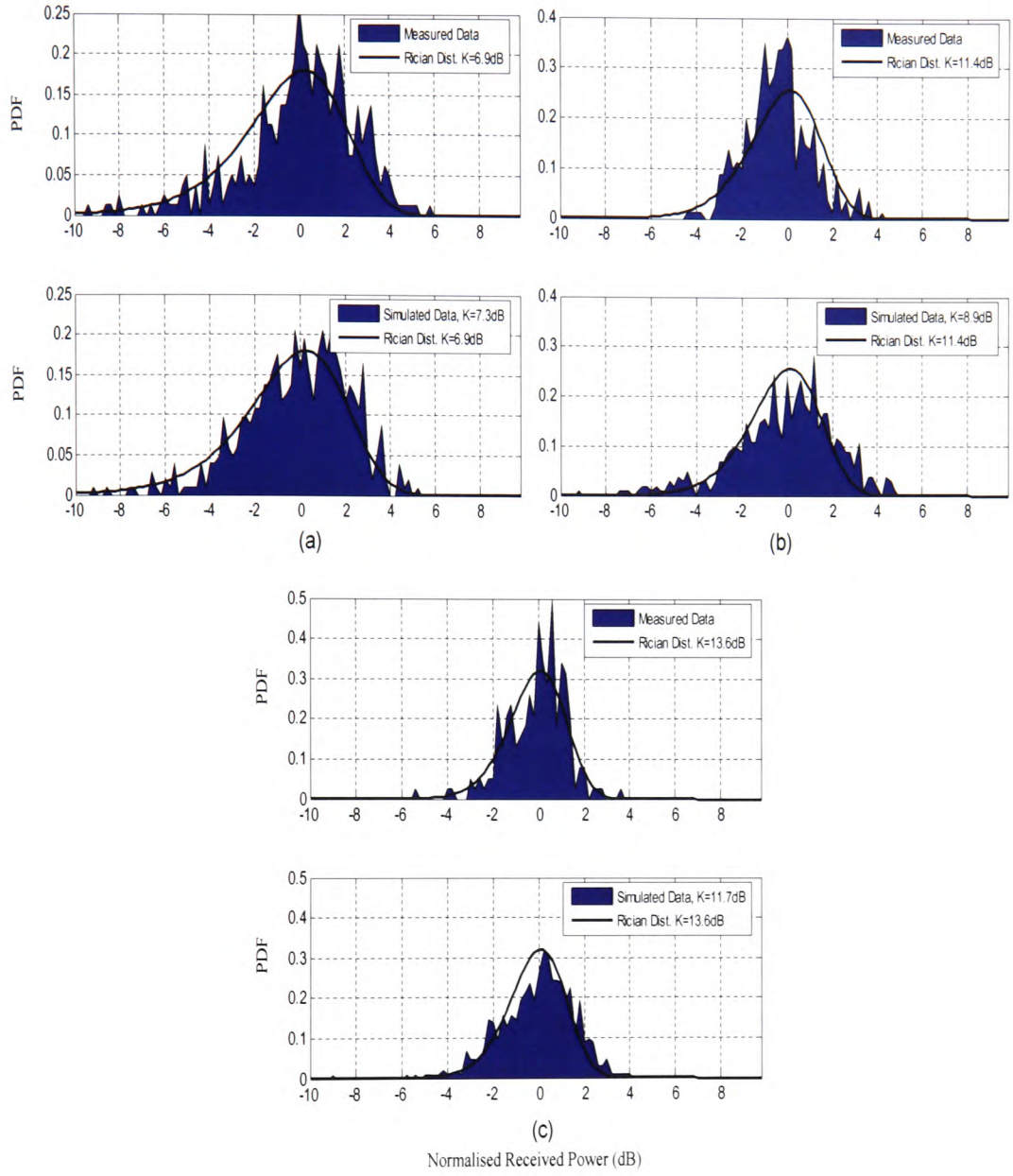

Figure 6.12: PDF of the received field and comparisons with the theoretical Rician and the distribution obtained from simulations for the Tx2-Rx0 127 m cross-polarized link using antenna gains (a) 10, (b) 20 and (c) 29 dBi.

6.2.1.4 Discussion

The PDFs of the normalized received signal power, as obtained from either measurements or model simulations (predictions) are shown and compared with a

normalized Rician theoretical distribution. The latter was noted to have superior fits for both, measured and simulated vertical and horizontal co-polarized short links, such as those of Tx1-Rx2 and Tx2-Rx0, which benefited from relatively high *K*-factor values. In such cases, the dominant field at the receiver is essentially, provided by the direct LOS path and hence, the associated PDFs are observed to be less spread about their mean values. Nevertheless, it is probably worth mentioning that the theoretical Rician distribution failed to represent data distributions that exhibited *K*-factor values greater than approximately 25 dB.

It is evident from the PDF plots that high *K*-factor values are connected with short links and high antenna gains. Due to their narrow antenna directivities, propagation paths are limited and, as a result, the randomly scattered field is reduced significantly. The standard deviation of the received field in this case is reduced, while the occurrence probability of a signal value close to that of the deterministic direct received signal in free space is increased. Conversely, the distribution of longer links exhibit a wider spread about their means, lower *K*-Factor values, due to higher levels of scatter and signal variations.
Considering the PDF obtained from the Tx2-Rx0 route, although the link was clear of any buildings, vegetation or any moving objects, the channel was observed to be time varying mainly due to the scatter arising from ground patches and metal surfaces of nearby parked cars. When compared with the other links, the signal variation, which is related to the standard derivations of a distribution, exhibited lower values of the latter and consequently higher *K*-factor values.

In contrast to the vertically co-polarized links, horizontally polarized links showed relatively less signal variations for all links. It is considered that the stability of the horizontally polarized links is not necessarily associated with better simulation predictions, due to the channel physical considerations taken into account in the EM model.

For the horizontally polarized links, it was also noted that PDF peaks always occurred at the mid points of the graphs, i.e. at their mean levels. Although the wavelength at 40 GHz

is very short, the aforesaid effect indicates the high sensitivity of the antennas used with different positions and channel variations. From Fig. 6.8, an offset is noticed between the theoretical and measured distributions for the Tx2-Rx0 link. This is believed to be due to the azimuth misalignment angle between the transmitter and the receiver, i.e. the Rx0 axis was not perfectly aligned with the Tx2 antenna axis.

Of equal importance to the co-polarization links is the cross-polarized reception of horizontally and vertically polarised transmitted waves. In a cellular structured network, cross-polarized signals determine the discrimination levels from adjacent cells. Theoretically, a cross-polarized reception should produce a zero direct field. However due to the impracticality of implementing such orthogonal antenna patterns in a realistic propagation environment, reception peaks do occur in the main- and side-lobes of the cross-polarized antenna radiation pattern. As a result, the PDF of these links showed higher variations and more deviations spread from their mean levels. In particular, these peaks are further aggravated in misaligned links and with higher gain antennas as observed from Figs. 6.9 - 6.12.

An interesting remark about the K-factor values for these cross-polarised links is noted here. With longer paths, such as the Tx1-Rx0 link, the K-factor trend was seen to increase with distance, in contrast to the trend observed in the co-polarization case. Justification of such an effect is related to the fact that in longer links, antennas can be misaligned and the chances of the cross-polarized signal being depolarized once again by vegetation or by the surface irregularities is more likely to be higher. On the other hand, for the co-polarized links of Tx2-Rx0 link and at each position along the Tx1-Rx0 route, the K-factor values did increase with higher gain antennas as expected.

In cross polarization cases, the theoretical Rician distribution still gave a good representation of the received signal for both, measurements and model simulations. This statement is true when the K-factor value was above zero. The minor discrepancy between measurements and simulations is due to the assumption of ideal orthogonal

radiation patterns in the model, which as proven from measurements, is not the case in practice.

Most of the comparisons yielded comparable statistical distributions with good agreement. In fact, all of the abovementioned remarks and notes obtained for different antennas and positions are not only applicable for the measured data, but also are valid and consistent with the simulated results obtained from the EM stochastic model. Such good agreements, supported by the RMSE calculations of the statistical parameters obtained from each of the PDF presented, can be attributed to the physical and radiowave propagation assumptions in the proposed model in terms of the channel representation, the scattering formulation, the modelling of the topography and the antenna radiation patterns.

6.2.3 Signal and *K*-Factor Levels

The purpose of this section is to investigate the attenuation of the received signal power and the variation of Rician *K*-factors with distance. The measurements conducted for Section 6.2.2 are utilized for this purpose for the three discrete receiver positions in Tx1-Rx2, Tx1-Rx1 and Tx1-Rx0 links of Fig. 5.8. The attenuation of the average received signal power is plotted on a logarithmic distance scale in Fig. 6.13 for a vertically and horizontally polarized, measured and simulated links, for receiver antenna gains of 10 and 20 dBi.

Since the channel has been adequately characterized by the Rician distribution as demonstrated in Section 6.2.1, for each receiver location of Fig. 6.13, the Rician *K*-factor is extracted from measurements and simulations, and plotted on a logarithmic distance scale as shown in Fig. 6.14.

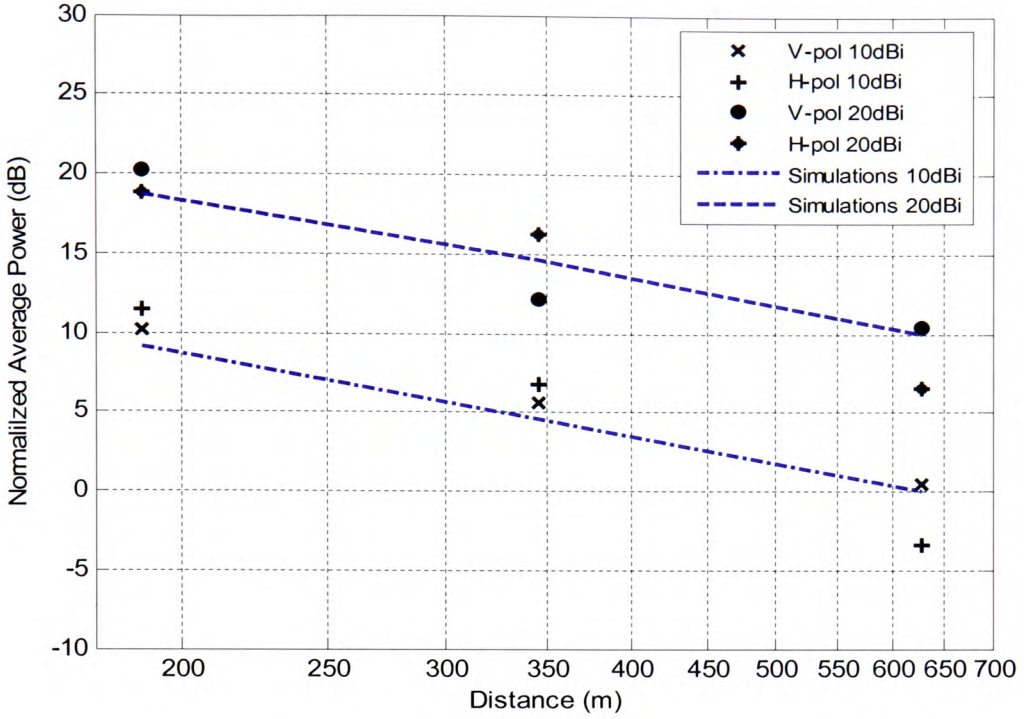

Figure 6.13: Attenuation of the received signal power with distance (logarithmic scale) for the Tx1-Rx0 route.

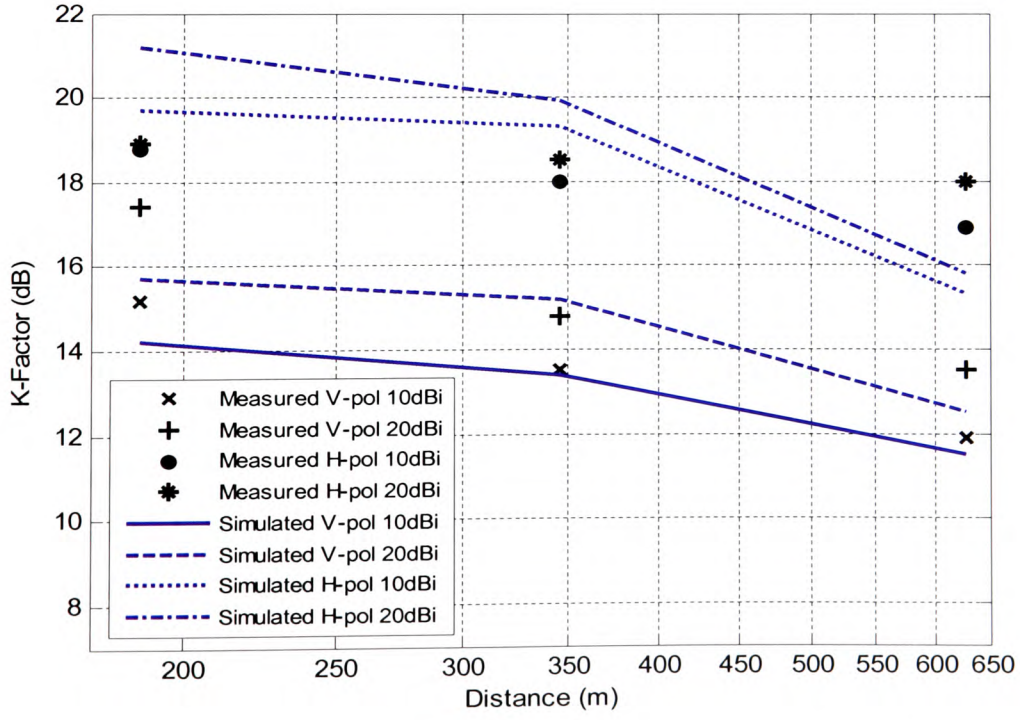

Figure 6.14: Rician *K*-factor variability with distance (logarithmic scale) for the Tx1-Rx0 route

6.2.3.1 Discussion

It is noted that for the relatively large values of the K-factor observed for LOS links with highly directive antennas, the average received power is approximately equal to the power of the direct field component and, hence, it recedes by approximately 6 dB for every doubling of the distance. In other words, the path loss is represented by a propagation exponent whose value here is close to 2. Further, for receiver antenna orientation that achieves maximum received power at each position and large values of the K-factor, the average power for the horizontal and vertical polarization cases are approximately equal.

In terms of measurements, it is clearly noted that the K-factor values of the horizontally polarized links were higher than those obtained from the vertically polarized links. This discrepancy was exceptionally high in the longer links and reached up to 5 dB, as depicted in Fig.6.14. On the other hand, in terms of the simulations, K-factor predictions did generally display good agreement with those obtained from the statistical analysis of the measured data, especially for small and medium antenna gains. From the K-factor tabulated in the Section 6.2.1, among all the measurements conducted on the IE site, the average and highest discrepancies between the measurements and predictions was 1.2 dB and 2.3 dB for co-polarized links and 1.7 and 4.5 dB for cross-polarized links, respectively.

The accuracy of predicting, as well as measuring, large values of K-factors for high gain and narrow beamwidth antennas in boresight LOS links is generally affected by the alignment of the two boresight axes and a number of measurements needs to be conducted to improve the accuracy of such estimates. As expected, although the K-factor exhibits small variations for relatively small antenna gains (10-20 dBi), it rapidly increased for higher gains (29 - 44 dBi). The monotonic decrease of the K-factor with distance for the same antenna gain is also noted.

6.3 University of Glamorgan Campus

The selected campus site and transmitter-receiver arrangement established a short NLOS path link via building reflections in an urban environment, which can provide useful insight into the deployment of such NLOS links. An aerial photo of the measurement site showing the transmitter and receiver position and measurement setup was given in Fig. 5.7.

Predictions of the received power level as a function of the azimuth angle in this propagation scenario is attempted in the EM model by accounting for the multiple reflections and scattering mainly from the vertical surfaces of the surrounding buildings. These predictions are compared with the conducted measurements in the following section. During the measurements a 10 dBi gain antenna was used on the transmitter side to illuminate the widest extent of the façade of building A, while at the receiver side, a 29 dBi gain antenna was utilized for its narrow 3 dB beamwidth and spatial discrimination.

6.3.1 Received Average Power of the Azimuth Plane

Average power measurements are performed for a number of azimuth angles of the receiver antenna beam for the UC site of Fig. 5.7. The receiver scanned the azimuth plane in steps of 2° in a clockwise rotation sense, starting from $\varphi_R = 0$. One objective of the measurements is to illustrate reflection and building scattering contributions in urban cells. Another objective was to test the ability of the model to predict the average power for different antenna orientations in a relatively rich multipath environment. Fig. 6.15 shows the average received power over the azimuth angle of the receiver antenna axis, obtained from measurements and simulations.

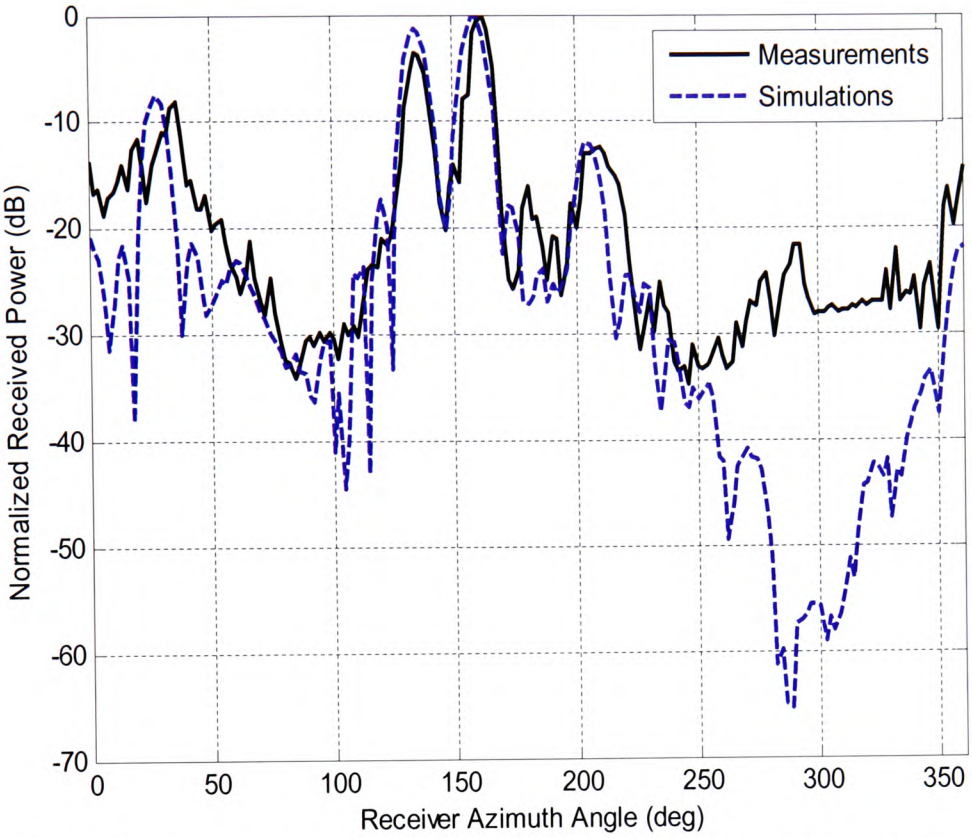

Figure 6.15: Average power gain variation vs. azimuth angle of the receiver 29 dBi antenna rotation.

Moreover, for illustration purposes, the 360° measured received azimuth radiation pattern is represented by a polar plot (coloured in blue) and placed over the receiver's actual position in the aerial photo of Fig. 6.16, showing exactly the orientation and the amount of reflection and scatter contributions of peaks from different building surfaces at each of the measured angles. It is also clear that there are several angles at which the received power can be severely low.

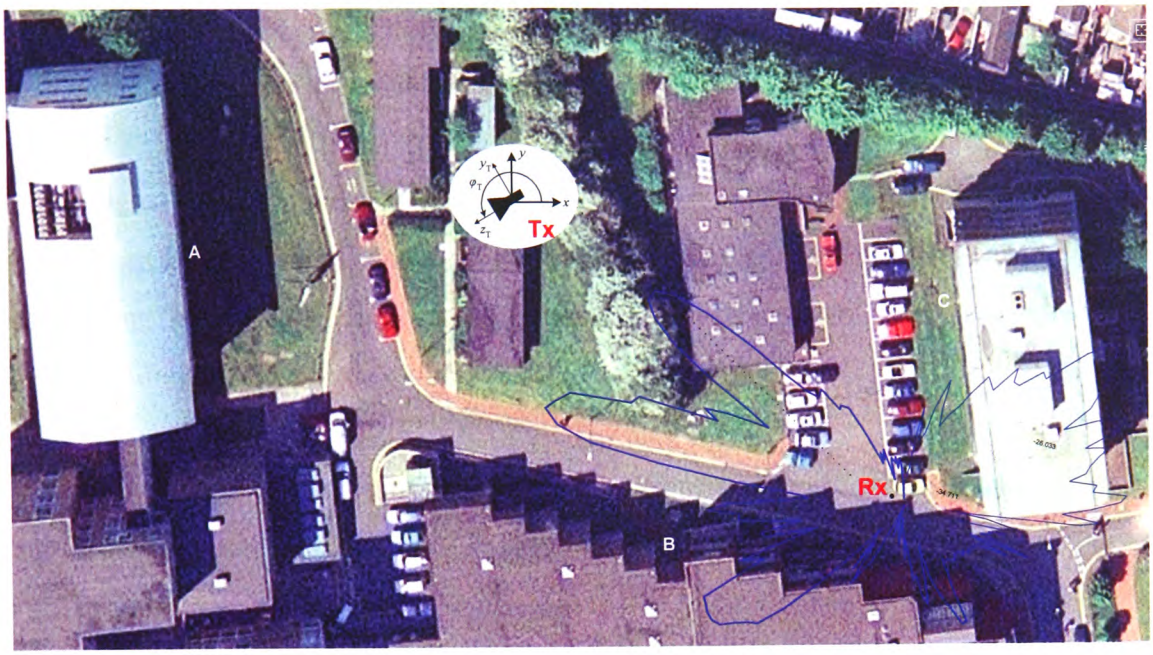

Figure 6.16: Polar plot of the received radiation pattern overlaid on the receiver position.

6.3.1.1 Discussion

From Fig. 6.15, the direct field due to transmit antenna side-lobe radiation was found to peak at an angle of 134° of the receiver beam. At orientation angles of 162° and 36°, the received signal is believed to be dominated by reflections from building A in front of the transmitter and building C behind the receiver location, respectively (see Figs. 5.7 & 6.16).

The fact that the direct field (at the angle of 134°) is only approximately 2 dB below the main reflected field (at an angle of 162°) received from the façade of building A is not surprising and can be explained as follows. From the geometry of the measurement setup shown in Fig. 5.7, due to the orientation of the transmitter, the angle between the main axis of the transmit and receive antennas was approximately 115°. Considering the measured radiation pattern of the 10 dBi transmit antenna given in Fig. 5.5, the gain obtained at the observed side-lobe angle is approximately -22.5 dB. By taking into account the average reflection coefficient of the façade surface of building A, which is

expected to be in the region of -20 dB, the measured 3.8 dB difference between the direct and reflected field appears reasonable.

A third pattern lobe at around 210° is observed. This is believed to be due to double reflection from building A and subsequently from building B. This effect is incorporated by introducing an image of the transmitting antenna with respect to the plane of the facade of building A, attenuated by the average reflection coefficient.

The discrepancy between measurements and predictions for observation angles from 244° to 350° is firstly due to scattering mechanisms from outside the main topography of Fig. 5.10 not included into the model; secondly, due to the use of theoretical radiation patterns for the transmitter and receiver antennas; and, thirdly, due to the side-lobe peaks of the 29 dBi lens-horn antenna that augmented the reception of reflections from buildings B and C.

6.3.2 Building Surface Scatter Maps

A map of the scattered field from a surface can be obtained from the digitization of building information provided by GIS data and digital photos. An example of such a scatter map is shown in the surface plot of Fig. 6.17 & 6.18. These surface plots show the rectangular array of the elements sampled representing the illuminated façade surface areas of building A and C respectively. The colour plot essentially illustrates the contribution to the scattered field of each constituent elements of the surface and depicts which parts of the surface provide the most significant contributions for a given transmitter and receiver antenna orientation and location with respect to the surface. This is shown by the colour code bar of the normalized average power displayed on the right of the above mentioned figures.

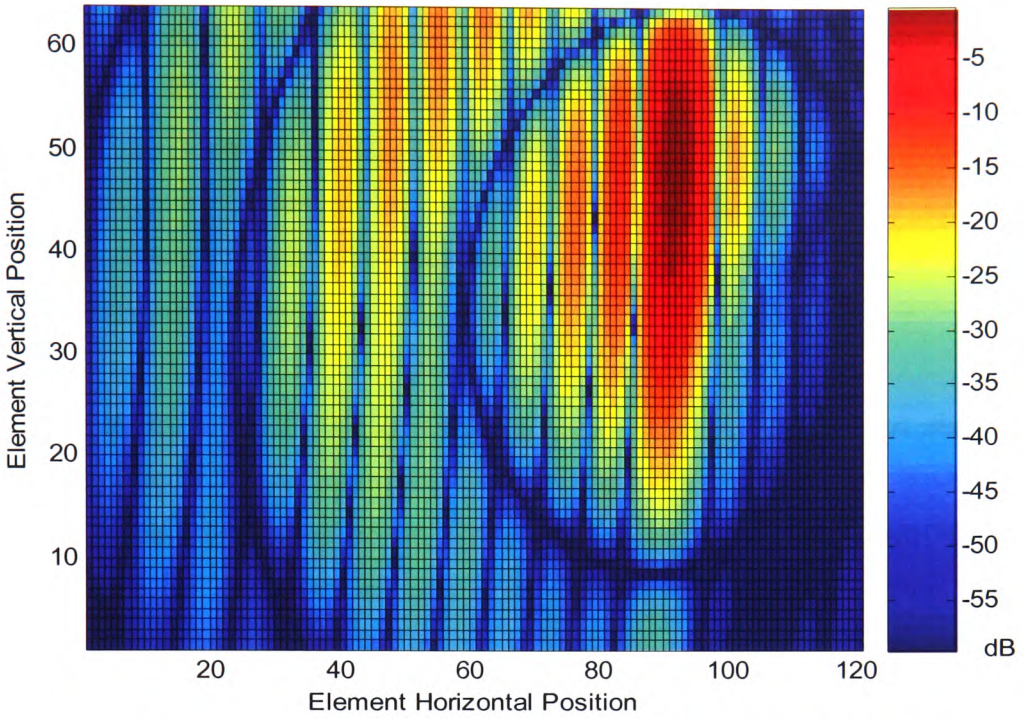

Figure 6.17: Pseudo-colour scatter map of the façade surface of building A.

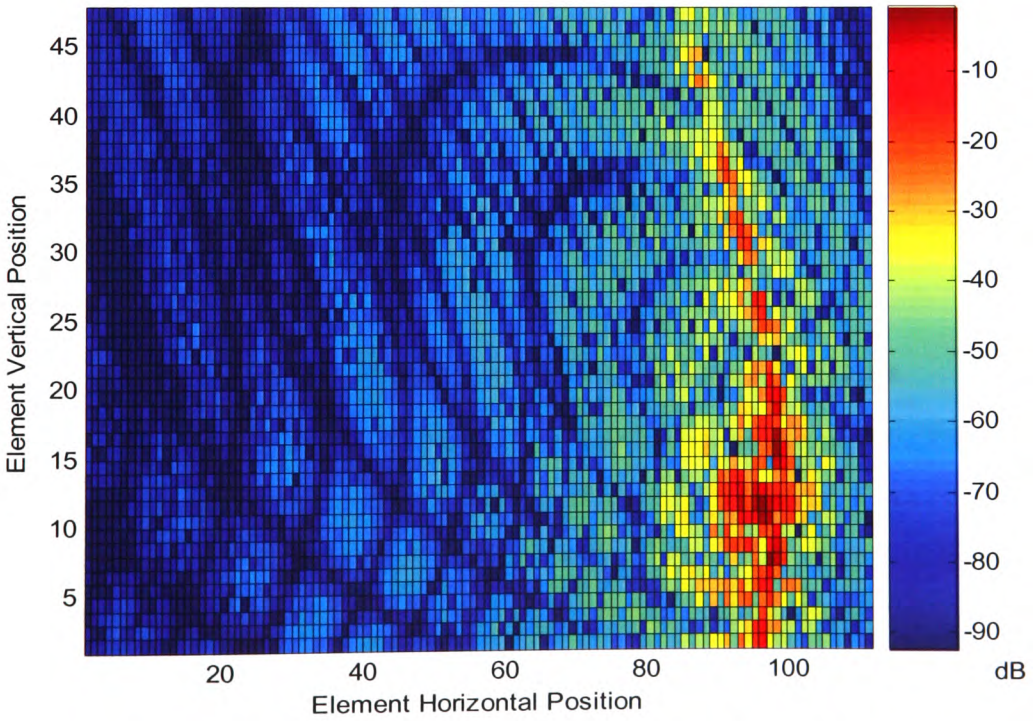

Figure 6.18: Pseudo-colour scatter map of the façade surface of building C.

6.3.2.1 Discussion

For building A, as shown in Fig. 6.17, surface elements around the point of specular reflection provide contributions in the range of 0 to -15 dB relative to the total received power, and form a narrow vertical strip on the façade between elements 80 and 100 of the horizontal axis. Areas of the façade that are not illuminated by the transmitter antenna main beam provide rather negligible contributions of the order of -15 to -30 dB below the maximum received power.

The scattering from the façade of building C is rather more involved since it is not illuminated directly by the main beam of the transmitter and reflects fields emanating from the side- and back-lobe of the transmitter antenna. The main contributions to the received power are due to reflections from a direct field stemming from the transmit antenna side-lobe, and the second due to second order reflections from building A and subsequently from building B. According to the simulations in Fig. 6.18, areas of the surface with a substantial contribution to the scattered field are very limited and are observed to be isolated in the bottom-right corner of the façade. However, as pointed out in the discussion of the azimuth radiation patterns of Fig. 6.15 there is a deviation between predictions and measurements. Most of the façade of building C is observed to have rather more significant amount of contributions to the received signal. The explanations for these discrepancies are given in Section 6.3.1.1.

6.3.3 Average Power and *K*-Factor for Different Antenna Gains

At the particular azimuth angle of 162° (Fig. 6.15) in the direction of building A where the maximum power was received three other antennas with gains of 10, 15 and 20 dBi were also used for power dispersion measurements. The objective was to illustrate how these antennas would perform and to compare the power statistics to those with the 29 dBi antenna used at the receiver for the azimuth measurements. The average mean power level received from each antenna together with the extracted *K*-factor values are plotted in Fig. 6.19, showing performances of the antennas in terms of the main power statistics.

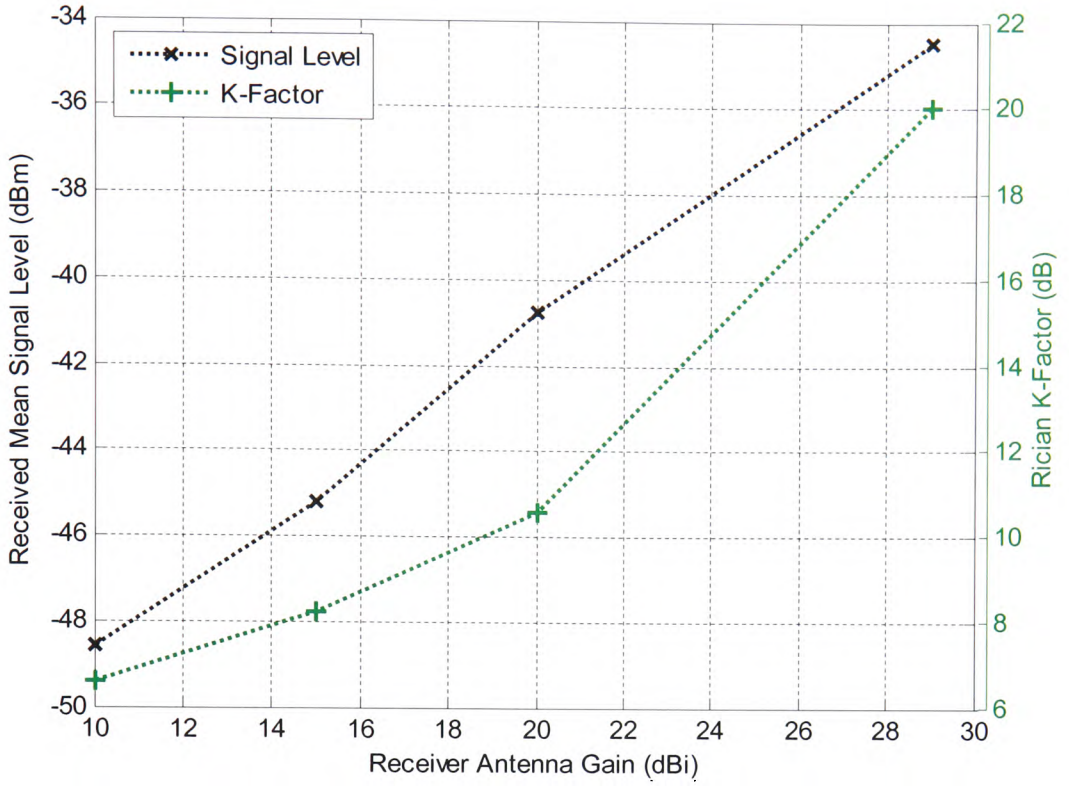

Figure 6.19: Comparison of the average received signal power and the Rician *K*-factor for different antenna gains at a fixed azimuth angle of 162° (Fig. 5.10).

6.3.3.1 Discussion

In Fig. 6.19, average signals and *K*-factor values are shown to increase with higher antenna gains for the main NLOS link reflected from building A of Fig. 5.7. Due to the reflection losses, the received signal levels captured were relatively low for the 10 and 15 dBi gain antennas. The corresponding *K*-factor values obtained were approximately 6.6 and 8.2 dB, respectively. Higher *K*-factors are always preferred, although threshold values of acceptability in a wireless system depend on how the *K*-factor relates to the relevant communication channel performance metrics, such as coverage and reliability constraints, and the specific applications. For example, in an ideal LMDS network, in order to support sufficient modulation schemes, *K*-factor values are required to be above 10 dB. Hence, in establishing a reliable link in this NLOS propagation scenario an antenna gain of less than 15 dBi had to be ruled out in this measurement setup.

The *K*-factor increased steeply between the 20 and 29 dBi gain antennas (from 10.5 to 20 dB). This indicates an inherent capability of such higher gain antennas in suppressing unwanted scatter signals, captured by the wider beamwidth of lower gain antennas (such as the 10 dBi) in dense multipath environments. For the same reason, the 29 dBi antenna was deemed to be the best antenna choice for conducting the azimuth plane measurements.

Although the results from the NLOS link measurements were rather satisfying in terms of the Rician *K*-factor, especially at the higher antenna gains, the effects of delay spreads and intersymbol-interference are amongst other important metrics that require further investigation in order to establish reliable NLOS propagation paths. The results obtained here are indicative of the feasibility of such links and should not be generalized, since different paths will have different propagation characteristics causing the received signal to vary considerably in strength and delay. Furthermore, the quality of the signal is expected to also vary depending on the exact location of the receiver and any significant motion in the channel is expected to further enhance the fading effects.

6.4 Cellular Interference Measurements

The main two frequency and polarization reuse plans and strategies for cellular LMDS networks are reported and discussed in Section 2.8. These plans, referred here to as the Sub-Optimum Plan (SOP) and the Alternative Plan (AP), are designed to provide optimum capacity and spectral efficiency. However, as acknowledged in the literature, these plans generate co- and adjacent-channel inter- and intra-cell interference due to the LOS constraints between the transmitting and receiving (directional) antennas. Such operational constraints are sought to be investigated since they limit the system capacity and affect link performance in a fully deployed network. The interference scenarios that are expected to arise from these plans are derived in detail in Section 2.9. One of the four scenarios reported for each plan was chosen for this investigation, namely case (I) of the SOP and case (I) of the AP. These are arguably of most concern in a fully deployed LMDS network. During the measurements, the 20 dBi horn antenna was always used at

the transmitter, which due to its moderate radiation beamwidth, was the most suitable transmission antenna for interference analysis. Equivalently, in a commercial network, a sectored antenna with directional beam patterns is most likely to be employed at the BTS. At the receiver side, a range of receive antenna gains (10 - 44 dBi) is recommended in the technical literature and, hence, were employed in the measurements.

The outcomes are presented in terms of the PDF of the normalized SIR between the desired and unwanted links (see Fig. 5.1), as obtained from measurements and model predictions. Each PDF is individually compared with the theoretical distribution given by Otteing's model in Eq. (4.96). The Rician parameters, which define Otteing's theoretical distribution, are extracted from measured and predicted data. It is worth noting here that in Otteing's theoretical distribution of the SIR displayed in the following sections; the Rician parameters used in Eq. (4.96) are those obtained from measurements.

6.4.1 *K*-Factor vs. Antenna Gains

This section endeavours to examine the model predictions of *K*-factor values compared to those extracted from field measurements for the desired and interfering links, utilizing a range of receiver antenna gains. Higher *K*-factor values (K_0) are naturally expected and required for the desired link since they correspond to better detection levels and link availability, whereas higher values for the interference link (K_1) are undesired and imply stronger interfering levels and consequently, greater outage probabilities. The following subsections examine the most common and occurring interference scenarios which are the co- and adjacent-channel of the SOP and AP frequency-reuse plans, respectively.

6.4.1.1. SOP Scenario I

This typical inter-cell co-channel, co-polarization scenario was illustrated in Fig. 2.6(a). The interference occurs between $F1DH_1$ & $F1DH_2$ as well as between $F2UV_1$ & $F2UV_2$ where as defined in Section 2.9; "F" refers to the frequency channel, "U" & "D" refer to the transmission direction (uplink or downlink), "V" & "H" refer to the transmission polarization (vertical or horizontal) , and finally, the numeric subscript at the end refers to

the number of the associated BTS. As an example of this interference scenario, users A and B in Fig. 2.6, not only operate at the same frequency band and polarization, but also lie within the boresight of a co-channel path at the uplink or downlink routes. Moreover, from the same figure it can be noted that a similar inter-cell co-channel scenario does occur between BTS 1 & 3, 2 & 4 and 3 & 4. Accordingly, it is possible that a BTS is affected by multiple co-channels on the uplinks from other adjacent BTS's, as in $F2UV_1$ & $F2UV_2$ & $F2UV_3$. Such multiple interference effects, however, have not been investigated due to their rarity. In terms of measurements, the interference link was chosen to be Tx1-Rx0, whilst the desired link was chosen to be Tx2-Rx0 shown in Fig. 5.1. Fig. 6.20 compares the *K*-factors obtained from measurements with the predictions using the model for the desired signal and co-channel interference paths.

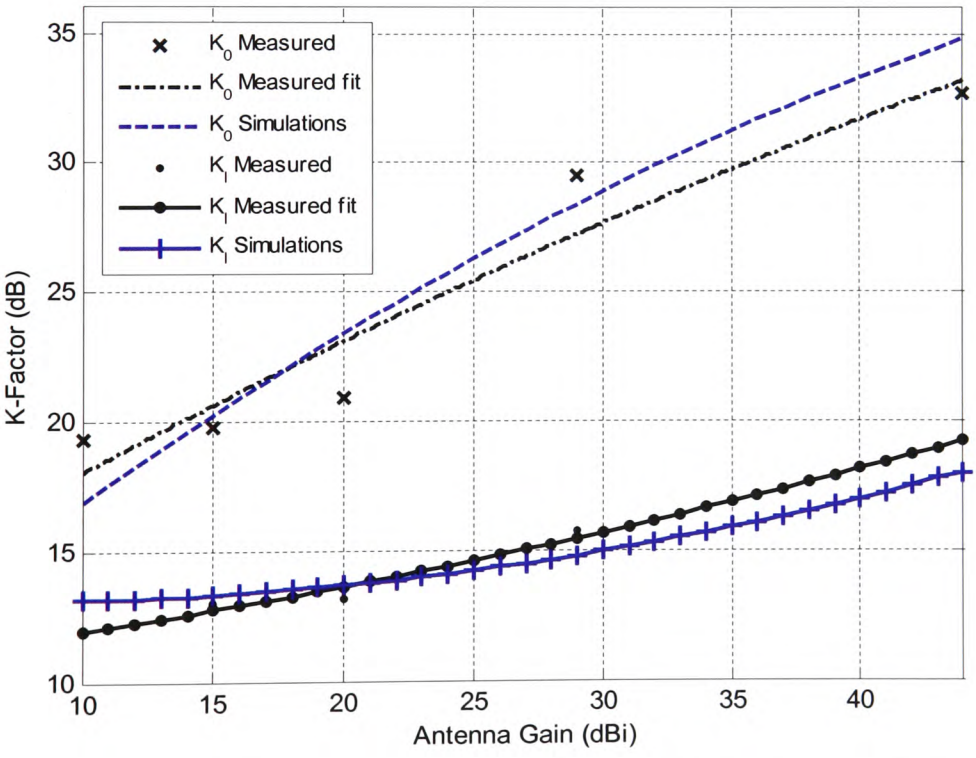

Figure 6.20: Rician *K*-factor values obtained for a number of antenna gains for the case of SOP (I) $F2UV_1$ & $F2UV_2$ interference scenario.

6.4.1.2. AP Scenario I

Referring to Fig. 2.6(b), intra-cell co-channel, cross-polarization interference is observed at the downlink ($F2DV_4$ & $F2DH_4$) and uplink ($F1UH_4$ & $F1UV_4$) and is mainly experienced by users that are near to the edges of adjacent cells, due to the depolarization effects of scatter, vegetation or rain. This scenario occurs at every single BTS and is referred here as adjacent-channel interference since it is caused by adjacent cells. As an example, users F and G in Fig. 2.6(b) may encounter a co-channel, cross-polarization interference when either of them or both are positioned close to the cell boundaries.

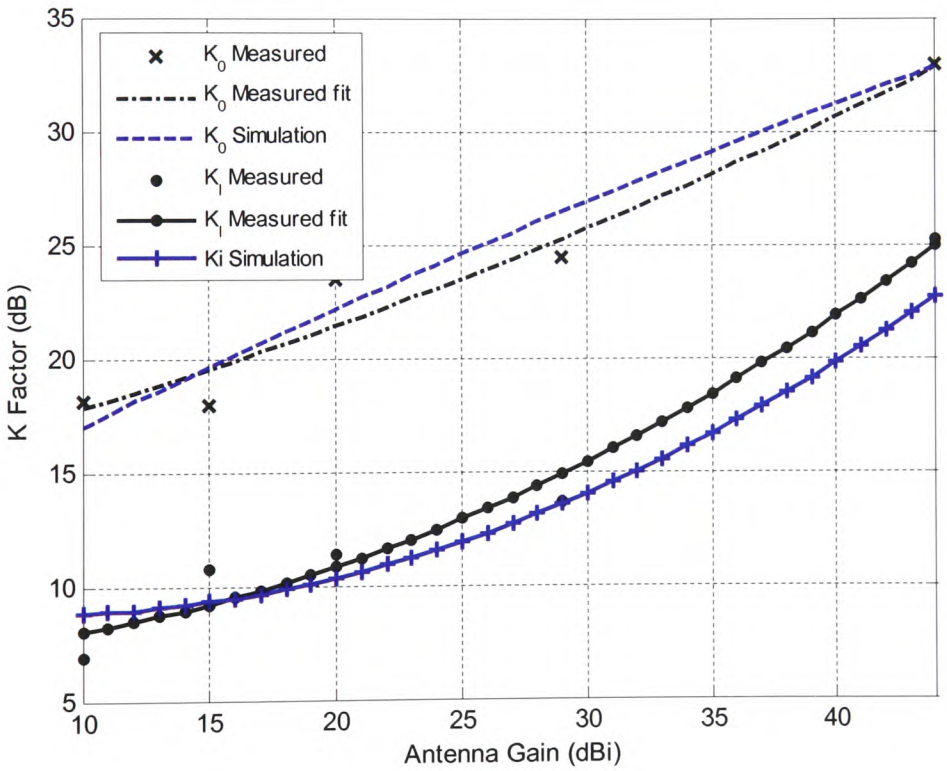

Figure 6.21: Rician *K*-factor values obtained for a number of antenna gains for the case of AP (I) $F1UH_4$ & $F1UV_4$ interference scenario.

In an actual network deployment, a lower antenna gain may not be suitable in such a case, since it may result in the reception of interfering signals from a wide reception angle. On the other hand, a high-gain antenna may intercept or transmit high levels of

cross-polarized signals through the main and side-lobes. Therefore, the selection of a suitable antenna gain becomes critical. In terms of measurement implementation, Tx2-Rx0 was chosen to be the desired link while Tx3-Rx0 was chosen to be the interfering link shown in Fig. 5.3. Results of the K-factor values obtained from both, measurements and the model for a worst-case scenario, whereby the LOS path of the receiving antenna is within the boresight of the desired and the interfering transmissions are depicted in Fig. 6.21.

The results obtained from the SOP (I) co-channel interference and from the AP (I) adjacent-channel interference shown in Figs. 6.20 and 6.21 are only for one set of transmission, i.e. either an uplink or a downlink. A full set of results for K_0 and K_I obtained from measurements and model simulations are given in Table 6.13. Additionally, for each interference scenario, the ratio of the statistical scattered fields given by Otteing's theoretical SIR distribution of Eq. (4.96), as measured and predicted from the desired and interfering links is provided for comparison purposes with a corresponding RMSE evaluation.

6.4.2 Signal-to-Interference Ratio

This section compares the raw data of the normalised SIR PDF distributions of measured and predicted results and compares them with the theoretical Oetting's distribution of the SIR. The latter is plotted with a solid line and is provided by Eq. (4.96). The PDF comparisons shown in Figs. 6.22 and 6.23 are for 10, 20, 29 and 44 dBi receiver antenna gains employed for the co- and adjacent-channel interference scenarios discussed in the previous section. Statistical measures are given in the previous section by Table 6.13 in terms of the Rician K-factors and the ratio of the scattering field of the desired and interfering links.

SOP1 Co-Channel Interference							AP1 Adjacent-Channel Interference						
Ant. Gain (dBi)	**Scenario**		***Ko* (dB)**	***Ki* (dB)**	***b* (dB)**	**Mean Error %**	**Ant. Gain (dBi)**	**Scenario**		***Ko* (dB)**	***Ki* (dB)**	***b* (dB)**	**Mean Error %**
10	$F1DH_1$ & $F1DH_2$	Measured	18.2	16.9	25.1	7.7%	10	$F1UH_4$ & $F1UV_4$	Measured	18.2	6.9	35.6	4.7%
		Simulated	19.4	15.3	23.3				Simulated	19.4	7.3	35	
	RMSE			1.5				RMSE			0.7		
15	$F1DH_1$ & $F1DH_2$	Measured	17.92	17.5	25.3	9.6%	15	$F1UH_4$ & $F1UV_4$	Measured	17.9	11	34.2	9.3%
		Simulated	19.82	15.84	23.1				Simulated	19.5	9.3	33	
	RMSE			1.9				RMSE			1.5		
20	$F1DH_1$ & $F1DH_2$	Measured	23.4	18	22.7	9.0%	20	$F1UH_4$ & $F1UV_4$	Measured	23.4	11.4	25.7	15.0%
		Simulated	23.8	15.8	19.7				Simulated	23.8	6.9	26.7	
	RMSE			1.9				RMSE			2.0		
29	$F1DH_1$ & $F1DH_2$	Measured	n/a	n/a	n/a	n/a	29	$F1UH_4$ & $F1UV_4$	Measured	24.8	13.6	22.3	8.6%
		Simulated	n/a	n/a	n/a				Simulated	24.1	11.7	24.3	
	RMSE							RMSE			1.5		
44	$F1DH_1$ & $F1DH_2$	Measured	n/a	n/a	n/a	n/a	44	$F1UH_4$ & $F1UV_4$	Measured	33.5	25	13.7	8.4%
		Simulated	n/a	n/a	n/a				Simulated	31.6	22.5	15	
	RMSE							RMSE			1.9		
10	$F2UV_1$ & $F2UV_2$	Measured	19.2	11.9	10.4	8.1%	10	$F2DV_4$ & $F2DH_4$	Measured	19.2	2.3	16.3	20.6%
		Simulated	17.5	11.5	11.7				Simulated	17.5	4.4	19.9	
	RMSE			1.1				RMSE			2.5		
15	$F2UV_1$ & $F2UV_2$	Measured	19.8	13.1	11.6	8.2%	15	$F2DV_4$ & $F2DH_4$	Measured	19.8	n/a	n/a	9.9%
		Simulated	18	11.9	10.7				Simulated	18	n/a	n/a	
	RMSE			1.3				RMSE			1.8		
20	$F2UV_1$ & $F2UV_2$	Measured	20.9	13.5	11.4	7.1%	20	$F2DV_4$ & $F2DH_4$	Measured	20.9	2.6	18.9	24.9%
		Simulated	18.9	12.5	10.9				Simulated	18.9	3.7	23.2	
	RMSE			1.2				RMSE			2.5		
29	$F2UV_1$ & $F2UV_2$	Measured	29.4	15.7	10.1	9.0%	29	$F2DV_4$ & $F2DH_4$	Measured	29.4	16.9	19.6	7.9%
		Simulated	28.3	16.7	8.4				Simulated	28.3	15	17.9	
	RMSE			1.3				RMSE			1.6		
44	$F2UV_1$ & $F2UV_2$	Measured	32.7	19.8	7.5	5.8%	44	$F2DV_4$ & $F2DH_4$	Measured	32.7	25	19.3	6.5%
		Simulated	33.8	17.8	7.2				Simulated	33.8	22.5	18.1	
	RMSE			1.1				RMSE			1.6		

Table 6.13 A full list of measured and predicted statistical parameters for the co- and adjacent-channel interference scenarios.

As the antenna gain is increased, the beamwidth is decreased and hence, less, scattered field contributions are expected. Although this effect is evident in the co-channel distributions, it is less obvious in distributions obtained from the adjacent channel interference, mainly due to the difference in the distance between the desired and interference hubs and the non-orthogonal cross polarization radiation patterns of the antennas used. Consequently, it is noted from Fig. 6.22 and 6.23 that the co-channel interference distributions are much less spread around their mean values when compared to the adjacent-channel interference (SIR) distributions.

Moreover, from the values obtained in Table 6.13 for parameter b, which represents the ratio of the scattered fields, the fact that this ratio decreases with higher antenna gains is reasonable, since antennas with high gains antennas, although their main beamwidths are more directional, their radiation patterns will have higher levels of side-lobes. Bearing in mind that the axis of the interfering antenna is not necessarily precisely aligned with that of the receiver antenna, more scatter contributions will result from the interfering link due to these side-lobes. Accordingly, values obtained for b decrease with higher antenna gains.

6.4.3 Discussion

Overall, Rician K-factor values increased with higher gain antennas for the desired and interference links. For the co-channel interference link, the K-factor values were approximately found to be in the range of 12 -19 dB. The fact that these were higher than the adjacent-channel interference link values that ranged between 8 - 25 dB does not make the latter type of interference less significant than the former. In actual fact, the radio link of the adjacent-channel path is much shorter in length, clearer from any buildings or vegetations, and most crucially, is discriminated by cross-polarization. The effects of these factors were also observed in the signal trend analysis of Section 6.2 for longer cross-polarized links. In general, longer links can be slightly misaligned and, hence, effects of the side-lobes of the receiving antenna can become more significant.

Chapter Six

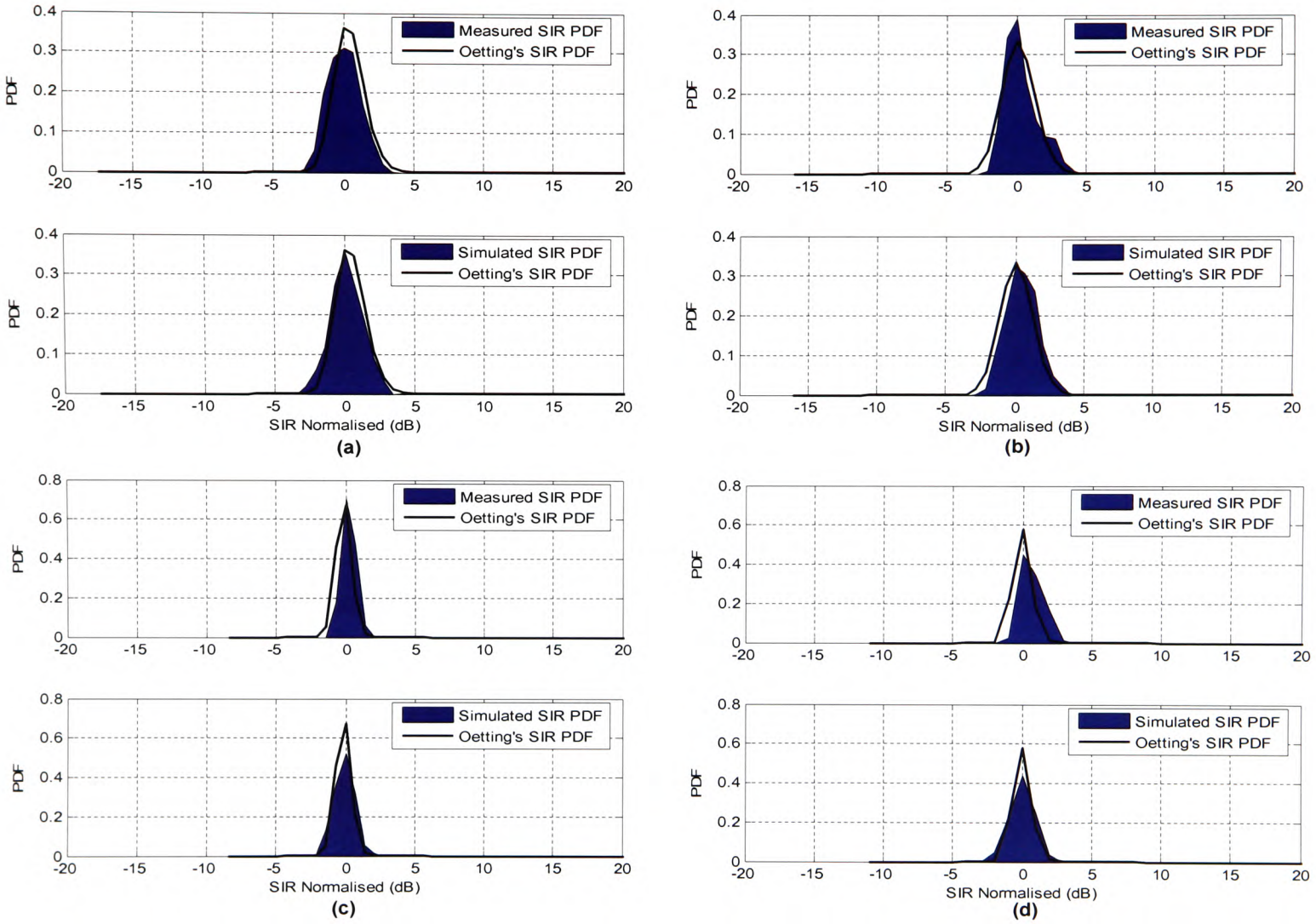

Figure 6.22 Normalised PDF of the co-channel SIR interference for a 20 dBi transmit and (a) 10, (b) 20, (c) 29, (d) 44 dBi receive antenna gains.

Chapter Six

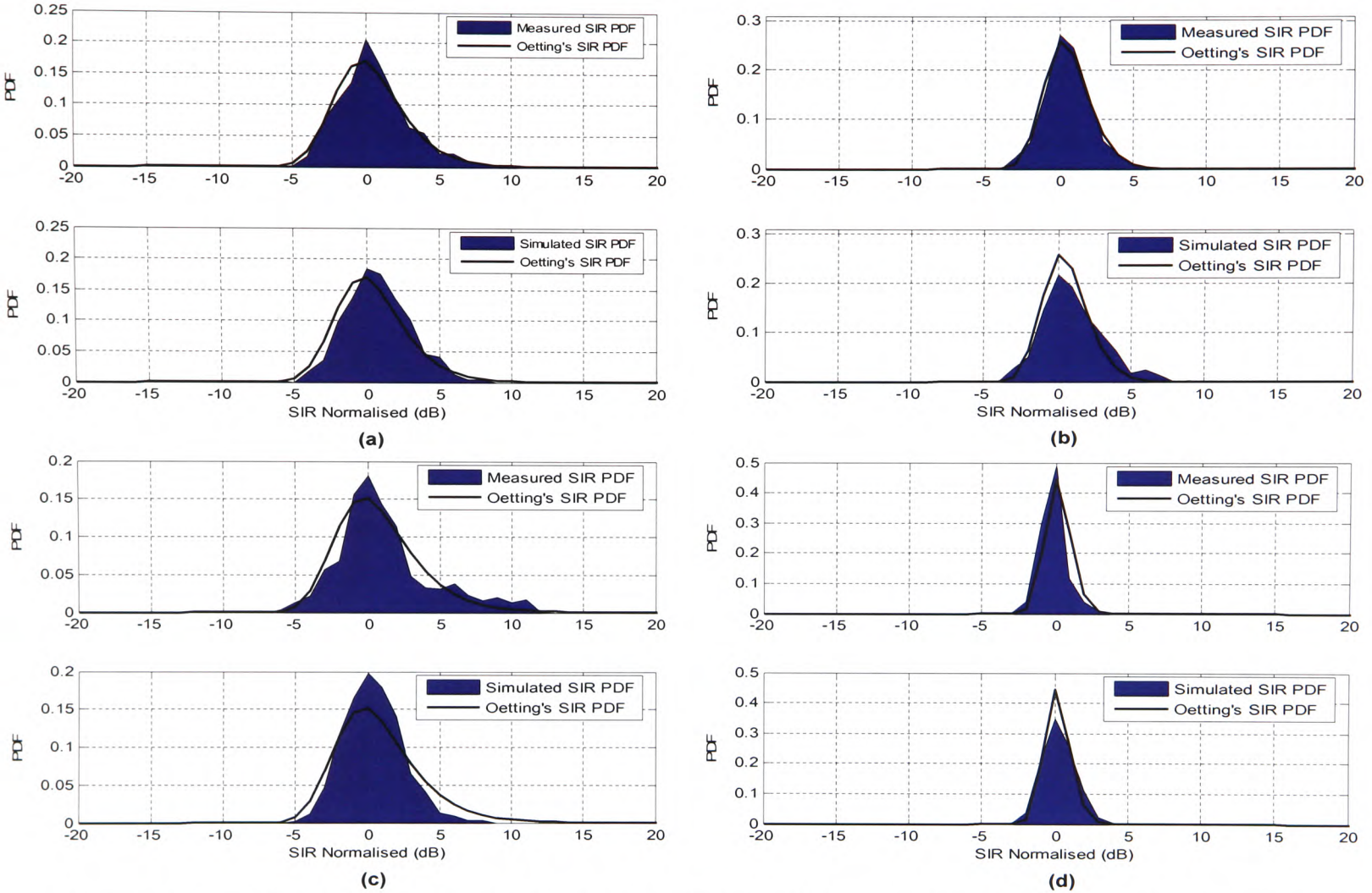

Figure 6.23 Normalised PDF of the adjacent-channel SIR interference for a 20 dBi transmit and (a) 10, (b) 20, (c) 29, (d) 44 dBi receive antenna gains.

Additionally, the likelihood of higher accumulation of vegetation and rough surfaces between transmit and receive hubs in longer distance links could have depolarized the originally cross-polarized signal, thus resulting in K-factor values that increased with the distances measured.

Moreover, in the adjacent channel interference, despite the polarization discrimination provided by the horn and lens-horn antennas, it was noted that for a cross-polarization reception, sufficient K-factor values for the interfering link are still probable, particularly with the high antenna gains (29 and 44 dBi). As such, adjacent-channel interference associated with the AP frequency-reuse scheme is perceived to be just as harmful as co-channel interference found in the SOP. The effects of the latter however, did improve with higher antenna gains, as the difference between K_0 and K_1 increased from approximately 5 dB to 13 dB for receiving antennas gain of 10 to 44 dBi, respectively, while for the adjacent-channel interference, this difference was constantly 7.5 dB for any antenna used. A higher difference between the values of K_0 and K_1 is clear indication of less interference levels.

The comparison of measurement statistics with those obtained from predictions of the model were consistent and yielded good agreement as shown in Table 6.13. From the interference PDF and comparisons with the theoretical curve, it becomes evident that the SIR observes the distribution of the ratio of two Rician channels (desired and interferer), given by Oetting's distribution. The theoretical distribution depends on the K-factor and the ratio of scattering field powers of the two links, as derived from the statistical analysis of the measured data samples and application of Eqs. (4.96) and (4.97). The probabilistic distributions and the underlying statistical parameters of the theoretical expressions show good agreement with measured data and signal samples obtained from model predictions.

Within this assessment, the SOP plan is seen to be best suited for the following radio links: (i) long cell paths with radii of 1 km or larger and low receiver heights, where the co-channel power is most likely to decrease with larger distances; (ii) in shorter urban cells that benefit from adequate building shielding to the interfering BTS. In both cases, highly directional antennas are strongly recommended in order to avoid any unwanted alignments of the victim receiver with the interfering BTS.

On the other hand, since the AP utilizes adjacent-channels via cross-polarization discrimination, it is expected to be more capable of serving small cells with a large number of users. Receivers with smaller antenna gains (up to 20 dBi) are highly recommended for the AP (unlike the SOP), since: (i) they are less affected by cross-polarized signal peaks that appear in the main- and side-lobes of highly directional antennas, and (ii) their antenna beamwidths are not required to be precisely aligned with the transmitter. Consequently, to minimize the effects of building scatter and rain depolarization, the AP is probably best suited for links that are short to medium in length, with sparse vegetation between the transmit and receive hubs. Elevation of antenna heights in the case of AP is not a concerning issue and can probably aid system performance by keeping them as high as possible and away from any vegetation.

Central to the above observations is the argument regarding the selectivity and suitability of the pyramidal-horn and lens-horn antennas. Pyramidal-horns have practically limited gains that do not exceed 20 dBi at millimetre-wave length frequencies and, consequently, suffer from scatter and cellular interference reception due to their relatively wide beamwidths. At the same time, these horns are more compact, less complex and widely available at a low cost. Lens-horn antennas, on the other hand, mainly benefit from their high gains; however, they are expensive, more complex in their design, and more vulnerable to alignment and cross-polarization problems associated with their narrow beamwidths and side-lobe peaks.

In general, higher antenna gains are beneficial in obtaining the required dominant signals from desired transmitters. However, due to their narrow beamwidths, they are much more susceptible to alignment problems and, similar to satellite dishes, self-installation might be problematic for end-user customers. From the measurements conducted, given that distant interfering sources are not within the receiver antenna boresight, moderate to high gain antennas can be more preferable provided that they are precisely aligned. From an operator point of view, the selection of receiving antennas in an actual network deployment will not only depend on the interference mechanisms and frequency-reuse cell plan employed, but also on the capital cost and system requirements for throughput and quality of service.

CHAPTER SEVEN

SUMMARY, CONCLUSIONS & FUTURE WORK

7.1 Summary

The final chapter of this thesis is devoted in presenting a summary of the work undertaken and achievements accomplished against the original aims and objectives. In Section 7.2, a general summary of the thesis is given, outlining the results achieved. Section 7.3 summarizes the contributions resulting from the EM stochastic radio propagation model. This section also summarizes the author's contribution to the technical literature. Finally in Section 7.4, potential avenues of future work mainly concerning the model's applications are proposed.

7.2 Review of the Thesis

The ever increasing demand for broadband multimedia communications coupled with the new millimetre-wave spectrum bands released by radio regulation authorities throughout the world has motivated extensive research in establishing a new generation of wireless systems, namely, the Local Multipoint Distribution Systems (LMDS) also known as Broadband Fixed Wireless Access Systems (BFWA).

Radio communication systems rely in their design and implementation on the availability of reliable propagation models that can describe accurately the interaction of radiowaves with any obstacles present in the radio path between the transmitter and receiver.

The main objective of this thesis was to implement a physical millimetre-wave propagation model aimed at facilitating design and planning of future cellular LMDS networks. Due to the lack of such radio propagation models, the main considerations in the proposed model were set as follows:

- Satisfactory electromagnetic and stochastic representation of the millimetre-wave channel.
- The characterization and modelling of the scattering from irregular surfaces in urban and suburban propagation environments.
- Incorporation of realistic transmit and receive antenna radiation patterns.
- Utilization of GIS data for accurate positioning and data processing of surface information. These surfaces to include building rooftops, facades and ground patches.

The above factors were addressed through the combination of well-established electromagnetic scattering methods and field measurements. The experiments have been conducted within the University of Glamorgan and a neighbouring Industrial Estate in order to acquire deeper insight into the behaviour of the urban channel at millimetre-wave frequencies, as well as towards the aim of validating the proposed model.

Chapter one provides a brief introduction on fixed wireless access systems operating at the millimetre-wave frequency bands and the need of statistical models, as opposed to deterministic ones such as ray-tracing. Further, the motivations and objectives for this research are also outlined in this chapter.

Chapter two focuses on the concept of LMDS networks. The architectural structure of LMDS, which is very similar to the conventional mobile cellular structure except that the terminal users are fixed, is described in detail. The benefits LMDS provides to end-users and operators are highlighted. These include superior system capacity, rapid deployment of broadband services, scalable architecture and on-demand bandwidth, the ability to integrate with other wireless technologies, and small size subscriber antennas that can be easily mounted on or below the roof levels. A recent comprehensive market survey clearly noted that a number of local and international operators have already deployed system trials and in some countries, such as Portugal, Japan and the United States, LMDS has been commercially available in confined areas.

At millimetre wavelength and high frequency bands the behaviour of the wireless channel differs from that at lower frequencies (less than 10 GHz). A detailed literature review is reported on millimetre-wave propagation along with its impairments and challenges. The main propagation mode at millimetre wavelength is the direct LOS or, in general, paths

with dominant signal components. Coherent specular reflection is unlikely to occur from buildings or ground surfaces due to the shortness of the wavelengths. Diffused scatter is perceived to be the main channel impairment which causes degradations and variations to the dominant signals. A more detailed description of scatter is given in Chapter 3. A fair amount of publications on measurements, with regard to rain, path loss and vegetation models are available in the literature. However, it was noted that there is a considerable lack of complete realistic models for millimetre-wave propagation, particularly those that accurately quantify the predominant scattering mechanisms in urban and suburban environments.

The deployment of LMDS networks is intended to be cellular in architecture in order to maximise system capacity and spectrum efficiency. For this purpose, two main frequency-reuse plans are suggested in the technical literature. It is noted that significant amount of research has been carried out in determining the effects of cellular interference in mobile radio frequencies. However, LMDS being a new technology, the interference mechanisms associated with the recently established frequency-reuse plans have received less consideration. Moreover, due to the employment of directional antennas, cellular LMDS is expected to result in numerous interference scenarios, mainly from co- and adjacent-channels. As part of the objectives of this thesis, potential interference scenarios have been identified and discussed in details. Once again, the literature appears to fall short in providing models and measurements for LMDS cellular interference.

The first part of *Chapter three* focuses on illustrating the principles of scattering from irregular and rough surfaces. Presented is the problem of high-frequency scattering of electromagnetic millimetre-waves, where the latter becomes comparable with or is smaller than the surface irregularities. As a result, unwanted incoherent diffuse components of scattered signals are generated. This drawback verified by measurements conducted in this thesis and elsewhere in the literature, is extremely significant on the average received signal level and its variability. While incoherent scatter is neglected at lower frequencies, its consideration at millimetre-wavelengths is essential. One of the most suitable and versatile methods established for dealing with scatter from irregular surfaces is the Kirchhoff (Physical Optics) method. This method is based on the assumption that each point on the random surface is replaced by its tangent plane, and the reflected wave field is represented by the summation of the incident field and the field

reflected from a point on the plane tangent to the incident surface, provided that the local radius of curvatures is much larger than the wavelength of the incident ray.
Section 3.2 reports on model classifications at millimetre-wavelengths and justifies the use of statistical approaches due to the random nature of surface irregularities. Section 3.3 deals with the classification of channel models and reported on methods for the extraction of important statistical parameters from measured and simulated data, such as the first and second order moments of the received power.

Chapter four presents a physical statistical model for the electromagnetic propagation, suitable for fixed wireless links at millimetre-wavelengths. Model derivations are based on the following key factors:

- Although the wireless link is fixed, the propagation channel is assumed to be time-varying due to the motion of objects within and the perturbation of the EM properties of scattering objects.
- A relatively coarse description of the radio path geometry based on GIS data and digital imaging is included.
- Surface irregularities are considered random and the pertinent surface statistics are those obtained from GIS data and digital images.

With the above taken into consideration, the calculated signal strength at the receiver was treated as a random variable and from such a representation the expected value, variance and probabilistic distributions of the main link parameters are deduced via simulations and subsequently employed in link calculations. This random nature of the EM fields suggests a presentation in terms of the PDF and the associated first and second order moments. Of particular interest is the parameterization of the random simulations and their association with the Rician distribution, i.e. the description of the received field strength and the characterization of the channel in terms of the parameters that define this particular distribution.

The propagation topography and, in particular, the perimeter of rooftops and facades, as well as the ground patches illuminated by both the receive and transmit station antenna beams, are modelled using widely available, relative coarse, digital GIS data and digital images. In the EM field and signal at the receiving station are calculated using irregular

surface scattering methods (Kirchhoff), augmented by geometrical optics techniques over different possible realizations of the surface geometry and its architectural features, namely, the height above or below a mean plane and their inclination with respect to the unit vector perpendicular to the mean surface plane. The calculations assume realistic transmitting and receiving antenna systems and directive gain patterns, as well as non-uniform illumination and near field observation of the scattering surface.

Chapter five presents site surveys processed from the GIS data showing the measured link profiles for two different sites and the variety of buildings and ground surfaces existing between various transmit and receive terminal positions. Also presented in this chapter is the hardware of the 40 GHz measurement system and the antennas used along with their measured radiation patterns.

In *Chapter six*, detailed statistical analyses of the experimental results for the links considered is presented. Results are compared with the probabilistic distributions and statistical parameters from the proposed model predictions. Furthermore, the effects of the environmental scatter on both the direct hub-subscriber and possible interfering links in the uplink or downlink of the same or adjacent frequency-duplex channels, which can occur in a fully deployed LMDS, are simulated based on the proposed model. Below is a summary of the findings obtained from each measurement scenario. All of these finding are found to be consistent with the predictions obtained.

Co-Polarized Links

- In short links with radii of up to 200 m, the Rician distribution was noted to have very good fits with those distributions obtained from measurements and simulations. Distributions of longer links were more spread out about their mean levels, i.e. exhibited higher signal variations and consequently showed lower K-factor values.
- The theoretical Rician distribution representation for measured and simulated data failed for extremely high K-factor values (above 25 dB).
- K-factors exhibited small variations for relatively small antenna gains (10 – 20 dBi).

- A monotonic decrease of the K-factor with distance was noted for the antennas considered.
- Horizontally co-polarized links showed less signal variations and consequently higher K-factor values when compared to the vertically polarised links.
- The millimetre-wave channel is always time-varying even with clear and unobstructed links due to the random nature of scatter and the sensitivity of the channel to any movements such as wind and traffic.
- The accuracy of predicting, as well as measuring, large values of K-factors for high gain and narrow beamwidth antennas in the boresight of LOS links is generally affected by the alignment accuracy of the transmit and receive antenna axes.

Cross Polarization

- Measured radiation patterns showed reception peaks occurring in the main- and side-lobes of the antennas used. These peaks were further aggravated by the use of high gain antennas and misalignment links.
- The cross-polarization effects of vegetation and scatter were observed in the measurements.
- K-factor trend was seen to increase with distance as opposed to the co-polarized case.
- High K-factor values for a cross-polarized interfering link is possible. These values ranged from 8 dB at the lowest antenna gain (10 dBi) rising up to 25 dB for the highest antenna gain (44 dBi) used.

Non-line-of-sight Links

- Reflected signals have longer paths and caused time delayed replicas of the transmitted signal.
- Signals received from the direct path between a transmit antenna side-lobe and a receiver were comparable with the signals obtained due to reflection from a building facing the transmitter.
- A continuum of multipath components and diffuse scatter were observed from the first and second order reflections.
- Despite the attenuation losses, scatter, and in some cases, large received signal variations, the Rician distribution reasonably represented the measured data.

- Reasonable K-factor values (from 10 to 20 dB) were obtained when utilizing a pyramidal-horn or a lens-horn antenna at the receiver placed in the direction of maximum signal power obtained from a building surface reflection.
- The model provided good predictions with the 360° azimuth-plane measurements. Discrepancies however occurred outside the main-lobe regions of the receiving antenna.

Cellular LMDS Interference Measurements

- The two assigned LMDS cellular plans of dual-frequency and dual-polarization discriminations, namely, the Sub-Optimum Plan (SOP) and the Alternative Plan (AP) generate co- and adjacent-channel inter- and intra-cell interference due to the LOS constraints among the transmitting and receiving antennas.
- Measured signal-to-interference distributions of the main interference scenarios were compared with Oettings's theoretical distribution given by the ratio of two Rician channels; namely, the desired and interference channels.
- Rician K-factor values were found to increase with higher gain antennas for both, the desired and interference links.
- Relatively high K-factor values were obtained for the co- and adjacent-channel interference scenarios. These scenarios represents the main interference mechanisms of the Sub-optimum (SOP) and Alternative (AP) cellular frequency plans assigned for LMDS networks, respectively.
- In general, interference effects were aggravated by the use of high directional antennas.
- The AP claims to provide better SIR ratios as the cell repetitions, i.e. co-channelling, are given in every fifth cell compared to every third cell in the SOP. However, the AP neglects the effects of scatter and specular reflections from adjacent cells.
- Suitability of deploying either frequency-reuse plans (AP & SOP) depends on many factors such as; cell sizes, building topography and their shielding levels; antenna types and their gains, antenna elevation height, transmitter-receiver alignment, amount of vegetation in radio links, number of simultaneous users and system capacity.

In all of the simulated links, distributions of the received power appeared to be rather insensitive to any assumptions on the distribution of the height of the surface elements with respect to the mean building plane. Not surprisingly, such random simulations for the real and imaginary parts of the received power provided Gaussian-like distributions with zero mean or, equivalently, a Rayleigh distributed envelope and a phase uniformly distributed in $(0,2\pi)$. Hence, for fixed antenna positions of known volumetric patterns, scatter by each building surface is characterized by the standard deviation of the envelope, which is a function of the position and orientation of the transmitter and receiver antennas with respect to the mean building surface.

7.3 Conclusions

With the phenomenal growth in broadband wireless communication systems due to their potential implementation in a wide variety of high data rate and multimedia services, higher frequency bands have been recently allocated and utilised for these services. New devices and components for high frequency and millimetre-wave integrated front-end receivers are widely available, active and low cost antennas are being designed, and advanced software techniques in coding, modulation, switching, and networking are being researched and developed. In addition to these advances, which are needed to enable the next generation wireless technology, developing new and more computationally efficient propagation models are desirable. Developments of these effective propagation models, which must be verified by measurements, are crucial for a successful implementation of future LMDS terrestrial wireless systems.

7.3.1 Contributions to Modelling

The major contribution in this thesis is the statistical EM model proposed for millimetre-wave LMDS applications, whereby the problem of approximating the scattered field is dealt with in a successful manner. At millimetre wavelengths any surfaces, especially buildings facades and rooftops, are no longer considered plane, but irregular (rough) with periodic or random variations of elevation from a certain mean plane. These height elevations are comparable or larger than the wavelength. In an effort to tackle and model these scattering situations, a high-frequency scattered field approximation was formulated

on the basis of Physical Optics/Kirchhoff approximation and the Stratton-Chu integral. The model was established on a physical representation of the EM scatter by the main constituents of such propagation environments, namely, the buildings surrounding the main link and the ground, along with plausible assumptions about the statistical behaviour of the cumulative scattered, ground reflected and direct fields. The formulation resulted in approximations of the mean field, mean power density and scatter distribution of the scattered field.

The model was also employed in analysing the effects of building scatter in the received signal variance of not only the main desired link but also the adjacent- or co-channel interfering link from a close by base-station, enabling expected distributions of signal-to-interference ratios (SIR) for a particular underlying propagation environment to be predicted and evaluated. In comparison with deterministic models, such as ray-tracing, where intensive computations and detailed knowledge of topographical data are required, the proposed model yields a computationally efficient and reasonably accurate solution.

Random simulations over different realization of the building surfaces comprising the propagation environment have been carried out and compared with measurements. The comparisons showed good agreement in the prediction of main statistical parameters and, in particular, the average received power and the relative power of scattered field contributions, thus, verifying the main assumptions relating to the received signal strength, as well as the validity of the Rician model in describing the signal envelope variability in complex propagation environments. Hence, the model has successfully incorporated the underlying propagation mechanisms that contribute to the statistical behaviour of the received signal due to multipath scattering and fading at millimetre-wavelength frequencies.

The Rician parameterization was found to be very useful in the classification of the environment and can readily be utilized in network design deployment, since it quantifies in a simple manner the effects of the environmental scatter. The determination of the K-factor, along with the average power allows a simple, narrow-band characterization of the flat-fading effects of the wireless propagation channel, including the effects of building and ground scatter to the received signal.

Only a limited amount of work has appeared in the technical literature on propagation of outdoor urban and suburban environments at millimetre wavelength band and to the author's best knowledge, no work has been published yet on interference measurements that are associated with the frequency-reuse plans proposed for cellular LMDS network architectures.

The experimental campaign, mainly aiming at the validation of the principal model assumptions and the statistical description of the channel, has only incorporated narrow-band measurements. Field simulations, however, allow in principle derivation of the delay spread and power delay profiles pertinent to the link via a Fourier transform. The nature of the propagation mechanisms suggests power delay profiles of clusters, each comprising a continuum of multipath components, in addition to the usually dominant direct field. This continuum corresponds to diffuse scatter by building surfaces and usually attains a maximum at approximately the time-delay of the specular reflection by the mean plane of the surface. Model predictions of the building and ground scatter over a band-limited spectrum can be used in obtaining approximations of the envelopes of power delay profiles in a broadband characterization of the channel.

7.3.2 Contributions to Millimetre-wave Measurements

This part of the research programme is particularly valuable since it provided a unique opportunity for both exploring propagation factors at millimetre-wave lengths and validating the outputs of the developed EM stochastic propagation model. Overall, more than 180 sets of valuable measurements were conducted at 40 GHz; these are believed to be of significant contribution to the knowledge in this area and the literature. Two measurement sites were carefully selected. The first represents a typical urban microcell (radius up to 150 m) embedded with a number of buildings that guided the propagation of multipaths within the cell. The second represents a suburban environment (radius up to 670 m) conducted in an industrial estate containing a number of buildings that are widely diverse both in their shapes and footprints. These measurements consisted of point-to-point, vertical and horizontal, co- and cross-polarized links; several transmit and receive positions; and five different antenna gains ranging from 10 dBi to 44 dBi. The data

recorded was either in a Matlab™ (*.mat) or ASCII text (*.txt) format of the amplitude power received for a predefined number of samples.

7.3.3 Contributions to the Technical Literature

The author has contributed the following papers to the technical literature (all as a first author apart from paper number VIII):

I. Muhi-Eldeen Z., Ivrissimtzis L.P., Al-Nuaimi M.O. and Caldeirinha R., "Modelling and Measurements of Millimetre Wavelength Propagation in Urban Environments", submitted to the *IET Microwave Antenna & Propagation journal.*

II. Muhi-Eldeen Z., Ivrissimtzis L.P. and Al-Nuaimi M.O., "Measurements and Modelling of Cellular Interference in Local Point-to-Multipoint Distribution Systems", to appear in the *IET Microwave Antenna & Propagation journal.*

III. Muhi-Eldeen Z., Ivrissimtzis L.P. and Al-Nuaimi M.O., "Measurements and Physical Electromagnetic Statistical Modelling of mm Wavelength Propagation", *Progress in Electromagnetic Research Symposium Proceedings*, Hangzhou, China, March 2008.

IV. Muhi-Eldeen Z., Al-Nuaimi M.O., Richter J. and Ivrissimtzis L.P., "Measurements and Statistical Modelling of Channel & Interferences Distributions at mm Wavelengths", *International Symposium on Performance Evaluation of Computer and Telecommunication Systems*, SPECTS, San Diego, July 16-18 2007.

V. Muhi-Eldeen Z., Al-Nuaimi M.O., Richter J. and Ivrissimtzis L.P., "Performance Analysis of Reflection Paths for Millimetre Wavelength Systems", *IEEE International Conference on Computer Systems and Applications*, AICCSA, May 13-16, 2007.

VI. Muhi-Eldeen Z., Al-Nuaimi M.O., Richter J. and Ivrissimtzis L.P., "Statistical Modelling of an Adjacent Channel Interference Scenario for Cellular Local Point-to-Multipoint Distribution Systems", *European Modelling Symposium*, London, August, 2006.

VII. Muhi-Eldeen Z., Al-Nuaimi M.O., Richter J. and Ivrissimtzis L.P., "Measurements and Statistical Modelling of Co-Channel Interferences for Local Point-to-Multipoint Distribution Systems", *Workshop on Performance of Wireless Networks and Communication Systems* (WiNCS'06), July 2006.

VIII. Zhang J., Muhi-Eldeen Z., Al-Nuaimi M.O., Richter J. and Ivrissimtzis L.P., "Statistical Modelling of Building Scatter in Metropolitan Cells at 20 and 40 GHz for Fixed Wireless Access Links", *The 6th International Conference on ITS Telecommunications,* (ITST2006) China June 2006.

IX. Muhi-Eldeen Z., Al-Nuaimi M.O., Richter J. and Ivrissimtzis L.P., "Measurements And Modelling For Fixed Wireless Access Systems At 40 GHz In Urban/Semi-Urban Cells", *IEE/IEEE LAPC Loughborough Antennas & Propagation Conference*, Loughborough-UK, April 2006.

X. Muhi-Eldeen Z., Al-Nuaimi M.O., Richter J. and Ivrissimtzis L.P., "Statistical Characterisation of Building Rooftop Scatter On Performance of Fixed Wireless Links In Urban/Semi-Urban Cells ", *IADAT International Conference on Telecommunications and Computer Networks* (IADAT-tcn2005), Portsmouth-UK, September 2005.

7.4 Recommendations for Future Work

Further work to extend and build on the research work conducted in this thesis may include the following topics:

With regards to frequency-reuse plans for LMDS networks, the interference scenarios investigated were from co- and adjacent-channels operating at the same frequency and discriminated either by polarization or distance. The frequency band on each of the

uplinks and downlinks is divided into two frequency bands separated by small guard bands. Frequency drifts between the bands are expected due to the time-varying nature and the sensitivity of the millimetre-wave channel, especially in radio channels with considerable amounts of moving objects. Hence further investigation in terms of measurements could be carried out, taking into consideration the effectiveness of the frequency duplexers and filters required at the transmit and receive terminals.

Since the model is successfully able to predict statistics of interference, actual mean signal-to-interference ratios can be predicted in a straightforward manner. This will enable the evaluation of LMDS cells in terms of the most suitable modulation scheme supported, by accounting for the threshold values for signal-to-interference ratios, which are modulation and capacity dependent. Furthermore, LMDS cells and the deployments of frequency-reuse plans can be evaluated by estimating, the minimum frequency reuse distances and average cell radii lengths. These parameters can not be simply estimated from the link budget calculations. Knowing such design parameters can further aid into minimizing interference levels for optimum system performances. In the interference limited environment of LMDS networks, electromagnetic model predictions incorporating antenna heights and patterns become essential for the millimetre radio system design.

Propagation channels in millimetre-waves are characterized by multipath scatter, in addition to a nominally strong direct field. Representation in the time-domain of the delayed reflections (e.g. ground) and scattering contributions to the total field, i.e. the channel impulse response, can reveal valuable information on channel dispersive effects. By sweeping the frequency in the proposed model, along with a Fourier transformation, it could be possible to observe signals in time domain and estimate the channel impulse response.

In terms of hardware implementations, a straightforward way to characterise the millimetre-wave propagation channel in the time-domain with the existing used Farran GV-22H varactor controlled Gunn oscillator is to employ a swept frequency scalar domain channel sounding method, which only requires a scalar measurement over a wide bandwidth. It can be shown that if the propagation channel is causal, a sufficient and

necessary condition for the channel transfer function is to be of minimal-phase. Hence, for a causal channel, a scalar measurement of the magnitude of the received signal suffices to completely characterize the channel impulse response.

APPENDIX

Appendix A: Model Flowchart

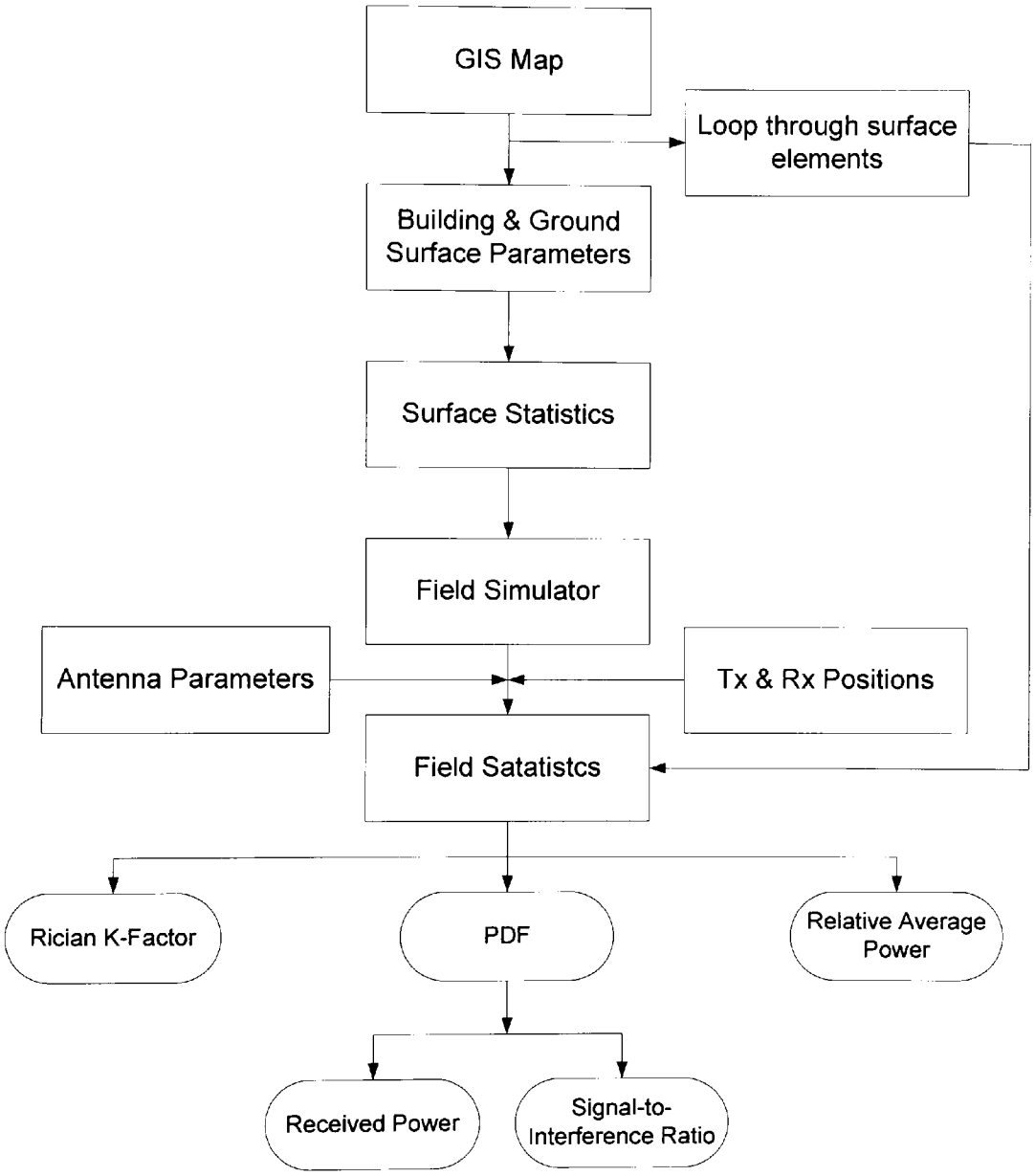

Appendix B: Outage Probabilities

LMDS, as in any communication system, are required to be available essentially at all times with adequate signal reception levels. Outage probability provides an effective statistical measure of the radio link performance in an interference limited environment, where frequencies are reused over relatively short distances. It can be defined as the probability that the ratio of the desired signal power to the interference power (SIR) falls below a predefined threshold that depends on the modulation type and other system design requirements. The analytical expression of the outage probability of a Rician/Rician channel is given by:

$$P_{out} = Q\left[\sqrt{\frac{2K_I R}{b_1 + R}}, \sqrt{\frac{2K_0 b_1}{b_1 + R}}\right] - \frac{b_1}{b_1 + R}\exp\left[-\frac{K_I R + K_0 b_1}{b_1 + R}\right] I_0\left(\frac{\sqrt{4K_I K_o R b_1}}{b_1 + R}\right) \quad \text{(AB.1)}$$

where $Q(.)$ the Marcum Q-function, K_0 & K_I is the Rician K-factor of the desired and interfering link, the I_0 is the zeroth order modified Bessel function of the first kind, R is the predefined protection ratio and $b_1 = \sigma_0^2/\sigma_I^2$.

Fig. AB.1 illustrates the effects of the protection ratio R on the outage probabilities for the three different antenna gains, namely 10, 15 and 20 dBi pyramidal-horn antennas. The choice of receiver antenna gain for R values up to 12 dB is vital as it places large difference on outage probability. Modulation schemes such as 16-QAM are beneficial for providing high data rates and are generally associated with R values that are greater than 14 dB. At these high threshold values it is found that the outage probability is most likely to increase. Therefore a trade-off is implied between the choice of the modulation scheme and the outage probabilities.

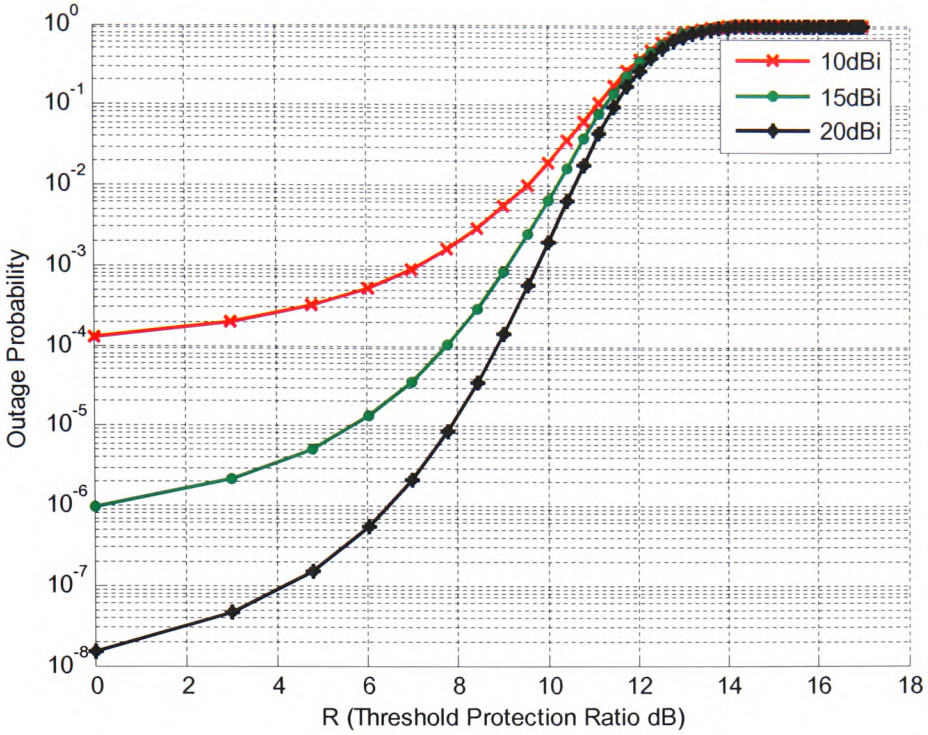

Figure AB.1: Measured outage probability for different threshold values.

Appendix C: Surface Reflectivity Constants

Table AC.1 lists the complex dielectric constant for different building materials at microwave and millimetre-wave frequencies [AC1]-[AC6].

Frequency	5.8GHz		30GHz		38GHz		41.5GHz		57.5GHz		59.5GHz		60.2GHz		62GHz	
MATERIAL	er'	er''	er'	er''	er'	er''	er'	er''	er'	er''	er'	er''	er'	er''	er'	er''
Asphalt													3.18	0.10		
Brick Wall	3.29	0.35			3.85	0.33									4.40	0.31
Concrete					1.00	0.51							4.17	0.36		
Ceramic Tile							1.70	0.20								
Slate Tile					1.71	0.20										
Glass	6.02	1.08	7.66	0.63			3.41	0.11	7.51	0.18			5.29	0.25	4.04	0.00
Plasterboard	2.12	0.00					2.33	0.10			2.58	0.01	2.81	0.04	2.44	0.01

Table AC.1: Complex dielectric constant of building materials.

References

[AC1] I. Cuinas, J.-P. *et al*, "Frequency dependence of dielectric constant of construction materials in the microwave and millimeter wave bands", *Microw. & Opt. Tech. Lett.*, vol. 30, no. 2, pp. 123-124, July 2000.

[AC2] L. J. Li, Y. Wang, and Gong Ke., "Measurements of building construction materials at Ka band", *Int. J. Infr. & mm-waves*, vol. 19, no. 9, pp. 1293-1298, 1998.

[AC3] Lahteenmaki J. and Karttaavi, T. "Measurements of dielectric parameters of wall materials at 60 GHz", *Electron. Lett.*, vol. 32, no. 16, Aug. 1996.

[AC4] Dillard C. L. *et al*, "Rough surface scattering from exterior walls at 28GHz", *IEEE Trans. Antennas Propag.*, vol. 52, no. 12, pp. 3173-3179, Dec. 2004.

[AC5] Sato, K, *et al*, "Measurements of reflection and transmission characteristics of interior structures of office building in the 60 GHz band", *Personal, Indoor and Mobile Radio Communications*, 1996, vol. 1, Oct 1996 Page(s):14 - 18

[AC6] Hayn A., Bose R. and Jakoby R., "Mulitpath Propagation and LOS Interference Studies for LMDS Architecture", *11th International Conference on Antennas and Propagation*, April 2001.

Appendix D: Results of Ofcom's Fourth Spectrum Auction

In February 2008 Ofcom has awarded licences to ten organisations following Ofcom's fourth auction of radio spectrum. According to Ofcom, the licences will allow the organisations to operate services in the higher frequency bands at 10 GHz to 40 GHz, which is suitable for high-capacity wireless services. Details of the companies who bought the license are as follows:

Name of licensee	Spectrum Awarded
Arqiva	2 x 224 MHz in 28 GHz band (national)
BT	2 x 126 MHz in 32 GHz band
Digiweb	2 x 20 MHz in 10 GHz band
Faultbasic	2 x 112 MHz in 28 GHz band (regional)
MLL	2 x 126 MHz in 32 GHz band & 2 x 250 MHz in 40 GHz band
Orange	2 x 252 MHz in 32 GHz band
Red-M	2 x 112 MHz in 28 GHz band (regional)
T-Mobile	2 x 80 MHz in 10 GHz band & 2 x 252 MHz in 32 GHz band & 2 x 250 MHz in 40 GHz band
Transfinite	2 x 112 MHz in 28 GHz band (regional)
UK Broadband	2 x 1 GHz in 40 GHz band

Table E1: Results of Ofcom's fourth spectrum auction
http://www.ofcom.org.uk/media/news/2008/02/nr_20080222

Appendix E: Samples of Publications

Sample 1: Muhi-Eldeen Z., Ivrissimtzis L.P., Al-Nuaimi M.O. and Caldeirinha R., "Modelling and Measurements of Millimetre Wavelength Propagation in Urban Environments", submitted to the *IET Microwave Antenna & Propagation journal.*

Sample 2: Muhi-Eldeen Z., Ivrissimtzis L.P. and Al-Nuaimi M.O., "Measurements and Modelling of Cellular Interference in Local Point-to-Multipoint Distribution Systems", to appear in the *IET Microwave Antenna & Propagation journal.*

Sample 3: Muhi-Eldeen Z., Al-Nuaimi M.O., Richter J. and Ivrissimtzis L.P., "Measurements and Statistical Modelling of Co-Channel Interferences for Local Point-to-Multipoint Distribution Systems", *Workshop on Performance of Wireless Networks and Communication Systems* (WiNCS'06), July 2006.

Sample 1

Modelling and Measurements of Millimetre Wavelength Propagation in Urban Environments

Zaid Muhi-Eldeen[(1)], Leonidas P. Ivrissimtzis[(2)], Miqdad Al-Nuaimi[(1)], and Rafael F. S. Caldeirinha[(3)]

[(1)] Faculty of Advanced Technology, University of Glamorgan, Pontypridd, United Kingdom. Email: zmuhield@glam.ac.uk
[(2)] Department of Physics, University of Ioannina, Ioannina, Greece. Email: livrisim@uoi.gr
[(3)] School of Technology, Polytechnic Institute of Leiria, Portugal. Email: rcaldeirinha@estg.ipleiria.pt

Abstract: A statistical model based on a coarse representation of urban wireless channel topographies and the prediction of the electromagnetic (EM) propagation in fixed wireless links operating at millimetre wavelengths are presented, with potential applications into the characterization, design and deployment of point-to-point and point-to-multi-point fixed wireless networks. A specific goal of the study is the parameterization of the main physical attributes of the propagation mechanisms, which at millimetre waves predominantly incorporate scatter from building and ground surfaces, both non-uniformly illuminated by a directive transmitting antenna. The line-of-sight (LOS) received signal is presented in terms of universal probabilistic distribution functions (PDF) and quantified in terms of their first and second order moments. Experimental results validate the Physical Optics (PO) based approximation of the building and ground scatter and the resulting stochastic representation of the propagation channel.

I. INTRODUCTION

Fixed Wireless Access (FWA) and Local Multi-Point Distribution Systems (LMDS) link design and deployment [1,2] require the understanding of the underlying propagation channel behavior and benefit from a quantitative description of the fundamental mechanisms that affect the integrity of the link, namely attenuation, noise, and interference. Development of analytical and numerical modeling tools will enable the rationalization and optimization of the system design and its main constraints, such as cost of deployment (cell size, frequency and polarization planning), antenna parameters (positioning and radiation characteristics), and link performance (coverage and outage probability at the receiver) by accounting for the impairments introduced by the wireless channel.

In LMDS networks, although the wireless link is fixed, the propagation channel is time-varying due to the motion of objects within and the perturbation of the EM properties of scatters due to varying weather conditions. In addition, at high frequencies, a geometric description of the environment at sub-wavelength scale, including the coordinates of the hub and subscriber antenna location and orientation, is impossible. Due to the coarseness of the geometrical presentation, as well as the time-varying nature of the channel, the analysis of the propagation mechanisms merits

a statistical description employing a coarse, macroscopic depiction of the geometry. With this approach, the calculated signal strength at the receiver is treated as a random variable and from such a representation the expected value, variance and probabilistic distributions of the main link parameters can be deduced via simulations and employed in link calculations.

Papazian *et al.* [3] reported on radio coverage estimates and identified fundamental impairments on the attenuation and its variability, as well as the delay spread, due to obstruction by buildings and vegetation for LMDS with narrow- and broad-band measurements at 27.5-29.5GHz in small suburban cells. Further, Xu *et al.* [4] investigated the broadband and dispersive channel behavior due to multipath for LOS links at 38-GHz under different weather conditions and proposed a Rician model along with a rain-rate dependent K-factor for the short term variability of the signal attenuation.

High-frequency scattering by building surfaces and its effect in fixed wireless link studies, particularly in the mm-wave spectrum, has received less attention. Elaborate ray tracing solutions, incorporating edge and vertex diffraction, as well as higher order effects, are of limited efficacy due to the unavailability of detailed building information. On the other hand, classic random rough surface scattering techniques established on an asymptotic reduction of the PO integral [5,6] can be useful around the specular region of surfaces with random deviations of their height above a mean plane presenting a continuous distribution (e.g. corrugated rooftops or ground patches). The study by Al-Nuaimi and Ming [7] on the near-field scatter by conducting, flat building surfaces, highlighted high scattering signal levels within the specular region at around 10GHz. In a more recent work [8], Pongsilamanee and Bertoni investigated the scattering from building facades with nearly periodic placement of their features employing PO and random realizations of their periodicity.

Incorporating rooftop scatter in a stochastic representation of the received signal in fixed links at 20GHz, employing statistics of the elevation of reflection points above the ground has been studied in [9,10]. However, the link geometry assumed antennas elevated above the maximum

rooftop level and did not incorporate scattering effects from vertical building surfaces and the ground. The present work aims at extending and generalizing the statistical model proposed in [9,10] for the urban propagation channel and the physical (EM) representation of building and ground scatter, with particular emphasis on fading margins in LOS links, and validating it against experimental results from realistic propagation scenarios. The frequency of propagation is 40GHz, according to the bands allocated for future LMDS systems. The study focuses on the analysis and measurements of fading effects of scattering by building surfaces (rooftops and facades) and ground on the direct field in a FWA link at mm-waves, taking place in urban residential or industrial environments. The propagation topography and, in particular, the perimeter of rooftops and facades, as well as the ground patches illuminated by both the receive and transmit station antenna beams, is modeled using widely available, albeit coarse, digital Geographic Information System (GIS) data and digital images. The EM field and signal power at the receiver are considered random and are calculated employing the PO method over different possible realizations of the surface geometry and its architectural features, namely, the height above or below a mean plane and their inclination with respect to the unit vector perpendicular to the mean surface plane. The scattering from surfaces with random height deviations and, especially, irregular ground sections and corrugated rooftops, is approximated using classic random rough surface scattering methods, with surface statistics obtained from sampling GIS elevation data. The calculations assume realistic transmitting and receiving antenna systems and directive gain patterns, as well as non-uniform illumination and near field observation of the scattering surface.

The random nature of the EM fields suggests a presentation in terms of the PDF and the associated first and second order moments. Of particular interest is the parameterization of the random simulations and their association with the Rician distribution, i.e., the description of the received field strength and the characterization of the channel in terms of the parameters that define this particular distribution. Such parameterization is useful in the classification of the

environment and can readily be utilized in network design deployment, since it quantifies in a simple manner the effects of the environmental scatter.

The experimental campaign has involved narrow-band measurements only, since it primarily targets the validation of the principal model assumptions regarding urban scatter and the statistical description of channel fading effects. The nature of the propagation mechanisms suggests power delay profiles of clusters, each comprising a continuum of multipath components, in addition to the usually dominant direct field. This continuum corresponds to diffuse scatter by building surfaces and usually attains a maximum at approximately the time-delay of the specular reflection by the mean plane of the surface. Model predictions of the building and ground scatter over a band-limited spectrum can be used in obtaining approximations of the power delay profiles envelopes in a broadband characterization of the channel.

The article is organized as follows: Section II outlines the propagation geometry and describes the fundamental geometrical attributes used in the model. In Section III, a theoretical formulation based on the PO method of the elementary scattering mechanisms is outlined, while Section IV presents the proposed statistical model for the propagation channel in terms of a Rician distribution and pertinent parameters. Representative narrowband measurements and comparisons with the predictions of average total and scattered power from EM field simulations for directive antenna patterns are presented in Section V. The following notation is adopted throughout: bold-faced characters are used to denote vectors, while the hat above a character signifies a unit vector or one of its Cartesian components; script bold characters correspond to dyadic (double-vector) operator; subscripts R and T refer to the receiver and transmitter, respectively.

II. THE PROPAGATION GEOMETRY

Two propagation sites for link measurements were selected, namely, a site from the University of Glamorgan Campus (UC) and another in a nearby Industrial Estate (IE) as shown in Figs. 1 and 2, respectively. The UC site area is relatively small and is surrounded by buildings. A 5-storey

building (building A in Fig. 1) is in front of and is illuminated by the transmitter antenna. Specular reflection from this building dominates the received signal. On the other hand, the longer links established within the IE are affected by scattering from a number of buildings, widely diverse both in their shapes and footprints. The antennas are not necessarily elevated above the highest rooftop and, in the case of the UC, the LOS link between the transmitter and the partially receiver is obstructed by vegetation. In this case, the effect of vegetation is accounted for using the signal attenuation model in [11] corroborated by direct field measurements. The building surfaces, as well as the location and orientation of the antennas, are expressed in a global reference system of coordinates used in GIS maps.

The field radiated by the transmitter antenna in free space and in the direction of the unit vector $\hat{\boldsymbol{s}}_T$ and at a distance s_T , as shown in Fig. 3, is written as

$$\boldsymbol{E}(\hat{\boldsymbol{s}}_T; s_T) = \boldsymbol{e}_T(\hat{\boldsymbol{s}}_T)\frac{e^{-jks_T}}{s_T}, \tag{1}$$

where $\boldsymbol{e}_T(\hat{\boldsymbol{s}}_1)$ is a vector pattern function, depending only on the direction of the observation point with respect to an antenna-associated coordinate system, and k is the wave-number of propagation. On the other hand, the scattered field $\boldsymbol{E}_S = \boldsymbol{e}_S \cdot e^{-jks_R}/s_R$ emanating from a scattering center at a distance s_R and direction $\hat{\boldsymbol{s}}_R$ with respect to the receiving antenna position, induces an *emf* at the receiver terminals that is proportional to

$$r_S = \boldsymbol{e}_S \cdot \boldsymbol{e}_R(\hat{\boldsymbol{s}}_R)\frac{e^{-jks_R}}{s_R}, \tag{2}$$

where $\boldsymbol{e}_R(\hat{\boldsymbol{s}}_R)$ and $\boldsymbol{e}_S$ correspond to the receiving antenna and scattering vector pattern functions, respectively.

Link area and GIS data, augmented with digital images of important geometric elements, are translated and processed to provide M building surfaces, either rooftops or facades, as well as ground patches, within the LOS of both the transmitter and receiver antennas. Each building surface is further divided into L flat plate elements comprising building materials of uniform

electromagnetic and reflective properties including a surface roughness factor where applicable. The reflectivity properties for a wide range of building materials are available in the technical literature [12-15]. Each flat element (l) of a building surface (m) is geometrically characterized by the coordinates (x_l, y_l, ζ_l) of its mid-point $\boldsymbol{r}_l = \boldsymbol{\rho}_l + \zeta_l \hat{\boldsymbol{z}}_m$ and a unit vector $\hat{\boldsymbol{n}}_l$ perpendicular to the plane of the panel, as illustrated in Fig. 3. For notation simplicity, the building surface index (m) is usually suppressed, but implied. The dimensions of each elementary panel (l) are sufficiently small to approximate the size of the most prominent building features, yet much larger than the wavelength of operation. Although the building surface is non-uniformly illuminated by the incident transmitted spherical waveform, while the receiver can be within the near-field region of the building, each elementary surface is sufficiently small so that incident plane wave can be considered locally plane and a far-field scattering approximation can be applied.

III. BUILDING SCATTER FORMULATION

Employing the well-established PO approximation, we consider the contribution to the cumulative scatter of a flat element (l) of the building surface (m). The derivation is based on the Stratton-Chu integral representation of the scattered field $\boldsymbol{E}_{S,l}$ from the surface element (e.g. [16]), which for an $\exp(j\omega t)$ time-dependence reads

$$\boldsymbol{E}_{S,l} \approx \frac{-jk}{4\pi} \frac{\exp(-jks_{R,l})}{s_{R,l}} \iint_{(\Delta s)_l} \left[\eta_0 \boldsymbol{n}_l \times \boldsymbol{H}_r + \hat{\boldsymbol{s}}_{R,l} \times (\boldsymbol{n} \times \boldsymbol{E}_r) - (\boldsymbol{n}_l \cdot \boldsymbol{E}_r)\hat{\boldsymbol{s}}_{R,l}\right] \cdot \exp(jk\hat{\boldsymbol{s}}_{R,l} \cdot \boldsymbol{r}) \cdot dxdy \quad , \qquad (3)$$

where $\hat{\boldsymbol{s}}_{R,l}$ is the unit vector from the projection of the mid-point of element (l) on the mean plane of the building surface to the receiver, $\boldsymbol{n}_l$ is related to the unit vector $\hat{\boldsymbol{n}}_l$ perpendicular to surface element via $\boldsymbol{n}_l = \hat{\boldsymbol{n}}_l / n_{z,l}$, η_0 is the characteristic impedance of free space, and $(\boldsymbol{E}_r, \boldsymbol{H}_r)$ are the electric and magnetic field reflected by the plane of the flat element due to a locally plane wave incident from the direction $\hat{\boldsymbol{s}}_{T,l}$, as shown in Fig. 3. The double integration in

eq. (3) takes place over the projection $(\Delta s)_l$ of the surface element onto the mean building surface plane (x_m, y_m). Without presenting the details of a rather straightforward derivation, the PO approximation yields a scattered field expression in the form

$$\boldsymbol{E}_{S,l} \approx \frac{-jk}{4\pi} \frac{\exp\left[-jk\left(s_{R,l}+s_{T,l}\right)\right]}{s_{R,l}s_{T,l}} \exp\left(j\beta_l\zeta_l\right)\mathfrak{T}_l \cdot \boldsymbol{e}_T(\hat{\boldsymbol{s}}_{T,l}), \tag{4}$$

where the dyadic scattering coefficient $\mathfrak{T}_l$ can be written as

$$\mathfrak{T}_l = \mathfrak{R}_l \iint_{\Delta s_l} \exp\{j\beta_l(\boldsymbol{q}_l - \boldsymbol{n}_l)\cdot\boldsymbol{\rho}'\}dx'dy', \tag{5}$$

with

$$\mathfrak{R}_l = R_{h,l}\left[\hat{\boldsymbol{s}}_{R,l}\times\left(\boldsymbol{n}_l\times\hat{\boldsymbol{h}}_l\right)-\left(\hat{\boldsymbol{s}}_{T,l}\cdot\boldsymbol{n}_l\right)\hat{\boldsymbol{h}}_l\right]\hat{\boldsymbol{h}}_l + R_{v,l}\left[\boldsymbol{n}_l\times\hat{\boldsymbol{h}}_l+\left(\hat{\boldsymbol{s}}_{T,l}\cdot\boldsymbol{n}_l\right)\left(\hat{\boldsymbol{h}}_l\times\hat{\boldsymbol{s}}_{R,l}\right)\right]\hat{\boldsymbol{v}}_{i,l}. \tag{6}$$

In eqs. (5) and (6) above, we have introduced the vectors $\boldsymbol{q}_l = \boldsymbol{u}_l / u_{z,l}$ and $\boldsymbol{u}_l = \hat{\boldsymbol{s}}_{R,l} - \hat{\boldsymbol{s}}_{T,l}$, the large parameter $\beta_l = ku_{z,l}$, along with the equation $\zeta(x,y) = \zeta_l - \boldsymbol{n}_l\cdot(\boldsymbol{\rho}-\boldsymbol{\rho}_l)$ for a point $(\boldsymbol{\rho},\zeta(x,y))$ on the flat surface element (l) and the far-field approximation $s_T + s_R \approx s_{T,l} + s_{R,l} - (\boldsymbol{u}_l - u_{z,l}\boldsymbol{n}_l)\cdot(\boldsymbol{\rho}-\boldsymbol{\rho}_l) - u_{z,l}\zeta_l$.

On the other hand, the unit vectors $\hat{\boldsymbol{h}}_l$ and $\hat{\boldsymbol{v}}_{i,l}$, perpendicular and parallel to the plane of incidence, respectively, are given by

$$\hat{\boldsymbol{h}}_l = \frac{\hat{\boldsymbol{s}}_{T,l}\times\hat{\boldsymbol{n}}_l}{\left\|\hat{\boldsymbol{s}}_{T,l}\times\hat{\boldsymbol{n}}_l\right\|}, \quad \hat{\boldsymbol{v}}_i = \hat{\boldsymbol{h}}_l\times\hat{\boldsymbol{s}}_{T,l}, \tag{7}$$

and the coefficients $R_{h,l}$ and $R_{v,l}$ in eq. (6) are the standard reflection coefficients from a plane interface of a medium with a complex dielectric permittivity and correspond to polarizations perpendicular and parallel to the plane of incidence. For slightly rough surface elements with statistically isotropic and homogeneous roughness, Snell's law still applies, however, the coefficients $R_{h,l}$ and $R_{v,l}$ are represented in terms of an effective surface impedance incorporating a roughness factor [6]. It is noted that the double integral in eq. (5) can obtain closed form expressions for polygonal plates in terms of the coordinates of their corners. From eqs. (2) and (4) it follows that the signal captured by the receiver antenna due to the field scattered by a building surface (m) becomes

$$r_{S,(m)} \approx \frac{jk}{2\pi} \sum_{l} \frac{\exp\left[-jk\left(s_{R,l} + s_{T,l}\right)\right]\exp\left(j\beta_l \zeta_l\right)}{s_{R,l} s_{T,l}} \boldsymbol{e}_R(\hat{\boldsymbol{s}}_{R,l}) \cdot \mathfrak{I}_l \cdot \boldsymbol{e}_T(\hat{\boldsymbol{s}}_{T,l}) \qquad (8)$$

In random simulations, the building surface is divided into rectangular or triangular elements and the received signal from eq. (8) and its power are obtained for different building surface realizations over distributions of the unit vector $\hat{\boldsymbol{n}}_l$ normal to each surface element (l), the surface element parameters $(\zeta_l, \Delta s_l)$, and the effective complex dielectric permittivity (ε_r) of its material. Furthermore, given the large value of the parameter β_l, distributions of the received power appear to be rather insensitive to any assumptions on the distributions of the heights (ζ_l) of the surface elements with respect to the mean building plane. Not surprisingly, such random simulations for the real and imaginary parts of r_S provide Gaussian-like distributions with zero mean or, equivalently, a Rayleigh distributed envelope $|r_S|$ and a phase uniformly distributed in $(0,2\pi)$. Hence, for fixed antenna positions of known volumetric patterns, the scatter by each building surface is characterized by the standard deviation of the envelope $|r_S|$, which is a function of the position and orientation of the transmitter and receiver antennas with respect to the mean building surface.

Building facades with periodic features are analyzed in a similar manner. However, the periodicity is accounted for in the definition of the coordinates of the mid-point $\boldsymbol{r}_l = \boldsymbol{\rho}_l + z_l \hat{\boldsymbol{z}}_m$ and the unit vector $\hat{\boldsymbol{n}}_l$, as well as the effective reflection coefficient associated with each elementary surface. On the other hand, scattering from irregular surfaces is treated using classic methods of statistically rough surface scattering, where surface statistics are obtained from the processing of sampled elevation data. A simple expression for the received signal due to scatter from such types of surfaces can be deduced from a generalization of the analysis in [6] for the three-dimensional case and it is given in the Appendix, along with the necessary surface statistics required for scattering calculations.

IV. STATISTICAL FORMULATION

The scattering contribution from the propagation environment at the receiver is represented by the superposition of randomly distributed scattered components from building surfaces, i.e.

$$r_S = a_S e^{j\phi_S} = \sum_{m=1}^{N} r_{S,(m)} , \tag{9}$$

where $a_S = |r_S|$, $\phi_S = \arg r_S$ and $r_{S,(m)}$ is given by eq. (8). The random scattered field power intercepted by the receiving antenna is incoherently superimposed to a deterministic direct field in the direction $\hat{s}_0$ from the transmitter to the receiver location, namely,

$$r_D = \frac{\boldsymbol{e}_T(\hat{s}_0)\cdot \boldsymbol{e}_R(-\hat{s}_0)}{s_0}, \tag{10}$$

and possibly a field reflected (in a Geometrical Optics sense) from a large ground. This Geometrical Optics approach with an effective reflection coefficient accounting for the surface roughness at the points of ground reflection and spherical wave incidence is adopted. If only small isolated patches are illuminated, a random rough surface scattering approach is employed. Eventually, the signal at the receiver antenna terminals can be represented by the complex random variable

$$r = r_D + a_R \exp(j\phi_R) + a_S \exp(j\phi_S) , \tag{11}$$

in which a_D, a_R, and a_S are the envelope amplitudes of the direct, reflected and scattering components respectively. The envelope of $a_R \exp(j\phi_R) + a_S \exp(j\phi_S)$ is Rayleigh distributed, while the relative phases are independent random variables and uniformly distributed over the range $(0,2\pi)$.

Given this stochastic nature of the reflected and scattering contributions, the envelope of the total received signal, in the presence of a deterministic direct field, will have a Rician distribution, i.e.

$$f_a(a) = \frac{a}{\sigma^2} \exp\left(-\frac{a^2 + s^2}{2\sigma^2} \right) I_0\left(\frac{as}{\sigma^2} \right), \tag{12}$$

where $a = |r|$, I_0 is the modified Bessel function of the first-kind and zero-order, $2\sigma^2 = (a_R)^2 + (a_S)^2$ and the direct field power equals $s^2 = |r_D|^2$. Introducing the Rician *K*-factor $K = s^2/(2\sigma^2)$, where σ^2 corresponds to the scattered field power, the distribution of the total received power $p = a^2/2$ for a normalized direct field ($s^2 = 1$), becomes

$$f_p(p) = 2K \exp[-K(2p+1)] \cdot I_0\left(2K\sqrt{2p}\right). \tag{14}$$

It readily follows that, given a set of random simulated or measured data, the *K*-factor can be derived from the mean $\mu_p = \sigma^2 + s^2/2$ and standard deviation $\sigma_p^2 = \sigma^4 + s^2\sigma^2$ of received power samples via

$$K = \frac{\sqrt{\mu_p^2 - \sigma_p^2}}{\mu_p - \sqrt{\mu_p^2 - \sigma_p^2}}. \tag{15}$$

The determination of the *K*-factor allows a simple, albeit complete, narrow-band characterization of the flat-fading effects of the wireless propagation channel, including the effects of building and ground scatter to the received signal. Hence, the characterization of the wireless channel with fixed LOS links reduces to an approximate derivation of average power and the Rician *K*-factor. The latter is expected to attain high values for short LOS links or high directivity antennas, where the direct boresight field from the transmitter dominates the received signal, nevertheless, it can reduce to small values for longer links or antenna polarization and beam misalignments.

V. MEASUREMENTS AND DISCUSSION

Experiments have been conducted within the UC and the neighbouring IE in order to acquire insight into the behaviour of the urban channel at millimetre wave frequencies, as well as towards the aim of validating the proposed model. A statistical analysis of the experimental results for the links shown in Figs. 1 and 2 is presented, discussed and compared with the probabilistic distributions and statistical parameters from the proposed model predictions. The propagation

analysis of the UC link involves simulation of the scatter from facades of buildings A, B, and C in Fig. 1. On the other hand, for the IE links, up to 50 surfaces were identified that could cause a measurable effect on the scatter. These surfaces represent building rooftop and facades, as well as ground patches. Standard 10dBi and 20dBi horn antennas were employed at the transmitter for the UC and IE measurements, respectively. The receiver is placed on top of a mobile platform at approximately 3.5m above the ground. Standard horns with gains of 10, 15 and 20dBi and lens-horns with 29 and 44dBi of nominal gain were utilized at the receiver. In the simulations, the horn antenna radiation patterns are described in terms of analytical expressions [17], whereas lens-horn antennas are represented by equivalent circular apertures with field distributions that yield the same gain, beamwidth and first-sidelobe level with anechoic chamber measurements. The transmitter comprises a temperature-controlled Gunn diode oscillator, which provides a stable reference between 39.75 and 40.25GHz. The received signal is down-converted to an intermediate frequency, amplified, peak-held and sampled with a resolution bandwidth of 1MHz.

The associated distribution functions are obtained from sampling of the received signal, while translating the receiver antenna in directions longitudinal or transversal to the direct link axis, with a maximum displacement of 50 wavelengths from its central position. Within this displacement window the orientation of the two beams, as well as the moving average of the signal power samples remain relatively constant. The statistical behaviour of the building and ground scatter is presented to the receiver station, due to the random variations of the phase scattered waves intercepted by the receiver. In Fig. 4, representative snapshots of the normalized received signal power from measurements and simulations are shown, illustrating the variability of the received power and the dynamic range for the TX1-RX0 and TX2-RX0 links (Fig. 2).

Average power measurements are performed for a number of azimuth angles of the receiver antenna main bean for the UC link of Fig. 1 and discrete positions of the receiver station at various distances from the transmitter in the IE, as shown in Fig. 2. The objective of these measurements is to illustrate reflection and building scattering contributions in urban cells and test the ability of the model to predict average power for different antenna orientations in such a

scattering rich environment. Fig. 5 depicts the average received power over the azimuth angle of the receiver antenna axis. The direct field, due to transmit antenna sidelobe radiation, peaks at an angle of 134°, while at orientation angles of 162° and 36° the received signal is believed to be dominated by specular reflections from building A in front of the transmitter and building C behind the receiver location, respectively. A third pattern lobe at around 210° is due to double reflection from building A and subsequently from building B. This effect is incorporated by introducing an image of the transmitting antenna with respect to the plane of the facade of building A, attenuated by the average reflection coefficient. The discrepancy between measurements and predictions for observation angles from 244° to 350° is first, due to scattering mechanisms from outside the main topography of Fig. 1 not included into the simulation model and, second, the use of theoretical antenna radiation patterns.

Fig. 6 shows the attenuation of the received signal power with distance from the transmitter for different positions of the receiver along an IE route shown in Fig. 2. The orientation of the receiver antenna on an horizontal plane is adjusted so that maximum power is attained at each location along the route. It is noted that, for relatively large values of the K-factor that are observed for LOS links with highly directive antennas, the average received power is approximately equal to the power of the direct field component and, hence, it recedes by approximately 6dB for every doubling of the distance. Further, for receiver antenna orientation that achieves maximum received power at each position and large values of the K-factor, the average power for the horizontal and vertical polarization are approximately equal.

The K-factor is derived from the received power samples from measurements and model prediction for a number of links, antenna polarization and gains. Fig. 7 shows the variation of the K-factor against the distance of the receiver from the transmitter along the IE route, for two different receiver antenna gains. The LOS between the two antennas is maintained and both the transmitter and receiver antenna axes remain within the 10dB beamwidth of each other. Fig. 8 depicts K-factor values obtained from measured and simulated power samples against the receiver antenna gain and two polarization cases. In general, K-factor predictions display good agreement

with those obtained from a statistical analysis of the measured data and the definitions of Section IV, especially for small and medium antenna gains. The accuracy of predicting, as well as measuring, large values of K-factors for high gain and narrow beamwidth antennas in boresight LOS links is generally affected by the alignment of the two boresight axes and a number of measurements need to be conducted to improve the accuracy of such estimates. As expected, although the K-factor exhibits small variations for relatively small antenna gains (10-20dBi), it rapidly increases for higher gains (29dBi and 44dBi). The monotonic decrease of the K-factor with distance for the same antenna gain is also noted.

In Figs. 9-10 the PDF of the normalized received signal power, as obtained from either the measurements or the EM simulations are shown for a vertical and horizontal polarized links. Each PDF is compared with the theoretical distribution for a normalized envelope of a Rician distribution given for the two main links considered (TX1-RX0 and TX2-RX0). The K-factor of the theoretical Rician distribution (plotted with a solid line) is the same as the one obtained from the measured data statistics.

VI. CONCLUSIONS

A stochastic model for the characterization of fixed wireless links operating at millimetre wavelengths in urban propagation environments, relying on a macroscopic description of the topography, was presented. The model is established on a physical representation of the EM scatter by the main constituents of such propagation environments, namely, the buildings surrounding the main link and the ground, along with plausible assumptions on the statistical behavior of the cumulative scattered, ground reflected and direct fields. Random simulations over different realization of the building surfaces comprising the propagation environment have been carried out and compared with measurements. The comparisons showed good agreement in the prediction of main statistical parameters and, in particular, the average received power and the relative power of scattered field contributions, thus verifying the main assumptions relating to the received signal strength, as well as the validity of the Rician model in describing the signal envelope variability and in such complex propagation environments.

APPENDIX

For an irregular surface (Δs), for which the random height of each surface point above the mean plane follows a continuous distribution, the Kirchhoff approximation to the Stratton-Chu integral can be estimated asymptotically in terms of the large parameter β at the stationary points, i.e. the points of specular reflection from the surface where $\hat{\boldsymbol{q}} = \hat{\boldsymbol{n}}$. Here, plane wave incidence and far-field observation is assumed. By taking the slowly varying factor of the integrand outside the integral of eq. (3), the random signal at the receiver reads

$$r_S \approx \frac{jk}{4\pi} \frac{\exp[-jk(s_R + s_T)]}{s_R s_T} \boldsymbol{e}_R(\hat{\boldsymbol{s}}_R) \cdot \boldsymbol{\mathcal{T}} \cdot \boldsymbol{e}_T(\hat{\boldsymbol{s}}_T) \tag{16}$$

where, as above,

$$\boldsymbol{\mathcal{T}} = \boldsymbol{\mathcal{R}} \iint_{\Delta s} \exp\{j\beta[\zeta(x,y) + \boldsymbol{q} \cdot \boldsymbol{\rho}]\} dxdy \tag{17}$$

and $\boldsymbol{\mathcal{R}}$ is given by eqs. (6) and (7) by setting $\hat{\boldsymbol{n}}_l = \hat{\boldsymbol{q}}$. We are primarily interested in the second order moment of the received signal, which can be written approximately as

$$E\{r_S r_S^*\} \approx \left(\frac{k}{4\pi s_R s_T}\right)^2 F(\hat{\boldsymbol{s}}_R, \hat{\boldsymbol{s}}_T) E\{J(\hat{\boldsymbol{q}})\} \tag{18}$$

with $F(\hat{\boldsymbol{s}}_R, \hat{\boldsymbol{s}}_T) = |\boldsymbol{e}_R \cdot \boldsymbol{\mathcal{T}} \cdot \boldsymbol{e}_T|^2$ and

$$J(\hat{\boldsymbol{q}}) = \iint_{\Delta s} \iint_{\Delta s} \exp\{j\beta[\boldsymbol{q} \cdot (\boldsymbol{\rho} - \boldsymbol{\rho}') + \zeta(\boldsymbol{\rho}) - \zeta(\boldsymbol{\rho}')]\} \cdot dxdydx'dy'. \tag{19}$$

Bass and Fuks [6] provide an asymptotic approximation of a double integral of the form of eq. (19) for an homogeneous Gaussian surface with $\beta\sigma >> 1$, with σ being the standard deviation of the elevation above the rough surface mean plane. Assuming a Gaussian correlation function for the random heights $\zeta(\boldsymbol{\rho}), \zeta(\boldsymbol{\rho}')$ and angles of incidence and observation not close to grazing incidence, it turns out that

$$E\{J(\hat{\boldsymbol{q}})\} \approx \frac{2\pi(\Delta s)}{\beta^2 \chi_x \chi_y} \exp\left\{-\frac{1}{2}\left(\frac{q_x^2}{\chi_x^2} + \frac{q_y^2}{\chi_y^2}\right)\right\}, \tag{20}$$

where χ_x and χ_y are standard deviations of the (random) slope angles $\partial\zeta/\partial x$ and $\partial\zeta/\partial y$.

Sampling of GIS elevation data yields approximations for the standard deviations of χ_x and χ_y.

ACKNOWLEDGEMENTS

This work is part of a research program of the Radiowave Propagation and System Design Unit and was supported by a University of Glamorgan Scholarship.

REFERENCES

[1] ACTS Project 215, *Cellular Radio Access for Broadband Services (CRABS)-Specification of Next Generation of LMDS Architecture*, D2P1B, Feb. 1999.

[2]] Roman, V.I., "Frequency reuse and system deployment in local multipoint distribution service", *IEEE Personal Communications*, pp. 20–27, Dec. 1999.

[3] Papazian P. B., *et al.*, "Study of the local multipoint distribution service radio channel", *IEEE Trans. Broad.*, vol. 43, no. 2, pp. 175-184, June 1997.

[4] Xu H., Rappaport T. S., R. Boyle J., and Schaffner J. H., "Measurements and models for 38-GHz point-to-multipoint radiowave propagation", *IEEE J. Sel. Areas Comm.*, vol. 18, no. 3, pp. 310-321, March 2000.

[5] Bass F. G. and Fuks I. M., *Wave Scattering from Statistically Rough Surfaces,* Pergamon Press, 1979.

[6] Beckmann P. and Spizzichino A., *Scattering of Electromagnetic Waves from Rough Surfaces*, Artech House Publishers, 1987.

[7] Al-Nuaimi M. O. and Ding M. S., "Prediction models and measurements of microwave signals scattered from buildings", *IEEE Trans. Antennas Propag.*, vol. 42, no. 8, pp. 1126-1137, Aug. 1994.

[8] Pongsilamanee P. and Bertoni H. L., "Specular and nonspecular scattering from building facades", *IEEE Trans. Antennas Propag.*, vol. 52, no. 7, pp. 1879-1889, July 2004.

[9] Ivrissimtzis L. P., Al-Nuaimi M. O., Richter J., and Zhang J., "A statistical model of the urban propagation channel in fixed wireless systems", *Int. Union of Radio Science 27th General Assembly URSI 2002*, Maastricht, Netherlands, Aug. 2002.

[10] Zhang J., Richter J., Ivrissimtzis L. P., and Al-Nuaimi M. O., "Statistical modeling at 20GHz for fixed wireless access systems in urban multipath environments", *IEE Proc.-Microw. Antennas Propag.*, vol. 152, no. 4, pp. 278-283, Aug. 2002.

[11] Al-Nuaimi M. O. and Stephens R. B. L., "Measurements and prediction model optimization for signal attenuation in vegetation media at centimeter wave frequencies", *IEE Proc.-Microw. Antennas Propag.*, vol. 145, no. 3, pp. 201-206, June 1998.

[12] Cuinas I., Pugliese J.-P., Hammoudeh A., and Sanchez M. G., "Frequency dependence of dielectric constant of construction materials in the microwave and millimeter wave bands", *Microw. & Opt. Tech. Lett.*, vol. 30, no. 2, pp. 123-124, July 2000.

[13] Li L. J., Wang Y., and Gong Ke, "Measurements of building construction materials at Ka band", *Int. J. Infr. & mm-waves*, vol. 19, no. 9, pp. 1293-1298, 1998.

[14] Lahteenmaki J. and Karttaavi T., "Measurements of dielectric parameters of wall materials at 60 GHz", *Electron. Lett.*, vol. 32, no. 16, Aug. 1996.

[15] Dillard C. L., Gallagher T. M., Bostian C. W., and Sweeney D. G., "Rough surface scattering from exterior walls at 28GHz", *IEEE Trans. Antennas Propag.*, vol. 52, no. 12, pp. 3173-3179, Dec. 2004.

[16] Kong J. A., *Electromagnetic Wave Theory*, EMW Pub., 2000.

[17] Balanis C. A., *AntennaTheory and Design,* Harper & Row, 1981.

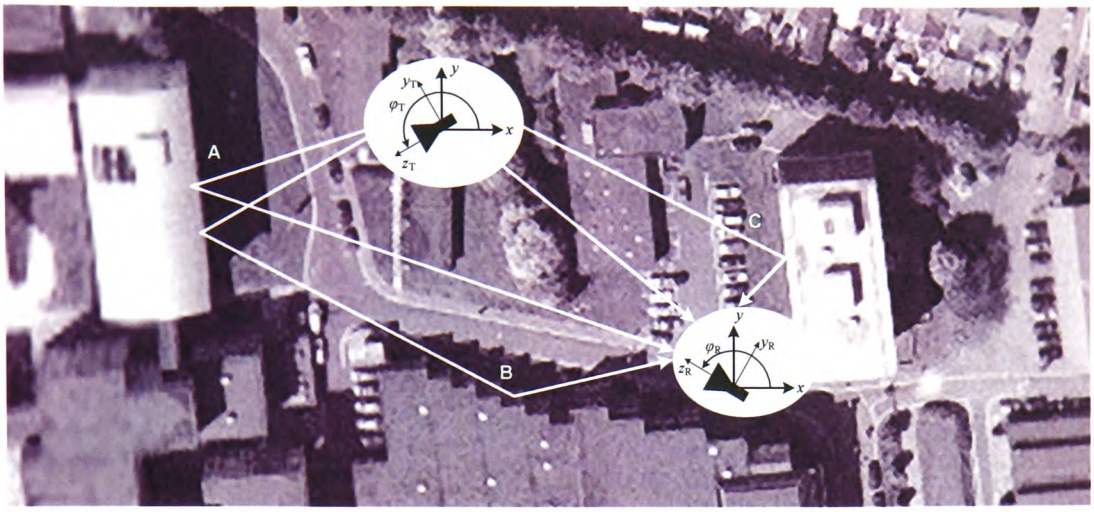

Figure 1: Campus site and measured link, with main building scatter contributions.

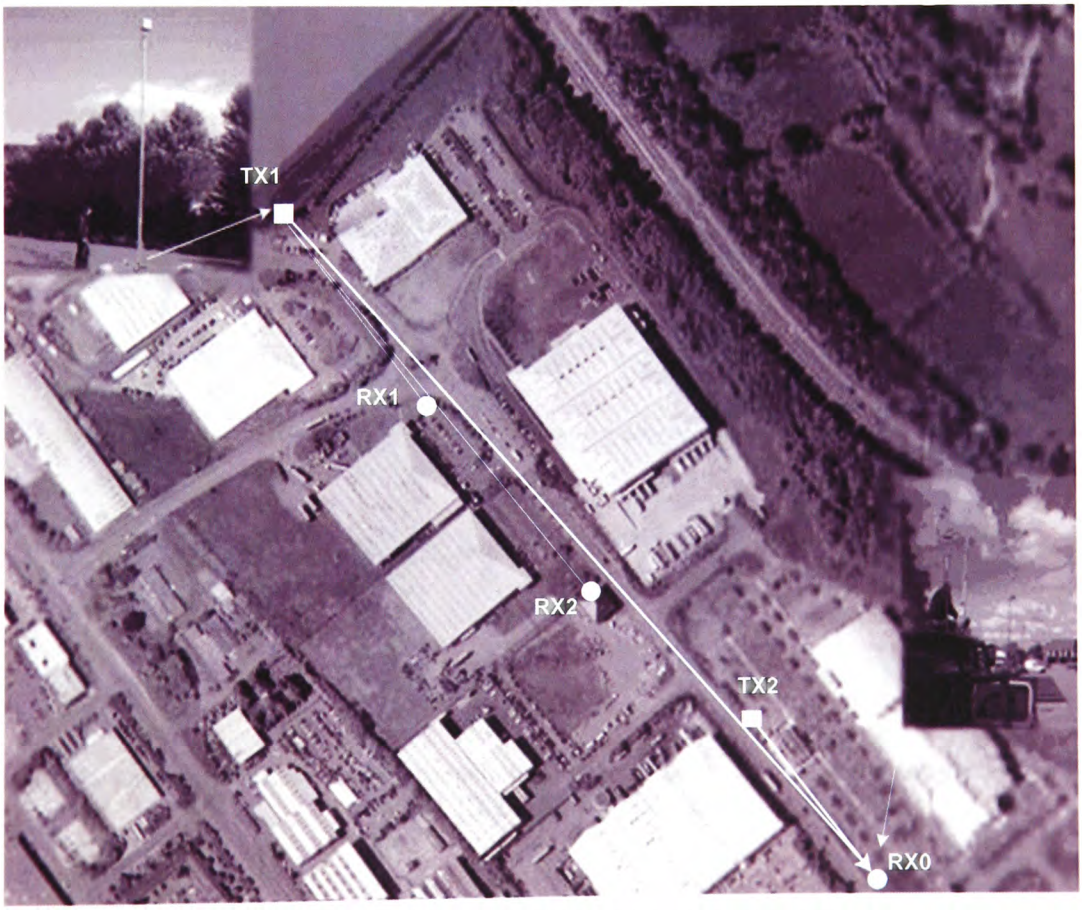

Figure 2: Industrial site and measured links.

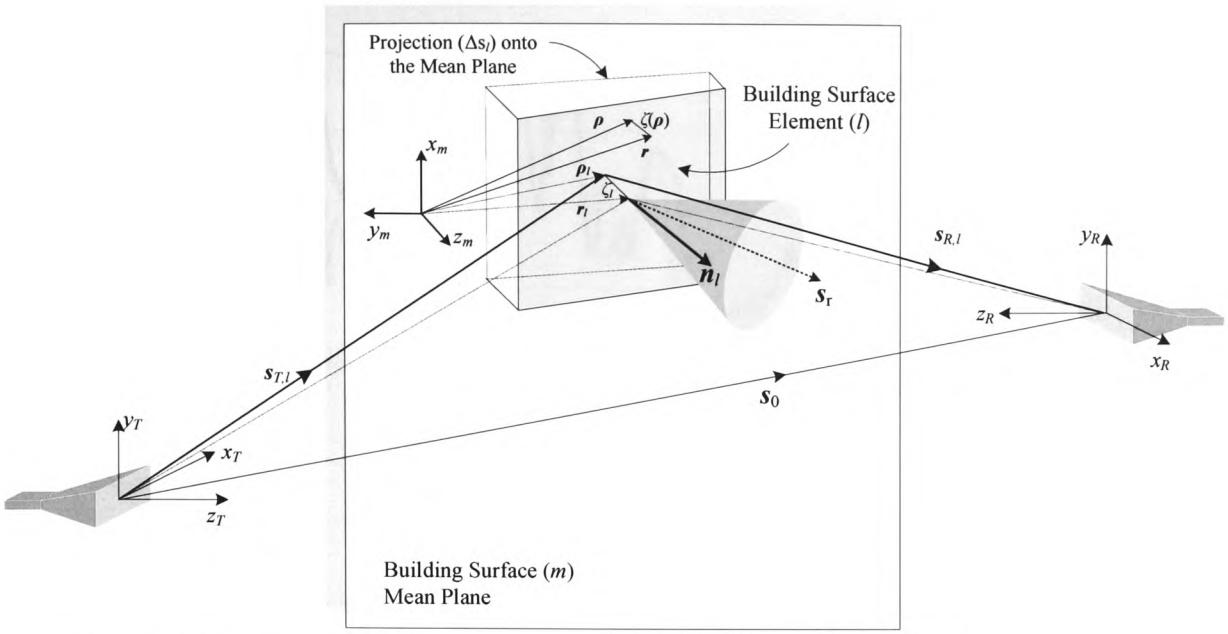

Figure 3: Geometry of the main link and an element of a scattering building surface.

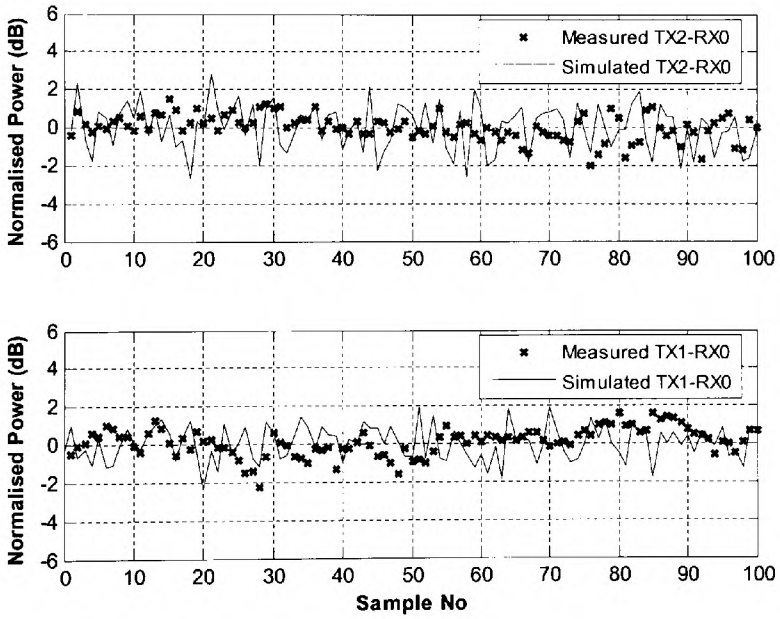

Figure 4: Measured and simulated snapshots of normalized received power for the TX1-RX0 (top) and TX2-RX0 (bottom) links.

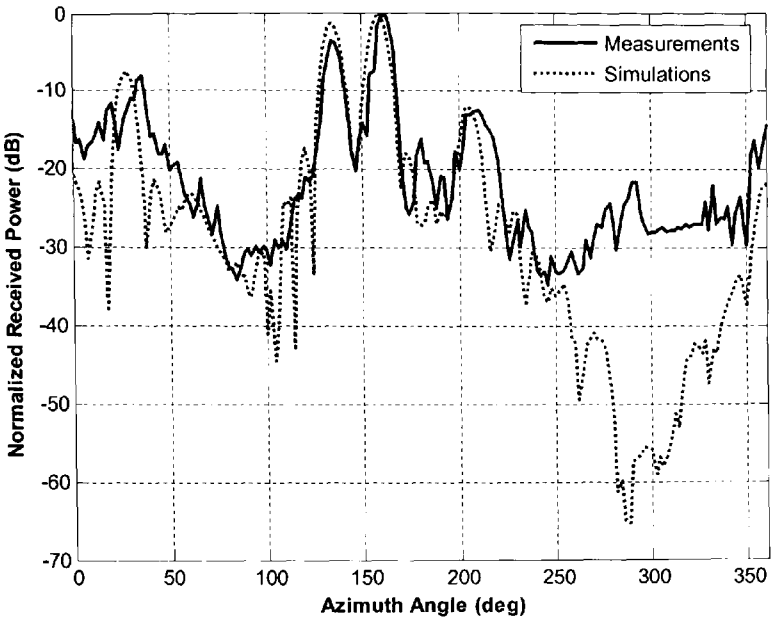

Figure 5: Average power gain variation vs. azimuth angle of receiver rotation for the UC link.

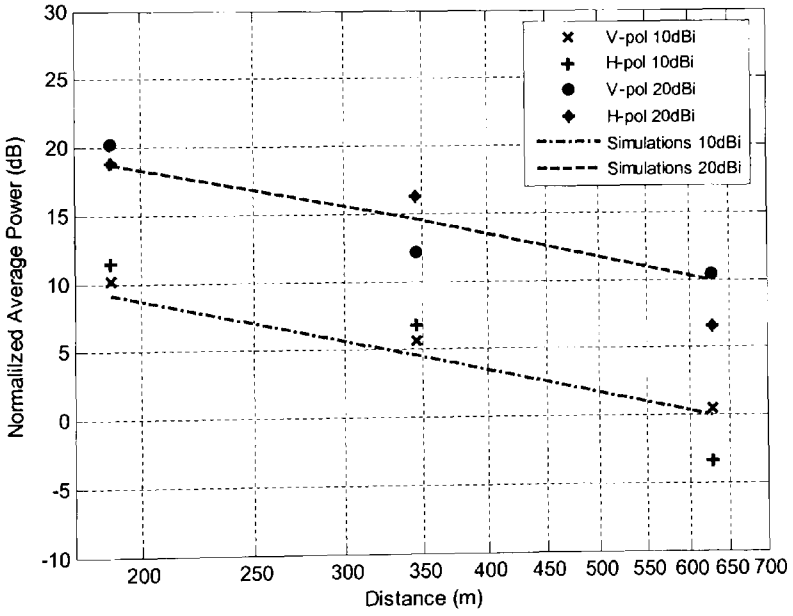

Figure 6: Average power variation vs. distance in the IE site.

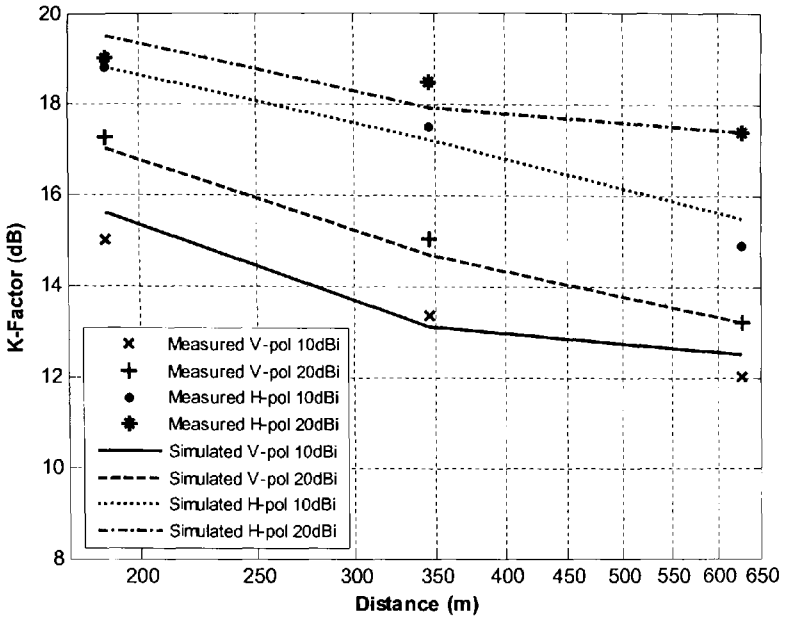

Figure 7: Rician *K*-factor vs. distance in the IE site.

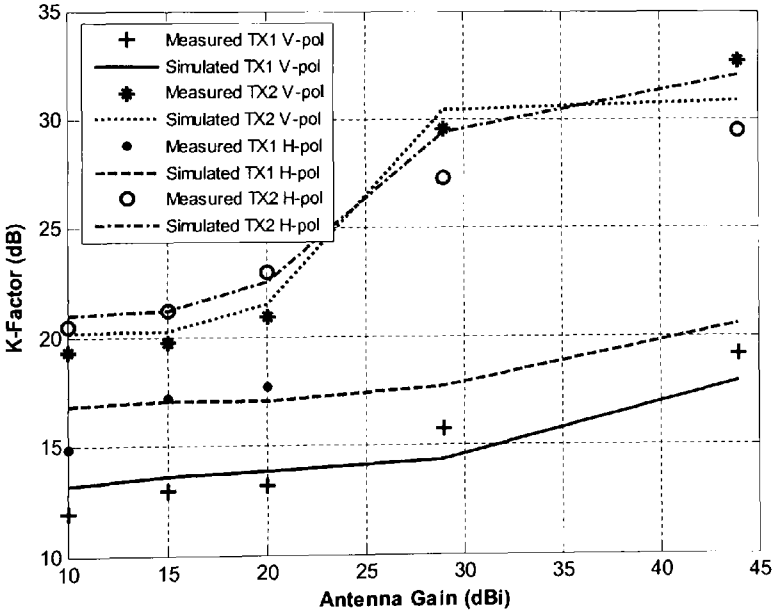

Figure 8: Rician *K*-factor vs. receiver antenna gain for transmitter positions TX1 and TX2 using a 20dBi gain transmitter antenna.

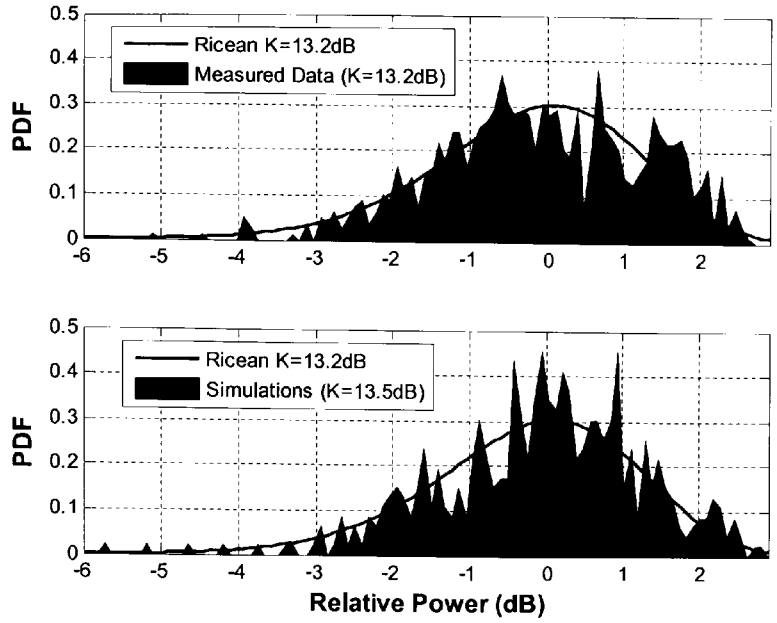

(a)

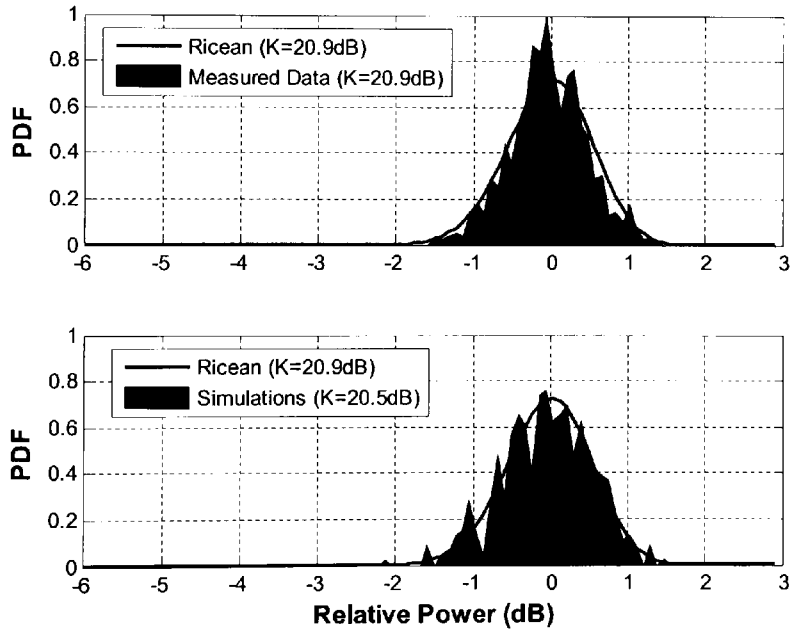

(b)

Figure 9: PDF of the received field and comparisons with the theoretical Rician and the distribution obtained from simulations for the vertical polarization: (a) TX1 link; (b) TX2 link.

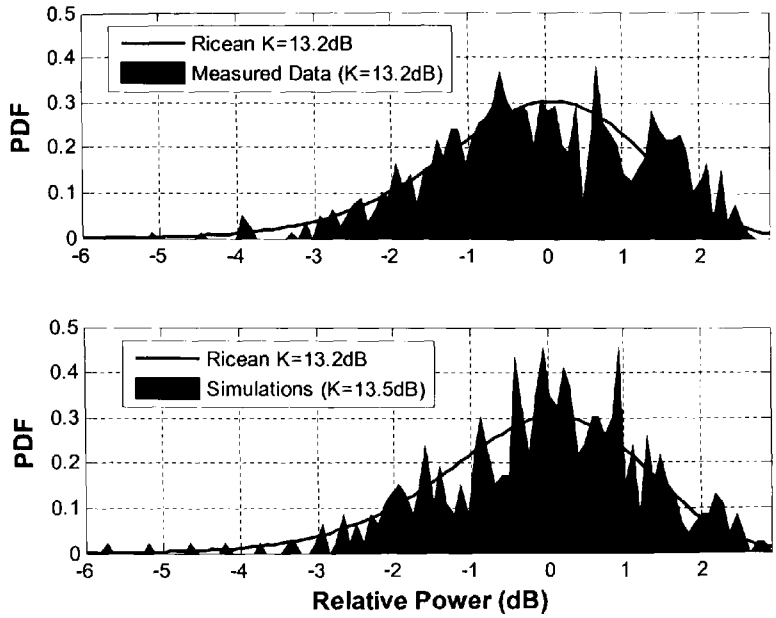

(a)

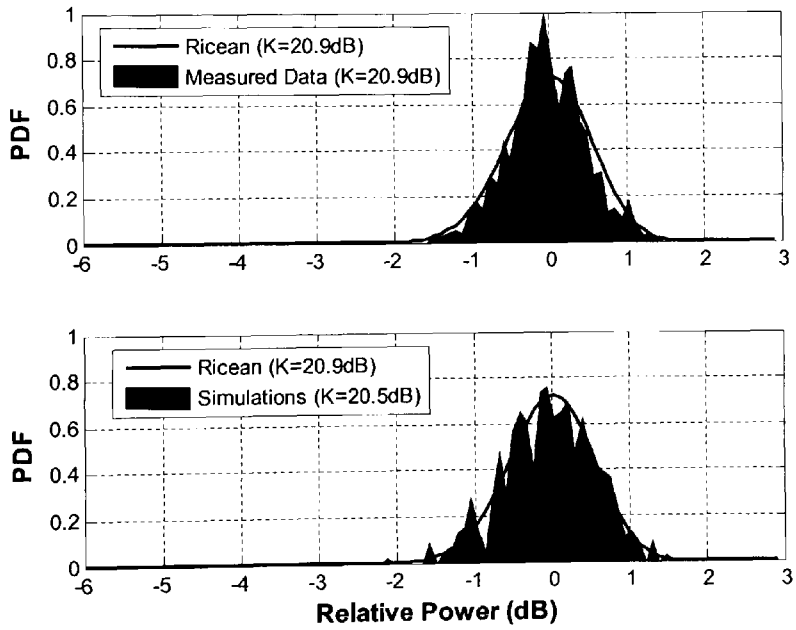

(b)

Figure 10: PDF of the received field and comparisons with the theoretical Rician and the distribution obtained from simulations for the horizontal polarization case: (a) TX1 link; (b) TX2 link.

Sample 2

Measurements and Modelling of Cellular Interference in Local Point-to-Multipoint Distribution Systems

Z. Muhi-Eldeen [(1)], L.P. Ivrissimtzis [(2)], M.O. Al-Nuaimi [(3)]
[(1)(3)] Faculty of Advanced Technology, University of Glamorgan, Pontypridd, UK
E-mail: zmuhield@glam.ac.uk
[(2)] Department of Physics, University of Ioannina, Greece.
Email: livrisim@uoi.gr

Abstract- **Frequency and polarization reuse for optimum spectral efficiency in local multipoint distribution systems (LMDS) networks generate co- and adjacent-channel inter- and intra-cell interference due to the line-of-sight (LOS) constraints among the transmitting and receiving antennas. Such operational constraints limit the system capacity and affect link performance. The paper presents measurements from a number of possible interference scenarios for two different LMDS reuse cellular plans of dual-frequency and dual-polarization discriminations. An electromagnetic (EM)-stochastic propagation model is employed, which successfully predicts the interference parameters, by taking into account the effects of multipath and depolarization caused by reflection and scatter from building surfaces at millimetre-wave frequencies. The probability density function (PDF) of the signal-to-interference ratio (SIR) and the statistical channel parameters, such as the average signal strength and the Rician *K*-factor, are extracted from the measured data and compared with model predictions.**

I. INTRODUCTION

LMDS structures employ point-to-point and point-to-multipoint configurations for the network uplink and downlink routes respectively, [1-2], and utilize narrow beam directional antennas at the subscriber's premises, forming a classical cellular network structure. Unlike conventional UMTS networks, service areas in LMDS are normally designed for short operational distances, with a maximum cell radius typically of the order of a few kilometres [1-5]. LMDS is a broadband network that is assigned to operate mainly in the millimetre-wave band. The radiowave propagation in this band is heavily influenced by the channel's topography, thus restricting the wireless channel to LOS paths only. In an urban or suburban environment, it is particularly affected by the diffuse scattering caused from buildings surfaces and facades. In a typical cellular deployment of LMDS networks, the Base Transceiver Station (BTS) is generally placed at elevation heights that are relatively lower than those used in UMTS networks. Receivers at the subscribers' premises are usually fixed at lamp-post heights, typically at roof-tops or side walls of buildings [6]. In effect, this aids in reducing any interference from surrounding

cells. With judicious radio system planning, frequency channels can be reused in small cells leading to the attainment of higher system capacity levels. Owing to the relatively short frequency and polarization reuse distances, operators will require more cells to achieve ubiquitous coverage of the service areas in a fully deployed network [7]. Short reuse distances are expected to provide better frequency spectrum utilization. However, reusing cells can be subject to severe interference levels on the uplink and downlink signal streams that will arise from nearby cells. Cellular interference is aggravated further by the use of highly directional antennas and the scatter effects of the propagation environment. Interfering signals comprise a dominant direct field, which is subject to propagation fading with a relatively long coherence time, due to the fixed nature of the link. Accordingly, the amplitude of the interference envelope can be considered random and is best described by a Rician statistical distribution and its associated parameters [8]. Interfering signals may share the same bandwidth with the desired signal and hence, their levels in a network can determine signal quality (BER) and ultimately, system capacity. In fact, addressing interference issues turns out to be a significant challenge in system deployment [9] and frequency reuse planning schemes [10]. The level of interference can be directly related to a number of factors, such as the frequency and polarization of the radio wave, frequency reuse strategy, antenna patterns and wave depolarization due to building surfaces, vegetation and rain droplets in the propagation environment. Depending on its source, interference can be characterized as co- or adjacent-channel interference. In the former case, interference is caused by a distant cell operating at the same channel frequency and polarization, whereas in the latter case, interference is caused by an adjacent cell operating with a cross-polarized signal at the same channel frequency.

Significant amount of research has been carried out in determining the effects of interference in mobile radio frequencies. While LMDS networks bear similar characteristics, deterministic EM techniques, such as ray tracing or classical propagation models are not applicable to millimetre-wave frequencies, mainly due to the following: the fundamental differences in the underlying propagation modes, requirements of a coarser description of the geometry, and the usage of more directive antenna technologies [9]. On the other hand, radio channel numerical and analytical modelling approaches developed for microcellular networks [6, 11-13] can be extended for the treatment of interference in LMDS. A general analysis of LMDS networks, including rain effects on inter-cell interference, has been presented by Panagopoulos *et al.* [14]. Bose *et al.* [15] carried out two-dimensional LOS interference simulations using one of the same frequency reuse plan discussed in this paper. However, their analysis is based on simple antenna and link design parameters, independent of the propagation geometry. More recently [16], the same authors incorporated terrain information from an urban topology data to focus on obstructions by tall buildings, based on half-power antenna beamwidths. System and co-channel interference characteristics of representative LMDS links were studied analytically and numerically by Gong and Falconer [17]. Their analysis accounted for the subscriber and hub antenna parameters, site diversity, and power control. A cell diversity method to mitigate co-channel interferences in fixed wireless access links is presented in [18].

Generally, measurements of interference mechanisms in LMDS networks have not yet been reported in the literature. Moreover, most of the millimetre-wave propagation models currently available are extrapolated from measurements and, hence, are mainly empirical and lack applicability in more general and complex propagation scenarios. GIS-based prediction models combining EM field predictions, system characterization, and

network planning can play a significant role in the study of LMDS employments and architectures. With regard to the above, the main objectives of this work are: (a) the investigation of interference mechanisms via measurements at 40 GHz with reference to the standard frequency reuse structures and (b) employment of an EM-stochastic propagation model, given by the authors, and comparison of the received signal and interference predictions with the measured data.

The paper is organized as follows: Section II presents an overview of the frequency plans and the corresponding interference scenarios. The EM model is briefly described in Section III. The measurement site and experimental setup is provided in Section IV. Comparisons between model predictions and measurements are provided and discussed in Section V. Finally some conclusions are given in Section VI.

II. LMDS Frequency Reuse Cell Plans and Interference Mechanisms

Cellular LMDS is based on FDD with TDMA and TDM access scheme at the uplink and downlink, respectively. The two dual-frequency and dual-polarization (double capacity) cellular plans investigated in this work are widely accepted in the literature and are referred to here as the conventional Sub-Optimal Plan (SOP) and the Alternative Plan (AP) [1]. For both plans as illustrated in Fig. 1, the 360° service area illuminated by the BTS is typically divided into 90° sectors. Dual signal polarization and frequency discrimination are used to provide the necessary isolation between cells. Both plans consist of expandable 16 (SOP) and 36 (AP) cell clusters. The main interference scenarios for the two dual-frequency and -polarization plans are depicted in Fig. 1. Throughout the paper, the following notations are adopted: F1 and F2 for the frequency channel used where F1 plus F2 is the total bandwidth available, U (uplink) and D (downlink) for the transmission direction, V (Vertical) and H (Horizontal) for the wave

polarization, and finally the subscript at the end indicates the associated cell number in the frequency plan. Given the LMDS cell structure description, the following interference mechanisms can be identified:

A. Sub-Optimal Plan (SOP)

IV. Inter-cell co-channel, co-polarization interference at the downlink ($F1DH_1$ & $F1DH_2$) and uplink ($F2UV_1$ & $F2UV_2$) from and to subscribers A and B. User A and BTS_1 will be affected by the uplink transmission of user B and, most likely, the latter will be affected by the downlink transmission of BTS_1. The level of interference is mainly determined by the relative distance between the subscribers and the BTS, as well as the receiving antenna beamwidth and elevation. Any building or vegetation obstructions of the unwanted link may aid in decreasing the level of interference.

V. Intra-cell adjacent-channel interference due to narrow guard bands between F1 & F2 in the downlink ($F2DH_4$ & $F1DH_4$) and uplink ($F1UV_4$ & $F2UV_4$) of the two users operating near the cell edges and served by the same BTS (for instance, to and from users C and D, and to and from BTS_4). Interference can be particularly severe in the uplink, since the channel frequency separation is only 10 MHz when compared with 39 MHz in the downlink. The level of interference depends on system parameters, such as the separation between the two FDD bands, the adjacent-channel rejection ratio provided by the diplexer at the BTS, the subscribers and the antenna radiation patterns, as well as scattering caused by the surrounding environment.

VI. Inter-cell co-channel, cross-polarization interference from the downlink of one cell to the uplink of an adjacent cell ($F2DV_3$ to $F2UH_4$ & $F1DV_4$ to $F1UH_3$) served by a different BTS and vice versa. Interference takes place between two adjacent sectors operating at the same frequency and different wave polarization. For example, leakage

from the downlink of BTS_3 interferes with the uplink of user E served by BTS_4. Such interference can be particularly significant in the case of a 90° BTS antenna beam. Reductions in interference would be expected if narrow multi-beam sectored BTS antenna were deployed. The level of interference is mainly determined by depolarization effects due to rainfall and environmental (building and vegetation) scatter, as well as the radiation characteristics of the antennas used at the BTS.

B. Alternative Plan (AP)

I. Intra-cell co-channel, cross-polarization interference at the downlink ($F2DV_4$ & $F2DH_4$) and uplink ($F1UH_4$ & $F1UV_4$), experienced by users F & G near the edges of the adjacent cells, to and from BTS_4, due to the depolarization effects mentioned earlier.

II. User intra-cell, co-channel interference in the uplink and downlink of users H and I. The transverse sectors $F2UV_1$ and $F2DV_1$, served by the same BTS share the same frequency (F2) between the uplink of one sector and the downlink of the other. The same case applies to the other transverse pair (F1). However, a BTS is normally placed on a building roof-top, and along with the utilization of narrow beamwidth receiving antennas, the LOS interfering paths between any two transverse intra-cell users are quite likely to be shielded.

III. Inter-cell co-channel interference at the downlink ($F1DH_2$ & $F1DH_5$) and uplink ($F2UV_5$ & $F2UV_2$), potentially due to specular reflections from a nearby building surface. For instance, on the downlink of user K served by BTS_5, the received signal can interfere with a signal transmitted by BTS_2 reflected by structures in the vicinity of the terminal. Similarly, the uplink of user K may interfere with the uplink of user J. The level of the interfering signal is determined by the presence of potential specular reflections.

IV. Inter-cell co-channel, co-polarization interference at the downlink ($F1DV_7$ & $F1DV_9$) and uplink ($F2UH_9$ & $F2UH_7$). A similar situation occurs in the SOP I. However, the fact that use of co-channels is repeated at every fifth sub-cell, such as the case of users L and M, and in addition to low probabilities of an existing LOS for paths longer than 1 km, renders in low interference levels for such a scenario.

III. A Stochastic Electromagnetic Propagation Model

In LMDS networks, although the wireless link is fixed, the propagation channel is time-varying, mainly due to the motion of objects within it and the perturbation of their electromagnetic properties caused by varying weather conditions. In addition, at high frequencies, an accurate geometric description of the environment at sub-wavelength scale, including the coordinates of the hub and subscriber antenna locations and orientation, is an impossible task. Hence, owing to random errors in the geometrical presentation and the time-varying nature of the channel, the analysis of the propagation mechanisms merits a statistical description, where in essence, the calculated fields and received signals are random variables. From such a description, the expected value, second-order statistics, and probabilistic distributions of the main link parameters can be deduced.

The EM field and signal level at the receiving station are considered random and are calculated using a Physical Optics (PO) approximation of the Stratton-Chu integral [19] representation of the scattered field by a closed surface, whereby the total EM field on the illuminated part of the surface is approximated by the superposition of the incident and reflected components arising from plane interface fields. The calculations assume realistic transmitting and receiving antennas radiation patterns. In particular, the stochastic-EM model describes the total induced emf at the receiver as the summation of

scattering contributions from buildings, a ground reflection component, and a direct LOS signal component. Furthermore, the scattered field intercepted by the receiver is given by the superposition of distinct waves scattered from the building surfaces in the propagation environment that are illuminated by both the receiver and transmitter antenna radiated fields. The details of the physical propagation model are presented in [20] and only a brief outline is presented below.

Buildings are considered to comprise flat surface elements and, hence, the total scattered field is the sum of the PO approximation of the scattering from such surface elements. Statistics for the elevation of their mid-points above or below the building surface mean plane, as well as their orientation are obtained from relatively coarse GIS data and digital images. The approximation of the total field at each surface also references a database of reflection coefficient measurements from building materials. Given the uncertainty of knowing the exact position and orientation of these surface elements and the specific materials used, the field scattered by a building surface can be considered approximately as a Gaussian random variable with first- and second-order moments obtained from a Monte-Carlo simulation of the PO scattering approximation carried out over different realizations of the building surface and the given statistics of the elevation, orientation, and surface material reflection coefficients.

Thus, the scatter contribution to the received signal for N building surfaces concerned may be expressed as

$$r_S = a_S e^{j\phi_S} = \sum_{m=1}^{N} r_{S,(m)} \tag{1}$$

where $a_S = |r_S|$, $\phi_S = \arg r_S$ and

$$r_{S,(m)} \approx \frac{jk}{2\pi} \frac{\exp\left[-jk\left(s_{R,m} + s_{T,m}\right)\right]}{s_{R,m} s_{T,m}} e_{R,m} \cdot \sum_{l} S_{l,m} \cdot e_{T,m} \cdot \tag{2}$$

In Eq. (2), k is the wave number, $\boldsymbol{e}_{R,m}$ and $\boldsymbol{e}_{T,m}$ are the receiver and transmitter radiation pattern vectors in the far field regions of surface m at a distance of $s_{R,m}$ and $s_{T,m}$ from the receiver and transmitter, respectively, and $\boldsymbol{S}_{l,m}$ is a dyadic obtained from the PO approximation of the scattered field from a flat surface element l and m is a function of its elevation with respect to the mean plane and orientation, its reflectivity properties, and the directions of incidence and observation. As pointed out, the statistics of $\boldsymbol{S}_{l,m}$ and, consequently, $r_{S,(m)}$ are obtained from relatively coarse, albeit sufficient, statistical description of the position, orientation, and EM properties of the surface elements comprising the building surface.

The random scattered field power intercepted by the receiving antenna is incoherently superimposed on the direct field power as well as that of a Geometrical Optics (GO) field reflected from a presumably infinite ground. Eventually, the signal at the receiver antenna terminals can be represented by the complex random variable

$$r = a\exp(j\phi) = a_D \exp(j\phi_D) + a_R \exp(j\phi_R) + a_S \exp(j\phi_S), \tag{3}$$

in which a_D, a_R, and a_S are the envelope amplitudes of the direct, reflected and scattering components respectively. The envelope of $a_R \exp(j\phi_R) + a_S \exp(j\phi_S)$ is Rayleigh distributed, while the relative phases are independent random variables, uniformly distributed over the range $(0,2\pi)$.

Given this stochastic nature of the reflected and scattering contributions, the envelope of the total received signal, in the presence of a deterministic direct field, will have a Rician distribution, i.e.,

$$f_a(a) = \frac{a}{\sigma^2}\exp\left(-\frac{a^2+s^2}{2\sigma^2}\right) I_0\left(\frac{as}{\sigma^2}\right), \tag{4}$$

where I_0 is the modified Bessel function of the first-kind and zero-order,

$$2\sigma^2 = (a_R)^2 + (a_S)^2 \tag{5}$$

and $s^2 = (a_D)^2$. Introducing the Rician K-factor $K = s^2/(2\sigma^2)$, where σ signifies the scattered field power, the distribution of the total received power $p = a^2/2$ for a normalized direct field ($s^2 = 1$), becomes

$$f_p(p) = 2K \exp[-K(2p+1)] \cdot I_0\left(2K\sqrt{2p}\right). \tag{6}$$

From the definition of Eq. (5), given a set of random, simulated, or measured data, the K-factor can be derived from the mean $\mu_p = \sigma^2 + s^2/2$ and standard deviation $\sigma_p^2 = \sigma^4 + s^2\sigma^2$ of the received power samples and is given by the following formula:

$$K = \frac{\sqrt{\mu_p^2 - \sigma_p^2}}{\mu_p - \sqrt{\mu_p^2 - \sigma_p^2}}. \tag{7}$$

The determination of the Rician K-factor allows a narrowband characterization of the flat-fading effects of the wireless propagation channel, namely the effects of building and ground scatter on the received signal and the SIR variability. Hence, the characterization of the wireless channel can be reduced to an approximate derivation of the Rician K-factor. The latter attains high values for LOS links, where the direct boresight field from the transmitter dominates the received signal, nevertheless, it reduces to smaller values for longer interfering links and, eventually, degrades to zero for a severe non-LOS reception paths, which are described by a Rayleigh distribution.

As already pointed out, interference in LMDS channels is constrained to LOS paths for both the interfering and wanted links. The envelope for both links, as shown in the next section, follows a Rician distribution with different K-factors, nominally a much higher

value for the desired link. It can be shown from [21] that the SIR is distributed according to the following PDF:

$$f_z(z) = \frac{2zb}{(b+z^2)^2} \exp\left(-\frac{K_I z^2 + K_0 b}{b+z^2}\right) \cdot \left[\left(1 + \frac{K_0 z^2 + K_I b}{b+z^2}\right) I_0(c(z)) + c(z) I_1(c(z))\right], \quad (8)$$

with

$$c(z) = \frac{\sqrt{4K_0 K_I b z^2}}{b+z^2}, \quad (9)$$

where $b = \sigma_0^2 / \sigma_I^2$ is the ratio of the scattered field power of the wanted and interfering link, z is the ratio of the direct field power of the wanted and the interfering link, K_0 and K_I denote the K-factor of desired and interfering link respectively. In the rest of the paper, Eq. (8) will be referred to as Oetting's distribution.

IV. MEASUREMENT SITE AND SETUP

An extensive measurement campaign has been carried out at 40 GHz within an industrial area in order to acquire deeper insight on some of the interference mechanisms defined in section II. A GIS top view of the measurement site is shown in Fig. 2. The geometry corresponds to the co-channel interference scenario (SOP I) discussed in Section II, and the light shaded area refers to positions where a LOS can be achieved, from both the interfering source and the desired transmitter. Along the interfering path, there are a number of industrial buildings that are widely diverse both in their shapes and footprints. Apart from a few nearby parked vehicles, the radio path of the desired link was almost clear of any obstacles. The cross symbols in Fig. 2 refer to the locations of either a transmit or receive terminal. By combining these locations it was possible to produce a few of the interference scenarios discussed in Section II. In all measurements, the desired and interfering transmitters were placed on top of a mast at an elevated point above the

ground. The heights of the transmitting antennas in Fig. 2 are 14 and 6.3 m above the street level, with a transmitter–receiver distance separation of 127 and 627 m for the desired and interfering links, respectively.

The transmitter comprises a Gunn diode oscillator, in a temperature-controlled environment that provides a stable reference between 39.75 and 40.25 GHz. The received signal is down-converted to an intermediate frequency, amplified, peak-held, and sampled with a resolution bandwidth of 1 MHz. Distribution functions were obtained from the samples of the received signal, using approximately 800 signal power samples recorded per measurement run. In all links, a 20 dBi pyramidal-horn antenna was used for transmission, while at the receiver side, different antenna gains and types were employed, including three pyramidal-horns with gains of 10, 15, and 20dBi (beamwidths 39–20°), and two lens-horns with gains of 29 and 44 dBi (beamwidths 5–1.8°).

V. MEASUREMENT RESULTS AND COMPARISONS

A. Signal and K-factor trends

Since the channel can be adequately characterized by Rician parameters, for each receiver location the Rician *K*-factor is extracted from measurements and plotted adjacently next to the received signal level, as shown in Fig. 3. During measurements, extra caution was taken to ensure that each position attained a clear unobstructed LOS path. These measurements were conducted approximately over separation distances of 188, 346, and 627 m from the BTS and employed a 10 and 20 dBi pyramidal-horn antenna at the receiving side. A quadratic MMSE curve fit is applied, whence a number of observations can be made. In the vertical polarization case, the signal trend falls roughly by 5 dB per 100 m. This is true for both antenna gains. Reception levels are lower for the horizontal polarization case; however, the latter shows lower decreasing

rates. For both polarization cases, the K-factor decreases towards the cell edges by approximately 1.5 dB per 100 m.

B. Measured and predicted distributions

In Fig. 4, the PDF of the normalized received signal power, as obtained from measurements and model predictions, is shown and compared with the theoretical Rician distribution for the interfering and desired links depicted in Fig. 2. The K-factor values extracted from both measured and predicted data are used in the theoretical Rician distribution (plotted with a solid line) formula given by Eq. (6). The comparisons yield comparable statistical distributions with good agreement. The horizontal polarization case, not shown here, exhibits a similar probabilistic behaviour with that of the vertical polarization. Fig. 5 illustrates the PDF of a cross-polarization case (transmitted field horizontally polarized and vertically polarized receiver antenna). The minor discrepancy between the measurements and the simulations is due to the assumption of ideal orthogonal radiation patterns in the model, which is not the case in reality, thus resulting in higher direct field components.

Similarly, Figs. 6 & 7 compare the normalised SIR of the measured, predicted, and theoretical probabilistic behaviours of the selected co- and adjacent-channel interference scenarios discussed below in Section C. It becomes evident from comparisons with the theoretical curve that the SIR observes the distribution of the ratio of two Rician channels given by Oetting's distribution. Again, the theoretical distribution is based on the K-factors and ratio of the scattering field powers of the two links, as derived from the statistical analysis of the measured data samples and application of Eqs. (8) and (9). The probabilistic distributions and the underlying statistical parameters of the theoretical

expressions show good agreement with measured data and signal samples from the model predictions.

C. Interference measurements

Higher values of K_0 are expected and required for the desired link since they correspond to better detection levels and link availability, whereas higher values of K_I are undesired and imply stronger interfering levels and consequently, greater outage probabilities. This section endeavours to examine the model predictions of K-factor values compared to those extracted from field measurements. Two of the interference scenarios defined in Section II, namely case (I) of the SOP and case (I) of the AP are considered. These are arguably of most concern in a fully deployed network. A 20 dBi horn antenna was always used when transmitting; this is justified since a sectored antenna is most likely to be employed at the BTS. At the receiver side, a range of receive antenna gains (10–44 dBi) is recommended in the published literature and hence was used in the measurements.

1. SOP Scenario I

This typical scenario is illustrated in Fig. 1(a), where users A and B not only operate at the same frequency band and polarization, but also lie within the boresight of a co-channel path at the uplink or downlink. Fig. 8 compares the K-factors from measurements with the predictions using the model for the desired signal and co-channel interference paths. It is noted that the K-factor values for the horizontally polarised link are lower than those in the vertically polarised, whereas the latter maintains a larger difference between the values of Ko and K_I.

2. AP Scenario I

Users F and G in Fig. 1(b) may encounter a co-channel, cross-polarization interference when either of them, or both are positioned close to the cell boundaries. In an actual network deployment, a lower antenna gain may not be suitable in such a case since it may result in the reception of interfering signals from a wide reception angle. On the other hand, a high-gain antenna may intercept or transmit high levels of cross-polarized signals through the main and side-lobes. Therefore, the selection of a suitable antenna gain becomes critical. Results of the *K*-factor values obtained from both, measurements and the model for a worst-case scenario, whereby the LOS path of the receiving antenna is within the boresight of the desired and the interfering transmissions are depicted in Fig. 9. Despite the polarization discrimination provided by the horn and lens-horn antennas, it is was found that for a cross-polarization reception, high *K*-factor values for the interfering link are still possible. These ranged from zero at the lowest antenna gain (10 dBi) rising to 25 dB for the highest antenna gain (44 dBi).

VI. CONCLUSIONS

The employment of a stochastic model incorporating GIS terrain data combined with computationally efficient predictions and experimental measurements of interference levels in LMDS networks have been presented. With applicability at millimetre-wavelengths frequency bands in a suburban propagation environment, the model offers potential applications in the characterization, design, and deployment of fixed wireless access networks. Over 120 sets of measurement were conducted, involving several paths and distances at 40 GHz in order to provide deeper insight into interference mechanisms associated with two LMDS frequency and polarization reuse plans. The main co- and adjacent-channel interference mechanisms for each frequency plan have been highlighted and analysed.

Predictions of the signal and interference level statistics along with their distribution functions using the EM model, that is derived by the authors (see reference [20]), were compared with measurements and theoretical distribution curves. It has been shown that the fading characteristics of both the wanted and interfering links can each be adequately described by a Rician distribution. Hence, determination of the Rician K-factor becomes valuable in assessing the performance of LMDS cellular channels and thus it has been used as a key comparison and link evaluation parameter. The K-factor was obtained experimentally for a number of link and polarization cases, as well as antenna radiation characteristics at the transmitter and receiver locations and compared against the K-factor values derived from the stochastic-EM model for the millimetre-wave propagation channel. Good agreement was obtained in all cases. The slight discrepancy between the comparisons is mainly attributed to the theoretical antenna radiation patterns in which side-lobes levels were assumed to be negligible. This effect was found to be more significant in the cases involving cross-polarized waves and high antenna gains such as the lens-horn, where peaks exist in both, the main and side-lobes of the radiation patterns. In general, Rician K-factor values for the co-channel interference were found to be in the range of 13-23 dB. These were higher than the adjacent channel interference values that ranged between 0-25 dB despite the shorter path length. These ranges depend on the radio link parameters such as the receive antenna's position, type, and gain. Finally trends of the received signal levels and K-factors decreased at a maximum rate of 5 and 1.5 dB per 100 m, respectively.

The stochastic model employed has a number of potential applications one of which is the parameterization of the physical attributes of the channel and the associated electromagnetic mechanisms and, ultimately, the representation of the channel. In effect, the model permits predictions of the signal and SIR statistics and distributions. Knowing

the SIR threshold values, which are modulation and capacity dependent, LMDS cell plans can be evaluated by estimating from the model, the minimum frequency reuse distances and average cell radii lengths, which in turn, aid in minimizing interference levels for optimum system performances. In the interference limited environment of LMDS networks, such predictions incorporating antenna heights and patterns become essential for the millimetre radio system design.

REFERENCES

[1] ACTS Project 215, *Cellular Radio Access for Broadband Services (CRABS), Specification of Next Generation of LMDS Architecture D2P1B*, 1999.

[2] Nordbotten, A., "LMDS systems and their application", *IEEE Commun. Mag.*, vol. 38, no. 6, pp. 150–154, June 2000.

[3] Papazian, P.B. *et al.*, "Study of the local multipoint distribution service radio channel", *IEEE Trans. Broadcast.*, vol. 43, no. 2, pp.175–184, June 1997.

[4] Matsuda, M. and Watanabe, K., "26-GHz band FWA systems employing co-channel interference avoidance method using TDMA/TDD frame timing control", *IEEE Global Telecommunications Conference*, 2004.

[5] MPT 1560, "Performance specification for digital multi point video distribution systems (MVDS) transmitters and transmit antennas operating 40.5–42.5 GHz", *Radio Communications Agency*, UK, 1995.

[6] Muammar, H.R., "Co-channel interference in microcellular mobile radio systems" *IEEE Proc. VTC '91*, pp. 198–203, May 1991.

[7] Clark, M.V., Erceg, V., and Greenstein, L.J., "Reuse efficiency in urban microcellular networks", *IEEE Trans. Veh. Tech. '97*, vol. 46, no. 2, pp. 279–288, May 1997.

[8] Muhi-Eldeen, Z., Al-Nuaimi, M.O., Richter, J., and Ivrissimtzis, L.P., "Performance analysis of reflection paths for millimeter wavelength systems", *IEEE International Conference on Computer Systems and Applications*, AICCSA, May 2007.

[9] Roman, V.I., "Frequency reuse and system deployment in local multipoint distribution service", *IEEE Personal Communications*, pp. 20–27, Dec. 1999.

[10] Hughes Network Systems, "System analysis for point-to-multipoint networks Part 1: frequency reuse planning", *White Paper for Telecommunications Service Providers Using the AIReach® 9000 System*, 2003.

[11] Yu-Dong, Y. and Sheikh, U.H. "Investigations into cochannel interference in microcellular mobile radio systems", *IEEE Trans. Veh. Tech.*, vol. 41, no. 2, pp. 114–123, May 1992.

[12] Wijk, V.D., Kegel F., and Prasad A., "Assessment of a pico-cellular system using propagation measurements at 1.9 GHz for indoor wireless communications", *IEEE Trans. Veh. Tech.*, vol. 44, no. 1, pp. 155–162, 1995.

[13] Zhang, Q.T., "Co-channel interference analysis for mobile radio suffering lognormal shadowed Nakagami fading", *IEE Proc. Commun.*, vol. 146, no. 1, pp. 49–54, Feb. 1999.

[14] Panagopoulos, A.D. *et al.* "Intercell radio interference studies in broadband wireless access networks", *IEEE Trans. Veh. Tech.*, vol. 56, no. 1, Jan. 2007.

[15] Bose, R., Bauer, G., and Jakoby, R., "Two-dimensional line of sight interference analysis for LMDS networks for the downlink and uplink", *IEEE Trans. Antennas Prop.*, vol. 52, no. 9, pp. 2464–2470, Sept. 2004.

[16] Bauer, G., Bose, R., and Jakoby, R., "Three-dimensional interference investigations for LMDS networks using an urban database", *IEEE Trans. Trans. Antennas Prop.*, vol. 53, no. 8, pp. 2464–2470, Aug. 2005.

[17] Gong, S.Q. and Falconer, D., "Co-channel interference in cellular fixed broadband access systems with directional antennas", *Wireless Pers. Commun.*, vol. 10, pp. 103–117, Oct. 1998.

[18] Liolis, K.P., Panagopoulos, A.D., and Cottis, P.G., "Use of cell-site diversity to mitigate co-channel interference in 10-66 GHz broadband fixed wireless access networks", *Radio and Wireless Symposium*, IEEE 2006.

[19] Stratton, J.A., *Electromagnetic Theory*, McGraw Hill Book Co., New York, 1941, ISBN 0070621500.

[20] Muhi-Eldeen, Z., *et al.* "Measurements and Physical Electromagnetic Statistical Modelling of mm Wavelength Propagation", to appear in *Progress in Electromagnetic Research Symposium Proceedings*, Hangzhou, China, March 2008.

[21] Oetting, J.D., "The effects of fading on antijam performance requirements", *IEEE J. Sel. Areas Commun.*, vol. 5, pp. 155–161, Feb. 1987.

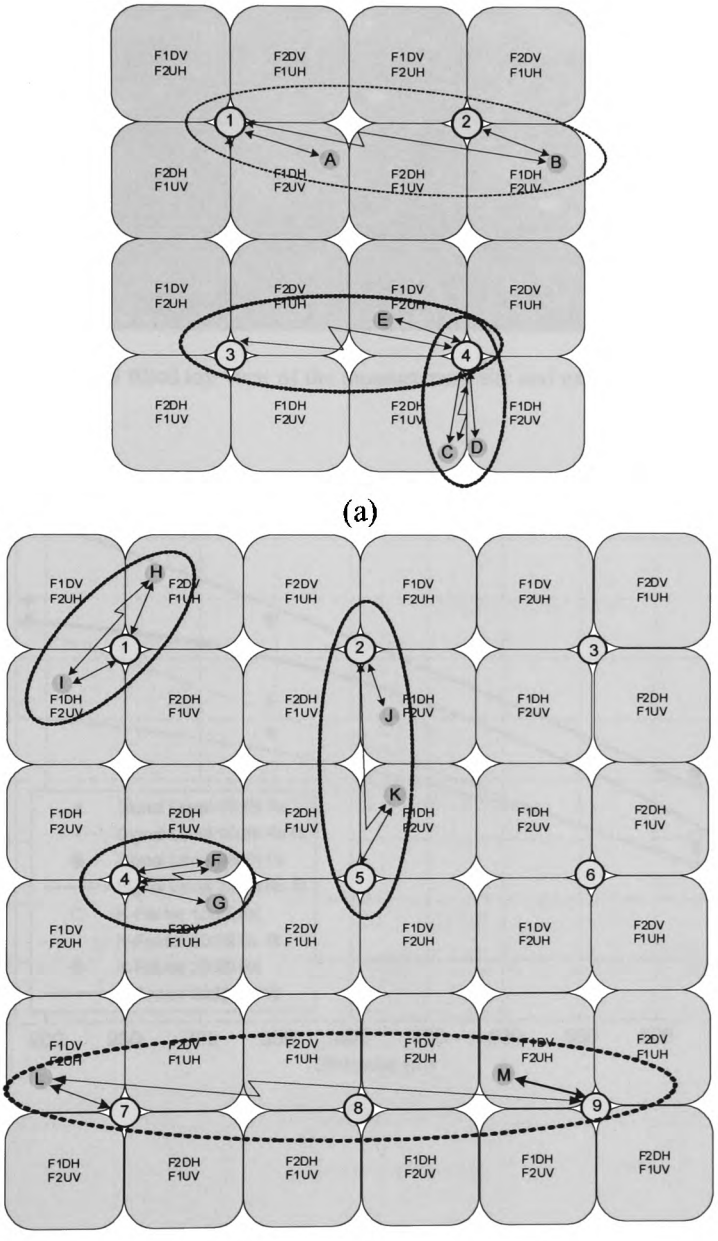

Figure 1: (a) 16 cluster SOP; (b) 36 cluster AP

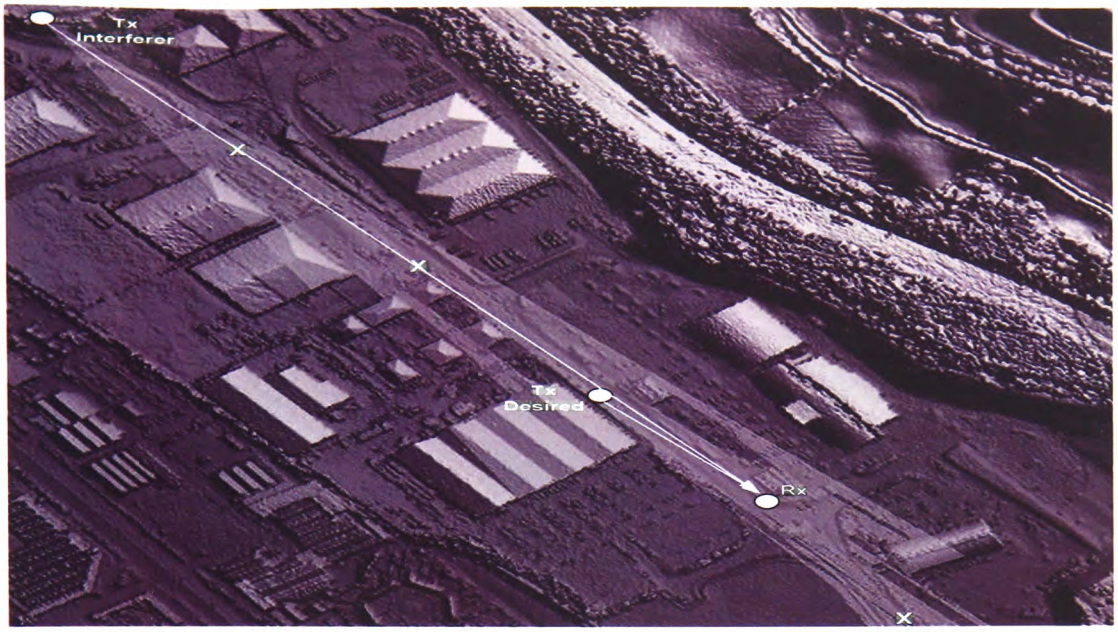

Figure 2: GIS tilted top view of the measurement site and experimental links

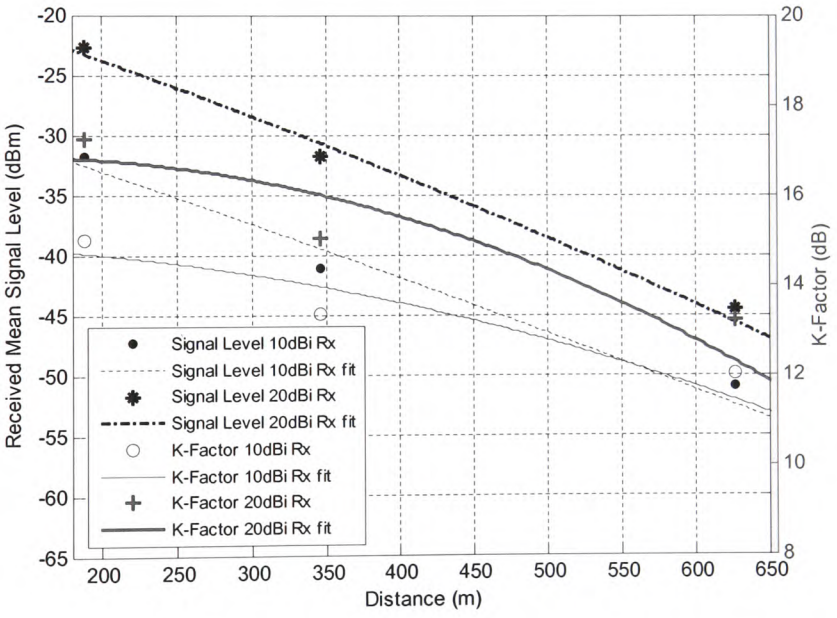

(a)

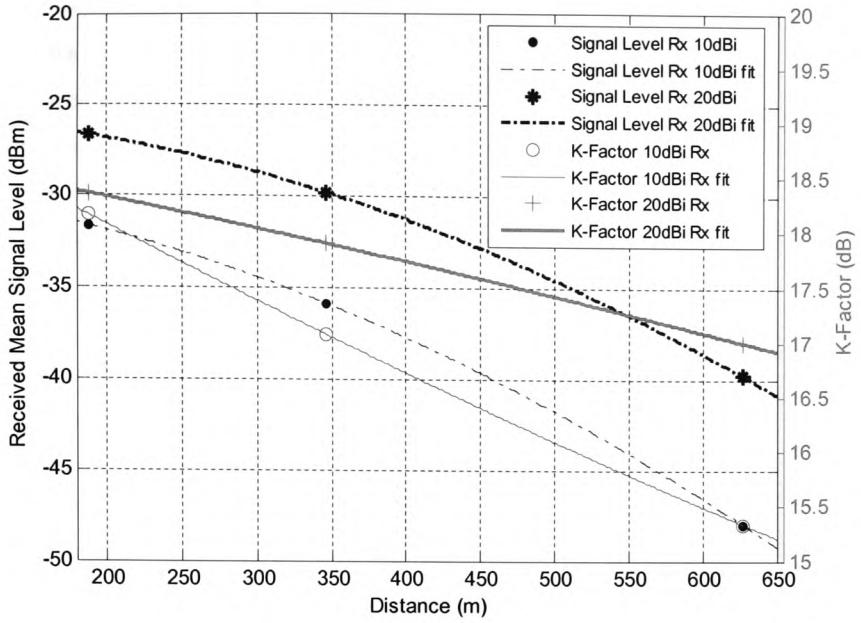

(b)

Figure 3: Received signal power and *K*-factor variability with distance: (a) Vertical polarization (b) Horizontal polarization

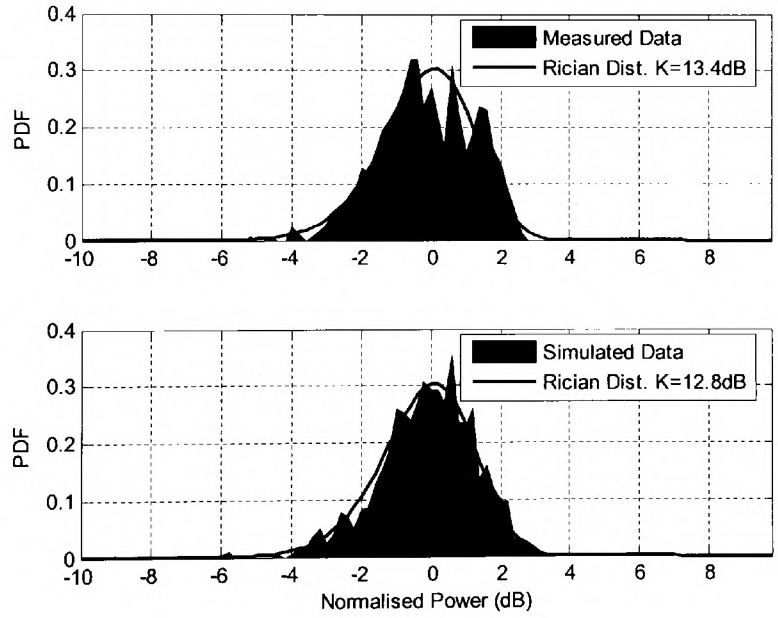

(a)

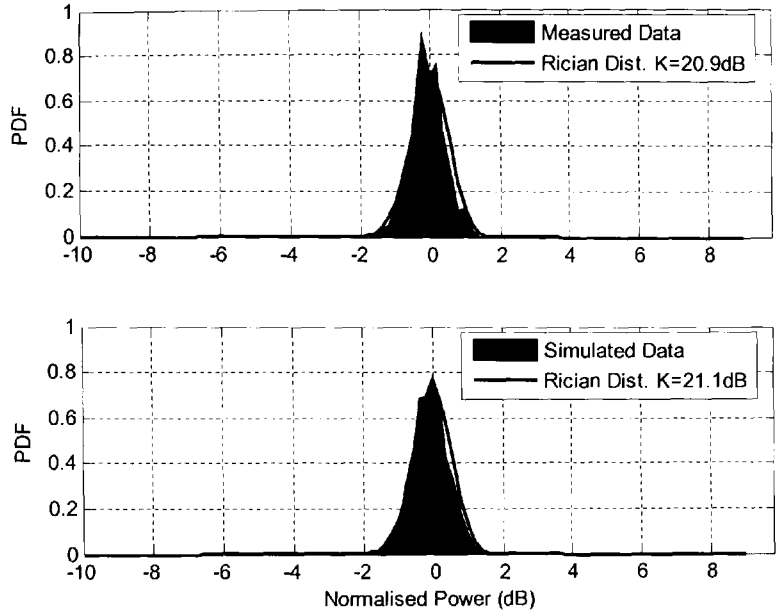

(b)

Figure 4: PDF of the measured and predicted received field, each compared with a theoretical Rician PDF for the vertical polarization case of: (a) TX interferer; (b) TX desired link shown in Fig. 2.

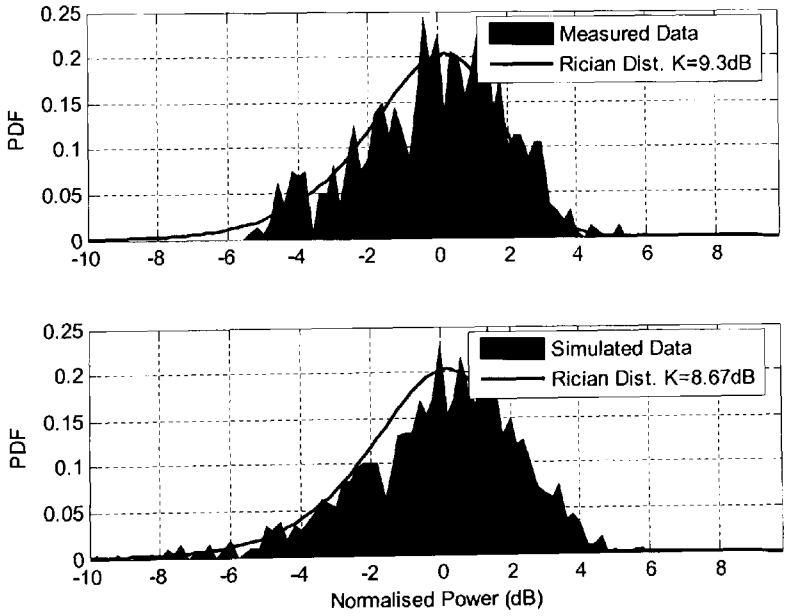

Figure 5: PDF of the measured and predicted received field each compared with a theoretical Rician PDF for a 200 m cross-polarized link.

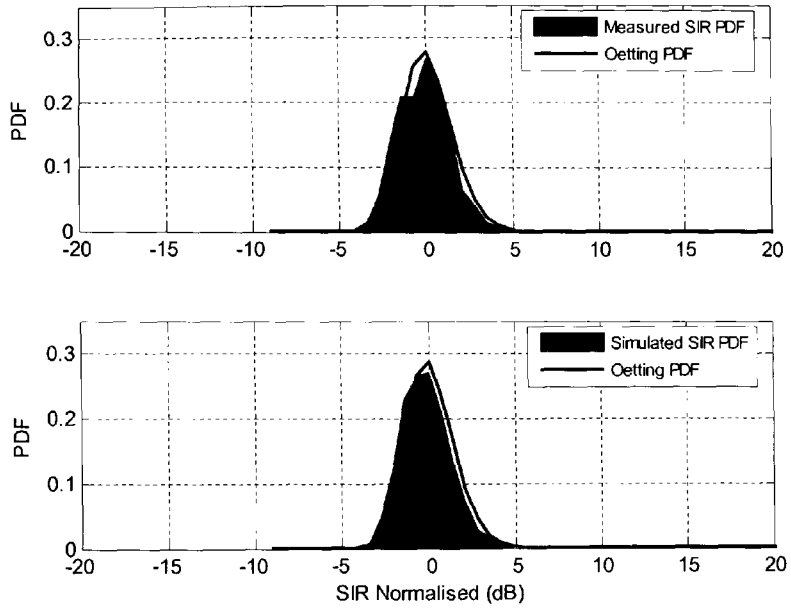

Figure 6: PDF of the co-channel SIR between two links (SOP (I): $F2UV_1$ & $F2UV_2$) for a 20 dBi transmit and receive antenna gains.

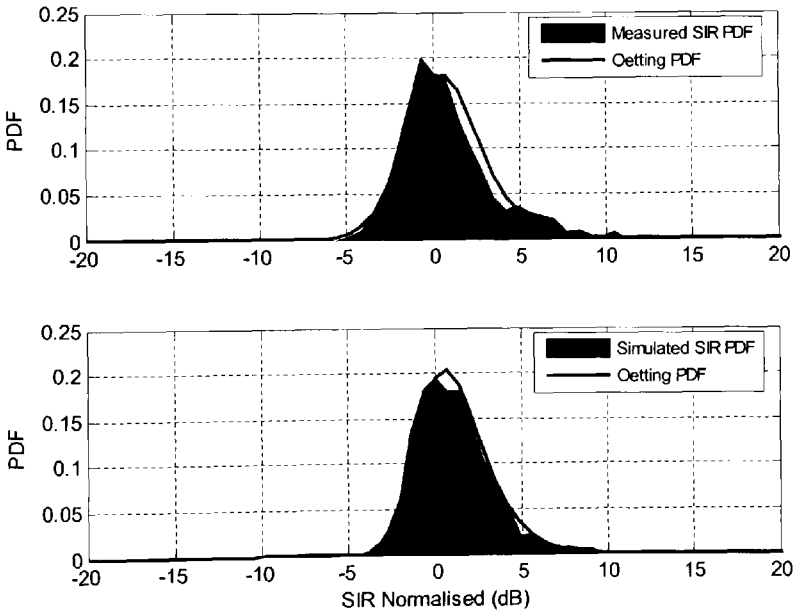

Figure 7: PDF of the adjacent-channel SIR between two links (AP (I): $F1UH_4$ & $F1UV_4$) for a 20 dBi transmit and receive antenna gains.

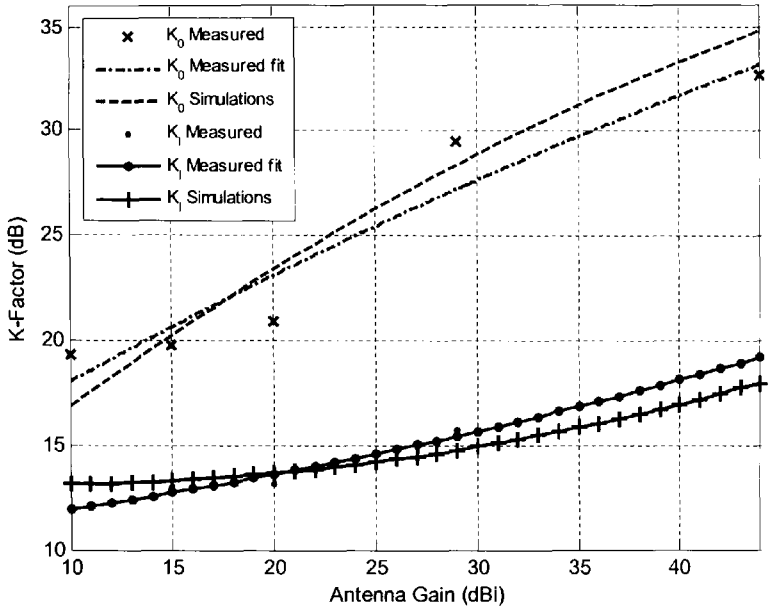

(a)

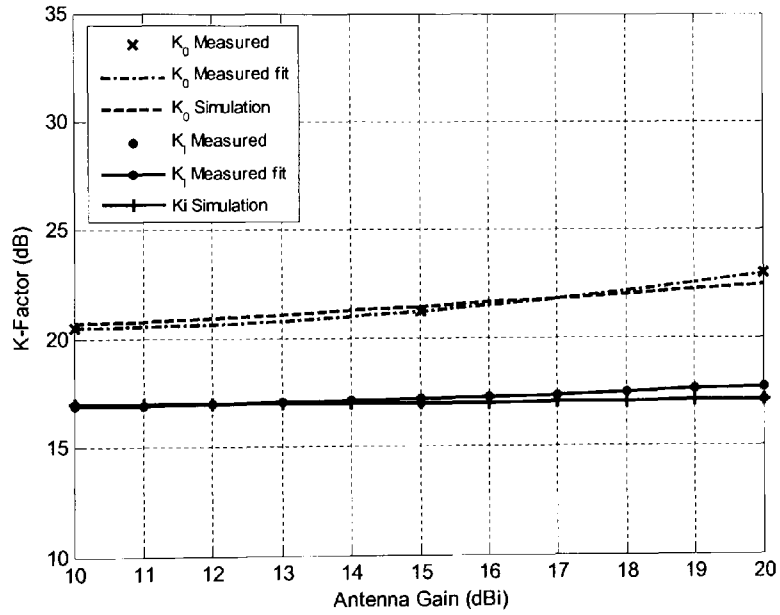

(b)

Figure 8: Rician *K*-factor values obtained for a number of antenna gains for SOP (I): (a) uplink for the case of $F2UV_1$ & $F2UV_2$ (b) downlink for the case of $F1DH_1$ & $F1DH_2$.

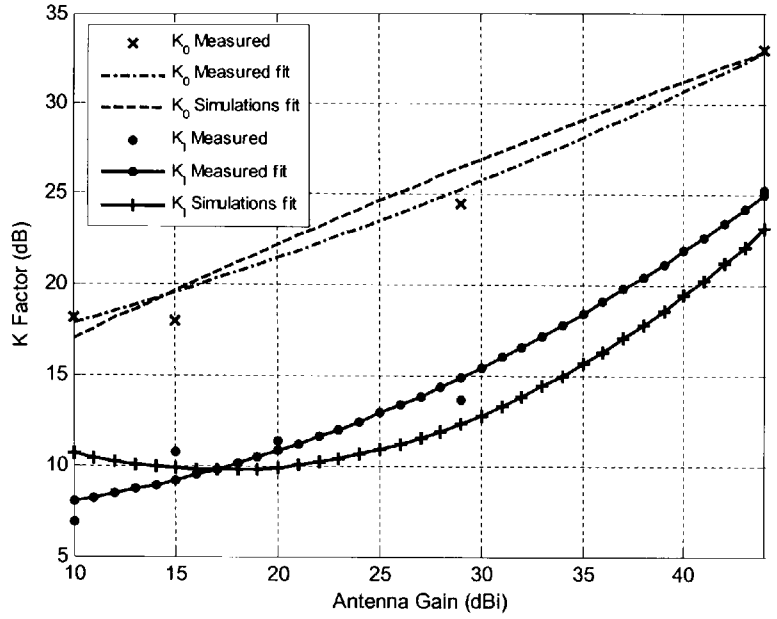

(a)

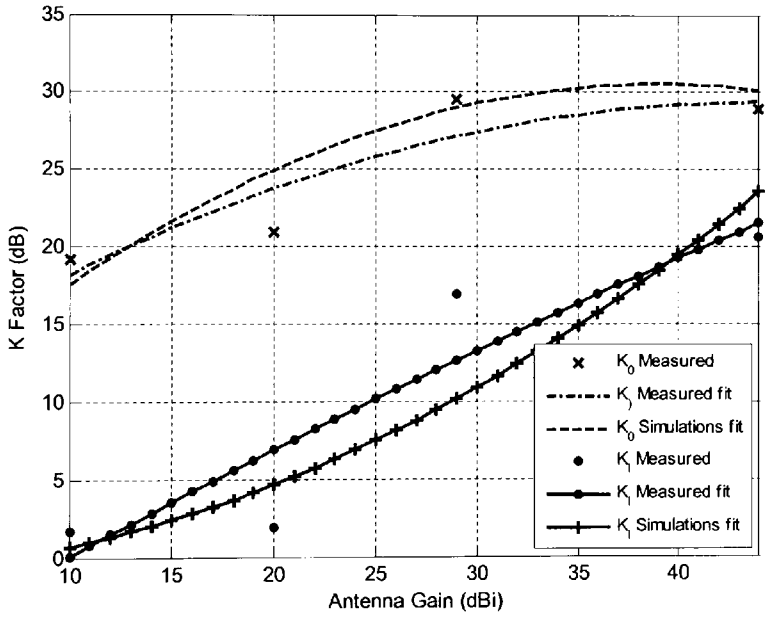

(b)

Figure 9: Rician *K*-factor values obtained for a number of antenna gains for the AP (I): (a) uplink for the case of $F1UH_4$ & $F1UV_4$, (b) downlink for the case of $F2DV_4$ & $F2DH_4$

Sample 3

Measurements and Statistical Modelling of Co-Channel Interferences for Local Point-to-Multipoint Distribution Systems

Z. Muhi-Eldeen [(1)], M.O. Al-Nuaimi [(2)], J. Richter [(3)], L.P. Ivrissimtzis [(4)]
[(1)(2)(3)] School of Electronics, University of Glamorgan, Pontypridd, CF37 1DL, UK
E-mail: zmuhield@glam.ac.uk
[(4)] Agere Systems, Microelectronics House, Ascot, SL5 8AD, UK
Email: leoivriss@agere.com

Abstract- **Due to the frequency reuse in Local Multipoint Distribution Systems (LMDS) networks, co-channel interference can occur from neighboring cells, leading to transmission errors and throughput degradations [1]. The paper presents and discusses measurements of a worst case scenario of co-channel interference, where the receiver falls in the bore-sight of a nearby cell transmitter operating at the same allocated band. A statistical propagation model has been used to predict the effects of multipath due to reflection and scatter by rooftops and building surfaces at millimeter wave frequencies. These are given in terms of Rician K-factor and CDF graphs. The model has been validated with narrowband field measurement campaigns conducted at 40GHz over radio links set up an industrial estate environment.**

Index Terms- **LMDS, cellular radio systems, co-channel interference, signal-to-interference ratio, statistical modeling.**

I. INTRODUCTION

Cellular LMDS are considered to be the next generation of Fixed Wireless Access systems (FWA) for providing wireless broadband communication links. Such radio systems are deployed using point-to-point (PTP) and/or point-to multipoint (PMP) topologies with the use of narrow beam directional antennas at the customer's premises.

Service areas in cellular LMDS are rather short in distances and are typically less than 2 kilometers [1-5]. At the millimeter frequency bands radiowave propagation in FWA systems is heavily dependent on the topographical conditions. This is due to many reasons and is primarily based on the fact that the wavelengths of the transmitted signals are very small (in the order of a few millimeters). At these frequencies it is well known that most building surfaces can be considered rough, causing diffuse scatter and low levels of specular reflections [2]. Moreover, at these high frequencies diffraction paths over and around buildings result in minimal contributions at the subscriber's terminal. Therefore the existence of dominant paths at large distances can be limited to some extent. In the deployment of the basic PTP systems, the base station transmitters are generally placed at lamp-post levels in order to limit the effects of any interference from the surrounding cells. With careful system planning, frequency channels can be more often reused in small cells leading to higher system capacities. Due to relatively short frequency reuse distances in the cell plan and the utilisation of highly directional antennas, such cells may be subject to significant interference levels arising from nearby co-channel cells, as shown in Fig.1.Therefore in the content of this work, a co-channel limited interference environment is considered.

The co-channel interference effects in cellular radio systems have been widely studied in the literature (see reference in [3]). However, neither measurements results nor statistical modeling of signal-to-interference ratios (SIR) at millimeter wave-length frequencies have been published yet.

This paper presents the co-channel measurement results conducted on industrial estate links in South Wales. The statistical propagation model presented in [4] was applied here with slight enhancements in order to predict variations and mean values of the received SIR at the receiver's terminals. The dual frequency plan for a 16 cluster of ATM data services specified in the UK MPT 1560 is implemented [5]. Such frequency plan is shown in Fig.1 where the 360° area of the base station is divided in 90° sectors. Each sub-cell has been given a unique frequency and polarization in order to mitigate adjacent cell interference.

From the CRABS project report [6], it has been shown that the in such a four cell repeat configuration, the total uplink capacity is about 386Mbit/s when using QPSK modulation. This claims to provide adequate capacities and SIR levels for at least the next generation of LMDS systems.

Description of a number of possible interference mechanisms in a FDD LMDS with TDMA access have been presented in [7]. The work presented here takes into

consideration the worst case co-channel intercell interference scenario. This is illustrated in Fig.1, where the remote terminal 1 and 2 not only operate at the same frequency band, but the latter also lies within the bore-sight of the co-channel transmitter of 1.

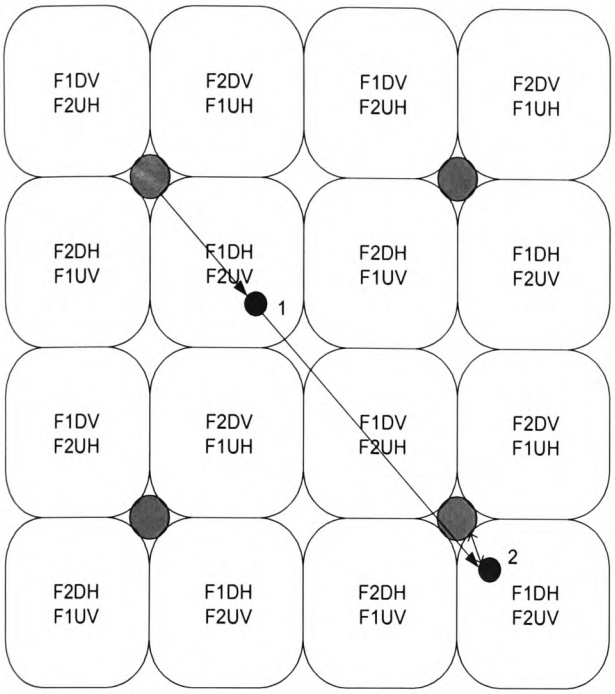

Figure 11 16 cell cluster for ATM data services of dual frequency/dual polarization plan.

II. MEASUREMENT SET-UP

The two links in the above were conducted using narrowband field measurements at 40 GHz. The Tx-Rx separations are 650m and 127m for the interferer and desired links, respectively. The interferer path consists of a number of industrial buildings that are widely diverse both in their shapes and footprints. Whereas for the desired path, apart from a few of nearby parked vehicles, the link is almost clear of any obstacles. Transmitter heights are 15m and 6.3m for the interferer and desired links respectively.

Standard pyramidal horn antennas were deployed during these measurements. In both links, the signal was transmitted from a 20dBi gain antenna and received through three antenna gains of 10, 15 and 20dBi used at the receiver terminal.

III. STATISTICAL MODELING

The statistical model developed at the University of Glamorgan describes the total received field as the superposition of the direct field and a sum of scattered field contributions that are randomly distributed representing either building rooftops, walls or illuminated ground patches. The phases of each of these scattered fields are due to the reflection or scattering process and are uniformly distributed over the interval 0 to 2π. Full details on this model can be found in [8].

IV. MEASUREMENT RESULTS AND ANALYSIS

A. Signal-to-Interference Ratios

Adequate signal-to-interference ratios are essential for any reliable communication system. The effect of co-channel interference can therefore be evaluated by investigating the SIR given by the following formula:

$$SIR(dB) = 10\log_{10}\frac{\Omega_0}{\Omega_i} \tag{1}$$

where Ω_0 and Ω_i are the average signal powers received from the desired and interferer paths respectively.

During the measurements, it was assumed that a line-of-sight existed between the transmitter and receiver and hence, a Rician fading environment can be effectively assumed for the measured received fields. Such a realistic assumption can be validated by the Rician K-factor values obtained.

Knowledge of the Rician K-factor is a principal measure in determining performances and signal strengths in LMDS channels. The K-factor is physically defined as the ratio of signal power in the direct component over the mean scattered power, given by:

$$K = 10\log 10\left(\frac{s^2}{2\sigma^2}\right) \tag{2}$$

where s^2 is the non-centrality parameter and σ^2 is the variance of the received field.

The Rician parameters s, σ and the K-factor have been extracted from the time-series measured data using the method of moments [9]. Given a fading channel with a Rician distributed signal and a Rician interferer (Rician/Rician), the SIR can now be described using these parameters and is given by [10]:

$$SIR(dB) = 10\log_{10}\frac{\sigma_0^2(1+K_0)}{\sigma_i^2(1+K_i)} \tag{3}$$

where K_o, K_i are the Rician K-factors and σ_o, σ_i are the incoherent power for the desired and interference signals respectively.

Higher values of K_o, are desirable and correspond to better detection levels and link availabilities, whereas higher values of K_i imply stronger co-channel interfering levels and greater outage possibilities.

The extracted values for K_o and K_i from the measured and the predicted data are summarized in Table 1.

TABLE I
RICAN K-FACTOR VALUES

Ant Gain	K_0(dB)		K_I(dB)	
	Measured	Predicted	Measured	Predicted
10	19.2	17.2	11.9	11.1
15	19.8	16.63	13.1	11.76
20	20.9	17.4	13.5	12.77

The variation observed in the Rician K-factor at the interferer link was expected due to several factors, including multipath scatters generated from the surrounding buildings and the existence of vegetation across the link. In comparison with the measured values, the statistical predictions are relatively precise.

Fig.2 shows the received mean SIR for different receiver antenna gains obtained form using Eq. (3). These correspond to the mid-point values obtained from the predicted CDF curves addressed in the next session.

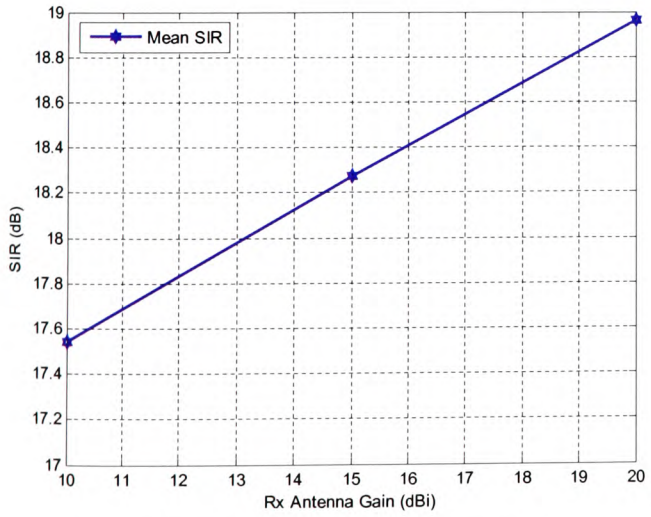

Figure 2 Measured mean SIR with different antenna gains

B. Cumulative Distributions

The received CDF curves of the SIR values derived from both the measurement results and the model predictions are presented in Fig.2. The purpose of the CDF graphs is to compare the simulated predictions against the measured distributions. The model's statistical predictions agree well with the measured parameters. More specifically, the mean values of SIR from the measured and simulated data are almost identical.

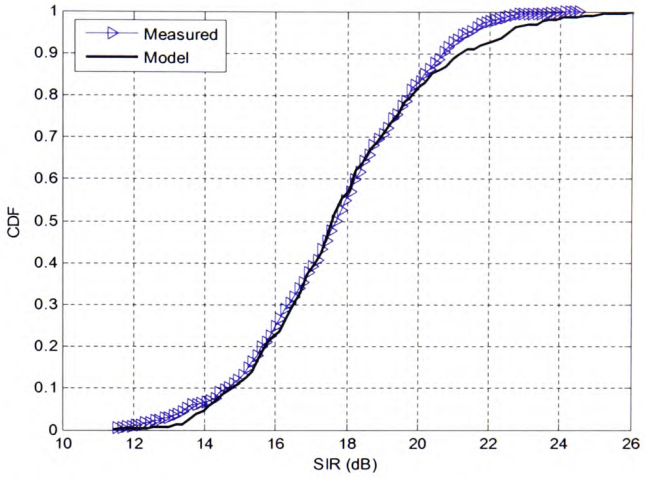

Figure 2.a Measured and predicted CDF for a 10 dBi antenna gain

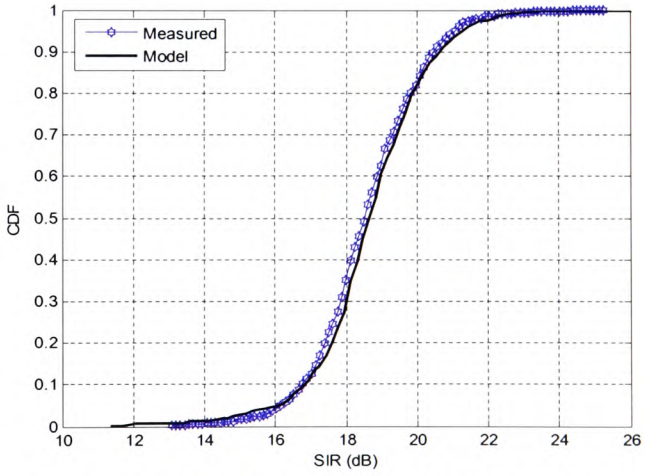

Figure 2.a Measured and predicted CDF for a 15 dBi antenna gain

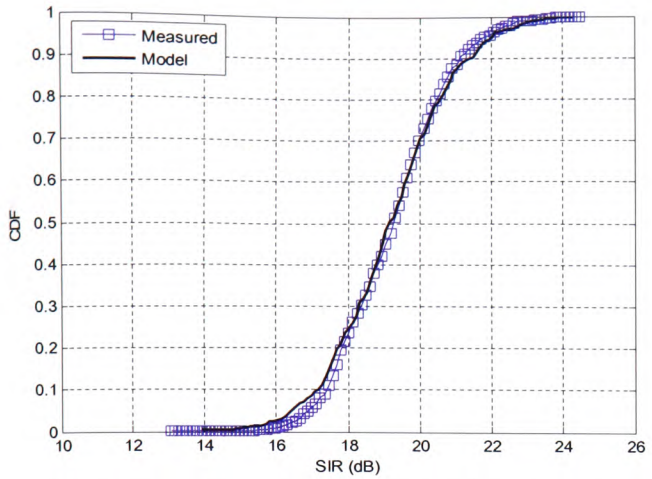

Figure 2.a Measured and predicted CDF for a 20 dBi antenna gain

From the above figures, for different antenna gain receivers it can also be observed that the CDF gradient reveals a slightly steeper slope as the antenna gain increases.

C. Outage Probabilities

LMDS are designed to be available essentially at all times with adequate signal reception levels. Outage probability provides an effective statistical measure of the radio link performance in a co-channel interference limited environment, where frequencies are reused over relatively short distances. It can be defined as the probability that the ratio of the desired signal power to the interference power (SIR) falls below a predefined threshold that depends on the modulation type and other system design requirements [11].

The analytical expression of the outage probability of a Rician/Rician channel is given by [12]:

$$P_{out} = Q\left[\sqrt{\frac{2K_I R}{b_1 + R}}, \sqrt{\frac{2K_0 b_1}{b_1 + R}}\right] - \frac{b_1}{b_1 + R}\exp\left[-\frac{K_I R + K_0 b_1}{b_1 + R}\right] I_0\left(\frac{\sqrt{4K_I K_o R b_1}}{b_1 + R}\right) \quad (4)$$

Where $Q(.)$ the Marcum Q-function, I_0 is the zeroth order modified Bessel function of the first kind, R is is the predefined protection ratio and $b_1 = \sigma_0^2/\sigma_I^2$.

The authors of [13] have exemplified the accuracy of (4) by overlaying the analytically determined average probability with simulation results, thus, validating the use of (4) in estimating the outage probability for a given system.

Fig.3 illustrates the effects of the protection ratio R on the outage probabilities for the three different antenna gains. The measured SIR values presented for the different antenna gains are within less than 2dB margin. Therefore the effect of receiver antenna gain on developing the system SIR performance in such case is rather minimal. Conversely the choice of receiver antenna gain for R values up to 12dB is vital and places large difference on outage probability. Modulation schemes such as 16-QAM are beneficial for providing high data rates and are generally associated with R values greater than 14dB. At these high threshold values it is found that the outage probability is most likely to increase. Therefore a trade-off is implied between the choice of the modulation scheme and the outage probability.

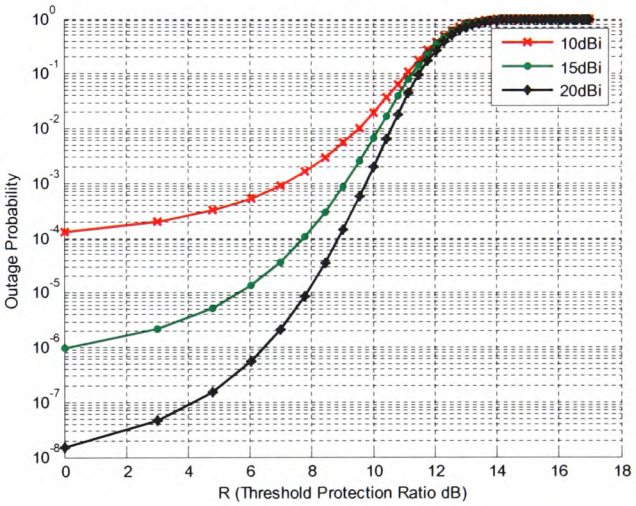

Figure 3 Measured outage probability for different threshold values

For illustration purposes, R is set to 15dB in (3). The outage probability obtained for the different antenna gains is shown in Fig.4.

Table 1 suggests that a small change in the obtained values of K_o and K_i at the associated gains results in significant changes in the outage probabilities. It is worth reminding that the measurements consider only the worst-case scenario, where the susceptible receiver lies in the bore-sight of a nearby interferering transmitter. Consequently, a higher gain antenna will provide higher values of K_i for this extreme case.

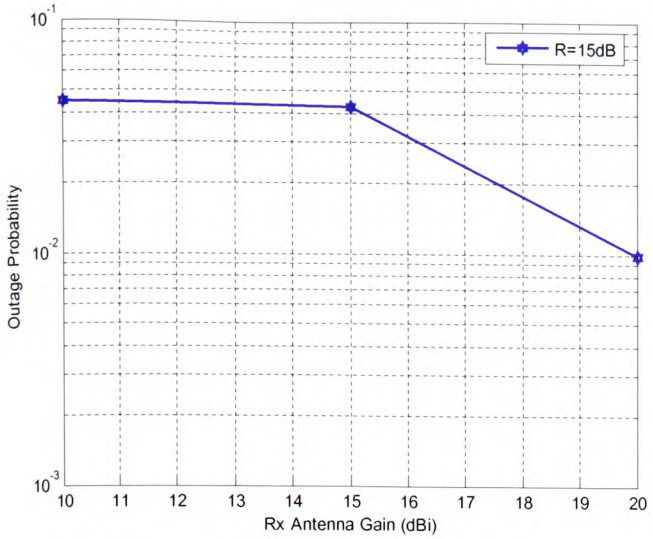

Figure 4 Outage probabilities (R=15) for the three antenna gains

Despite these increments in K_i, the outage probability indicates improved link availabilities with a 20dBi receiver antenna. The values of K_o are found to be relatively close at the different antenna gains, while K_i values experienced larger variations (in the range of 4dB). Furthermore, the variations observed in the received levels are partly due to displacements (in the order of a couple of wavelengths) in receiver positions along the link, which are introduced to demonstrate the multipath nature of the field and enable its statistical modeling.

Another set of measurements were conducted with alignment displacements perpendicular to the same link. Unlike the longitudinal link, these measurements yielded a decrease in the values obtained for K_i as shown in Table 2. In both cases, the benefit of deploying higher antenna gains is highlighted.

TABLE II
RICAN K-FACTOR VALUES EXTRACTED FROM THE PERPENDICULAR LINK

Ant Gain	K_0(dB)	K_I(dB)
10	9.3	5.7
15	12.1	5.2
20	13.5	4.8

V. CONCLUSIONS

Co-channel interference is one of the main focuses of LMDS cellular planners. Measurements were conducted at 40GHz to statistically model and assess the performance of a worst case scenario in co-channel interference limited LMDS cell. Good agreements have been presented between the measurements results and the model's prediction in terms of the Rician K-factor and CDF curves. The measurements conducted indicated that utilization of highly directional antennas in both the transmitter and receiver terminals is beneficial in increasing the associated SIR and, even more significantly, at decreasing the outage probabilities associated with protection ratios less than 12dB. It has also been shown from the measured data the importance of the Rician K-factor and the protection ratio in achieving the required outage probabilities.

Further measurements and research investigations planned will take into consideration the dual polarization effects on interfering mechanisms including the 36 cluster ATM data service channel configuration. Given that the level of interference is a function of the distances over which frequencies channels are reused, future research have to consider the statistical modeling and estimation of the minimum reuse distances for acceptable outage probability levels.

REFERENCES

[1] Matsuda, M. Watanabe, K. "26-GHz band FWA systems employing co-channel interference avoidance method using TDMA/TDD frame timing control", Global Telecommunications Conference, 2004. GLOBECOM '04. IEEE.
[2] Z .Muhi-Eldeen, M.O. Al-Nuaimi, J. Richter, L.P. Ivrissimtzis, "On the Performances of non-line-of-sight paths for fixed wireless access systems", 49th Annual IEEE Globecom Conference 2006, California, USA, 2006.
[3] Yu-Dong Yao, Asrar U. H. Sheikh, "Investigations into Cochannel Interference in Microcellular Mobile Radio Systems", IEEE Transactions on Vehicular Technology Vol 41, No 2, May 1992.
[4] L.P. Ivrissimtzis, M.O. Al-Nuaimi, J. Richter, J. Zhang, "A Statistical Model of the Urban Propagation Channel in Fixed Wireless Systems", International Union of Radio Science 27th General Assembly URSI 2002 Maastricht, Netherlands, August, 2002.
[5] MPT 1560, "Performance specification for digital Multi Point Video Distribution Systems (MVDS) transmitters and transmit antennas operating 40.5–42.5 GHz", Radio communications Agency, UK, 1995.
[6] Acts Project 215, Cellular Radio Access for Broadband Services (CRABS), Specification of Next Generation of LMDS Architecture D2P1B, 1999.
[7] L.P. Ivrissimtzis, M.O. Al-Nuaimi, J. Richter, J. Zhang, "A Statistical Model of the Urban Propagation Channel in Fixed Wireless Systems", International Union of Radio Science 27th General Assembly URSI 2002 Maastricht, Netherlands, August, 2002.
[8] J. Zhang, J. Richter, M.O. Al-Nuaimi, L.P. Ivrissimtzis, "Statistical Modelling at 20 GHz for Fixed Wireless Access Systems in Urban Multipath Environments", IEE Proceedings on Microwave, Antenna and Propagation, Vol. 152, No. 4, August 2005.
[9] L. J. Greenstein, D. G. Michelson, and V. Erceg, "Moment-Method Estimation of the Ricean K-Factor", IEEE Communications Letters, Vol. 3, No. 6, June 1999.
[10] G.K. Karagiannidis, S.A. Kotsopoulos, and P.T. Mathiopoulos, "A Generalised approach for evaluation of outage performance in micro- and pico-cellular networks", IEE Proceedings - Communications -- April 2002 - - Volume 149, Issue 2, p. 123-128.
[11] Annamalai, A. Tellambura, C. Bhargava, V.K., "Simple and accurate methods for outage analysis in cellular mobile radio

systems-a unified approach", IEEE Transactions on Communications, Vol 49, No. 2, February 2001.
[12] Tjhung, T.T., Chai, C.C., and Dong, X.: "Outage probability for a Rician signal in L Rician interferers", Electron. Lett., 1995, 31, (7), pp. 532–533.
[13] A.H. Wong, M.J. Neve, and K.W. Sowerby "Performance analysis for indoor wireless systems employing directional antennas", IEE Proceedings - Communications -- December 2005 -- Volume 152, Issue 6, p. 890-896